

INFORMATION TO USERS

This manuscript has been reproduced from the microfilm master. UMI films the text directly from the original or copy submitted. Thus, some thesis and dissertation copies are in typewriter face, while others may be from any type of computer printer.

The quality of this reproduction is dependent upon the quality of the copy submitted. Broken or indistinct print, colored or poor quality illustrations and photographs, print bleedthrough, substandard margins, and improper alignment can adversely affect reproduction.

In the unlikely event that the author did not send UMI a complete manuscript and there are missing pages, these will be noted. Also, if unauthorized copyright material had to be removed, a note will indicate the deletion.

Oversize materials (e.g., maps, drawings, charts) are reproduced by sectioning the original, beginning at the upper left-hand corner and continuing from left to right in equal sections with small overlaps. Each original is also photographed in one exposure and is included in reduced form at the back of the book.

Photographs included in the original manuscript have been reproduced xerographically in this copy. Higher quality 6" x 9" black and white photographic prints are available for any photographs or illustrations appearing in this copy for an additional charge. Contact UMI directly to order.

UMI

A Bell & Howell Information Company
300 North Zeeb Road, Ann Arbor, MI 48106-1346 USA
313/761-4700 800/521-0600

UNIVERSITY OF CALIFORNIA
Los Angeles

A Search for Emission-line Stars Near the Galactic Center

A dissertation submitted in partial satisfaction of the requirements for the degree
Doctor of Philosophy in Astronomy

by

Donald Frank Figer

1995

UMI Number: 9608057

UMI Microform 9608057

Copyright 1995, by UMI Company. All rights reserved.

**This microform edition is protected against unauthorized
copying under Title 17, United States Code.**


UMI

**300 North Zeeb Road
Ann Arbor, MI 48103**

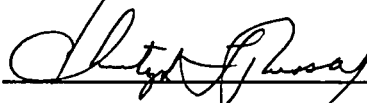
The dissertation of Donald Frank Figer is approved.



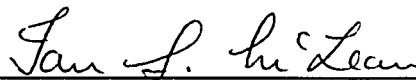
Mark Morris



Eric E. Becklin



Christopher T. Russell



Ian S. McLean, Committee Chair

University of California, Los Angeles

1995

This work is dedicated to my parents,
Donald L. Figer and Louise M. Vitantonio

TABLE OF CONTENTS

LIST OF FIGURES	vii
LIST OF TABLES	x
ACKNOWLEDGEMENTS	xi
VITA	xii
PUBLICATIONS	xiii
ABSTRACT OF THE DISSERTATION	xiv
I. Introduction	1
A. Motivation	2
B. Introduction to star formation	7
C. Molecular clouds in the Galactic Center environment	8
1. pressures, temperatures, densities, compositions	8
2. implications for star formation near the Galactic Center	10
D. Star formation near the Galactic Center	12
1. assessments of global star formation in the region	13
2. sites of star formation	14
3. central cluster	28
II. Massive stars	31
A. evolution through HR diagram	31
B. Wolf-Rayet stars	34
1. observational classification	35
2. the nature and evolution of WR stars	38
a. stages	39
b. mass-loss and evolution	41
3. wind theory	43
4. observations	44
a. M_v and luminosity	44
b. radius and temperature	47
c. mass	48
d. wind characteristics	49
e. numbers and distribution	49
III. A search for hot, young, emission-line stars near the Galactic Center	52
A. project goals	53
B. survey strategy	55
1. coverage	55
a. spatial	55
b. stellar types	56
c. wavelength	64

	1).	extinction	64
	2).	emission lines	67
2.	phase I: narrow-band survey		69
	a.	filter profiles	70
	b.	sensitivities and expected S/N for targets	72
	c.	observing procedures	77
	d.	analysis methods	78
3.	phase II: spectroscopy		82
	a.	grisms	82
	b.	sensitivities and expected S/N for targets	88
	c.	observing procedures	90
	d.	analysis methods	93
IV.	Observations		96
	A.	instrument and setup, dates, filters, grisms, telco	96
	B.	calibrations: standards, flats, bias, dark, sky, OH lines	98
V.	Data reduction		101
	A.	phase I	101
		1. IRAF script TWOCHANGC	101
		2. the spreadsheet engine	104
		3. choosing targets	104
	B.	phase II	111
		1. sky/bias/dark subtraction and flatting	112
		2. wavelength calibration	112
		3. aperture extraction	120
		4. correction for telluric absorption and filter profile	120
		5. flux calibration	123
		6. dereddening	123
		7. equivalent widths and line ratios	123
VI.	Data		124
	A.	Survey image	124
	B.	Photometry	124
	C.	Flux excess for template stars	131
	D.	Spectra	137
VII.	Analysis		175
	A.	Extinction from stellar data	175
	B.	Extinction from Br γ emission	182
	C.	Velocity	185
VIII.	Discovery of Emission-line Stars in the Quintuplet		190
	A.	Abstract	190
	B.	Introduction	190
	C.	Observations	191
	D.	Discussion	197

IX.	Conclusions	201
A.	Emission-line stars near the Galactic Center	201
B.	Remaining questions and future prospects	203
REFERENCES		206

LIST OF FIGURES

Figure 1. V-band and K'-band images of the survey region.	6
Figure 2. Positions of star-formation regions listed in Table 1.	16
Figure 3. 2 cm contour plot of G HII region from Ho et al. (1985).	17
Figure 4. HII regions A-D from Yusef-Zadeh & Morris (1987).	18
Figure 5. CS contours overlayed on a 6 cm radiograph. Positive velocity CS emission peaks just northwest of the A-D compact HII regions.	19
Figure 6. 6 cm radio contour plot of HII regions north of the Galactic Center. .	21
Figure 7. K' image of the Quintuplet cluster.	23
Figure 8. 6 cm radiograph showing the Sickles, Pistol, and non-thermal linear filaments.	24
Figure 9. K' image of the "Arches Cluster" near the Thermal Arched Filaments. The image is $\sim 42''$ square, or 1.7 pc at the distance of the Galactic Center.	27
Figure 10. M0.25-0.01 at $350 \mu\text{m}$ from Lis et al. (1994). A spectrum for the H_2O maser and a 3.55 cm contour plot for the compact radio source are also shown.	29
Figure 11. Upper-left region of HR diagram from Maeder (1991a).	32
Figure 12. Minimum mass limits for O-stars and WR stars from Maeder (1991b).	40
Figure 13. Upper HR diagram showing HD limit and evolutionary tracks for massive stars from Maeder (1989).	41
Figure 14. Theoretical surface abundances and evolution of $85 M_{\odot}$, $Z = 0.04$, star from Maeder (1991a).	41
Figure 15. M_V -subtype data for WR stars from Abbott & Conti (1987).	46
Figure 16a. R,T solutions using HeI and HeII emission lines from Hamann et al. (1993).	47
Figure 16b. L, T for WR stars from Hamann et al. (1993).	48
Figure 17a. WR/O vs. Z from Maeder & Meynet (1994).	51
Figure 17b. WC/WR versus Z from Maeder & Meynet (1994).	51
Figure 18. Schematic of the GC survey.	57
Figure 19. Near-infrared spectra for WN type stars from Williams (1983) (top) and Hillier (1983) (bottom).	60
Figure 20. K-band spectra for WC type stars from Smith & Hummer (1988). . .	61
Figure 21. K-band spectra of OB main-sequence stars from Hanson & Conti (1995).	62
Figure 22. Near-infrared spectra for LMC emission-line stars. The eight spectra on the left are from McGregor et al. (1988a), while the figure on the right is from McGregor et al. (1988b). See text for classifications.	63
Figure 23. Interstellar extinction law.	65
Figure 24. Apparent K magnitudes for luminous stars at the Galactic Center. . .	66
Figure 25. Predicted K magnitudes for WR stars at the Galactic Center.	67
Figure 26. Filter transmission profiles.	71
Figure 27. Last element of 6-element reimaging lens in the short-wave channel and the array. Rays for an off-axis field point are drawn.	81
Figure 28. Illustration for calculating path difference from Feynman (1963). . . .	83
Figure 29. Geometry for grism from Palmer & Loewen (1994).	84

Figure 30a. Wavelength versus pixel number in H-band. Variation from a straight line is shown on the right axis.	87
Figure 30b. Same as Figure 30a but for K-band.	87
Figure 31. Relative airmass correction for June 17.	100
Figure 32. Number versus $\Delta\text{sum}(\text{Br}\gamma)$ for frame 364.	109
Figure 33. Continuum image (top) and $\text{Br}\gamma$ -continuum difference image (bottom) for location 64.	110
Figure 34a. Deviation from a first order fit. Residuals are in \AA	114
Figure 34b. Deviation from a higher order fit. Residuals are in \AA	114
Figure 35. Sky spectrum. Intensity scale is in counts for a 300 second exposure per pixel for 10 summed rows.	116
Figure 36. Wavelength to pixel number fit for sky lines.	117
Figure 37. Raw spectrum for BS6378.	122
Figure 38. Color picture of survey where H has been coded as blue and K as red.	125
Figure 39. Difference between photometry from this study to published photometry from Haller (1992).	126
Figure 40. Flux excesses for template stars observed on June 17, 1994.	133
Figure 41. Flux excesses for template stars observed on June 18, 1994.	134
Figure 42. Flux excesses for template stars observed on June 19, 1994.	135
Figure 43. Flux excesses for template stars observed on June 21, 1994.	136
Figure 44. Spectra for water maser counterpart, object 37345, and SW Vir. ...	138
Figure 45a. Spectra for new Quintuplet emission-line stars, WC template stars, and Q1.	143
Figure 45b. Spectra for previously known Quintuplet stars: Q8, Q10, QG, QD, Q5, Q3.	144
Figure 45c. Identifying K' image for stars in the Quintuplet.	145
Figure 45d. Spectra for serendipitous Quintuplet stars: X1, X2, X4, X5, X6, X7.	146
Figure 45e. Spectra for serendipitous Quintuplet stars: X8, X9, X10, X11, X12, X13.	147
Figure 45f. Spectra for serendipitous Quintuplet stars: X14, X15, X16.	148
Figure 46a. Spectra for stars near H3: H3A, H3B, H3C, H3D, H3N.	151
Figure 46b. Spectra for stars near H1, H2, H5W: H1A, H1C, H1N, H2B, H5WN, H5WA.	152
Figure 46c. Spectra for stars near H5 and H6: H5EA, H5EB, H5EC, H5ED, H6.	153
Figure 47a. Spectra for stars in frame 364: 36614, 36415, 36416, 36417, 36422, 36429.	155
Figure 47b. Spectra for stars in frame 364 and h11: 36443, h1132, h1139, h1141, h1149.	156
Figure 48a. Spectra for stars near the "Parachute": nebular region, 3656, 3659, 36513, 36516.	158
Figure 48b. Spectra for stars in frames A11 and 371: A1133A, A1133B, A1133C, 37119, 37113.	159
Figure 49a. Spectra for water-absorption stars within 4 pc of the GC: 37321, 37336, 37345, 37351.	161

Figure 49b. Identifying K' image for water-absorption stars near the Galactic Center.	162
Figure 50. Spectra for water-absorption stars near G-0.14-0.09: 3926, 39211, 39217, 39228, and 39238.	164
Figure 51a. Spectra for Galactic Center objects: AF, AFN, IRS14NE/SW, IRS15NE, IRS8, IRS16C/SW.	168
Figure 51b. Spectra for Galactic Center stars: IA, IB, IC, ID, IE, IM.	169
Figure 51c. Spectra for Galactic Center stars: IRS14NE, IRS20, IRS33, IRS7.	170
Figure 51d. Spectra for Galactic Center stars: IF, IG, IH, IJ, IRS15NE, IRS16NW.	171
Figure 51e. Identifying K' image for stars near the inner parsec.	172
Figure 52. Spectra for Wolf-Rayet template stars: 108, 123, 124, 128, 130, 134.	174
Figure 53. K (K = 17 to 7) versus H-K diagrams (H-K = 0 to 4).	178
Figure 54. H-K versus K-m _{3,15} diagrams.	181
Figure 55. K-band spectrum (R~530) of star 2 (bottom) and the new WC9 star WR121 (top). The intensity scale of the spectrum for WR121 has been divided by 10. All spectra have been dereddened and flux-calibrated.	194
Figure 56. K-band spectrum of the new LBV candidate, star 3.	195
Figure 57. K-band spectrum of the new WN9 star, star 1.	196

LIST OF TABLES

Table 1: Star Formation Sites within 50 pc of the Galactic Center	15
Table 2: Observational Classification Scheme for WR Stars	37
Table 3: Observed Surface Abundances for WR Stars	38
Table 4: Extinction Law	65
Table 5: Strong Emission Lines in Emission-line Stars	69
Table 6: Filter Data	72
Table 7: S/N Model Parameters	76
Table 8: Expected S/N for Narrow-band Survey for 60 sec. Integration	77
Table 9: Grism Parameters	88
Table 10: Expected S/N for Spectroscopic Survey for 180 sec. Integration	89
Table 11: Vacuum Wavelengths for Emission Lines in the K-band	95
Table 12: Observing Log for Phase I	96
Table 13: Observing Log for Phase II	97
Table 14: Flux Excess for Frame 364	107
Table 15: Central Wavelengths for Sky Emission Lines	118
Table 16: Aperture Photometry for Targets	127
Table 17: PSF Photometry for Selected Targets	131
Table 18: Statistics for data used in Figure 53	179
Table 19: Bry line shifts and widths	187
Table 20: Parameters for the Quintuplet Emission-line Stars	193

ACKNOWLEDGEMENTS

I thank many of my patient elders who encouraged my interest in Astronomy and became my mentors. At an early age, my uncle, Carmen J. Vitantonio, stimulated my interests through many discussions as we stood under the stars. Richard Benz, my high school science teacher, motivated me to continue pursuing my scientific interests and provided me the opportunity to meet and study with professional astronomers.

Professor Robert A. Schluter played a most active role in my development as a scientist while I was an undergraduate student at Northwestern University. I am grateful, and fortunate, for the wisdom which he imparted to me on matters ranging from simple textbook problems to major life choices. To this day, he remains as my mentor, advisor, and friend.

I thank several individuals at the University of Chicago. Roger H. Hildebrand, my advisor, invited me into his research group, giving me the opportunity to learn from the best in the field. Al Harper was tirelessly patient and available to talk about my interest, regardless of the late hour. Mark Hereld helped me become more independent and methodical in my approach, with his daily proddings to "work faster, work harder!"

I am greatly indebted to Ian S. McLean, Mark Morris, and Eric E. Becklin, who welcomed me to UCLA. Through the opportunities they gave me, I was able to realize my wish to study the Galactic Center using the most advanced near-infrared technology available. I am especially grateful to Ian for the inspirational example he sets every day and for his endless support.

I also thank my friends and fellow students, in particular, Murray D. Silverstone, Steve Martin, and John Smetanka. Finally, I thank my family who have always supported me in my efforts.

VITA

October 5, 1966	Born, Euclid, Ohio
1986-1989	Undergraduate Researcher Northwestern University
1989	B.A. Physics/Mathematics/Astronomy
1989-1991	Research Assitant University of Chicago
1991	M.S. Astronomy & Astrophysics University of Chicago
1991-1992	Resarch Technician University of Chicago
1992-1993	Teaching Assistant University of California, Los Angeles
1993-1995	Research Assitant University of California, Los Angeles

PUBLICATIONS

- Figer, D. F., McLean, I. S., & Morris, M. 1995, *Two New Wolf-Rayet Stars and an LBV Star in the Quintuplet (AFGL2004) Near the Galactic Center*, Astrophysical Journal Letters, in press
- Levine, D. A., Figer, D. F., Morris, M., & McLean, I. S. 1995, *A Circumstellar H₂O Maser Associated with the Galactic Circumnuclear Molecular Disk?*, Astrophysical Journal Letters, in press
- Figer, D. F., McLean, I. S., & Morris, M. 1995, *Discovery of Two Wolf-Rayet Stars Near the Galactic Center*, Bulletin of the American Astronomical Society, 26, 1348
- Figer, D. F., Becklin, E. E., McLean, I. S., & Morris, M. 1994, *Discovery of Luminous NIR Sources Associated with Ionized Gas Near the Galactic Center*, in Infrared Astronomy with Arrays, ed. I. S. McLean (Dordrecht: Kluwer), 545
- McLean, I. S., Macintosh, B., Liu, T., Casement, L. S., Figer, D. F., Teplitz, H., Larson, S., Lacayanga, F., Siverstone, M. D., & Becklin, E. E. 1994, *Performance and Results with a Double-Beam Infrared Camera*, in Instrumentation in Astronomy VIII, ed. D. Crawford (Bellingham:SPIE) 457
- Hildebrand, R. H., Davidson, J. A., Dotson, J., Figer, D. F., Novak, G., Platt, S. R., & Tao, L. 1993, *Polarization of the Thermal Emission from the Dust Ring at the Center of the Galaxy*, Astrophysical Journal, 417, 565
- McLean, I. S., Becklin, E. E., Brims, G., Canfield, J., Casement, L. S., Figer, D. F., Henriquez, F., Huang, A., Liu, T., Macintosh, B., & Teplitz, H. 1993, *The UCLA Double-Beam Infrared Camera System*, in Infrared Detectors and Instrumentation, ed. A. Fowler (Bellingham:SPIE), 513
- Morris, M., Davidson, J. A., Werner, M., Dotson, J., Figer, D. F., Hildebrand, R. H., Novak, G., & Platt, S. R. 1992, *Polarization of the Thermal Arches at the Galactic Center*, Astrophysical Journal Letters, 399, L63

ABSTRACT OF THE DISSERTATION

A Search for Emission-line Stars Near the Galactic Center

by

Donald Frank Figer

Doctor of Philosophy in Astronomy

University of California, Los Angeles, 1995

Professor Ian S. McLean, Chair

The purpose of this dissertation is to find and characterize the hot, young emission-line stars within 50 parsecs of the Galactic Center. These stars are thought to be less than 10^7 years old, and they represent the most easily identifiable components of recent star formation. Inspired by the recent discovery of emission-line stars within the central parsec, this study constitutes the first wide-area search for such stars. New near-infrared techniques were developed and used to discover and characterize emission-line stars in the survey region. The efforts in this project formed the basis for commissioning the spectroscopic mode of the new UCLA double-beam infrared camera.

Several new emission-line stars were found, and they support the conclusion that star formation over the time period of ~ 0.2 to 1×10^7 years has been limited to regions near thermal radio emission in the survey range. The types of stars in each star formation region suggest considerable variation in birth times, such that stars in the younger sites are still enshrouded by dust and have not yet evolved into the Wolf-Rayet

phase. Measured velocities for the emission-line stars and HII regions are consistent with a physical connection between the hot stars and radio continuum features.

The variations in extinction over the survey region support earlier suggestions that the obscuring molecular clouds along the line of sight are actually at the distance of the Galactic Center. Two molecular clouds revealed in the extinction data are thought to be star-formation sites, but no emission-line stars were found at or near them.

Two new emission-line stars have been found in the inner parsec where approximately two dozen similar stars are known to exist. These stars are thought to be in a transitional evolutionary phase between the main sequence and the Wolf-Rayet stage. Their existence provides important clues about recent star formation in the Galactic Center, but a rigorous explanation for their origin, stellar mergers versus starburst, still awaits an assay of the OB-star population or an accurate determination of the number of carbon versus nitrogen Wolf-Rayet stars.

I. Introduction

Previous near-infrared searches for evolved hot stars within $r_{\text{proj}} < 50$ pc of the Galactic Center have been based upon targeted surveys of radio selected regions. This approach has confirmed the presence of several recent star formation sites near, and perhaps at, the Galactic Center. This thesis describes a wide-area search for such stars using near-infrared narrow-band filters and near-infrared spectroscopy. The purpose of the project is to assess the ubiquity of these evolved massive stars and to use them as probes of recent star formation near the Galactic Center.

This thesis has been possible due to two recent technological advances. First, sophisticated infrared arrays with high quantum efficiency and low dark current are now readily available and being used in astronomical instruments. These instruments have arrays with up to 256^2 pixels while their technological predecessors of just a few years ago contained single element bolometers. Modern infrared cameras can now image moderately large areas of sky. The rapid pace of infrared array technology will soon bring even larger arrays with 1024^2 pixels (McLean 1995).

The second technological achievement came from the UCLA Infrared Imaging Detector Laboratory where Prof. Ian S. McLean established a new group which conceived, built, and commissioned the world's first high-throughput, multi-channel infrared camera (McLean et al. 1993; McLean et al. 1994). This camera contains two infrared arrays allowing imaging, spectroscopy, and polarimetry at two wavelengths simultaneously. In ten nights during the Summer of 1994, we accumulated more data with the UCLA double-beam camera than could be obtained with a suite of other existing near-infrared instruments with even more observing time.

The survey successfully detected six new emission-line stars. Four of these stars are in the "Quintuplet" cluster located ~ 35 pc in projection from the Galactic Center. Two of them have been spectroscopically classified as WC9 and WN9, while the other two have quite weak HeI 2.058 μm emission and otherwise relatively flat spectra without CO absorption. Their spectral classifications are somewhat ambiguous because a unique match could not be found between their spectra and the spectra of the template stars. The last two stars are within the inner parsec of the Galactic Center and are probably in a transitional evolutionary state between the main-sequence and the Wolf-Rayet stage. In addition to these six stars, a previously known emission-line star was classified as an LBV-candidate based upon its enormous luminosity and spectral features. Lastly, a star targeted from an earlier imaging survey was verified as an emission-line star.

B γ emission was seen in previously known HII regions, and the spectra were used to measure velocities for the ionized gas. These velocities are largely in agreement with velocities measured in radio recombination-lines. Measured velocities for the Quintuplet emission-line stars and the "Pistol" HII region show that they are all moving with a common velocity similar to what would be expected from stars obeying the Galactic rotation curve.

A. Motivation

The concentration of many complex phenomena near the Galactic Center makes it an excellent laboratory for testing theories concerning a large array of astrophysical topics, i.e. star formation, stellar evolution, galactic metallicity, magnetohydrodynamic (MHD) processes, interstellar medium (ISM) enrichment, and active galactic nuclei (AGN). These phenomena have been attributed to a variety of physical processes

including shocks, inflows, outflows, photoionization, magnetic field reconnection, and stellar mergers to name a few.

It is now clear that star-formation has recently occurred near and, perhaps, at the Galactic Center (Krabbe et al. 1991, 1995; Sellgren et al. 1987; Eckart et al. 1995; Haller 1992). This is evidenced by the existence of hot, luminous stars and red supergiants; stars in both classes must have formed within the past 10^7 years. The central cluster in the inner parsec of the Galaxy contains, at least, a dozen hot emission-line stars (Krabbe et al. 1991, 1995), and at least one supergiant, IRS7 (Lebofsky et al. 1982; Sellgren et al. 1987). This remarkable concentration of evolved massive stars suggests that there was recent star formation in the inner parsec approximately 10^7 years ago.

Many more stars which formed in that star formation episode must still be on the main-sequence, but these stars are quite faint and do not have the prominent emission lines found in the more luminous stars. A key challenge is to find and classify these upper main-sequence stars in an effort to describe the initial mass function (IMF) for the Galactic Center starburst. Also, once the rapidly evolving population, i.e. massive stars, is firmly known, the appearance of the Galactic Center can be estimated for all times from the previous starburst to the next starburst. These estimates can be compared to presently observed AGN to test whether our Galaxy's nucleus can be considered as an AGN currently in a starved, quiescent state.

Elsewhere near the center, hot emission-line stars have been found in a handful of star-formation sites (Geballe et al. 1994; Cotera et al. 1994; Nagata et al. 1995). Determining how many of these luminous stars exist will give, within uncertainties of the IMF, a total mass in stars recently formed. Alternatively, an estimate of the total

cluster mass, calculated by requiring that the cluster be bound, can be used to constrain the IMF. This argument requires that stars above a particular mass limit are all in an emission-line phase or that some scaling can be made between the number of observed emission-line stars and the total number of stars above the mass limit.

The total mass in stars can be compared to current estimates of mass in the gas phase to give a mass efficiency for star formation. There are grounds to expect that this efficiency might be lower near the Galactic Center. Cloud collapse, fragmentation, and, eventually, star formation could be inhibited by the high cloud temperatures, magnetic fields, tidal forces, and internal bulk motions in clouds near the Galactic Center (Morris 1993). This might imply a lower star formation efficiency, but Gusten (1989) has estimated a ratio of mass in stars to that in gas which is roughly the same as in the disk.

This star-to-gas mass estimate relies on the number of ionizing photons and far-infrared luminosity as accurate probes of mass in stars. This can be tested by actually observing the stars which contribute the ionizing flux, i.e. O-stars and hot emission-line stars. Currently known emission-line stars near, and at, the Galactic Center are relatively cool and thus contribute relatively little ionizing flux compared to the hotter O-stars (Najarro et al. 1994; Panagia 1973). However, the emission-line stars are generally found in sites of star-formation where O-stars are probably located. Finding and counting the emission-line stars can give the number of O-stars in a cluster assuming simultaneous star formation for all stars in the cluster and a known cluster age, and the number of O-stars will give a reliable independent measure of the number of massive stars in the cluster.

The existence and classification of the emission-line stars can also be used to argue that some radio features are due to photoionization. This question is important because models depending on magnetic processes have been proposed to explain the source of ionized gas near the Galactic Center while the presence of hot stars might offer an alternative viable explanation. It is critical to estimate the total rate of ionizing flux from the emission-line stars in order to test whether they can explain the thermal radio features. Harris et al. (1994), Cotera et al. (1994), and Nagata et al. (1995) have estimated the ionizing flux implied by the population of emission-line stars to argue that some of the thermal radio features on the northern side of the Galactic Center are produced by photoionization.

Advances in understanding the Galactic Center have partially been due to the advent of sensitive near-infrared ($1\ \mu\text{m} < \lambda < 5\ \mu\text{m}$) instruments which operate at wavelengths where interstellar extinction is low, compared to the situation at optical wavelengths, and where stellar fluxes are still high, compared to the situation at mid- or far-infrared wavelengths. These realities are dramatically borne out in images at optical and infrared wavelengths. Figure 1 shows images of the Galactic Center region in the V-band and K'-band. Notice the obvious Galactic Center and disk which can be seen only in the infrared image.

Modern infrared instruments contain arrays which give critically sampled images over areas as large as $3' \times 3'$ with a single telescope pointing. The current state of technology, and the advances which are bound to follow (McLean 1995), should propel near-infrared imaging and spectroscopy so that resolutions and spatial coverage usually associated with optical astronomy will become more common.

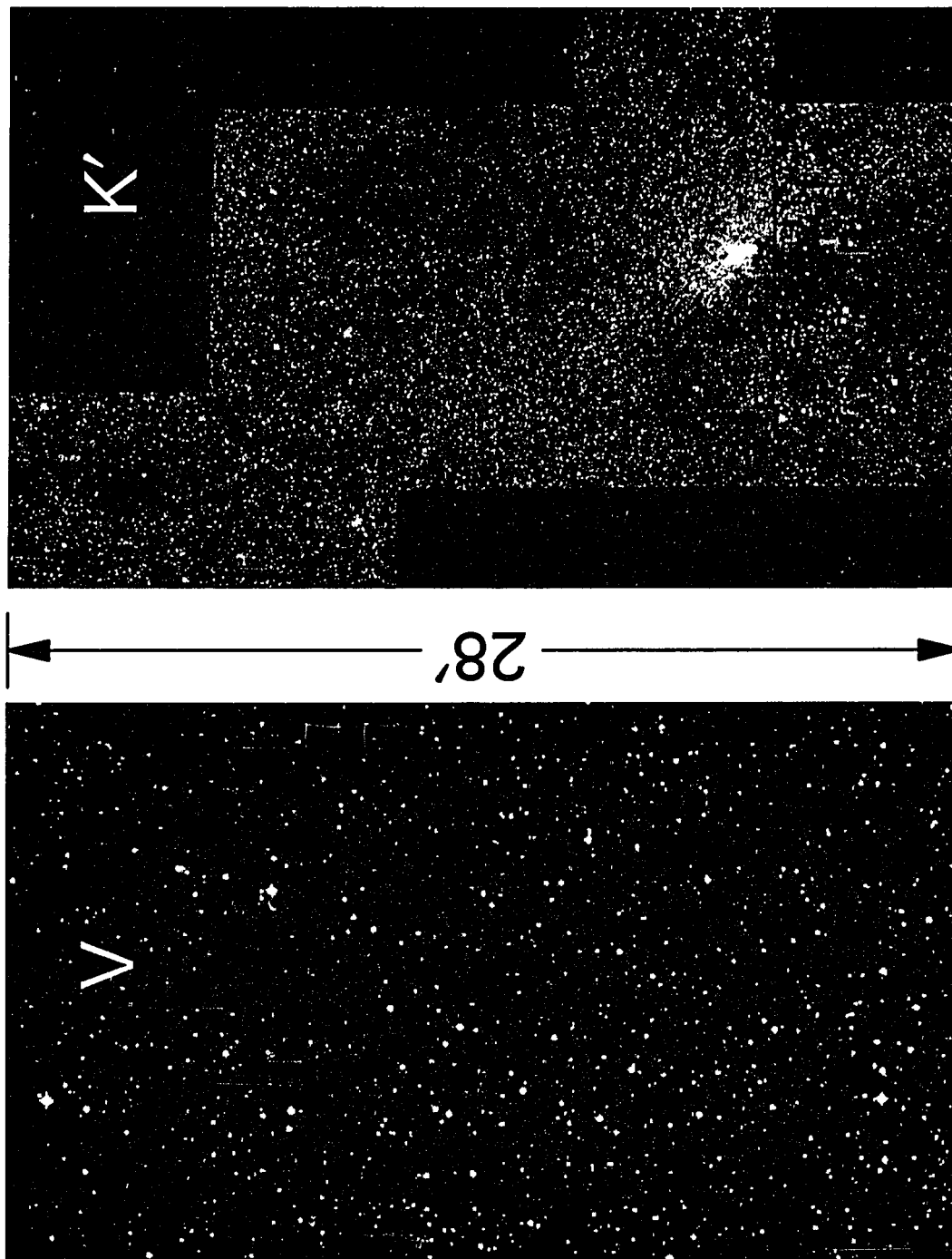


Figure 1. V-band and K'-band images of the survey region.

The purpose of this dissertation is to use the new near-infrared technology to determine the number of young, hot, and luminous stars in the Galactic Center. Recent projects with similar goals have been based on targeted searches of areas which were already known to be likely sites of star formation. We chose to observe a large filled area of the Galactic Center, providing coverage of many known features and sites of star formation as well as the areas inbetween these features.

B. Introduction to star formation

Star formation is generally thought to proceed by the collapse of gravitationally bound clouds (Shu et al. 1987). An initial perturbation in density will lead to inward acceleration unless opposing pressures stop the infall. These opposing pressures might be due to a non-isothermal distribution, large tidal forces, angular momentum, magnetic pressure, bulk motions, etc. In fact, disruptive forces can be so great that gravitationally bound clouds cannot exist in equilibrium. External forces are then needed to compress material to high enough densities for star formation to take place. These forces might come from cloud-cloud interactions, supernovae winds, or powerful winds from massive stars.

The initial mass function, $f(m)$, describes the number distribution versus mass for stars which form out of a cloud (see Shu et al. 1987 and references therein). The usual parameterization follows a power law as shown in equation (1), where the total

$$f(m) = Am^{-n}, \quad M_{stars} = \int_{m_l}^{m_u} f(m) m dm = \int_{m_l}^{m_u} Am^{-n+1} dm. \quad (1)$$

mass of stars formed is the integral of the mass weighted IMF. There are three free parameters in calculating the total mass of stars formed: the lower mass cutoff, m_l , the

upper mass cutoff, m_u , and the slope, n . The slope has been empirically measured for moderate stellar masses to be ~ 2.35 by Salpeter (1955). Arguments for bimodal star-formation are based upon the lack of high-mass stars, $M > 1-2 M_\odot$, in regions between the spiral arms, and the presence of high-mass stars in star-forming regions within the spiral arms (see Shu et al. 1987 and references therein). Some argue that the warmer and more turbulent giant molecular clouds (GMCs) in spiral arms require external triggering to form stars, and the net result is a larger m_l versus more normal interarm clouds.

C. Molecular clouds in the Galactic Center environment

1. pressures, temperatures, densities, compositions

Galactic Center molecular clouds are quite unique in many ways compared to molecular clouds in the disk. Their uniqueness results from the large tidal forces which would rip apart more "normal" disk clouds. The condition against tidal disruption requires H_2 number densities of $\geq 10^4 \text{ cm}^{-3}$ ($75 \text{ pc}/r_{GC}$)^{1.8}, or about a factor of 1000 greater than the densities required to overcome tidal disruption at the galactocentric radius of the Sun (Gustén 1989). A typical cloud, having a radius $\sim 10 \text{ pc}$, which could withstand tidal disruption would have to be very massive with $M \sim 8(10^6) M_\odot$ for $r_{GC} = 35 \text{ pc}$. This condition ensures that any clouds which can exist in equilibrium near the center will be very dense and very massive. More "normal" clouds will be torn apart, their matter being dispersed into a smooth lower density component (Linke et al. 1981).

The clouds which are dense enough to maintain their structure will necessarily have large internal velocities, and, thus, the cloud will have large turbulent pressure (Stark et al. 1989). This can be seen by equating the potential energy of these massive clouds to the kinetic energy of internal motion via the virial theorem. For instance, a

cloud with $r = 10$ pc and $r_{GC} = 35$ pc would have $V_{FWHM} \sim 100$ km/s assuming $v_{circular} \sim 130$ km/s. As measured, the linewidths are about a factor of 2 or 3 smaller than this value (Tsuboi et al. 1994), but the theoretical argument does give some insight as to why the velocity dispersions in Galactic Center clouds are so much greater than those in more normal disk clouds.

Relatively high gas temperatures can be found in the Galactic Center with $T_g \sim 70$ K compared to ~ 15 K for disk clouds (Gusten 1989). The dust temperatures are much lower, $T_D \sim 20$ to 30 K, arguing against collisional heating of warm gas by the dust particles. The heating mechanism for the gaseous component is not well understood, but the dust is probably heated by the cool population of K and M giants with some small contribution from OB stars (Cox & Mezger 1989).

Many Galaxy evolution scenarios predict or presume a metallicity gradient with radius from the Galactic Center, where the metallicity, Z , is the mass fraction of gas in atoms heavier than helium. Cosmic abundances are thought to be modified toward progressively larger metallicities as stars convert hydrogen and helium into heavier atomic species and replenish the interstellar medium with their nuclearly processed matter. Some observations of the Galactic Center are consistent with this paradigm giving Z a few times greater than the solar value. Unfortunately, these observations rely on relative ratios of abundances atomic nuclides within the same species, e.g. $^{13}\text{C}/^{12}\text{C}$, as proxies for absolute abundance. There are also some observations which do not fit simple evolutionary models which predict higher metallicity for the Galactic Center, i.e. $^{17}\text{O}/^{18}\text{O}$ is not enhanced in the Galactic Center like it is in red giants (Wannier 1989).

The Galactic Center environment is unique in having very strong magnetic fields as compared to the disk of the Galaxy. The large-scale magnetic field is thought to be

poloidal in the center, as opposed to along the spiral arms in the disk, with strengths at least 2 orders of magnitude above the disk field strength, 3 μG ; however. These statements are less certain for fields in molecular clouds, as there are very few measurements of it to date. The sparse available data suggest that the field strength is $< 0.3 \text{ mG}$ in most cases for clouds outside of the central few parsecs (Uchida & Gusten 1995) and \sim a few mG for molecular material within the circumnuclear ring (Killeen et al. 1992). See Morris (1994) for a review of magnetic phenomena near the Galactic Center.

2. implications for star formation near the Galactic Center

The unique characteristics of Galactic Center molecular clouds most likely lead to modified IMFs compared to what is found in the disk (Morris 1993). The tidal force experienced by clouds within a few parsecs of the Galactic Center is so high that only clouds with $n \sim 4(10^7) \text{ cm}^{-3}$ can survive. This density can probably be achieved only through compression, so that normal clouds would be ripped apart as they travel near to the Center. Any contracting core in the molecular material near the Center will be subject to these same tidal forces so that gravitational collapse will always be strongly inhibited unless some external process can compress the material.

As described earlier, compressed GMCs in the disk are thought to preferentially produce stars with increased m_i , and the Galactic Center GMCs probably are similar in this respect assuming that they are compressed by cloud-cloud collisions or other interactions. In fact, Morris (1993) argues that the inhibiting factors for star-formation in Galactic Center clouds are consistent with an elevated m_i of $\sim 1 M_\odot$.

Current observations reveal hot, young stars which probably formed in the central parsec where there is now a low density of molecular material (Jackson et al.

1993). These helium emission-line stars (Krabbe et al. 1991) have also been explained as the result of compact object-giant interactions (Morris 1993) or giant-giant interactions (Lee & Nelson 1988). These types of explanations are attractive because they argue against the "assertion that we live at some privileged time" (Gatley 1989). On the other hand, the emission-line stars' spectra and luminosities can be accurately modelled using parameters which are reasonable for other emission-line stars around the Galaxy (Najarro et al. 1994). In addition, several Wolf-Rayet carbon stars (WC9) were found in the central parsec (Blum et al. 1995b; Krabbe et al. 1995). Any merger theory now has the requirement to explain hot, emission-line stars, including some which have enormous carbon enrichment without any hydrogen at their surfaces. Also, there appear to be emission-line stars just outside the inner few parsecs all the way out to at least 35 pc. A merger theory would then have to be used within some critical radius while emission-line stars outside of this radius, where the stellar density is not high enough for merger theories, would have to be explained by stars formed via traditional gravitational collapse. One observational test distinguishing continuous mergers versus a starburst would be to measure the relative numbers of Wolf-Rayet to O-stars (Parker et al. 1995; Meynet 1995).

Star-formation outside of the inner parsec is much less inhibited as the critical density to overcome the large tidal force scales as $r^{-1.8}$. In fact, the dense clouds scattered within the inner 50 pc have such large densities, and unambiguous star-formation regions are seen near these clouds. In these cases, the relatively low stellar density, as compared to the inner parsec, would not lead to the number of mergers necessary to produce hot, emission-line stars.

D. Star formation near the Galactic Center

The most direct way to observe star formation is to find a star which is in the act of achieving the critical core temperature to begin hydrogen burning. Unfortunately, the material which is contracting onto the star also extinguishes most of the light from the star so that only the reradiated light is visible. Stars only spend a very short time in the contracting, protostellar phase as compared to their lifetimes burning hydrogen. These realities lead to the conclusion that protostars are very rare and most of their flux emerges at wavelengths $\gg 1 \mu\text{m}$.

Another approach to studying star formation is to observe stars which have recently formed. These stars will have evolved somewhat, but evolutionary models could be used to predict their ages and birth states, e.g. initial masses. The hottest stars are easily identifiable as young, and evolution theory for these stars is just becoming robust enough to reliably trace their history from observed states back to their birth. Some of these hot stars, with masses below some critical value, will quickly evolve into red supergiants, making the latter also an indicator of recent star-formation. Less luminous red giants are much more numerous in observed number at the Galactic Center, and evolution models are much more robust than for the hotter stars; but these cooler stars are much older ($\tau_{\text{age}} > 10^8 \text{ yrs}$) than the young hot stars ($\tau_{\text{age}} < 10^7 \text{ yrs}$).

Observers have been denied the opportunity to observe moderately bright single stars near the Galactic Center until the recent advent of two dimensional infrared arrays. Photometry for the very brightest stars was not significantly contaminated by nearby fainter stars in the relatively large apertures used in bolometer photometers in the past; however, it was impossible to derive accurate single star photometry for fainter stars using this type of instrument.

In the absence of high resolution cameras, a considerable body of work has accumulated over the past 30 years using radio telescopes and large aperture far-infrared photometers. One use of these studies is to assess star formation by observing the non-stellar components of the Galactic Center radiation. For instance, a measure of the radio flux from electron free-free emission can be used to place a limit on the ionizing flux from a particular region. This limit can then be used to estimate the maximum number of hot stars.

Far infrared emission ($25 \mu\text{m} < \lambda < 100 \mu\text{m}$), comes predominately from light which is absorbed and reradiated by dust, so it is related to the total stellar luminosity in a region; in fact, about one third of stellar light in the Galaxy is absorbed and reradiated by dust (Cox et al. 1986). Measuring the amount of this far infrared radiation will then place limits on the total mass of stars in a cluster assuming some reasonable average mass-to-luminosity ratio, M/L (see Cox et al. 1986 for caveats in assuming a single M/L for stars forming in giant molecular clouds versus less massive clouds between spiral arms).

1. assessments of global star formation in the region

As discussed above, most of the information on global star formation in the Galactic Center comes from radio and far infrared data. Far-infrared flux from the Galaxy comes from dust grains heated by the interstellar radiation field; OB stars contribute $\sim 20\%$ of the total far-infrared luminosity in the disk while the rest comes from red giants and disk stars (Cox & Mezger 1989). A total of 25% to 30% of the stellar luminosity is absorbed by dust and reradiated in the far-infrared. Evidently, then, the far-infrared luminosity is a good measure of the total stellar luminosity within a region.

Radio continuum flux in the interstellar medium is predominately due to electron free-free emission in gas ionized by the intense radiation field near hot OB stars. An absolute measure of this emission indicates how much ionizing radiation is being produced in a region, and thus how many hot stars are in the region. Of course, this assumes some particular distribution of stellar types. For instance, one O4V star produces the same ionizing flux as 370 B0V stars (Panagia, 1973).

The ratio of far-infrared to radio flux gives an indication of the relative ratios of cool, MK giants, to hot stars, OB stars. This infrared excess (IRE), defined as $L_{\text{IR}}/L_{\text{L}\alpha} - 1$, should be lower in regions where OB stars are still present. Gatley et al. (1978) claim that the IRE will be higher in regions where stars are still enshrouded by their dust cocoons, i.e. young star-formation regions. Values for HII regions surrounding the Galactic Center tend to be higher than for normal HII regions indicating that O stars contribute relatively little luminosity through the heating of dust. Sgr A West has a relatively low IRE $\sim 6-8$ (Cox & Mezger 1989).

The far-infrared flux and the free-free radio flux will be discussed for individual suspected star-formation regions near the Galactic Center in the following section.

2. sites of star formation

The known sites of star formation within 50 pc of the Galactic Center are listed in Table 1, and their positions are shown in Figure 2. Well-known GMCs, i.e. Sgr B, Sgr C, Sgr D, are massive star-formation sites near the Galactic Center, but they are not within the survey boundary.

Most of the regions listed in Table 1 have associated radio emission with a flat spectral index indicative of HII regions. The one exception to this is the "Dust Ridge" region which has been selected for its submillimeter emission and maser source (Lis

et al. 1994); the lack of radio emission in this region is taken to indicate that only stars later than B0 exist in it.

Table 1: Star Formation Sites within 50 pc of the Galactic Center

Galactic Coordinates of HII Region	Common Names	RA (1950)			DEC (1950)			Ref
		h	m	s	°	'	"	
G-0.14-0.09	G	17	42	27	-29	04	36	1
G-0.02-0.07	A-D	17	42	42	-28	58	47	2
G-0.010+0.015	H1	17	42	22	-28	55	02	3
G-0.015+0.027	H2	17	42	18	-28	54	54	3
G+0.04+.02	H5	17	42	29	-28	52	20	3
G0.15-0.05	Quintuplet	17	43	04	-28	48	30	4
G0.121+0.017	(Arches Cluster)	17	42	40	-28	48	13	5
G0.25+0.01	Dust Ridge	17	43	00	-28	41	30	6

References for coordinates: ¹Ho et al. 1985, ²Yusef-Zadeh & Morris 1987, ³Zhao et al. 1993, ⁴Okuda et al. 1990, ⁵Nagata et al. 1995, ⁶Lis et al. 1994.

G-0.13-0.08. This radio source was discovered by Downes et al. (1978) in their 6 cm radio continuum maps. Ho et al. (1985) label one of the radio peaks as source "G" and present 2 cm and 6 cm data which reveal a clumpy morphology (see Figure 3), suggesting multiple exciting sources. There are also two nearby radio features, "E" and "F", which lie to the northeast and to the north of "G" respectively.

Source E has $\alpha \sim -0.4$ and the 2 cm flux is polarized indicating a nonthermal emission process. Emission from source F also has a nonthermal origin, $\alpha = -1.1 \pm 0.2$. Source G has a thermal spectral index, $\alpha = 0.3 \pm 0.1$, and its emission is not polarized. Ho et al. (1985) suggest that this source is an HII region, and the excitation parameter is consistent with a single O9 main-sequence star or five B0 main-sequence stars. In

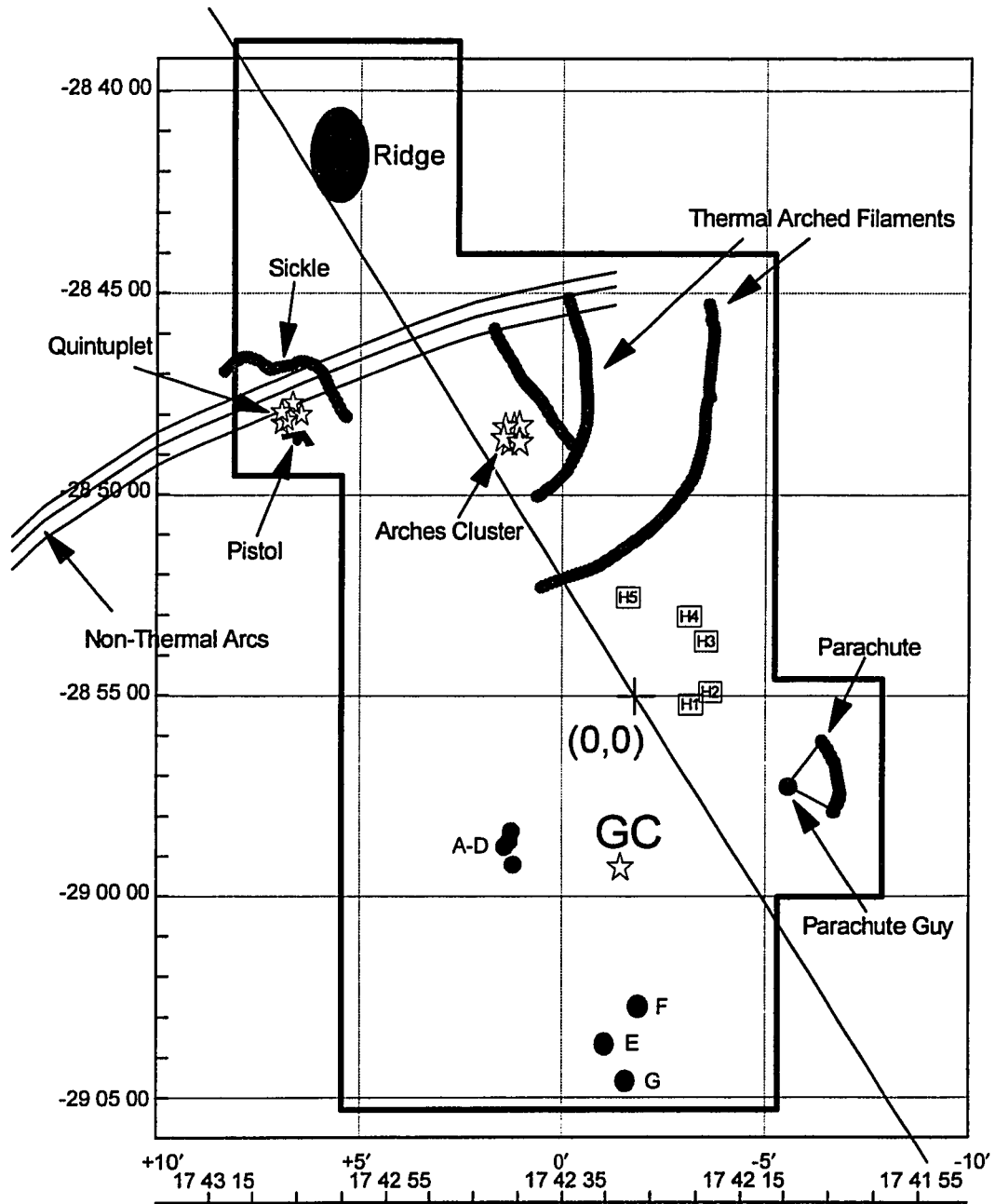


Figure 2. Positions of star-formation regions listed in Table 1.

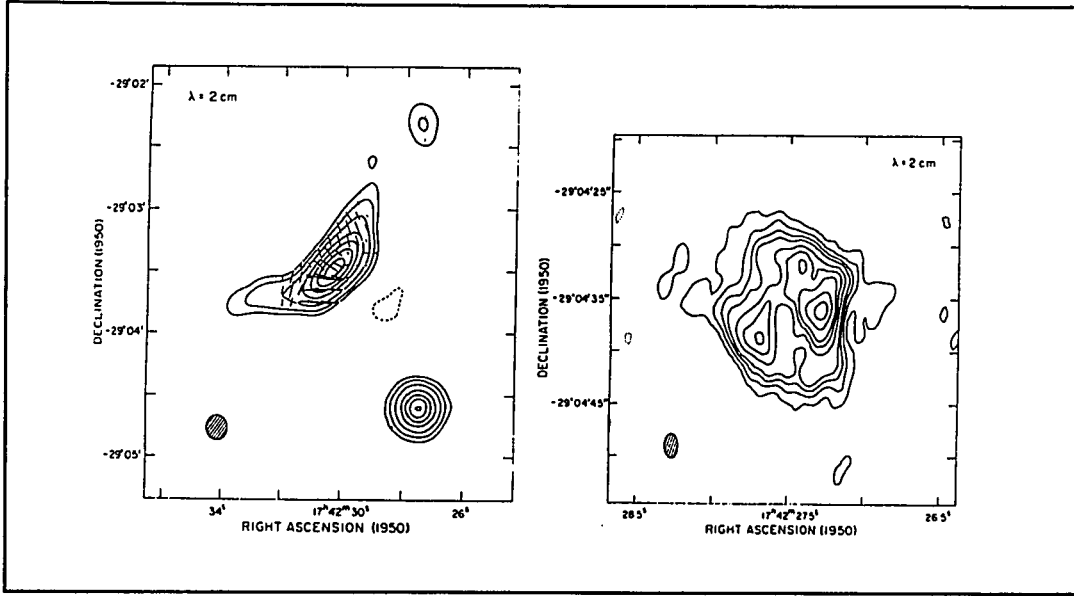


Figure 3. 2 cm contour plot of G HII region from Ho et al. (1985).

fact, Gusten & Downes (1983) find an H_2O maser, usually taken as a signpost for star formation, near source G.

The region containing source E, F, and G is spatially coincident with emission in molecular lines (Armstrong & Barrett 1985), and 1.3 mm dust emission (Zylka et al. 1990); although, only the latter shows an intensity peak at source G. This molecular material is part of a GMC, M-0.13-0.08, which shows a bulk velocity of 20 km s^{-1} in the molecular lines. Armstrong et al. (1985) find $\text{H}76\alpha$ radio recombination line flux at $V_{\text{LSR}} = 14 \pm 2 \text{ km s}^{-1}$ for G, suggesting a physical association between this HII region and the underlying molecular cloud.

Ho et al. (1985) argue that sources E and F are due to an explosive event, i.e. supernova, and that the G HII region represents an area of star formation triggered by the interaction between this explosive event and the underlying molecular cloud, M-0.13-0.08. Zylka et al. (1990) argue strongly against this scenario on the basis that the supernova which created Sgr A East must have occurred $< 50,000$ years ago. This

timescale is at least an order of magnitude shorter than the time necessary for shock interactions, collapse, star formation, and evolution to near the main sequence (Mezger et al. 1989).

Instead, Zylka et al. (1990) claim that M-0.13-0.08 is a GMC which has come too close to the Galactic Center and is being tidally disrupted. The G HII region is simply a result of recent star-formation activity triggered by some mechanism not involving Sgr A East.

G-0.02-0.07. These radio sources, labelled A, B, C1, C2, and D (see Figure 4), were first seen in the 6cm and 20 cm continuum maps of Ekers et al. (1983) and were later verified as HII regions by Goss et al. (1985) using H76 α radio recombination line data. Excitation parameters for these sources are consistent with the Lyman continuum

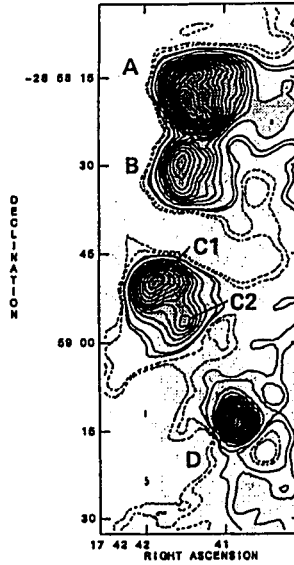


Figure 4. HII regions A-D from Yusef-Zadeh & Morris (1987).

rate produced by O7-O9 main-sequence stars (Goss et al. 1985). Observations of IR

fine-structure lines (Serabyn et al. 1992) indicate stellar surface temperatures of $\approx 35,000$ K, also consistent with late-type O stars.

These HII regions are located $\sim 30''$ east of the eastern edge of the Sgr A East non-thermal shell. Figure 5, taken from Serabyn et al. (1992), shows a contour plot of

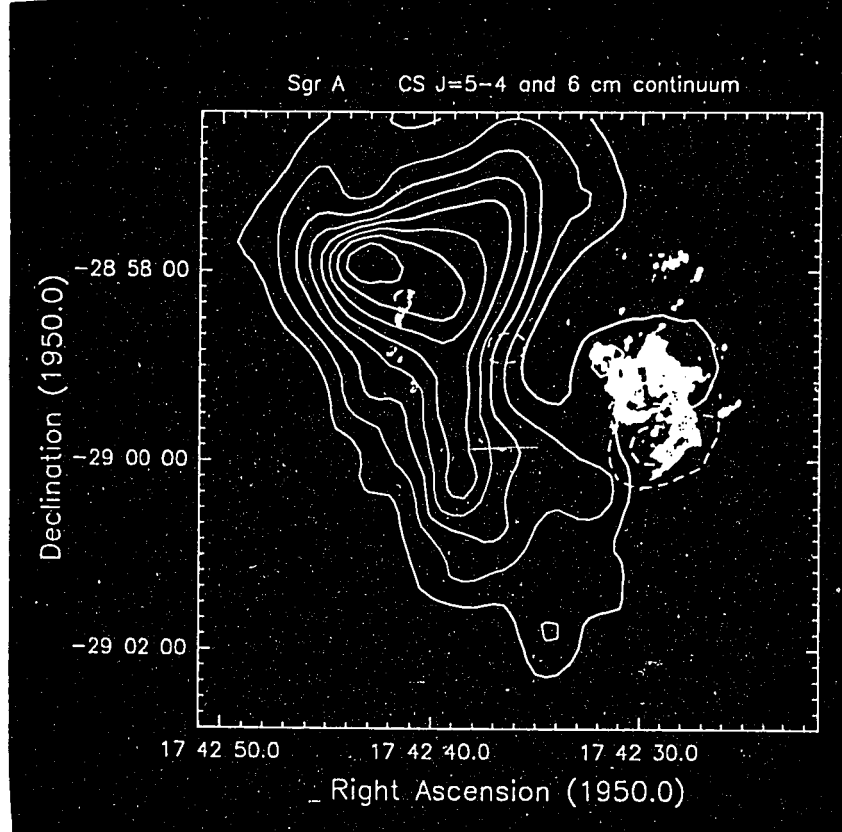


Figure 5. CS contours overlayed on a 6 cm radiograph. Positive velocity CS emission peaks just northwest of the A-D compact HII regions.

CS emission overlayed on a 6 cm continuum radiograph (Pedlar et al. 1989). This emission, as well as emission from NH_3 and HNCO (Armstrong & Barrett 1985), is most intense at $V_{\text{LSR}} \sim 50 \text{ km s}^{-1}$. This velocity is somewhat high compared to what would be expected for a molecular cloud along the line of sight, so this cloud,

M-0.02-0.07, is thought to be physically near the Galactic Center. H76 α emission (Goss et al. 1985) from A-D peaks at velocities between 43 and 52 km s⁻¹, so the cloud and HII regions are likely to be associated. [CII] emission is also seen at similar velocities (Poglitsch et al. 1991; Genzel et al. 1990), but it appears to be coming from the dense molecular ridge between A-D and Sgr A East. Taken together, these facts lead to a scenario placing the molecular cloud near the Galactic Center with its surface being photoionized by the UV field from the central cluster of stars, and the compact HII regions being photoionized by embedded O-stars.

Liszt et al. (1983) first suggested that the Sgr A East shell might be compressing this molecular cloud and that this compression might have led to triggered star formation; however, Serabyn et al. (1992) claim that the compression due to Sgr A East has not yet reached the cloud core or the HII regions. Instead, they propose that the HII regions are a result of some previous episode of star formation not associated with the event which caused Sgr A East. Mezger et al. (1989) also argue against induced star formation because Sgr A East is likely to be younger than the O stars powering the HII regions.

G-0.010+0.015, *G-0.015+0.027*, and *G+0.04+0.02*. This region contains a scattered group of HII complexes labeled H1-8 by Yusef-Zadeh & Morris (1987b) (see Figure 6). Pauls et al. (1976) show an intensity peak in their 2.8 cm continuum map centered on the H1 and H2. Their H85 α recombination line data shows that the emission is thermal with $V_{\text{LSR}} = -42$ km s⁻¹. Downes et al. (1978) show a contour plot of 6 cm data where H1 and H2 are blended together and appeared as one complex due to low spatial resolution; H5E and H5W also appear as a blended concentration. More recent data, i.e. that shown in Figure 6, show a cluster of separated emission peaks. See

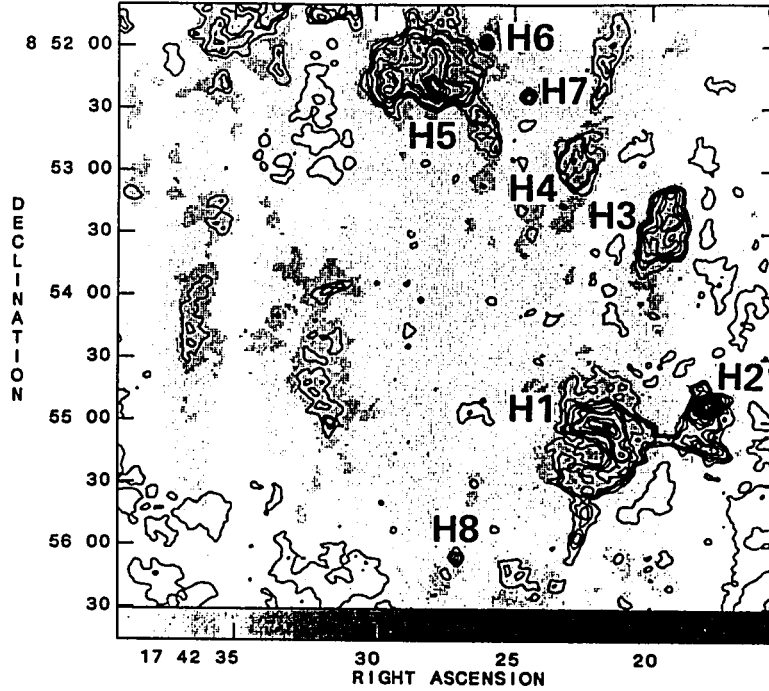


Figure 6. 6 cm radio contour plot of HII regions north of the Galactic Center.

also Zhao et al. (1993).

Yusef-Zadeh (1986) presents H110 α radio recombination line data showing detections for H5 as well as much of the Thermal Arched Filaments (TAFs); in fact, all of these features share similar velocities between -50 and 0 km s^{-1} . Zhao et al. (1993) detect H1-5 in H92 α and H110 α recombination lines and measure $V_{\text{LSR}} \approx -30$ to -60 km s^{-1} . They conclude that these objects are HII regions photoionized by middle to late-type O ZAMS stars.

Further evidence for the existence of photoionizing sources, i.e. OB stars, comes from the $158 \text{ } \mu\text{m}$ [CII] emission seen at the edges of molecular clouds in the region (Poglitsch et al. 1991). A chance line-of-sight might explain the spatial coincidence between the radio objects and the [CII] emission, but they have common velocities

forbidden in the sense of galactic rotation. In fact, an underlying molecular cloud shares similar negative velocities.

Serabyn & Gusten (1987) mapped an area containing these HII regions, as well as the TAFs to the north, in the CS J = 2→1 transition. A clump of emission can be seen abutting the H5 complex to the north and west while obvious molecular counterparts to the other HII regions are absent. The molecular emission near H5 peaks at $\approx -40 \text{ km s}^{-1}$, in coincidence with the recombination line data and the [CII] emission.

G0.15-0.05. The "Quintuplet" is a cluster of stars situated ~ 35 pc, in projection, from the Galactic Center. The cluster was first seen as a single source in the Two Micron Survey (Becklin & Neugebauer 1978). Kobayashi et al. (1983) resolved this object into two distinct peaks, GCS-3 and GCS-4, in their polarimetric survey. Okuda et al. (1990), Nagata et al. (1990) and Glass et al. (1990) further resolved GCS-3 into four bright sources; and, along with GCS-4, the cluster was dubbed, the "Quintuplet". Figure 7 shows a K' image of the Quintuplet, along with labels identifying the newly discovered emission-line stars from our study as well as identifying labels from Moneti et al. (1994). The image on the bottom is an enlargement of the densest part of the cluster.

Okuda et al. (1990) present near-infrared polarimetry for the five sources, and the magnitude and orientation are similar for all the sources and consistent with interstellar origins. Other Galactic Center sources, i.e. IRS7 and IRS1, show similar polarization (Eckart et al. 1995). Okuda et al. (1990) also detect deep silicate absorption near $10 \text{ }\mu\text{m}$, again, reminiscent of silicate absorption seen in IRS7 at the Galactic Center; these authors also detect CO absorption near $4.66 \text{ }\mu\text{m}$. The polarization, silicate absorption, and CO absorption are all thought to be interstellar in origin, and they

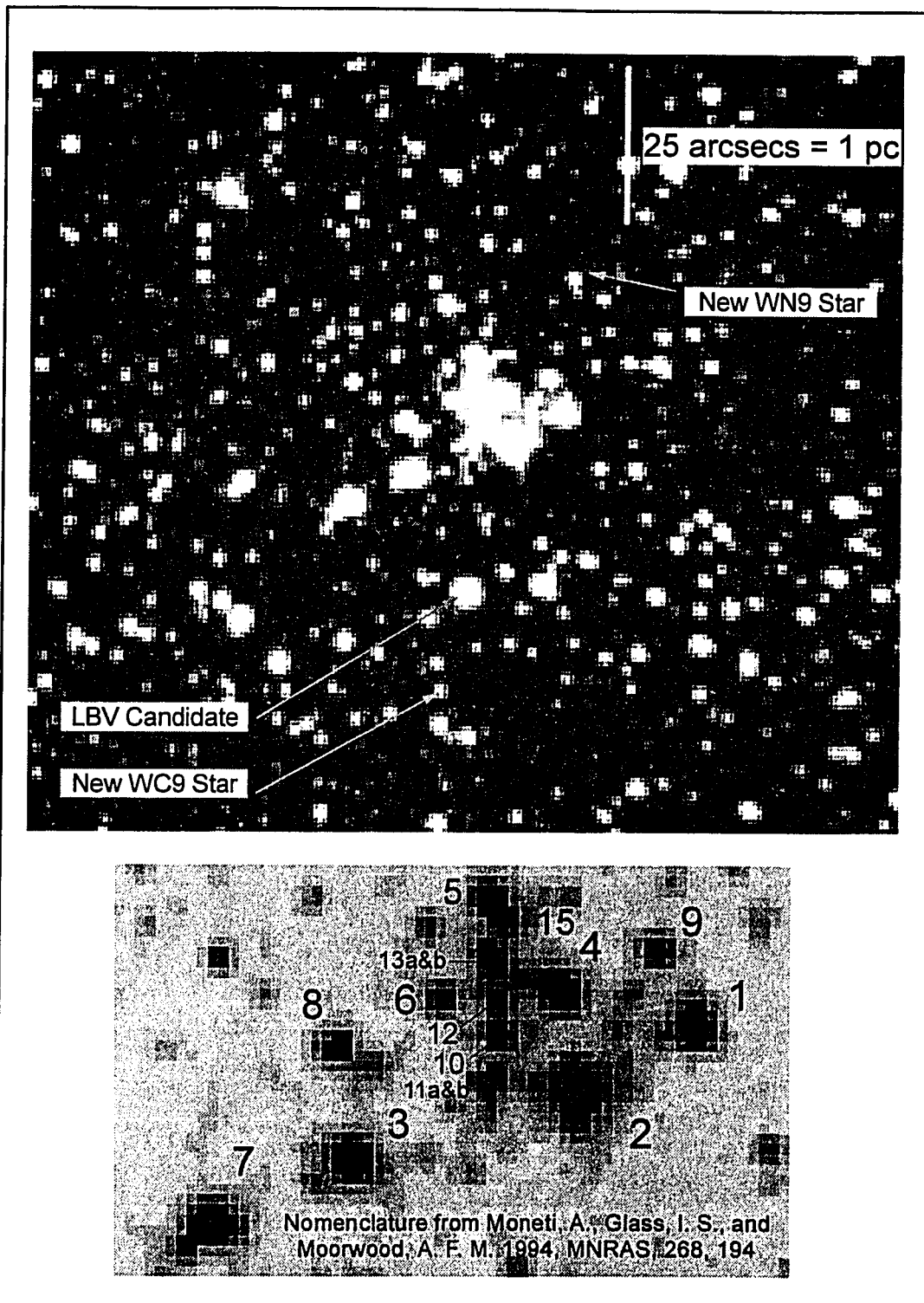


Figure 7. K' image of the Quintuplet cluster.

collectively suggest a distance to the Quintuplet which is similar to the distance to the GC.

These stars are quite peculiar for their cool, featureless infrared spectra. Similar spectra are seen from young stellar objects (YSOs) in star-forming regions (cf. Hanson & Conti 1995). Their luminosities are 10^4 to $10^5 L_{\odot}$ consistent with dust-enshrouded YSOs at the Galactic Center. Nagata et al. (1990) argue that these characteristics, along with the apparent clustering of the stars, suggest that the Quintuplet members are very young stars embedded in their natal dust cocoons. Glass et al. (1990) also argue that

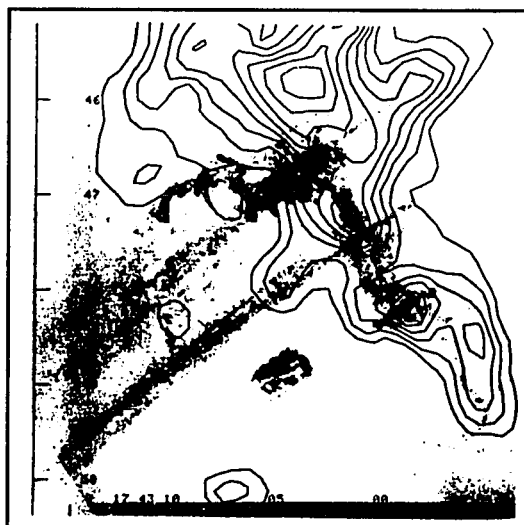


Figure 8. 6 cm radiograph showing the Sick, Pistol, and non-thermal linear filaments.

these stars are YSOs based upon their: spectral energy distributions, apparent clustering, absence of Br γ , prominent silicate absorption, and association with nearby radio continuum sources.

The Quintuplet sits inbetween two thermal radio features and it lies to the south of the non-thermal linear filaments as can be seen in the 6 cm radiograph in Figure 8 from Serabyn & Gusten (1991). The "Pistol" HII region, G0.15-0.05, lies $\sim 10''$ to the

south and east of the cluster, and the "Sickle" HII region, G0.18-0.04, is $\sim 2'$ to the north and west of the cluster at its closest approach.

Both HII regions emit strongly in radio recombination lines, and they have roughly flat spectral indices supporting their thermal nature (Pauls et al. 1976; Yusef-Zadeh 1986; Sofue et al. 1985). The velocities in the Sickle are between 20 to 40 km s⁻¹, while those in the Pistol are much higher, ~ 120 km s⁻¹ (Yusef-Zadeh et al. 1989).

A nearby molecular cloud, M0.20-0.033, with $v \sim 25$ km s⁻¹ can be seen abutting the Sickle to the north and west in ¹³CO (see Fig. 5g in Bally et al. 1988). Serabyn & Gusten (1991) have also mapped this cloud in CS. The apparent juxtaposition of M0.20-0.033 with the Sickle is not simply a coincidence as Serabyn & Gusten (1991) find a remarkable agreement between the CS spectrum and the [NeII] spectrum. Morris et al. (1995) observed the region at 50 and 90 μ m, and the far-infrared emission is coincident with the 25 km s⁻¹ cloud. The total far-infrared luminosity in M0.20-0.033 is $> 9(10^6)$ L_⊙. An intensity peak near the Pistol can be seen in the 50 μ m map, but there appears to be a lack of high velocity molecular material near the Pistol; although a 50 km s⁻¹ cloud is situated a few arcminutes to the south (Bally et al. 1988).

Recently, three members of the Quintuplet cluster have been found to have prominent helium and hydrogen near-infrared emission-lines (Moneti et al. 1994; Harris et al. 1994; Geballe et al. 1993). K-band spectra for two of the stars suggest that the stars are similar to some of the emission-line stars in the Galactic Center and the Ofpe/WN9 stars in the LMC (McGregor et al. 1988a). The third emission-line star was noted primarily for its Bry emission (Moneti et al. 1994). Cotera et al. (1994) suggest that this star has $L \sim 10^7$ L_⊙, and they point out the spectral similarities between this

star and emission-line stars in the LMC (McGregor et al. 1988b). These stars, along with the new emission-line stars discovered in this study, might be able to account for the ionized gas in the Pistol and the Sickle; although, the latter would probably require an associated population of O-stars.

As can be seen above, this region is very complex having thermal and nonthermal emission features, a nearby molecular cloud, and a cluster of recently formed stars producing considerable ionizing flux. A key challenge in the future will be to incorporate the recently discovered emission-line stars into the proposed models (Yusef-Zadeh & Morris 1987a; Serabyn & Gusten 1991; Serabyn & Morris 1994) which attempt to explain all the observed phenomena.

G0.121+0.017. Nagata et al. (1993, 1995) and Cotera et al. (1992, 1994) discovered a tightly packed cluster of emission-line stars at these coordinates placing it ~ 25 pc, in projection, north of the Galactic Center (see Figure 9). The cluster is situated $\sim 30''$ to the east of the E1 filament, *G0.10+0.02*, of the TAFs, and it is roughly at the radius of curvature of the E2, W1, and W2 filaments. These filaments were discussed above in the section on *G-0.01+0.02*.

The emission-line stars have H and K band spectra similar to WN8 and WN9 stars; however, Conti et al. (1995) has pointed out the spectra are also quite similar to O4I stars. The cluster contains about a dozen emission-line stars and several cool stars, and near-infrared colors are consistent with a location near the Galactic Center (Cotera 1994; Nagata et al. 1995). Background emission from the integrated flux of faint cluster members can be seen within a $15''$ radius (0.5 pc) circle.

Davidson et al. (1994) estimate the integrated far-infrared luminosity to be $\sim 1.2(10^8) L_{\odot}$ over a region extending from H1/2 up to the northern extent of the

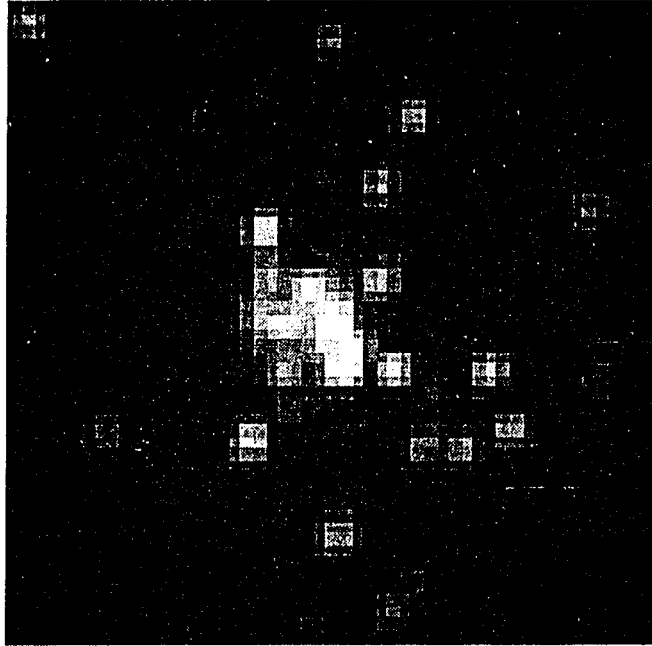


Figure 9. K' image of the "Arches Cluster" near the Thermal Arched Filaments. The image is $\sim 42''$ square, or 1.7 pc at the distance of the Galactic Center.

TAFs which themselves contribute $\sim 10\%$ of the total luminosity according to Morris et al. (1995). They argue that a single luminosity source, i.e. a cluster of hot stars, would have to be > 10 pc away from the filaments to evenly illuminate them as seen in the far-infrared maps. Given the geometrical dilution at this distance, this cluster must have a luminosity of $\sim 10^8 L_{\odot}$ to provide the luminosity in the filaments. It is still uncertain whether the stars in the cluster can contribute this much luminosity. Serabyn & Gusten (1987) suggest that one O6 or 20 B0 stars could provide the $\sim 10^{49}$ Lyman continuum photons/second needed to ionize the filaments. Nagata et al. (1995) use this figure and claim that the cluster plausibly contributes ionizing flux to the TAFs.

G0.25+0.01. This location corresponds to the southernmost dust condensation amongst a string of dust features between the nonthermal filaments and Sgr B1. Gusten & Downes (1980) estimate $M \sim 4(10^5) M_{\odot}$ for the cloud mass based upon their measurements of formaldehyde absorption ($1_{10} \rightarrow 1_{11}$), H_2CO , centered around 25 km s^{-1} ; additional H_2CO data ($2_{11} \rightarrow 2_{12}$) (Gusten & Henkel 1983) indicate a mass of $1.8(10^6) M_{\odot}$. NH_3 emission (Gusten & Downes 1981) also coincides with this position and velocity. Lis et al. (1994) find a peak in their $800 \mu\text{m}$ and $350 \mu\text{m}$ continuum maps and estimate a mass of $5(10^5) M_{\odot}$ and $1.6(10^5) M_{\odot}$ respectively; the variation in mass estimates is likely due to uncertainties in the grain temperature and emissivities. No far-infrared or radio emission can be seen at this location (Downes et al. 1978; Dent et al. 1982; Odenwald & Fazio 1984) as would be expected if hot O-stars are currently embedded in the cloud.

There is some support for star-formation in this cloud. Lis et al. (1994) found a 22 Ghz water maser $15''$ to the east of the $350 \mu\text{m}$ peak, and they conclude that the maser is due to a young stellar source instead of an older OH/IR star. They also found a compact radio source in their 8.44 Ghz data (3.55 cm) which they claim might be a B0-0.5 star. This assumes that the radio flux is due to free-free emission from an HII region surrounding the star. While it can be argued whether the water maser or radio continuum source indicate star-formation, the striking result from Lis et al. (1994) is that massive star-formation producing stars earlier than B0 is not occurring in this very massive cloud.

3. central cluster

The inner parsec of the Galactic Center is, perhaps, the most interesting site in the survey. The infrared cluster, first seen by Becklin & Neugebauer (1978), is now

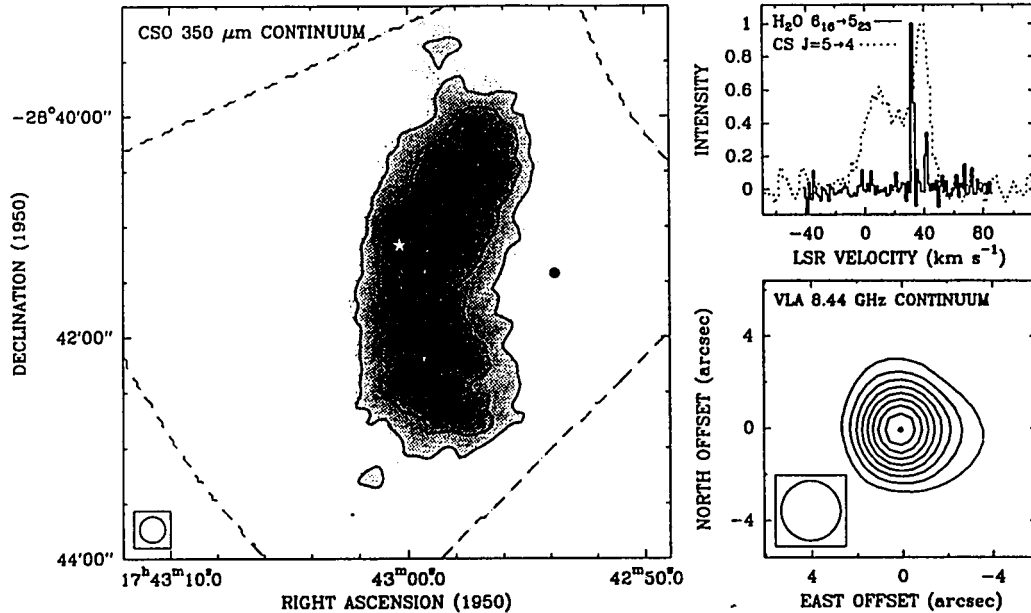


FIG. 1.—*Left panel:* The 350 μm continuum map of M0.25+0.01. The contour levels correspond to 20%, 40%, 60%, 80%, and 90% of the peak flux density, which is 170 Jy in the $14''$ (FWHM) beam indicated in the lower left corner. The white star symbol and the black dot mark, respectively, the positions of the 22 GHz H_2O maser and the 8.44 GHz continuum source detected with the VLA. *Upper right panel:* The H_2O maser spectrum (solid line) and the CS $J = 5 \rightarrow 4$ spectrum (dashed line) observed at $(\alpha, \delta)_{1950} = 17^{\text{h}}43^{\text{m}}00^{\text{s}}.32, -28^{\circ}41'10''.2$. The intensity scale has been normalized so that unity corresponds to a flux density of 0.5 Jy in the case of the H_2O spectrum and to a main-beam brightness temperature of 0.67 K for the CS spectrum. The H_2O intensity has been corrected for primary beam response. *Lower-right panel:* The 8.44 GHz map of the compact radio continuum source. Offsets are relative to the peak of the 8.44 GHz emission, which is at $(\alpha, \delta)_{1950} = 17^{\text{h}}42^{\text{m}}53^{\text{s}}.81, -28^{\circ}41'25''.4$. Contour levels run in steps of 10% from 20% to 99% of the peak flux density, which is 7.4 mJy beam $^{-1}$. The lowest contour value and the contour spacing correspond, respectively, to ~ 4 and 2 times the rms noise level. The restoring beam (FWHM = $2''.6$) is indicated in the lower left corner.

Figure 10. M0.25–0.01 at 350 μm from Lis et al. (1994). A spectrum for the H_2O maser and a 3.55 cm contour plot for the compact radio source are also shown.

thought to harbor at least one supergiant (Lebofsky et al. 1982; Sellgren et al. 1987) and at least a dozen hot, helium emission-line stars (Krabbe et al. 1991; Eckart et al. 1995; Krabbe et al. 1995). The supergiant, IRS7, has been firmly established as a true member of the cluster; and Lebofsky & Rieke (1987) estimate an age of ~ 40 Myr. The emission-line stars are thought to be evolved O-stars from a star formation episode \sim a few $\times 10^6$ years ago (Krabbe et al. 1991); although some argue that these stars might be the result of mergers between red giants or compact objects in the dense Galactic Center environment (Morris 1993; Lee & Nelson 1988).

This cluster of stars has about $L \sim 10^7 L_{\odot}$ (Krabbe et al. 1991), making it capable of providing the bulk of the $\sim 10^7 L_{\odot}$ inferred from far-infrared measurements (Becklin et al. 1982; Davidson et al. 1992). The cluster can also likely account for the necessary ionizing source and the low excitation temperature of the Sgr A West "mini-spiral" (Krabbe et al. 1991).

II. Massive stars

Massive stars quickly evolve away from the main-sequence advancing to later stages of evolution where they often have emission-line spectra. This behavior is only found in stars with initial masses $> 10 M_{\odot}$, so this mass limit essentially defines "massive stars" in the context of this thesis. Stars with lower masses will evolve up the asymptotic giant branch (AGB) and attain luminosities as great as $10^4 L_{\odot}$, so stars can have large luminosities without being massive. As will be seen later, it is fortunate that these lower mass giants are not hot enough, like their high mass counterparts, to have emission-line spectra.

Massive stars are useful probes for recent star formation because they only live for $< 10^7$ years. In fact, massive stars evolve so quickly that they do not have enough time to wander very far from their natal molecular cloud; thus they are usually observed in associations or clusters near molecular clouds, i.e. M17 (Hanson & Conti 1995). For example, a massive star with an average peculiar velocity, $v_p = 5 \text{ km s}^{-1}$, will travel $\approx 50 \text{ pc}$ away from the cluster in which it was born; of course, the star will not drift very far from the cluster if it is bound. With this in mind, it is reasonable to assume that the nearest molecular cloud to a massive star cluster or association is a site of recent star formation.

A. evolution through HR diagram

Massive stars begin their lives on the zero-age main sequence (ZAMS) in the upper left quadrant of the HR diagram. Figure 11 shows theoretical evolutionary tracks from the models of Maeder and coworkers (cf. Meynet et al. 1994; Maeder 1991a); these tracks correspond to the highest metallicity case yet modelled, $Z = 0.04 = 2Z_{\odot}$. The ZAMS is shown as a solid line spanning 4.45 to 4.73 in $\log(T_{\text{eff}})$ and 4.2 to 6.4 in

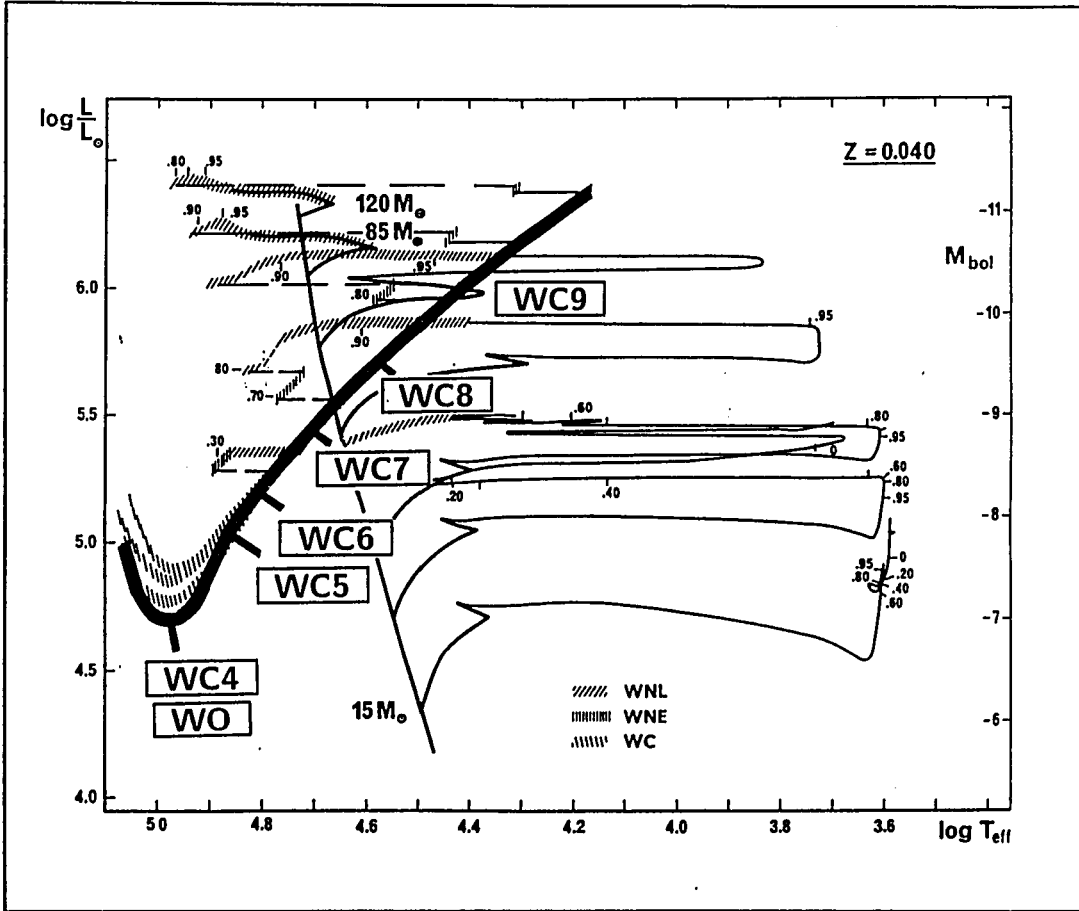


Figure 11. Upper-left region of HR diagram from Maeder (1991a).

$\log(L/L_{\odot})$. Each track has a label which gives the initial mass of the star on the ZAMS. The latest O-stars are observed to have $\log(T_{\text{eff}}) = 4.52$, and this corresponds to an initial mass of $17.1 M_{\odot}$ for $Z = 0.04$. The numerical values shown along the tracks give the core helium fraction during the helium burning phase. Hatch marks correspond to the Wolf-Rayet (WR) phase which appears in the final stages of evolution.

By definition, a main sequence star is powered by core H-burning. This condition is maintained throughout the rightward excursion from the ZAMS to the first blueward retracement. Figure 11 shows that the main sequence corresponds to a wide band for high mass stars (also see figure 15 in Maeder & Meynet 1989).

During this time, energy production proceeds via the CNO hydrogen-burning cycle in the core. Energy transport out of the core is by convection; radiative transport is inefficient due to the large electron scattering opacity. The situation is reversed in the envelope where energy transport is radiative. As the radiation escapes the star, atomic line opacity converts the radiation pressure into a wind which slowly removes the outer layers of the star. Chiosi & Maeder (1986) review the effects of stellar winds on evolution.

Semiconvection and convective overshoot both affect the evolution of massive stars (cf. Chiosi & Maeder 1986 and references therein). Semiconvection occurs at the interface between the convective core and radiative envelope for the condition where the temperature gradient exceeds the adiabatic value (Schwarzschild criterion), but the density gradient equals the adiabatic value (Ledoux's criterion). The net effect is to cause mixing. Maeder & Meynet (1987, 1989) argue for a value of ≈ 0.20 to 0.25 for the overshoot parameter, d_{over}/H_p , the ratio of the distance a convective cell will travel before thermalizing with its surroundings to the pressure scale height. Their argument is based upon successful predictions from models which assume this value for high mass stars. This moderate overshoot will reduce the lower mass requirement for WR star formation and increase the time a WR star spends as a WN versus WC type (see Maeder & Meynet 1989 for further effects). The models in Figure 11 are calculated for $d_{\text{over}}/H_p = 0.20$. See Maeder & Conti (1994) and references therein for a discussion of convection and mixing.

The continued rightward extension in the HR diagram from the ZAMS is initiated at core H-exhaustion when nuclear processing shifts from the core to an H-burning shell. This stage coincides with an expansion of the outer layers of the star at

nearly constant luminosity. This rightward excursion is limited, at least for stars between $15 M_{\odot}$ and $25 M_{\odot}$, by the opacity in dust which condenses out of the extended envelope. For some temperature around $\log(T_{\text{eff}}) \approx 3.6$, the star can no longer cool because of this, and it proceeds up the Hayashi track with a He-burning core. More massive stars move leftward on the HRD during core He-burning.

The most massive stars do not evolve rightward through the region above the Humphreys-Davidson (HD) limit, a temperature-dependent limit in the HR diagram defined by observations of the most luminous stars (Humphreys 1993). Stars near this limit sporadically lose large amounts of mass in a luminous blue variable (LBV) stage and retrace to the left. The star might have repeat mass-loss episodes, each time losing more mass and returning to the left as an Of/WN star. When the surface content of hydrogen finally falls enough (see next section), the star has lost enough mass to remain to the left of the HD limit as a WR star. The very latest stages of the most massive stars have carbon-burning cores.

B. Wolf-Rayet stars

Wolf-Rayet stars are hot, luminous, emission-line stars with strong winds. These stars represent the latest stages of evolution for massive O-stars, $M_{\text{initial}} > 20 M_{\odot}$; and they are younger than 10^7 yrs. The wealth of observational data gathered since their discovery by Wolf & Rayet (1867) has recently been supplemented by new models which show that mass-loss controls their evolution after leaving the main sequence.

It is now clear that stars which pass through the WR phase will lose almost all of their mass in a copious stellar wind. In fact, stellar models predict that even the most massive O-stars, with perhaps $M \approx 120 M_{\odot}$, will end their lives with a mass between 5 and $10 M_{\odot}$ before becoming supernovae. They are extremely rare in our Galaxy,

probably constituting no more than about 1 out of every billion stars; however, they make a significant contribution to heavy elements in the ISM due to their prodigious winds which carry away nuclearly processed material.

The "standard model" for these stars is discussed below, and further details can be found in recent reviews, i.e. Abbott & Conti (1987), Chiosi & Maeder (1986), Maeder (1991b), Maeder & Conti (1994), Chiosi et al. (1992), Conti (1988) and references therein.

1. observational classification

The most distinguishing observational feature of the Wolf-Rayet stars is the prominent complex of emission lines in their spectra. These emission lines are from low- to high-ionization species, i.e. NIII through NV, and CII through CIV. Subtypes comprising the WC and WN sequences are distinguished observationally by the specific flux ratios between low-ionization and high-ionization lines of carbon and nitrogen. The classification scheme from Smith (1968) is shown in Table 2.

The scheme has been codified so that lower numbered subtypes correspond to a higher ionization state and a higher temperature in analogy with the MK system. Low-temperature subtypes are referred to as "late", i.e. WNL and WCL while high-temperature subtypes are referred to as "early", i.e. WNE and WCE. Notice that the spectral discriminants are all at optical wavelengths, so near-infrared classification of new WR stars will rely on new near-infrared observations of optically classified stars.

Theoretical models predict surface abundances versus time and composition. These predictions can be associated with various WR stars in order to understand high mass stellar evolution. Surface abundances can be directly measured using optical and UV spectroscopy, and the results are shown in Table 3. The table shows that a

classification can be made based on surface abundance of H, He, N, C, and O. See Maeder (1991a) and references therein for more information about these surface abundances.

Table 2: Observational Classification Scheme for WR Stars from Smith (1968) with Extensions from van der Hucht et al. (1981) and Crowther et al. (1995)

Nitrogen Sequence			
Spectra l Type	Characteristic	Criteria	
WN11	NII~HeII, NIII weak or absent	NII λ 3995 ~ HeII λ 4686	
WN10	NIII~NII	NII λ 3995 ~ NIII $\lambda\lambda$ 4634-41	
WN9	NIII>NIV	NIII $\lambda\lambda$ 4634-41 present; NIV λ 4058 weak or absent; HeI, lower Balmer series P Cygni profiles	
WN8	NIII>NIV	HeI strong with violet absorption edges; NIII λ 4640 \approx HeII λ 4686; NIII λ 5314 present	
WN7	NIII>NIV	HeI weak; NIII λ 4640 < HeII λ 4686	
WN6	NIII \approx NIV	NV present but weak; nIII λ 4640 blend present	
WN5	NIII \approx NIV \approx NV	NIII λ 4640 blend present	
WN4.5	NIV>NV	NIII very weak or absent	
WN4	NIV \approx NV	NIII very weak or absent	
WN3	NIV<NV	NIII absent	
WN2	NIV<NV	NV weak or absent; strong HeII	
Carbon Sequence			
Spectra l Type	CIII λ 5696/ OV λ 5592	CIII λ 5696/ CIV λ 5806	Width of CIII,IV λ 4650
WC9	—	3.0	10
WC8.5	—	>1.0	
WC8	—	1.0	—
WC7	8.0	0.7	35
WC6	>1.0	0.3	45
WC5	<1.0	0.3	85
WC4	\approx 0	\approx 0	—

Table 3: Observed Surface Abundances for WR Stars
Adapted from Maeder (1991a)

Subtype	WN	WC
		(C + O)/He (in numbers)
9	H present	0.03 to 0.06
8		0.1
7		0.2
6		0.3
5	H absent	0.55
4		0.7 to 1.0
3		
2		

Evolutionary models do not generally have sophisticated line formation and wind modelling, so Table 3 is much more useful than Table 2 for determining when an evolving star is a particular WR subtype from a theoretical viewpoint. Maeder and coworkers use the following scheme for identifying WR subtypes in their models:

- WNL (WN9-6): $X_s \leq 0.40$ and $\log(T_{\text{eff}}) \geq 4.40$
- WNE (WN6-2): $X_s < 10^{-3}$
- WC: presence of He-burning products in abundances show in Table 3

2. the nature and evolution of WR stars

Recent reviews discuss the nature of WR stars and their evolution from main sequence O-stars. Chiosi & Maeder (1986) review the effects of mass-loss on the evolution through the HRD and on the appearance of processed material at the surfaces of massive stars. Abbott & Conti (1987) review observational data on Wolf Rayet stars. Chiosi et al. (1992) review new input physics and observations leading to a new

understanding of the HRD. Maeder & Conti (1994) review the impacts of massive stars on galactic environments.

a. stages

Recently, new models including updated opacities from the OPAL project and more accurate mass-loss have been calculated (cf. Maeder & Meynet 1994 and references therein). These models generally verify an increasingly accepted sequence for massive star evolution. Massive stars are thought to evolve through the following stages:

$$O \rightarrow Of/WN \leftrightarrow LBV \rightarrow WNL \rightarrow WNE \rightarrow WCL \rightarrow WCE \rightarrow SN,$$

where the double-arrow symbolizes recurrent phases of evolution between Of/WN and LBV stages where the heaviest mass-loss occurs in the latter.

Not all massive stars will go through each phase of this evolution as can be seen in Figure 11. The lowest O-stars will not become WR stars; for $Z=0.04$, the minimum mass for an O-star is $17.1 M_{\odot}$ whereas the minimum mass to form a WR star is $20 M_{\odot}$ (see Figure 12). There is also a small mass range where stars will become WN types without further evolving to WC types. Stars which do become WC types will enter the sequence at early types for lower masses so that only the most massive stars will join the carbon sequence as a WC9. Also, only the most massive stars will lose large amounts of mass in an LBV stage near the HD limit (see Figure 13).

While this evolutionary scenario seems internally consistent, it is not yet proven to be a unique explanation for the observations. For instance, Crowther et al. (1995) agree with the general trend of $O \rightarrow WR$, but they give the following sequences for WN7 and WN8 stars:

$$O \rightarrow Of \rightarrow WNL+abs \rightarrow WN7(\rightarrow WNE) \rightarrow WC \rightarrow SN, \quad \text{for WN7}$$

$O \rightarrow LBV \text{ or } RSG \rightarrow WN8 \rightarrow WNE \rightarrow WC \rightarrow SN,$ for WN8,

where the WNL+abs have high hydrogen content, high velocity winds, and the upper Balmer series is in absorption; these properties are in contrast to those found in regular WNL stars.

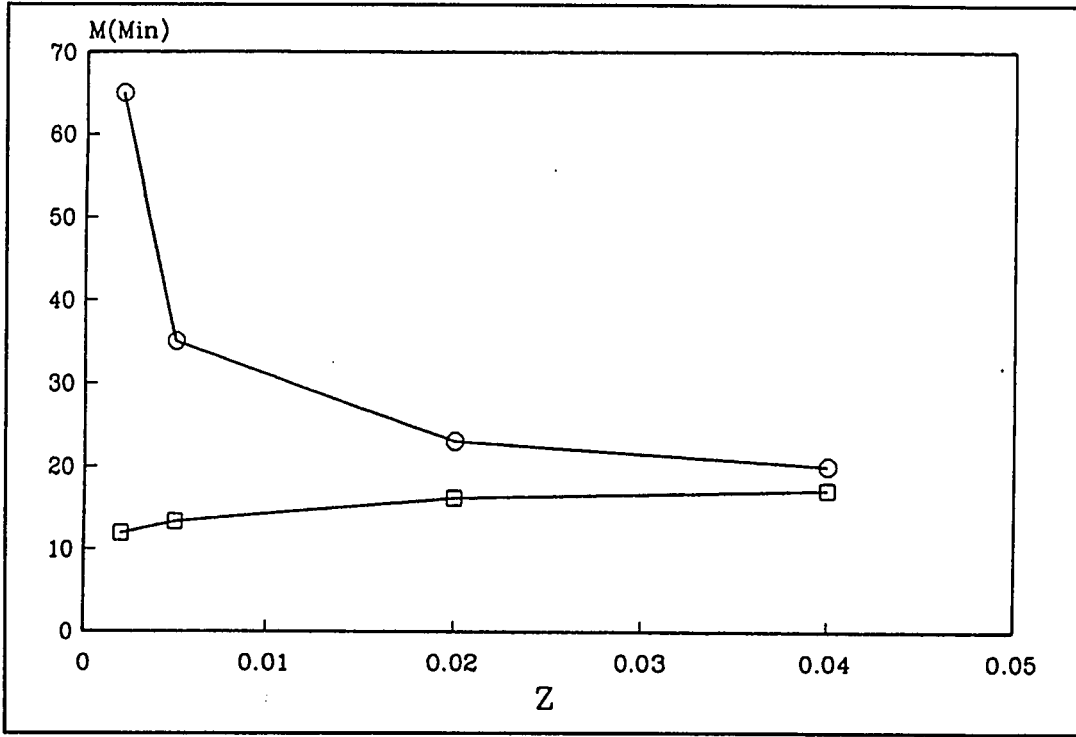


Figure 12. Minimum mass limits for O-stars and WR stars from Maeder (1991b).

Figure 14 shows model predictions for the surface abundances versus age and mass for two $M_{\text{initial}} = 85 M_{\odot}$ stars: one with $Z = 0.04$, and one with $Z = 0.002$. Various stages and WR subtypes are noted at the top of the diagram. The identification criteria from II.E.2.a have been used. Here is an example of two stars with the same mass, but dramatically different initial metal content. Their evolution is noticeably different.

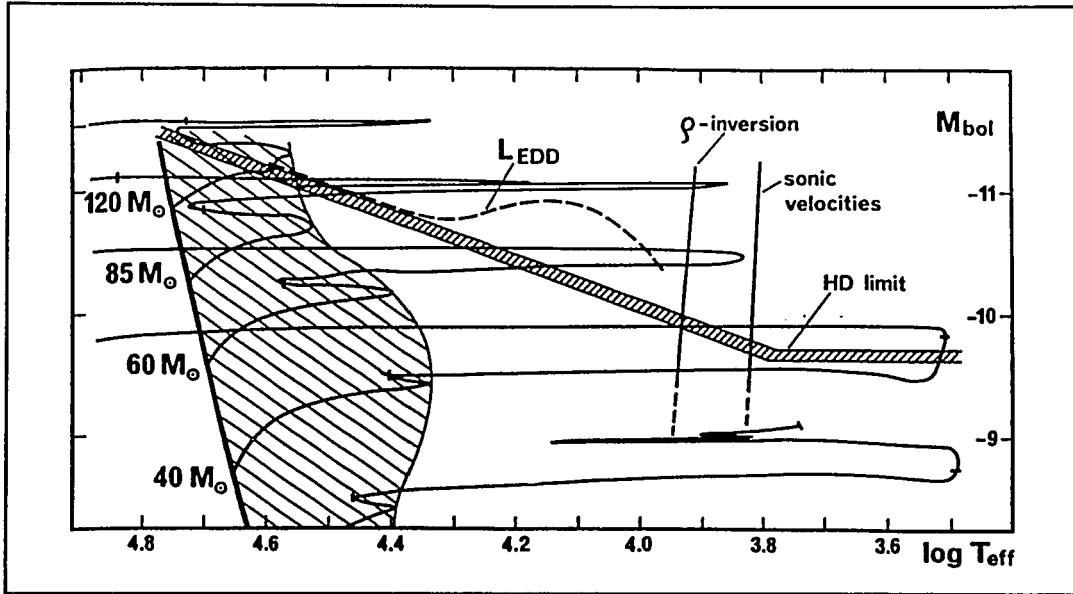


Figure 13. Upper HR diagram showing HD limit and evolutionary tracks for massive stars from Maeder (1989).

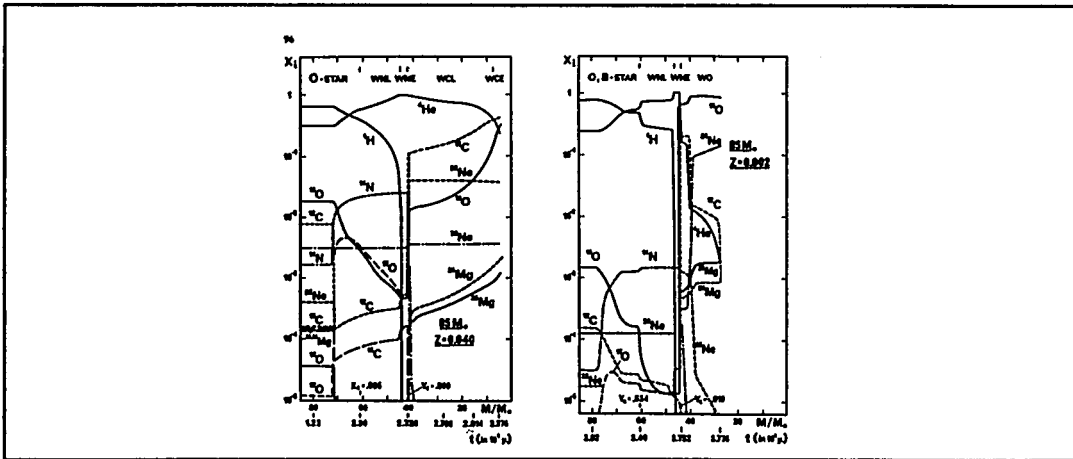


Figure 14. Theoretical surface abundances and evolution of 85 M_{\odot} , $Z = 0.04$, star from Maeder (1991a).

b. mass-loss and evolution

While the total lifetimes are about same, to within 15%, for the two example stars in Figure 14, the age when entering the WR phase are different. This is because the total lifetimes are mostly dependent on initial mass while surface features, which

give WR stars their classification, are mostly controlled by mass-loss. The high metallicity star will have more mass-loss in the O-star phase, and nuclearly processed material will be exposed more quickly. Electron scattering is the dominant opacity source in the convective core, so the metallicity effects on internal structure and main-sequence lifetimes are minimal (Maeder 1991b). Equation (2), from the models of

$$\frac{\dot{M}_z}{\dot{M}_{z_0}} = \left(\frac{Z}{Z_0} \right)^{0.5}, \text{ where } Z_0 \text{ is for } Z=0.02. \quad (2)$$

Maeder and Meynet, shows that the mass-loss for the high-metallicity star is higher by about a factor of five. Both stars enter the WR phase after losing over half of their original masses, i.e. $M_{\text{remaining}} \approx 40 M_{\odot}$.

Observational evidence (Conti 1988) suggests that mass-loss rates for WNL stars are nearly constant with $dM/dt = 4(10^{-5}) M_{\odot}/\text{yr}$. Maeder & Meynet (1994) have calculated models for this value and twice this value, and they find that the latter gives much better correspondence between output parameters, i.e. number ratios, and observations.

The model mass-loss law for WR stars does not depend on metallicity as it does for O-stars. Equation (3) (Langer 1989) is based on observations of WNE and WC

$$\dot{M}_{WR} = (0.60 - 1.00) 10^{-7} \left(\frac{M_{WR}}{M_{\odot}} \right)^{2.5}. \quad (3)$$

stars, and it shows the heavy dependance in the mass-loss relation on current mass; the first coefficient is for WNE types, and the last for WC types. This relation leads to large mass-loss rates at the beginning of the WNE stage when a star will still have large mass. The result at the end of the WC phase is a star with very low mass. For

instance, taking the example shown in Figure 14, we can calculate a mass-loss of $6(10^{-4}) M_{\odot}/\text{yr}$ for a star with $M_{\text{initial}} = 85 M_{\odot}$ and a mass of $\approx 40 M_{\odot}$ entering the WNE phase. Such a high mass-loss leads to rapid peeling of the external layers and a short WNE lifetime (see Figure 14). This mass-loss results in the nearly complete evaporation of the star. For the $85 M_{\odot}$ star, $M_{\text{final}} \approx 6 M_{\odot}$ after the carbon core is exhausted.

3. wind theory

In spite of great effort, wind models for evolved O-stars are still plagued by an inability to reproduce observed momentum rates, usually expressed as the dimensionless "performance number" (see equation (4)). Free-free electron scattering provides the

$$\eta = \text{performance number} = \frac{\dot{M}v_{\infty}}{L/c}. \quad (4)$$

dominant continuum force in O and WR stars, although adding line opacity will give a significant increase radiative acceleration. Models based on these assumptions give reasonable predictions for main-sequence O-stars where single-scattering models can achieve the observed performance numbers of order unity. WR stars have much more powerful winds, $\eta > 1$, and modifications to the standard radiation pressure mechanism must be made. Lucy & Abbott (1993) showed that multiple scattering can produce $\eta > 15$, but this assumes *a priori* that a wind with large Dm/dt , and thus high ionization gradient, exist. Most recently, Langer et al. (1994) and Kiriakidis et al. (1993) claim that pulsational instabilities can explain the rapid mass-loss for LBVs near the HD limit and the high mass-loss rates for WR stars as compared to O-stars.

4. observations

a. M_v and luminosity

The bolometric magnitude, M_B , can be calculated according to equation (5), assuming that the apparent magnitude (m), distance (d , in parsecs), extinction (A), and bolometric correction (BC) are known. Luminosities can then be calculated by

$$M_B = M_\lambda + BC_\lambda, \quad (5)$$

$$\text{where, } M_\lambda = m_\lambda + 5 - 5 \log d + A_\lambda.$$

$$\frac{L}{L_\odot} = 10^{-\frac{2(M_B - M_{\odot,B})}{5}} \quad (6)$$

measuring the absolute magnitude as shown in equation (6).

The extinction is related to the color excess, $E(\lambda_1 - \lambda)$, through a constant, C , which can be determined by examining the interstellar extinction law. Equation (7)

$$A_\lambda = C_\lambda E(\lambda_1 - \lambda), \quad (7)$$

$$\text{where, } E(\lambda_1 - \lambda) = (m_{\lambda_1} - m_\lambda) - (m_{\lambda_1} - m_\lambda)_0.$$

gives the general form for this relation while equations (8a) (Lundström & Stenholm 1984) and (8b) (Spitzer 1978) give concrete examples. These equations use the

$$A_v = 4.1 E_{b-v}. \quad (8a)$$

$$A_v = 3.09 E_{B-v} = 3.73 E_{b-v}. \quad (8b)$$

traditional subscripted notation of filter names to designate wavelength, where v (5160Å) and b (4270Å) are from the Westerlund-Smith narrow-band photometric system and are described by Smith (1968), and V (5500Å) and B (4400Å) are described by Johnson (1966). The interstellar extinction law, $A_\lambda \propto \lambda^{-1.5}$, was used to relate A_v to

E_{b-v} . Of course, the extinction can only be calculated in this simple way if the intrinsic colors, $(B-V)_0$ or $(b-v)_0$ in this case, are known.

Smith (1968) observed 43 WR stars in the Magellanic Clouds and 75 in the Galaxy. The stars were classified according to reddening-free parameters and then intrinsic colors and absolute magnitudes were found by assuming a small amount of extinction and a predetermined distance modulus to the Large Magellanic Cloud (LMC). These observations showed that WR stars have mean $(b-v)_0 \approx -0.15$ to -0.20 with little scatter from subtype to subtype but larger scatter for individual observations within subtypes. These observations directly yield M_v which showed a progression toward less luminosity for earlier subtype in the WN sequence and a constant for WC subtypes, except for WC8 and WC9 stars which appeared to be more luminous than the earlier subtypes.

Conti et al. (1983) reexamined the M_v -subtype relation and verified the trend found by Smith (1968) for WN stars; however, they find more negative M_v for later WC subtypes. Figure 15 shows the correlation between M_v and subtype for WR stars with data from the LMC and the Galaxy represented. Notice that the scatter within some subtypes is as much as 3 magnitudes. This scatter does not seem to correlate with any other observed parameter, i.e. line-widths (Leep et al. 1983).

M_v can be converted to a luminosity by assuming a BC, as shown in equations (5) and (6). In principle, a correlation could be made between BC and spectral-type by directly measuring and integrating the emergent flux at many wavelengths; if the distance is known, then the luminosity can be calculated. BCs determined this way could then be used for stars of the same spectral type which are much further away. This technique is difficult to use in practice for hot stars because most of the emergent

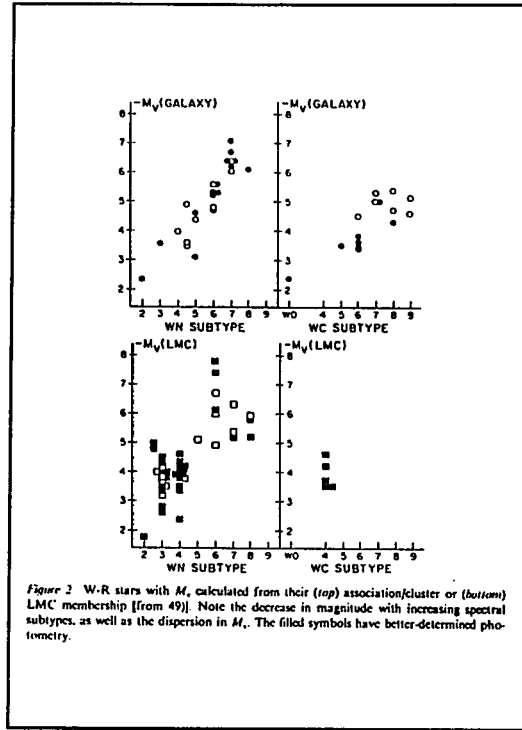


Figure 15. M_v -subtype data for WR stars from Abbott & Conti (1987).

flux is in the ultraviolet (UV) region. This flux is heavily absorbed near the star for wavelengths below the Lyman limit ($\lambda < 912 \text{ \AA}$) and through the ISM beyond this limit.

Luminosity could be estimated by determining the effective temperature, T_{eff} , and using this value as an input to atmosphere models. Unfortunately, the error in determining T_{eff} can be substantial for hot stars because the continuum is sampled in the near-UV, visible, and IR spectral regions where the slope is largely invariant to changes in temperature. In addition, the continuum can be formed by the wind or free-free emission depending on the wavelength, so a unique temperature cannot be easily determined.

b. radius and temperature

Hamann et al. (1993) use new data and the spectral analysis of Schmutz et al. (1989) to determine observed physical parameters for WN stars. The analysis is based upon comparing synthetic to observed Helium emission-line profiles. A pure helium core with a spherically symmetric expanding wind is used to calculate equivalent widths for a grid of radius and temperature. A unique solution pair (R_* , T_*) can be found by comparing predicted to observed equivalent widths for both HeI and HeII emission lines where "*" denotes values at the base of the wind. The luminosity is then defined to be $4\pi R_*^2 \sigma T_*^4$. The results of this analysis for most Galactic WN stars is shown in Figure 16a and b. The new suffixes, "w" and "s", have been added to the WNE (WN2 to WN6) subsequence to indicate whether the emission lines are weak or strong respectively. Notice that the WNL and WNE-w seem to form a continuous transition in these figures, but the WNE-s are quite distinct.

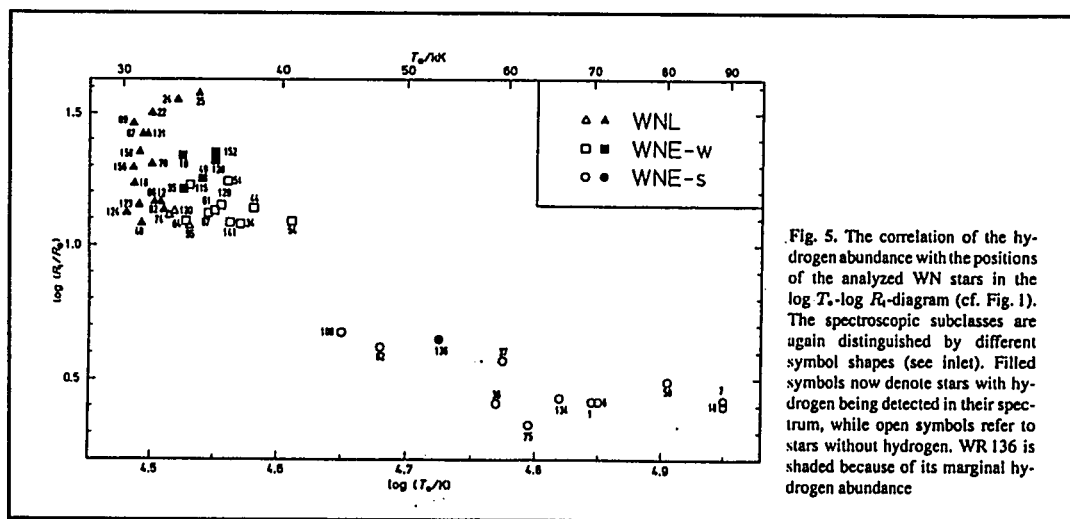


Figure 16a. R,T solutions using HeI and HeII emission lines from Hamann et al. (1993).

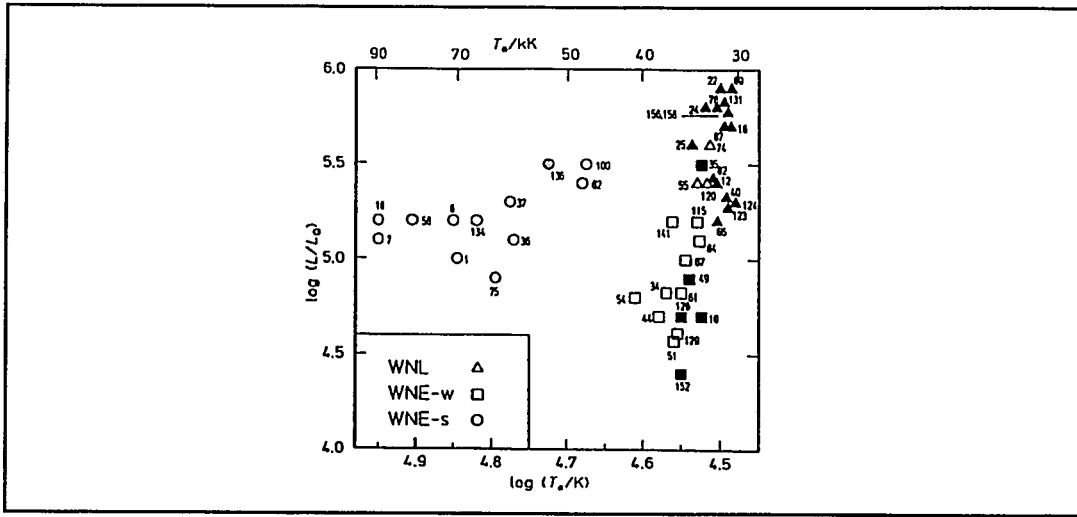


Figure 16b. L, T for WR stars from Hamann et al. (1993).

The coolest temperatures give $\log(T_{\text{eff}}) \approx 4.5$, slightly higher than the value for $\log(T_{\text{eff}})$ from section II.E.2.a. This is due to the fact that T_{eff} is defined by the observed continuum which is formed in the wind whereas T_{e} is the temperature at the core surface, R_{c} . The observed luminosities are lower than predicted by the models in Figure 11.

Hamann et al. (1992) developed a similar approach relying on spectral analysis for WC stars by adding carbon to a pure helium model. Koesterke et al. (1992) used this approach to generate isocontour plots in the $(R_{\text{c}}, T_{\text{e}})$ -plane for equivalent widths of CIII, CIV, HeI, and HeII. Unfortunately, they have not yet published analyses of a significant number of WC stars.

c. mass

Masses of WR stars can only be estimated for the stars in binary systems where two sets of spectra are observed. The velocity curves can be difficult to interpret as the emission lines from the WR components are produced at varying depths, and thus with

varying velocities, in the wind. For the dozen or so observed WR-O binary systems, the masses of the WR components are $\sim 20 M_{\odot}$ or less and are generally less than the masses of the O components (cf. Table 1-32 in Divan & Burnichon-Prevot 1988).

d. wind characteristics

Wind densities, velocities, and column densities are normally measured by theoretically fitting P Cygni line profiles of lines in the UV, but this technique is not trustworthy for WR stars. Instead, the density can be estimated by measuring the free-free emission at radio wavelengths. At these wavelengths, the emission comes primarily from the very outer parts of the winds where the flow has attained the terminal velocity, v_{∞} . The radio flux is related to the density at each point along the column where observations at higher frequencies probe deeper into the wind. Panagia & Felli (1975) and Wright & Barlow (1975) have shown that the total radio flux will be proportional to $\dot{v}^{0.6}$, and this flux can be related to the mass-loss rate and v_{∞} . The mass-loss rate can then be calculated from the radio flux once v_{∞} is known. The terminal velocity, v_{∞} , is calculated from the displacement of the absorption edge from line center for a P Cygni profile. UV lines are normally used for this simple measurement, but Williams & Eenens (1989) have argued that the $2.06 \mu\text{m}$ line in the IR is more suitable for estimating v_{∞} .

e. numbers and distribution

OB and WR stars are confined to the plane of the Galaxy, and there seems to be a relative minimum in the direction of the Galactic anticenter (Conti & Vacca 1990). The spiral arms can be traced through the distributions of both the OB and WR stars. While both the main-sequence and evolved stars show a similar Galactic distribution, there is a further trend toward larger WR/O inside the Solar circle. This trend is

probably a result of the increasing metallicity toward smaller Galactocentric radius. In fact, WR/O is seen to increase for higher metallicity in nearby galaxies as shown Figure 17a from Maeder & Meynet (1994). The observational trend for WC/WR versus Z is similar and is shown in Figure 17b. These ratios are for continuous star formation and are therefore time independent. It is important to realize that a starburst scenario, for a cluster or an entire galaxy, will have time dependent solutions for these ratios (Parker et al. 1995; Meynet 1995). This can be used to determine the age of a particular starburst.

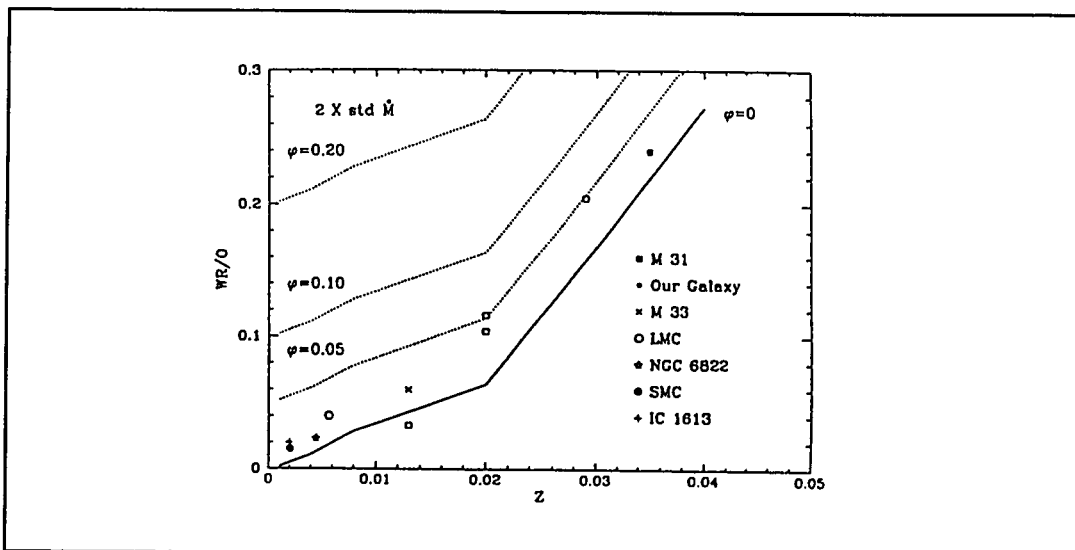


Figure 17a. WR/O vs. Z from Maeder & Meynet (1994).

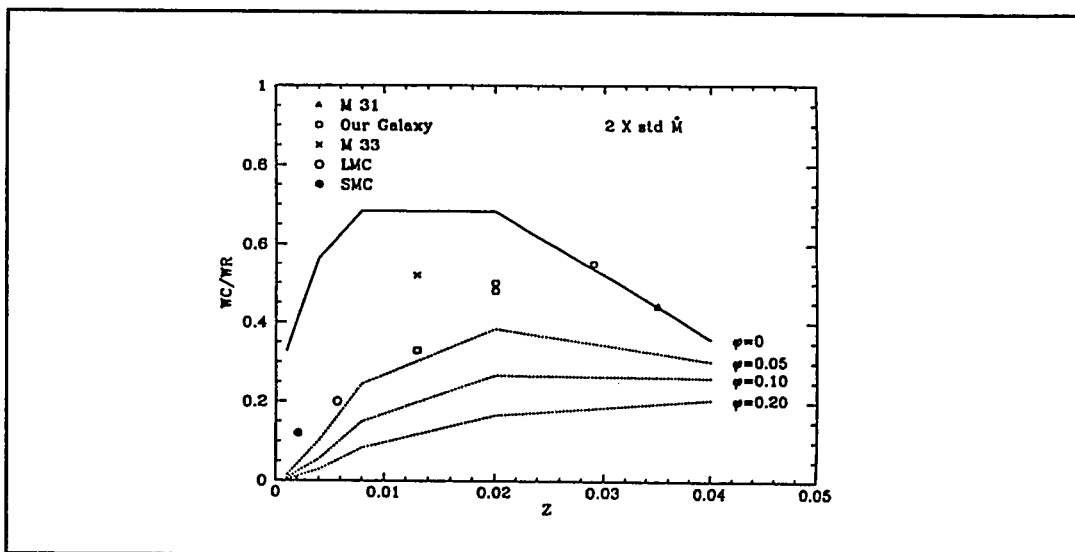


Figure 17b. WC/WR versus Z from Maeder & Meynet (1994).

III. A search for hot, young, emission-line stars near the Galactic Center

We performed a search for hot, young, emission-line stars near the GC by imaging through narrow-band filters and obtaining spectra in the H and K bands. The filters were designed to be centered on prominent near-infrared emission lines seen in evolved OB stars. Additional "continuum" filters were designed to sample the continuum very near to, but not including, these emission lines. The images were searched to find stars with emission-line excesses, and these targets were classified according to spectra obtained in the follow-up survey.

A similar method has been used previously at optical wavelengths, where a large body of spectra for evolved stars exists. Armandroff & Massey (1985) used custom design "WR" filters to image fields in NGC 6822, IC 1613, and M33 using a CCD. Their filters have narrow bandwidths of 50 Å giving $\lambda/\Delta\lambda \sim 100$. Their "WC" filter is centered on the $\lambda 4650$ CIII emission-line found in WC stars, and a "WN" filter is centered on the $\lambda 4686$ HeII emission-line; a third "continuum" filter is centered at a slightly longer wavelength to allow subtraction of stars without emission lines. This simple 3-filter system was capable of separating most WR stars from normal stars as well as further subdividing the WR stars as WN or WC types. They found 7 new candidate WR stars in NGC 6822 and 5 in IC 1613. As a test, they verified the 16 previously known WR stars in M33 and found 5 additional candidates.

While similar to the new filter system described here, their system was calibrated for all WR subtypes so that a star could be classified based solely on spectrophotometry. Such a system is useful in cases where low flux levels preclude spectroscopy, i.e. WR stars in other galaxies. Smith (1968) designed a similar system

to classify WR stars in the LMC based upon observations of Galactic WR stars using the Westerlund-Smith spectrophotometric system (see discussion in II.B.4.a.).

Of course, optical filter systems are inadequate for observing heavily obscured stars such as those along a line of sight to, and at the distance of, the GC. The visual extinction is about 30 magnitudes, so a typical WR star would have $V \sim 40$ assuming $M_V = -5$. Instead, we can use the fact that the extinction at K is $\sim 10\%$ of that at V to calculate $K \sim 12.5$ for the same star. This calculation neglects the effects of free-free emission and dust emission which will both increase the flux in the infrared. In fact, Conti (1991) has commented, "An intriguing project would be to devise narrow-band filters which isolate, say, the HeII 2.19 μm and CIV 2.09 μm emission-line features in WN and WC stars and attempt to detect WR stars at much deeper locations in our Galaxy than has heretofore been possible." We have designed just such a system to detect WR stars near the Galactic Center.

We chose to design filters centered on the HeI 2.06 μm emission-line, the CIV triplet near 2.08 μm , and the CIII/CIV/HeII 3.09 μm emission-line complex. We also chose to observe the 2.17 μm Bry line which is evident in emission in most evolved OB stars. We did consider observing the HeII 2.19 μm line, HeI 2.112/2.113 complex, and the HeI 1.70 μm lines, but decided that these were not the best lines, for reasons discussed later.

A. project goals

The project goals are the following:

1. find and characterize stars the hot, emission-line stars

Evolved O stars represent the best compromise between detectability and youth.

O stars are younger but difficult to find while red giants are easy to find, but not as

young; also, the red giants do not necessarily represent products from a single star formation episode. Red supergiants are very bright, but their spectra are not very different from the spectra of red giants (cf. Sellgren et al. 1987).

As well as being easily detectible, these stars are very interesting because they have been found within the central parsec where classical star formation processes are likely to be inhibited. Finding emission-line stars near, but still outside, the central parsec will help show that classical star formation near the Galactic Center has occurred recently. Also, newly discovered emission-line stars can be compared to the recently discovered emission-line stars within the central parsec to determine whether the latter group have spectra suggestive of peculiar evolution.

2. compare number ratios, WR/O and WC/WN, for the region

These number ratios will depend on the individual ages of star formation regions, and we can only hope to observe the time independent theoretical ratios for a large number of star formation episodes beginning at random times in the past, i.e. continuous star formation.

Recent starburst models, calculated by Parker et al. (1995) and Meynet (1995), indicate that these number ratios peak a few Myrs after an initial star-formation episode. Ages for individual star-formation sites can be estimated from these models assuming instantaneous star formation. Furthermore, star formation from mergers in the central parsec should produce number ratios consistent with continuous star formation. Higher values would suggest a recent burst of star formation.

3. determine whether star formation rates and IMF for star formation regions near the Galactic Center are similar to what is found in the disk

This essentially can be cast as seeking the number ratios, WR/stars or O/stars. We will need to use the observable stars as a proxy for all stars and compare the ratio to that in the disk. For instance, we could compare WR/red giants. The number of WR and O-stars can be used to estimate the total number of stars above a certain mass formed in the recent star-formation episode. The total luminosity can be used to infer the total number of stars produced. Combining this information, the IMF slope can be estimated to see if higher mass stars are preferentially produced near the Galactic Center.

4. compare individual target stars to their analogues in the disk

Calculate M_K and $(H-K)_0$ for target stars versus those in the disk to see if the Galactic Center environment produces anomalous values.

B. survey strategy

We would like to observe the largest area possible while still covering the relevant observational parameter space in a practical amount of time. The narrow-band survey (phase I) must be completed over a 5 night run where the Galactic Center is only observable ($2.5 < \text{airmass} < 3.5$) for ~ 3.5 hours. The spectroscopic survey (phase II) must be completed over a second 5 night run with the same nightly time constraints.

1. coverage

The survey was designed to cover all of the known star-forming regions within 50 pc of the Galactic Center, and the spectral coverage was chosen to find all hot emission-line stars in this region.

a. spatial

Figure 18 shows a schematic representation of the survey. Each square box represents one telescope pointing for the $3'$ square field of the UCLA double-beam

infrared camera (McLean et al. 1993, 1994). Each square can be referenced by row number and position, so that the Galactic Center, represented by a single large star, is in position 3 of row 7. The center of the survey is to the north and east of the Galactic Center so that the star-formation regions associated with the ridge (Lis et al. 1994) could be included. The general shape of coverage follows the $158\ \mu\text{m}$ [CII] ($^2\text{P}_{3/2} \rightarrow ^2\text{P}_{1/2}$) emission described by Poglitsch et al. (1991); this emission is thought to come from UV-excited photodissociation regions, and the source of exciting radiation is likely to be hot stars (Heiles 1994). In fact, Poglitsch et al. (1991) generally find that the [CII] emission is from the surface of molecular clouds, and thus, the exciting stars are near the boundary or outside of these clouds.

Figure 18 also shows several star-formation sites discussed in section I.D.2. The Quintuplet cluster, symbolized by a cluster of stars, is near $\text{RA } 17^{\text{h}}43^{\text{m}}05^{\text{s}}$ and $\text{DEC } 28^{\circ}47'00''$. This cluster contains several hot, young stars which are products of recent star formation. Another cluster of hot, young stars lies $\sim 5'$ to the west and is also symbolized by a cluster of stars. The A-D region is symbolized by 4 grey circles about $2'$ to the east of the Galactic Center. Sources E, F, and G lie a few arcminutes to the south of the Galactic Center. Several HII regions to the north of the GC are symbolized by open squares. IRAS GCC sources (Taylor et al. 1993) are shown as open circles, and OH/IR stars are shown as radio telescopes (Jones & Hyland 1986).

The survey is extended west of the Galactic Center to include the parachute-shaped region seen in radio maps (cf. Anantharamaiah et al. 1991). The southern extreme of the "dust ridge" is also included in the northeastern portion of the survey.

UCLA Near-Infrared Galactic Center Survey

Narrow-Band Filters: 2.058 μm (HeI), 2.085 μm , 2.166 (Br- γ), 3.092 μm (HeII/CIV), 3.150 μm
 Broad-Band Filters: H, K'

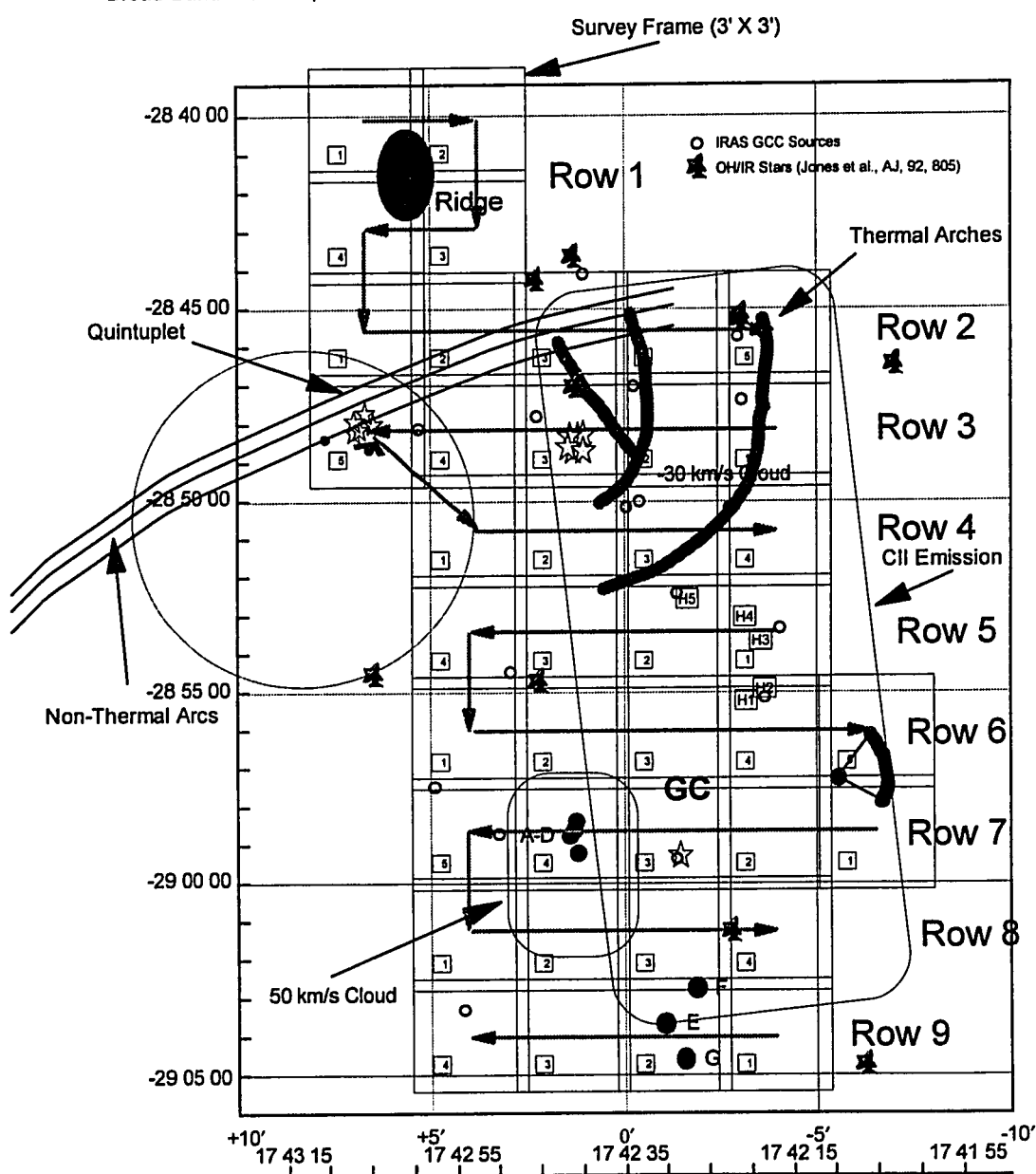


Figure 18. Schematic of the GC survey.

b. stellar types

The survey was designed to find the hot, young, emission-line stars which are indicators of star-formation within the past 10^7 years. The emission lines make these stars much easier to distinguish from other stars in crowded fields where confusion limits the depth. We rely on template spectra to classify the stars with suspected excess emission.

Figure 19 shows K-band spectra of some WN stars from Williams (1983) and Hillier (1983) (see also Blum et al. 1995a). As expected from optical classifications discussed in section II.E.2.a, earlier subtypes show stronger emission from higher ionization species. Unfortunately, there is a dearth of spectra in the literature for these types of stars at the spectral resolution used in our study. Consequently, we observed optically classified Galactic WN stars with our system.

Figure 20 shows K-band spectra of WC stars from Smith & Hummer (1988). These spectra were taken at an $R \sim 100$ while our system gives spectra with $R \sim 500$. Again, we observed known WC stars with our instrumental setup to provide better template data.

Figure 21 shows $R \sim 1350$ spectra of OB main-sequence stars from Hanson & Conti (1994). The "((f))" designation indicates NIII $\lambda 4634-41$ in emission and HeII $\lambda 4686$ in absorption (Walborn 1971). While these stars generally show absorption lines in the K-band, more luminous O-supergiants have HeI+NIII $2.112 \mu\text{m}$ and Br γ emission lines with HeII $2.189 \mu\text{m}$ in absorption. In fact, two O4 supergiants have HeII $2.189 \mu\text{m}$ in emission making their spectra quite similar to the spectra of WN7 stars (Conti et al. 1995).

McGregor et al. (1988a,b) studied Galactic and LMC emission-line stars, and some of the spectra ($R \sim 450$) are shown in Figure 22. The spectra show strong Br γ and HeI 2.058 μm emission in some supergiants and Ofpe/WN9 stars. η Car is classified as an LBV (Humphreys 1989). HD316285, HD326823, CD-42 11721, Hen S131, and Hen S101 have uncertain classifications while Hen S61 and Hen S9 have been classified as Ofpe/WN9 stars (see McGregor 1989 and references therein).

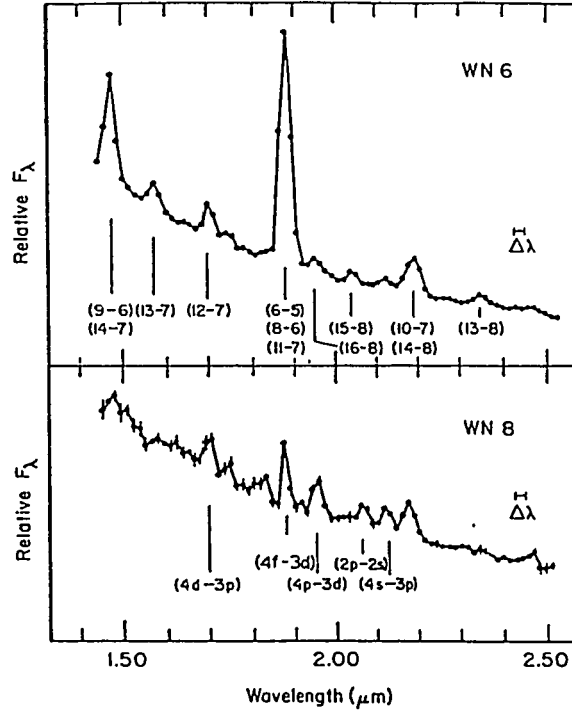


Figure 2. Excitation effects in WN stars HD 191765 and HD 177230. The He II are still dominant at WN6 while He I, mostly (4-3) triplets but also the (2s-2p) singlet, become important at WN8.

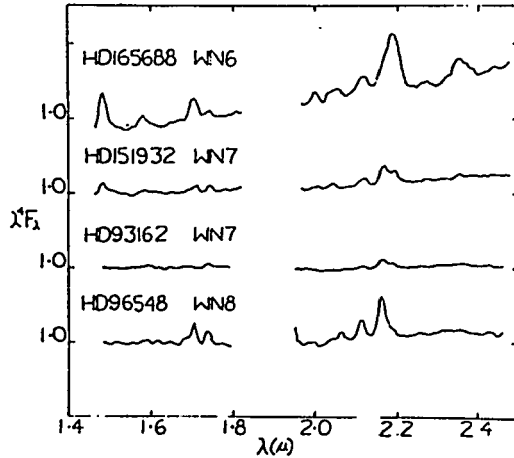


Fig. 2 CVF spectra of 4 WN stars.

(b) HD165688 (WN6). HeII emission lines dominate the spectrum and contribute approximately 8% and 12% to the H and K magnitudes respectively. Between 1.9μ and 2.1μ some of the features may be spurious due to incomplete cancellation of terrestrial CO₂. NIII at 2.113μ and NIV at 1.736μ are both present. A striking feature of HD165688 is its large IR excess. Using $E_{B-V}=1.06$ (Smith 1968) to correct for interstellar extinction implies that over 70% of the slope shown in Figure 2 is intrinsic to HD165688.

Figure 19. Near-infrared spectra for WN type stars from Williams (1983) (top) and Hillier (1983) (bottom).

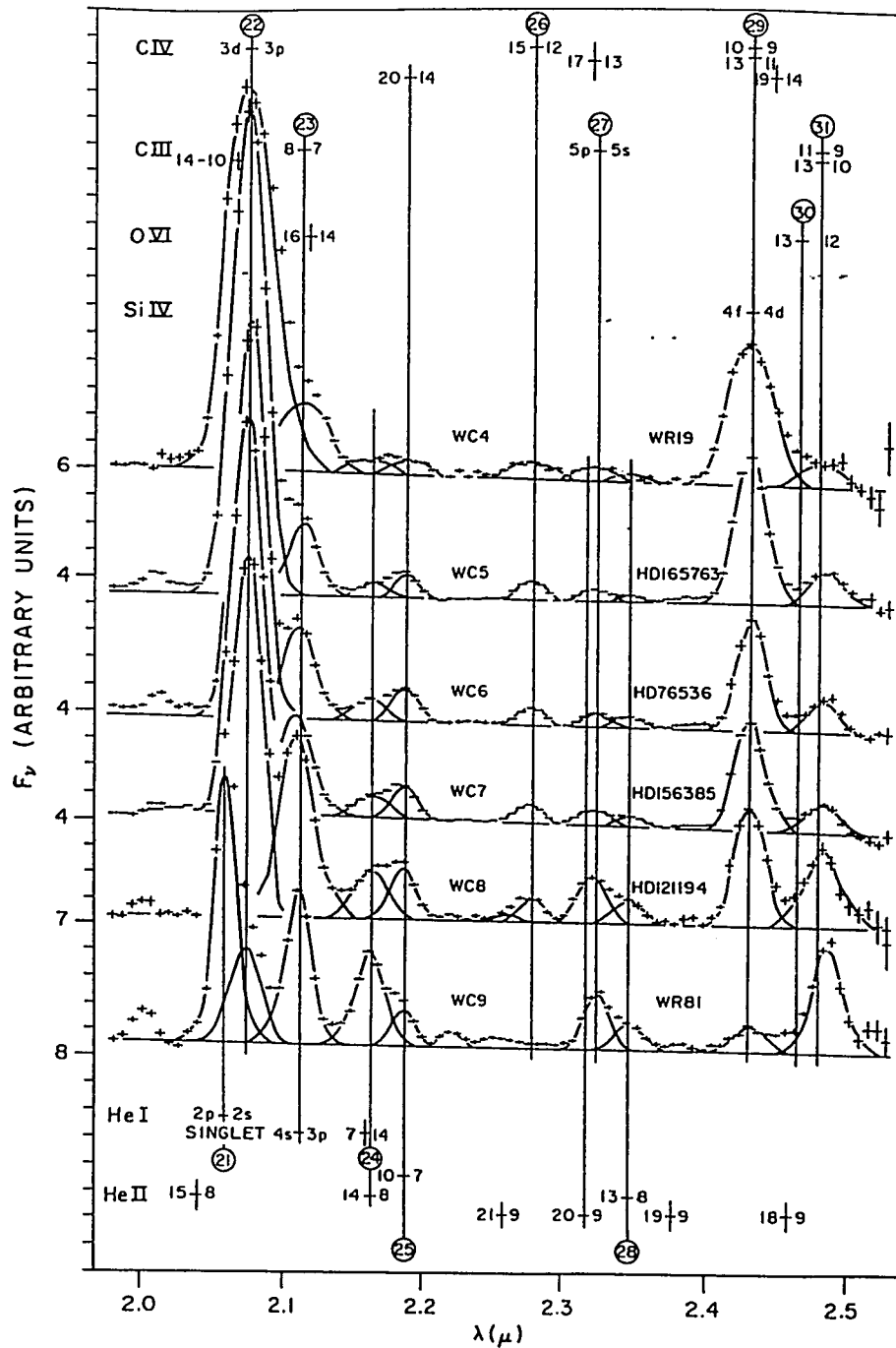


Figure 2. K band spectra of WC stars. Wavelengths of likely contributors are marked. Circled numbers are feature numbers (f) as in Table 1(b). A number on the flux axis is given for each spectrum, near the intersection of the continuum with the axis.

Figure 20. K-band spectra for WC type stars from Smith & Hummer (1988).

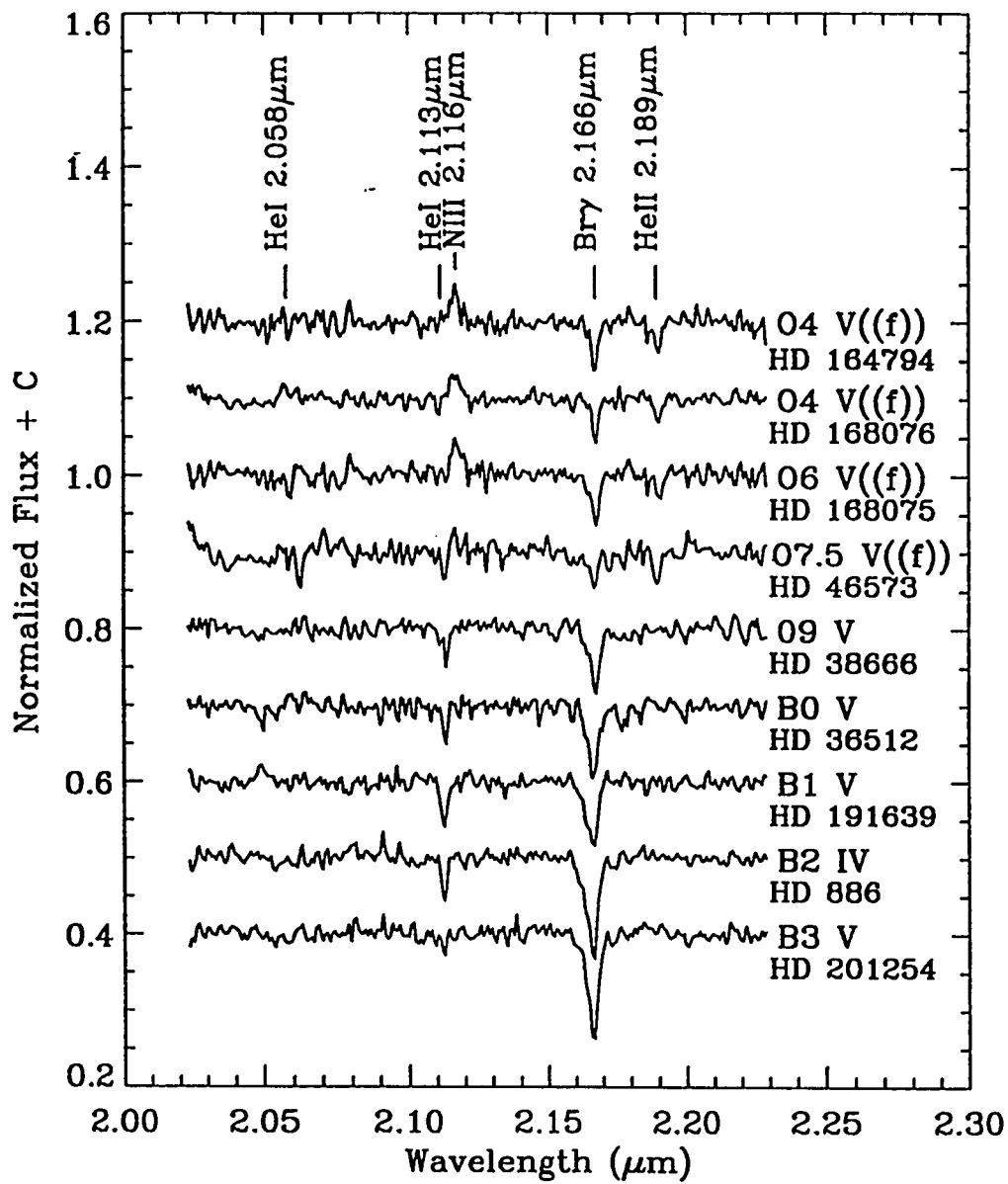


FIG. 1.—Dwarf spectral sequence from O4 to B3

Figure 21. K-band spectra of OB main-sequence stars from Hanson & Conti (1995).

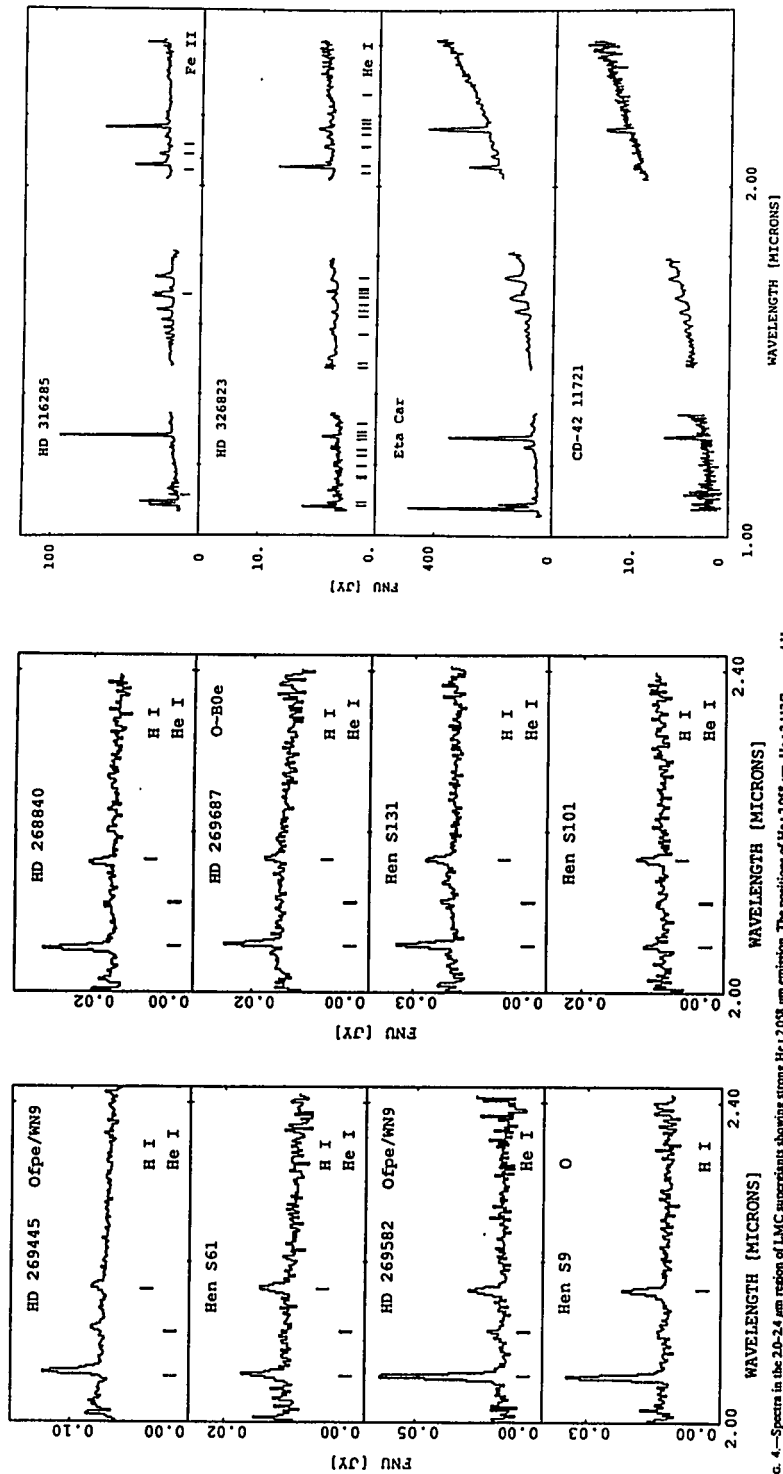


FIG. 4.—Spectra in the 2.0–2.4 μ m region of LMC supernovae showing strong He I 2.05 μ m emission. The positions of He I 2.05 μ m, He I 2.10 μ m, and He I Br γ are indicated.

Figure 22. Near-infrared spectra for LMC emission-line stars. The eight spectra on the left are from McGregor et al. (1988a), while the figure on the right is from McGregor et al. (1988b). See text for classifications.

c. wavelength

The survey is limited by the large amount of extinction to the Galactic Center, so the best compromise between apparent flux and sky thermal background is to observe in the K band ($\lambda_{\text{center}} = 2.2 \mu\text{m}$). The K' filter ($\lambda_{\text{center}} = 2.11 \mu\text{m}$) was used so that the contribution from steeply rising thermal background could be reduced as compared to using the K filter. Some measurement at another wavelength must be made so that the photometry can be corrected for extinction. For this reason, H-band images were taken. In addition, the continuum filter at $3.15 \mu\text{m}$ was used to provide photometry at a third wavelength. This third wavelength gives the crucial information needed to separate stars which are red due to extinction versus stars which are red due to local absorption and reradiation by circumstellar dust.

1). extinction

The interstellar extinction law has been discussed by Becklin et al. (1978), Landini et al. (1984), and Rieke et al. (1989). These authors agree that the extinction generally follows curve number 15 from van de Hulst (1946). Figure 23 shows the extinction at various wavelengths normalized to the V band as calculated by these authors. The extinction values adopted for this study are from Rieke et al. (1989), and they are shown in Table 4. The best fit curve for the measured values in the near-infrared is given in equation (9). The interpolated values for the table are referenced

$$\frac{A_{\lambda}}{A_K} = \left(\frac{\lambda}{2.2 \mu\text{m}} \right)^{-1.53} \quad (9)$$

with respect to the nearest measured value so as to maintain consistency. Rieke et al. (1989) give a measured value at $1.6 \mu\text{m}$, which they call "H", but the H-band filter is centered at $1.65 \mu\text{m}$. We use the interpolated value at $1.65 \mu\text{m}$ for H-band extinction.

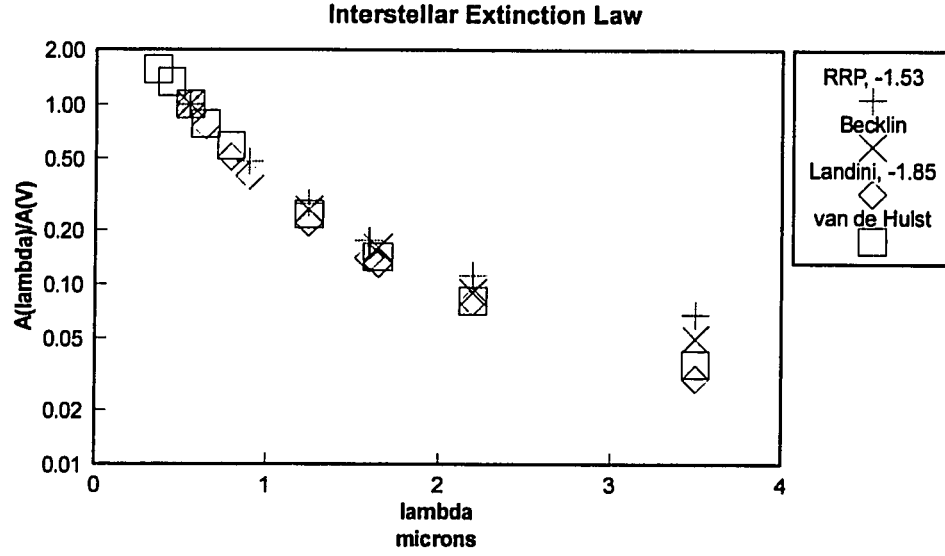


Figure 23. Interstellar extinction law.

Table 4: Extinction Law from Rieke et al. (1989) and interpolated values

Waveband	λ μm	A_λ/A_K Rieke et al. (1989)	A_λ/A_K Interpolated
V	0.55	8.9	
J	1.25	2.51	
	1.6	1.56	
H	1.65		1.49
	2.058		1.11
	2.085		1.09
K'	2.11		1.07
	2.166		1.02
K	2.2	1	
	3.092		0.73
	3.150		0.71
L	3.5	0.61	

Stars typically have $H-K \sim 2$ within the inner 50 pc of the Galactic Center. Most of the stars are giants with $(H-K)_0 \sim 0.3$. Using Table 4, we find $A_K = 2.0E_{H-K}$ giving $A_K = 3.4$ for the Galactic Center. This is somewhat large compared to $A_K = 2.7$ from Becklin et al. (1978) where a slightly different extinction law was used, i.e. $A_K = 1.3E_{H-K}$, and E_{H-K} was measured to be ~ 2.0 . Figure 24 shows the expected color-

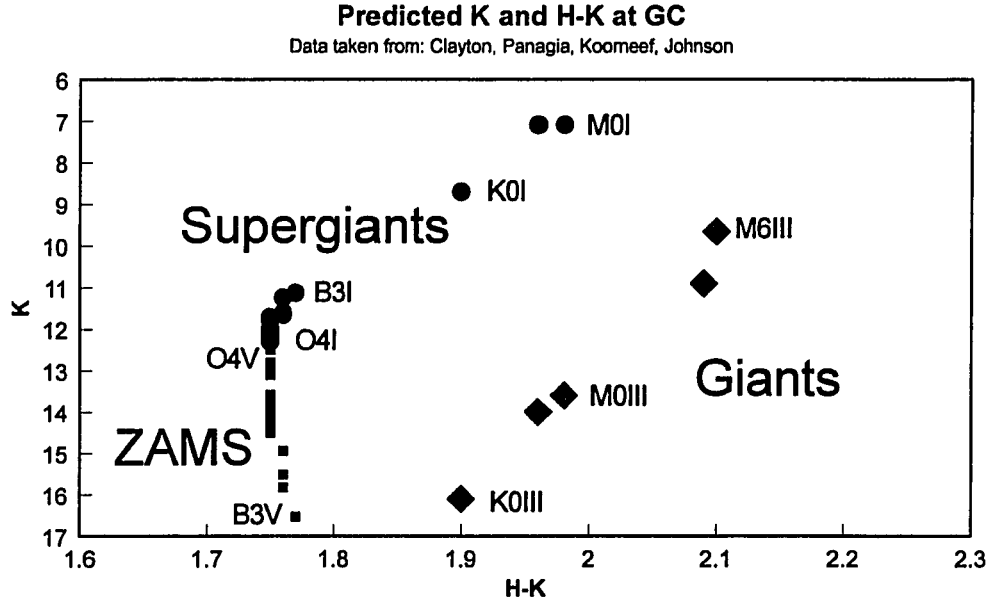


Figure 24. Apparent K magnitudes for luminous stars at the Galactic Center.

magnitude diagram (CMD) for luminous stars at the Galactic Center assuming $A_K = 3$. The data were compiled from Clayton (1983), Panagia (1973), Koornneef (1983), and Johnson (1966).

The supergiants are the brightest stars in Figure 24, but they are very rare; notice that the predicted magnitude for early M supergiants is consistent with $K = 6.7$ for IRS7 (Becklin et al. 1978), a suspected M2I star (Sellgren et al. 1987). The uppermost part of the zero-age main sequence (ZAMS) is at $K \sim 12.5$, and the apparent magnitude quickly drops for later types; these stars are also very rare. The giant stars have intrinsically red colors, and they dominate the stellar number density. In fact, a

typical image of the Galactic Center will be populated almost exclusively by red giants.

This explains why $H-K$ is ~ 2 instead of 1.7 for stars at the Galactic Center.

A similar graph is shown in Figure 25 where the predicted K magnitudes are

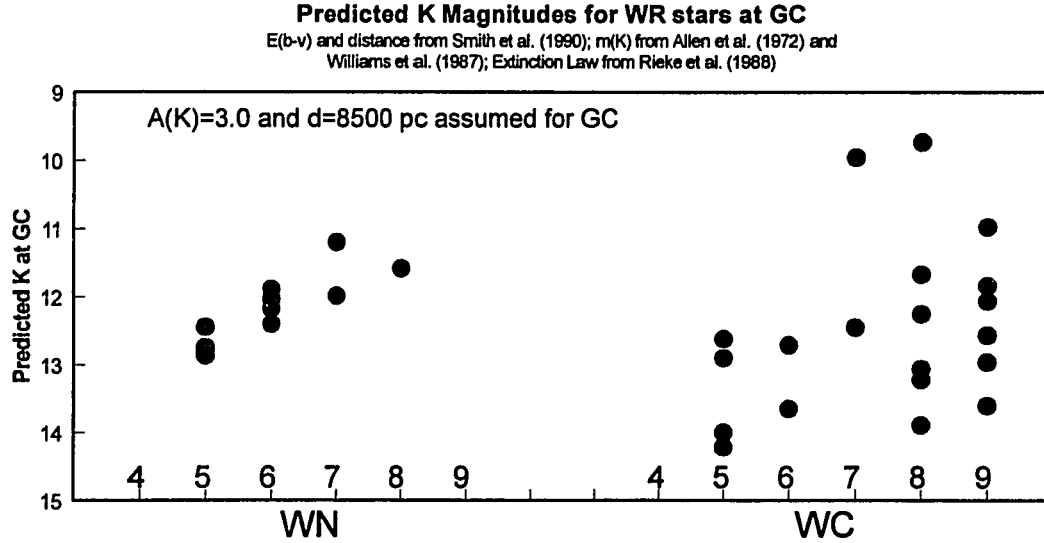


Figure 25. Predicted K magnitudes for WR stars at the Galactic Center.

based upon data for various Galactic WR stars. Literature values for d , m_K , and E_{b-v} were used to calculate M_K according the equation (5). These absolute magnitudes were then used to calculate m_K assuming $A_K = 3.0$ and $d = 8500$ pc for the Galactic Center. The distances to individual WR stars are from Smith et al. (1990) and van der Hucht et al. (1988). m_K are from Williams et al. (1987) and Allen et al. (1972). E_{b-v} are from Smith (1968) for the WC stars, and E_{b-v} is calculated from measured $b-v$ in van der Hucht et al. (1981) assuming $(b-v)_0 = -0.17$ for all WN stars. A_K were calculated using equations (8a) and (8b) along with Table 4, so that $A_K = 0.112A_V = 0.42E_{b-v}$.

2). emission lines

The survey strategy is to use the narrow-band survey to find potential emission-line stars, while the spectroscopic survey will give a unique spectral classification for

each star. The center wavelengths of the narrow-band filters must be chosen so that the emission-line stars will be most pronounced in continuum subtracted images.

The target stars have emission lines in the H band, but extinction at these wavelengths will be much greater than in the K band. These emission lines are also intrinsically weaker than the K band lines. For these reasons, we decided not to use narrow-band filters in the H band.

The template spectra in the previous section show that many emission-line stars have strong HeI emission at $2.058\ \mu\text{m}$ (e.g. WC9, WN subtypes, O7.5IIIe, Ofpe/WN9). Others show strong emission at $2.16\ \mu\text{m}$ due to Br γ , HeI, or HeII (e.g. all WR types, some of the stars in McGregor et al. (1988a,b)). The WR stars have strong emission near $2.11\ \mu\text{m}$ due to a HeI doublet, in late WC and WN subtypes, and a CIII complex in middle to early WC subtypes. This emission is lacking or weak in the Ofpe/WN9 stars and most other stars in the McGregor et al. (1988a & b) studies. The HeII line at $2.189\ \mu\text{m}$ is apparent in WN8 or earlier WN stars and all of the WC subtypes, but its excitation depends on higher temperatures than found in many emission-line stars. Table 5 summarizes the emission-lines found in many of the emission-line stars.

Table 5: Strong Emission Lines in Emission-line Stars

	2.058 μm	2.08 μm	2.11 μm	2.16 μm	2.189 μm
	HeI	CIV	CIII, HeI	HI, HeI, HeII	HeII, CIV
WNL	x		x	x	
WNE			>WN5	x	x
WCL	only WC9	<WC9	x	x	x
WCE		x	x		
Ofpe/WN9	x		x	x	
McGregor				x	
OeI	O7.5IIIe		some O8If	<O9	

2. phase I: narrow-band survey

Table 5 shows that most emission-line stars have some line emission near 2.16 μm , although HeII dominates for hotter stars and HeI dominates for WR types. A filter at 2.166 μm would be the best single filter for detecting emission-line objects, but it does not provide the best spectral discriminant. Almost all of the emission-line stars also have emission at 2.11 μm , but this emission is weaker than at other wavelengths for most emission-line stars. A filter at 2.189 μm would only pick out the hottest WN or late WC types. The HeI 2.058 μm line tends to be very strong in the objects where it is found, and it is present in the coolest hot emission-line stars. Emission at 2.08 μm only appears for WC subtypes.

With these characteristics in mind, we used three filters with the following center wavelengths: 2.058 μm , 2.085 μm , and 2.16 μm . The 2.085 μm filter can be used to measure the continuum level in all objects except WC subtypes where it is used to measure the CIV line flux; in this case, the 2.058 μm filter will measure the continuum.

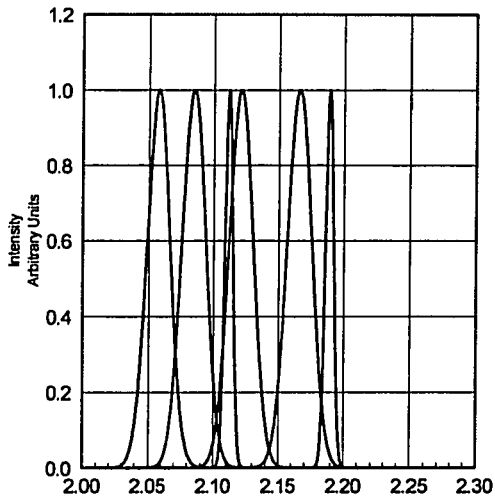
The UCLA double-beam infrared camera has the capability to image a field at two wavelengths simultaneously. The cutoff wavelength between channels can be set at 1.9 μm or 2.4 μm . The primary filters are all in the K band, so the dichroic beam splitter was set to 2.4 μm . This allows the long-wave channel to be used for wavelengths longer than 2.4 μm . We designed two more filters to compensate for the lack of coverage with the K band filters for the hottest stars. The WNE and WCE show strong emission near 3.09 μm due to HeII, CIII, and CIV emission. One filter with this central wavelength was used, and a second filter, centered at 3.15 μm , was used for measuring the nearby continuum level.

This filter system has been optimized for detecting emission-line stars, but they could probably be calibrated for uniquely classifying WR stars. This has not been done yet, but a survey of fainter targets would require spectrophotometric classifications as spectroscopy would be too difficult with present instrumentation.

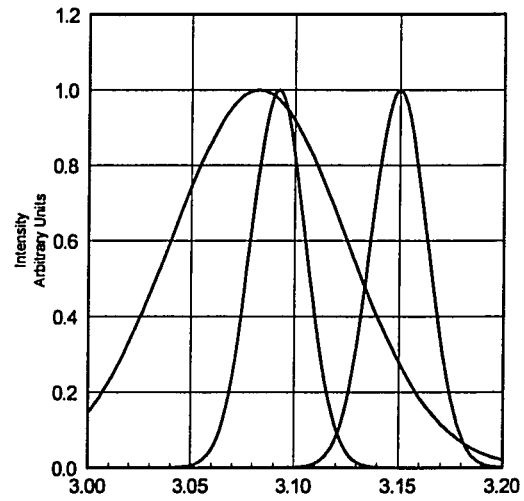
a. filter profiles

The 2.16 μm filter is often used to image ionized gas where recombining hydrogen emits Br γ photons (HI 7 \rightarrow 4), so it was amongst the filters in our filter set. The other four filters were custom made by Barr Associates for this study. The filter profiles are shown in Figure 26. The 2.058 μm filter has R=100 while the other three filters have R = 80. Originally, R = 100 was requested for each filter, but Barr Associates delivered only one filter with that width. Table 6 summarizes the filter characteristics.

Narrow-band Filters



K Band Filters



3 μm Filters

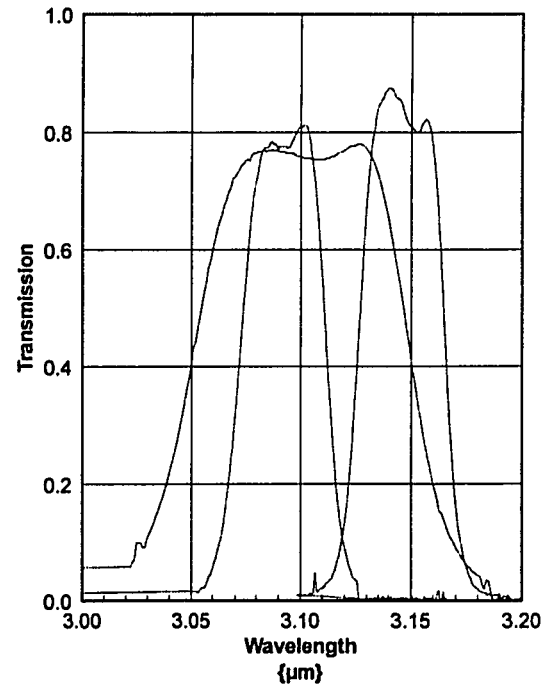
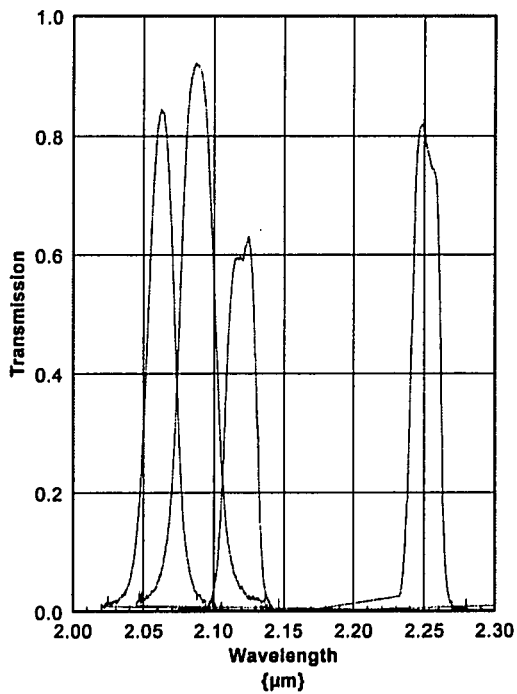


Figure 26. Filter transmission profiles.

Table 6: Filter Data

λ_{center}	Peak % Transmission	R	Emission Lines	
2.058 μm	85	100	HeI	2.058 μm
2.085 μm	92	80	CIV	2.078 μm
2.166 μm		100	HI, HeI, HeII	2.166 μm
3.092 μm	81	80	HeII, CIII, CIV	3.092 μm
3.150 μm	88	80	none	

b. sensitivities and expected S/N for targets

Figure 24 and Figure 25 give the expected K magnitudes for target stars, and the template spectra in section III.B.1.b show line strengths for various emission-line stars. This information can be used to estimate the exposure time required to detect excess emission in the emission-line filters. The model calculation assumes measured instrument and atmosphere parameters as well as literature data for the sky OH emission (Oliva & Origlia 1992). An example is given below for the 2.058 μm filter.

The ability to detect faint objects is determined by the signal to noise ratio, S/N. The noise is usually taken to be 1σ for a Gaussian distribution and can be approximated by the square root of the number of events in the case where Poisson statistics applies. This case applies when the event rate is controlled by quantum processes, i.e. the arrival of photons or the transfer of charge across a potential barrier. The total photon flux falling within a particular aperture will depend on the flux from any star within the aperture as well as background sources, e.g. thermal and non-thermal sky emission and thermal telescope emission. The intrinsic uncertainty for photometry within this aperture will be set by the square root of the total number of generated electrons within the synthetic aperture of the detector.

The signal, of course, comes from the star. The following equations show how the various object, sky, telescope, and instrumental parameters relate to S/N. The total number of electrons from each contributor is denoted by S. The read noise, N_R , is an intrinsic property of reading the array and is given in electrons/pixel. The total number of pixels in an aperture with radius r_p is given as πr_p^2 in pixels.

$$N = \sqrt{S_{sky} + S_{OH} + S_T + S_{line} + S_c + S_d + N_R^2 \pi r_p^2}. \quad (10)$$

The individual contributors to the total number of electrons in an aperture are given below where the symbols have the following meanings: A_T = area of telescope, Ω = solid angle of a pixel on the sky, $\Delta\lambda$ = effective bandwidth of the filter, ϵ = emissivity, η = efficiency, Q = quantum efficiency (electrons/photon), p = angular extent of a pixel in arcsecs, and t = exposure time. The subscripts correspond to the following: c = camera, T = telescope, p = pixel, line = emission-line, cont = continuum, A = atmosphere, ap = aperture, d = dark. The remaining symbols are physical constants and have the usual meanings.

$$S_{sky} = \frac{2hc^2}{\lambda^5} \frac{1}{e^{\frac{hc}{\lambda k T_{sky}} - 1}} \frac{A_T \Omega \Delta \lambda}{hc/\lambda} \epsilon_{sky} \eta_c \eta_T Q t \pi r_p^2. \quad (11a)$$

$$S_T = \frac{2hc^2}{\lambda^5} \frac{1}{e^{\frac{hc}{\lambda k T_T} - 1}} \frac{A_T \Omega \Delta \lambda}{hc/\lambda} \epsilon_T \eta_c Q t \pi r_p^2. \quad (11b)$$

$$S_{OH} = F_{OH,\lambda} A_T t p^2 \eta_c \eta_T Q \pi r_p^2. \quad (11c)$$

$$S_d = \dot{C}_d \pi r_p^2. \quad (11e)$$

$$S_{line} = F_{line} A_T \eta_c \eta_i Q t \eta_A \eta_{ap} \frac{F_{line}}{h\nu}. \quad (11f)$$

$$S_{cont} = \frac{F_{c,\lambda}}{h\nu} \Delta \lambda A_T \eta_c \eta_T \eta_A \eta_{ap} Q t. \quad (11d)$$

The model parameters are shown in Table 7, where observational data were used whenever possible. The efficiency of the camera, $\eta_c \sim 45\%$, was measured by comparing the measured count rate from a standard star to the expected count rate; this efficiency includes the transmission of the K prime filter. All of the filters in the table have about the same efficiency, so there is no explicit variation in η_c for the various filters.

The telescope temperature, T_T , was taken from the temperature sensors during the June and July runs. The sky temperature, T_{sky} , was estimated so that the measured and predicted flux at $3\text{ }\mu\text{m}$ matched. Atmospheric efficiencies were estimated from standard star spectra for the K-band filters. Published emissivities were used as starting points for the $3\text{ }\mu\text{m}$ filters; these were adjusted until the predicted background rates matched the measured values. The efficiencies were set so that the flux rate from a standard star matched the predicted rate.

OH data were taken from Oliva & Origlia (1992). Emission from individual lines in the filters was summed up to give the total contribution from OH emission lines. Some OH line emission will contribute to the background in the $3\text{ }\mu\text{m}$ filters (Maillard & Chauville 1976); but it will be much less than the contribution from thermal sources, so it is neglected here.

In general, a portion of the light from a star will fall outside the synthetic aperture or be lost due to a small slit size in the spectroscopic mode. Both types of losses will depend upon aperture size and seeing. These losses are combined in η_{ap} .

Table 7: S/N Model Parameters

λ	2.058 μm	2.085 μm	2.166 μm	3.092 μm	3.150 μm
$R = \lambda/\Delta\lambda$	100	80	100	80	80
T_{sky}	280 K				
T_{T}	285 K				
η_{A}	80%	90%	90%	10%	20%
η_{T}	85%				
η_{c}	45%				
η_{ap}	90%				
ϵ_{sky}	0.15	0.15	0.15	0.3	0.2
ϵ_{T}	0.15	0.15	0.15	0.15	0.15
r_{ap}	3 pixels				
$F_{\text{OH}} \{ \gamma/\text{s/m}^2/\square^2 \}$	94	94	69	–	–

The model was used to give expected S/N for the narrow-band survey. In this case, the signal comes from the emission-line only, and the noise is due to all contributors. The emission-line is modelled as a square function with velocity width = 1000 km/s, and a height, l/c , of 1.1 or 1.5 times the continuum flux. This ratio is related to the equivalent width, W_{λ} , by equation (12) where the second c refers to the

$$W_{\lambda} = \int_{\lambda_1}^{\lambda_2} \left(\frac{f_{\text{line}}}{f_{\text{cont}}} - 1 \right) d\lambda \quad (12)$$

$$\approx \left(\frac{l}{c} - 1 \right) \lambda \frac{\Delta V_{\text{FWHM}}}{c}.$$

speed of light. The "strong-line" case, $l/c = 1.5$, corresponds to $W_{\lambda} \sim 35 \text{ \AA}$ at 2.058 μm ; although, typical strong lines in WR stars can have much greater W_{λ} . For instance, the CIV complex at 2.078 μm can have $W_{\lambda} \sim 1000 \text{ \AA}$ for WC6 stars (Smith et al. 1988); this corresponds to $l/c \sim 15.5$. The "continuum" S/N is for the 2.085 μm

and 3.150 μm filters. Results for a 60 second integration are shown in Table 8. The OH emission levels were increased with respect to the values given in Table 7 to match the values measured in July. The OH emission was ~ 4 to 5 times greater than indicated in Oliva & Origlia (1991).

Table 8: Expected S/N for Narrow-band Survey for 60 sec. Integration

K	2.085 μm	2.058 μm		3.150 μm	3.092 μm	
		line/continuum			line/continuum	
		1.1	1.5		1.1	1.5
9	1510	38	182	75	1	5
10	828	20	95	30	–	2
11	411	9	45	12	–	1
12	186	4	19	5	–	–
13	78	2	8	2	–	–
14	32	1	3	1	–	–

c. observing procedures

The Galactic Center region has an airmass greater than 2.5 from Lick Observatory, and the airmass is less than 3.5 for ~ 3.5 hours. Each survey frame was imaged simultaneously in "on-line" filters in both channels. The filter wheels were then moved so that the "continuum" filters were in the beam. This series of exposures requires ~ 2.5 minutes. The telescope was then moved to the next position in the survey. In this way, 40 positions were imaged, as shown in the Figure 18. A nearby region with relatively few stars was imaged in each filter between every two survey rows, so that bias structure, dark current, and sky emission could be subtracted from the survey frames. The telescope was dithered 4 times on this "dark region" so that the frames could be medianed; the median frame then contained only array effects and sky

emission. Finding a guide star would add too much time between telescope moves, so guiding was not used for the survey or "dark region." The total amount of time to perform the survey, including observing the "dark region", was ~ 3.5 hours.

The rest of the night was used to observe WR stars using the new narrow-band filters. These observations were used to measure the flux excesses for WR stars of various subtypes. Photometric standards were also observed to measure the relative transmission of the atmosphere/telescope/instrument system in the various new filters. These standards were observed at various airmasses so that an extrapolation could be made to the high airmass of the Galactic Center.

d. analysis methods

The analysis was designed to most easily reveal the emission-line stars. Three methods can be used in conjunction. Each method requires that the "on-line" and "continuum" images be scaled so that stars without emission lines will have the same flux in both images. The most quantitative method uses photometry for every object in each frame. The "on-line" photometry can then be compared to the "continuum" photometry for each star. This method is easily automated, but false positives can be generated by an optical effect known as "ghosting."

A "ghost" is a second image of a star which appears in the focal plane due to reflections in the imaging cameras. There are two possibilities for where the ghosts are generated. A valid explanation must account for the following:

- 1). the ghost images are in focus,
- 2). the ghosts are in a position opposite to the real image of the star with respect to the center of the array,
- 3). the ghost position varies slightly depending on which filter is in the beam,

- 4). the energy in a ghost varies by about an order of magnitude between 4% for some narrow-band filters to 0.4% for broad-band filters, and
- 5). both channels have ghosts.

The first possibility is that the ghosts are formed between the filters and the first lens element of the imaging cameras. This might account for behavior #3 and #4, but the geometry does not account for #1, and condition #2 is dependent on condition #1, i.e. there needs to be a focused ghost to assess where it falls on the array. The second possibility is that the ghosts are formed between the very last surface of the last element in the reimaging lenses and the array. This might satisfy condition #1, #2, and #5; but I cannot see how condition #3 and #4 could be satisfied. Both possibilities are discussed below.

The UCLA dual-beam camera has two six-element imaging lenses, one for each channel (Casement et al. 1993). These lenses are each placed after the Lyot stop where there is an image of the telescope pupil in a collimated beam. The first element of each six-element lens has a negative curvature meaning that is bent toward the incoming beam. The filter wheels are positioned just after the pupil image. Some fraction of a star's light will reflect off the front surface of the imaging lenses and continue until it hits the filter. Some fraction of this light will then be reflected back into the lenses and fall on the array. The light will form an image if the beam reflected off the filter remains collimated. This condition is satisfied if the distance between the pupil image and the first lens element is equal to the radius of curvature for the first surface of that element. For both imaging channels, the separation distance is more than a factor of 2 greater than the radius of curvature so that the reflected rays from the first element will

form an image at $\sim \text{radius}/2$. Any light reflected back in the camera will result in an out-of-focus image contributing to the general background on the array.

The location of the ghost image depends on the angle between the chief ray of a field bundle and the normal of the first surface of the lens where the chief ray falls. The geometry is such that the ghost images fall on the opposite side of the array from the true image, so a bright star in the upper-right part of the array will have a ghost in the lower-left part of the array. Each filter in the wheel will have a slightly different tilt with respect to the optical axis, so that ghosts for each star in the on-line and continuum images will be slightly offset.

The back ends of the reimaging lenses in both channels are almost symmetric to the front ends, namely a strongly curved last surface facing a flat element, the array. The beams are telecentric onto the array, and the radius of curvature for the last surface is roughly equal to the separation between the last element and the array. An off-axis field point will generate an out-of-focus ghost on the opposite side of the array as shown in Figure 27. Condition #1, #2, and #5 are possibly satisfied, but conditions #3 and #4 cannot be reproduced in this model.

Despite the inability to fully explain these ghosts, their existence and affects on data reduction are indisputable. The photometric method of determining excesses will be affected by slight offsets in the ghosts because a ghost in the on-line image might fall within a synthetic aperture in that image while falling outside of that aperture in the continuum image. This effect ultimately makes the photometric method fallible, and other methods had to be used to examine each suspected star with a flux excess.

The other two methods are more subjective and qualitative, but they clearly identify target stars from the photometric method which were due to ghosting. The first

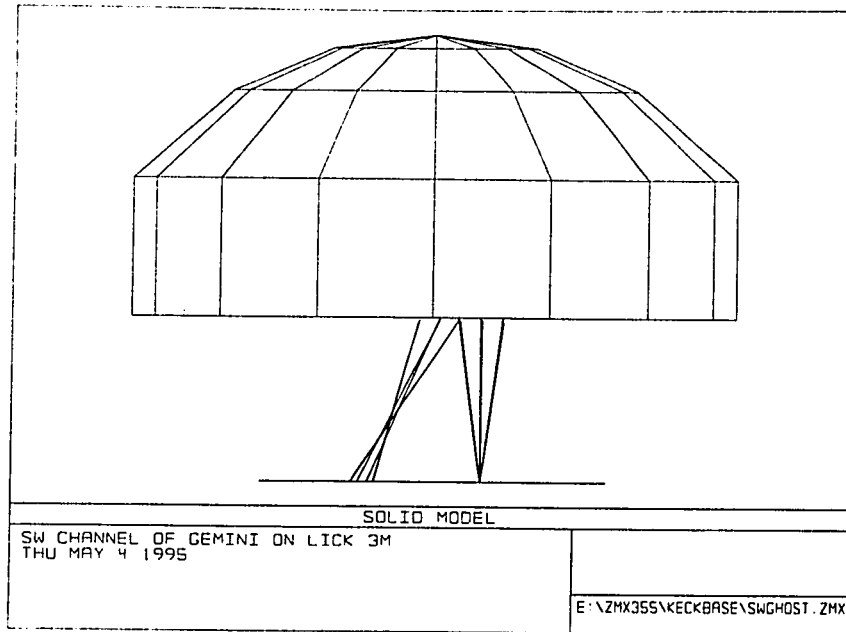


Figure 27. Last element of 6-element reimaging lens in the short-wave channel and the array. Rays for an off-axis field point are drawn.

involves "blinking" the two frames on the computer display; emission-line stars will appear to be brighter in the "on-line" images. This method can be quite powerful because the eye can easily pick out small differences amongst thousands of stars in an image. "Blinking" also reveals the characteristic offset between ghost images in the two filters.

The third method is closely related to the second, and it uses differenced images. A differenced image is the result of subtracting the "continuum" image from the "on-line" image. Most stars in the frame will disappear in the subtracted image, but the emission-line stars will still be visible.

3. phase II: spectroscopy

The template spectra show that emission-line stars have quite distinct K-band spectra except for the late-type WN stars, WN9/Ofpe, and some O4I stars which have similar spectra and probably represent stars at a similar stage of evolution. Most of the emission-lines will be resolved at an $R \sim 500$, and a spectrum covering a complete atmospheric window can be imaged onto an array with 256 pixels at this resolution. To this end, custom design transmission gratings were designed for the UCLA double-beam camera making it well suited for quickly obtaining spectra of these stars.

a. grisms

A grism is a prism with a ruled surface used to disperse light according to wavelength. The situation for a grism, i.e. a transmission grating, is similar to that for a reflection grating, except that there is an index change for the former. The reflective case is somewhat easier to analyze, so much of the following discussion is for that case.

The ruled surface is analogous to slits in a multiple slit spectrometer where the maximum and minimum intensity are due to interference between light from neighboring slits, called facets when discussing gratings. This ruling introduces a phase difference in the transmitted light from adjacent facets according to wavelength and output angle (see Figure 28). When the phase difference for light at a particular wavelength, $\Delta\psi$, between beams leaving each slit is some integer multiple of 2π , the light will constructively interfere for that wavelength. Each instance is referred to as a particular order, m , where $\Delta\psi = 0$ corresponds to $m = 0$, $\Delta\psi = 2\pi$ to $m = 1$, and so on. Nearby wavelengths will satisfy this condition in a particular order for slightly different output angles, and thus the output beam is dispersed according to wavelength.

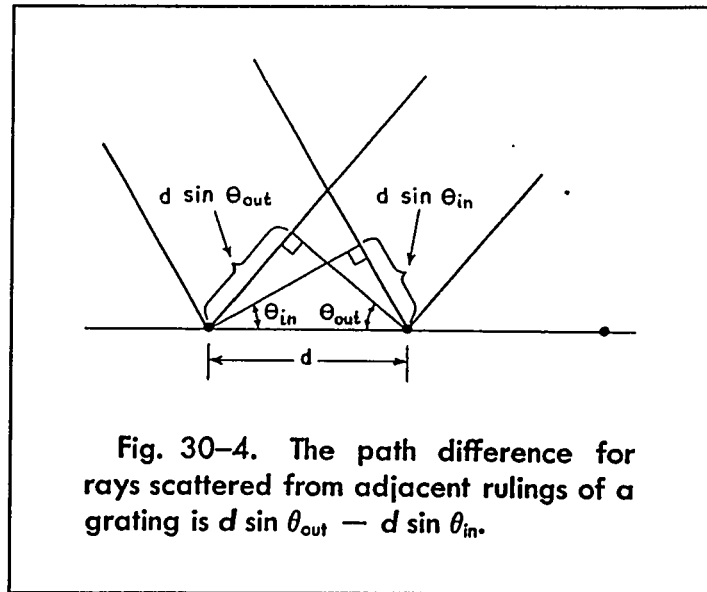


Figure 28. Illustration for calculating path difference from Feynman (1963).

This relationship between phase difference and ray geometry is given in equation (13) where the grating surface is reflective, and the input angle, α , and the output angle, β , are positive when on the same side of the grating normal. The groove density, $1/d$ in Figure 28 and T in equation (13), is measured in rulings per micron when λ is measured in microns. Notice that $m = 0$ corresponds to the classical law of reflection.

$$m\lambda T = \sin(\alpha) + \sin(\beta). \quad (13)$$

The interference intensity pattern generated by phase differences from facet-to-facet is modulated by a smooth diffraction envelope introduced by the phase difference across an individual facet. Again, this pattern is analogous to the intensity pattern on a screen in the multiple slit experiment. The maximum intensity will result by satisfying the condition for both an interference maximum and a diffraction maximum, where the

latter results by minimizing the phase difference across individual facets. Gratings are usually ruled so that the facets are at an angle with respect to the grating normal; this angle is referred to as the "blaze" angle of the grating. In this case, the condition for maximum intensity in the diffraction peak requires that the incoming and outgoing beams obey the law of reflection about the facet normal. By carefully choosing this blaze angle, the diffraction peak will coincide with a practically useful output angle for a given wavelength and order.

Another free parameter, the refractive index of the prism, is introduced when using a grism. Now, the beam angles are measured with respect to the hypotenuse normal. Figure 29 shows the basic geometry for a right-angle prism with refractive

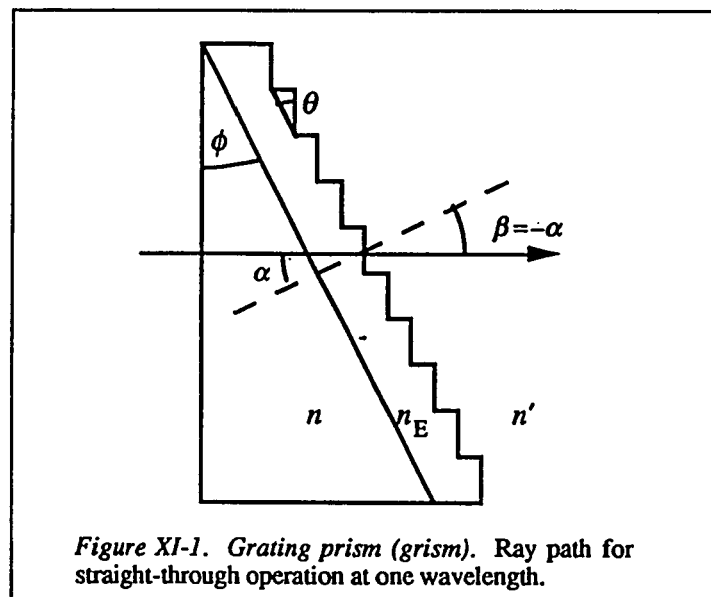


Figure 29. Geometry for grism from Palmer & Loewen (1994).

index n , and a grating ruled into a material which sits on the hypotenuse of the prism. The grating material is usually chosen so that the index, n_E , is nearly equal to n . With this condition, the grating equation for a grism can be easily calculated. Equation (14)

$$m\lambda T = n\sin(\alpha) + n'\sin(\beta). \quad (14)$$

is analogous to the grating equation for reflection, except the change in index for the refractive case is included. Notice that $m = 0$ corresponds to Snell's law. In this case, the maximum efficiency condition requires that the output beam obey Snell's law at the output interface of the grism.

The UCLA double-beam camera allows for grisms to be placed in the filter wheels. This requires that the chief ray for the central wavelength be undeviated when passing through the grism. In this case, equation (14) reduces to equation (15), where

$$m\lambda_{central}T = (n-1)\sin(\phi). \quad (15)$$

the grism sits in a vacuum, $n_E \approx n$, and $\alpha = \beta = \phi$ for the central wavelength, where ϕ is the apex angle of the prism. The wavelength dispersion with respect to output angle is shown in equation (16). The collimated beam at the grism will be split into many

$$\frac{d\lambda}{d\beta} = \frac{\cos(\beta)}{mT}. \quad (16)$$

collimated beams with various output angles related to their wavelengths. These beams will be brought to a focus by the imaging lens, and an individual image of the object will be formed at the array for each wavelength.

The wavelength dispersion in the image plane is given by the reciprocal linear dispersion (RLD) in equation (17), where EFL is the effective focal length of the

$$\frac{d\lambda}{dx} = \frac{1}{EFL} \frac{d\lambda}{d\beta} = \frac{\cos(\beta)}{EFLmT}. \quad (17)$$

imaging lens. As stated earlier, $R \sim 500$ is a reasonable value for obtaining spectra

which can be used to uniquely identify emission-line stars and for placing a whole atmospheric window on the array. This requirement can be expressed through the RLD by assuming that two pixels are to be matched to one resolution element as shown in equation (18), where p is the pixel size, and "res" stands for resolution element, and $\alpha = \beta = \phi$ as in equation (15); this condition only holds for the central wavelength. Notice that the resolution is linearly dependent upon the prism index of refraction.

$$R = \frac{\lambda}{\Delta \lambda_{res}} = \frac{\lambda}{\Delta x_{res}} \frac{dx}{d\lambda} = \frac{EFL}{2p} (n-1) \tan(\phi). \quad (18)$$

Equations (15) and (18) must both be satisfied so that the desired wavelengths are imaged onto the array at the required resolution. Solutions are not unique because n , ϕ , m , and T are independent variables; although, the problem is constrained by available materials. For instance, there are only a dozen or so different T values for grating surfaces available from Palmer & Loewen (1994). Likewise, n is constrained by the few infrared transmitting substrates from which to choose. The apex angle, ϕ , is essentially a free continuous parameter as manufacturers can cut prisms to order. The ratio $EFL/p = 1375$ in equation (18) is the same for both channels in Gemini, i.e. the plate scales are the same. The problem of finding grism designs with the best efficiencies was approached by fixing the most stringently constrained parameters, and then searching for solutions which predicted the highest efficiency using simulations based upon the models of Schroeder & Hilliard (1980).

In practice, the highest efficiencies were found for the highest blaze angles and substrate index. The solutions for our grisms are given in Table 9 as calculated by Murray D. Silverstone (1994). The resolution varies by about 10% across the array as shown in Figure 30a and Figure 30b.

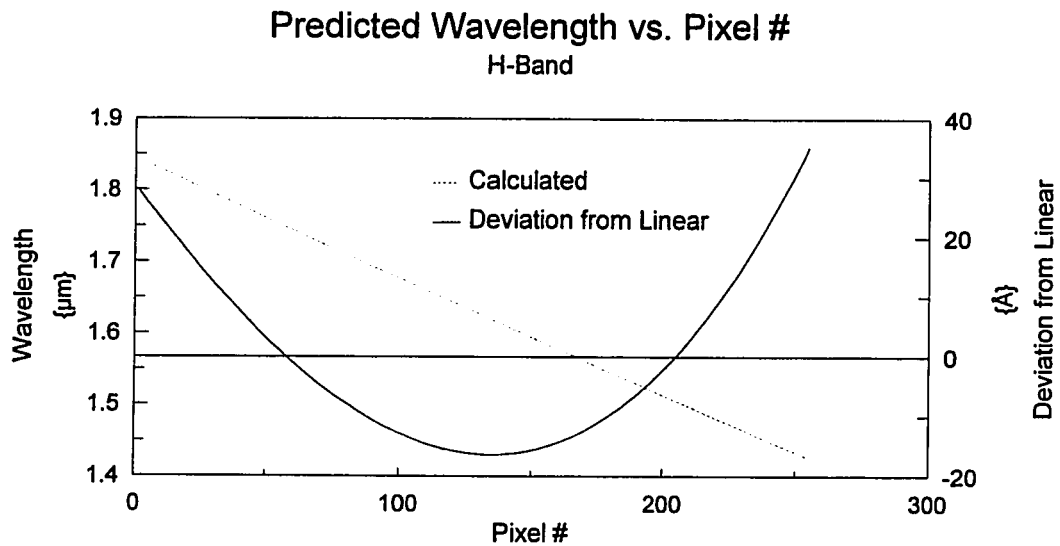


Figure 30a. Wavelength versus pixel number in H-band. Variation from a straight line is shown on the right axis.

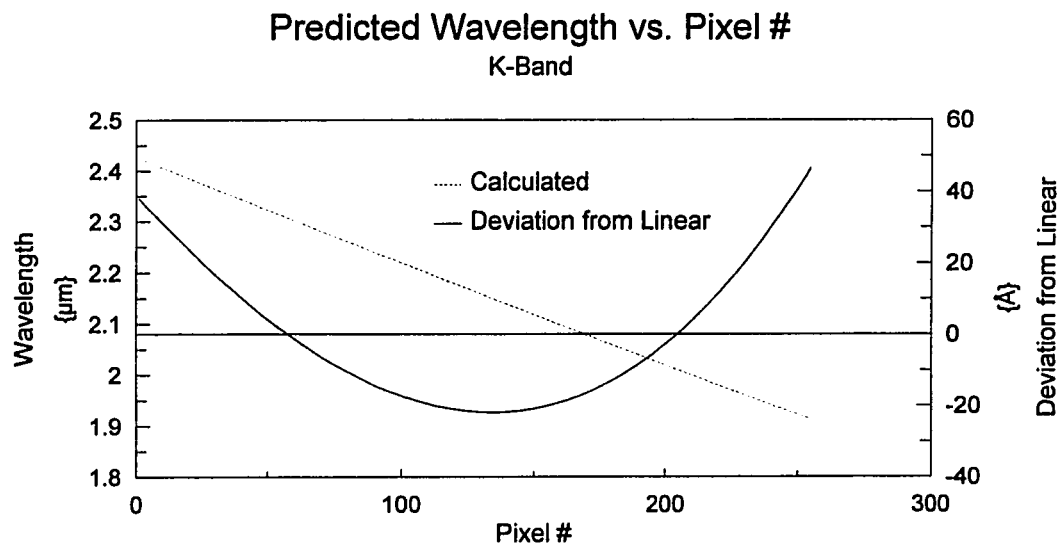


Figure 30b. Same as Figure 30a but for K-band.

Table 9: Grism Parameters

	J	H	K
λ range (μm)	1.071-1.379	1.426-1.843	1.913-2.424
R	463-543	455-537	500-573
m	1	4	1
T (l/mm)	534	98.7	316
n_{center} (ZnSe)	2.462	2.442	2.432
θ_{blaze}	46°9	63°5	70°0
ϕ	26°5	26°5	28°5

b. sensitivities and expected S/N for targets

Expected sensitivities were calculated using the model discussed in III.B.2.b where an additional term, η_{grism} must be added to the equations when appropriate. The effective number of pixels per synthetic aperture was reduced to 12 assuming that 6 rows will be summed to obtain a single spectrum. The wavelength range, $\Delta\lambda$, is $\sim \lambda/550$ for the H and K grisms. The S/N calculation for spectroscopy also differs in a more fundamental way from that for imaging because many of the parameters of the problem vary across the spectral range. For instance, the atmospheric transmission, grism efficiency, OH emission, and thermal emission each vary over an atmospheric window. In this situation, the S/N will vary with wavelength. The most complete approach would be to calculate the S/N for each wavelength for a template spectrum. This is quite tedious. Instead, we modelled the S/N at a specific emission line in analogy with the narrow-band case. The expected S/N near 2.166 μm is given in Table 10 where a slit-loss of 50% is assumed, and both grisms are assumed to have an efficiency of 45% (see discussion below). The S/N values are given for the center of the bands, and OH emission is neglected for the K-band calculations. An average value

of 100 ph/s/m²/□" is assumed for the OH emission in the H-band. The table reflects the fact that sources at the Galactic Center have H-K ~ 2.0.

Table 10: Expected S/N for Spectroscopic Survey for 180 sec. Integration

H	S/N	K	S/N
11	170	9	450
12	78	10	250
13	34	11	128
14	14	12	59
15	6	13	25
16	2	14	10

The grism efficiency/slit-loss product was measured on December, 15, 1994, and December, 16, 1994, using data for BS81 and BS797 respectively. The seeing gave $d_{\text{FWHM}} \sim 3.4$ pixels, so that the slit loss was large. The combined efficiency for the grism and the slit was ~ 15% where an appreciable loss is due to the small slit width of 2 pixels. There is probably a small error due to the fact that a K filter is used to block unwanted orders when using the grism, but the images were taken with the K' filter. The same procedure was used to estimate a combined grism/slit efficiency ~ 19% for the H grism using BS81.

The grism efficiency can be calculated by counting the flux from the sky with and without the grism inserted into the beam. In this case, the thermal background between 2.3 and 2.4 μm is considerable, so the total number of counts due to the background has to be measured only up to 2.3 μm . This number can then be compared to the background flux in a K' image. This method gives an efficiency of 45%. Frames for WR128, taken on July, 25, 1994, were used for measuring the background flux with the grism, and frames of a relatively blank field, taken later in the night, were used to

estimate the total background flux using the K' filter. The same procedure was attempted for the H grism, but the flux was too low to obtain a reliable efficiency. The H grism probably has an efficiency which is roughly equal to the K grism efficiency because they both had nearly the same grism/slit efficiency; therefore, we can assume $\eta_{K \text{ grism}} \sim \eta_{H \text{ grism}} \sim 45\%$.

c. observing procedures

Each target star from the phase I survey was observed for 3 minutes per exposure. The telescope was nodded in the NS direction so that the target star would be in a different position along the slit. This was done so that bias structure, dark current, and sky emission could be subtracted all in one step by differencing adjacent frames. Three nod positions were used to reduce the effects of an important part of the spectrum falling on a bad pixel in any individual spectrum. Due to intermittent functioning of a lower quadrant in the NICMOS array, the nod positions were sometimes set so that the object would always be in the upper half of the slit. This approach was used only when the star was bright enough to expect appreciable flux in the H-band; otherwise, the whole slit was used for nodding. In total, each object was usually observed for 9 minutes. Choosing a single exposure time for all objects will give varying S/N, but using a single exposure time for all stars is much simpler than tailoring exposure times for each star.

The convenient method of subtracting adjacent frames is only useful when there is no other star in the background frame at the same position in the slit as the target star in the object frame. Unfortunately, this condition is rare for positions near the Galactic Center due to the high source density. In cases where no suitable neighboring frames could be found, the sky emission had to be subtracted by sampling the

background in the object frame. This method requires that the bias structure and dark current be subtracted separately; therefore, bias+dark frames were taken throughout each night.

The data must be corrected for variable quantum efficiency (QE) across the array. This can be done by dividing the source frames by an image of a continuum source with the slit and grism in the beam. This method accounts for wavelength variations in the QE. Continuum lamps in the dome were used as light sources for the flat images. These lamps radiate like a black-body, so the flat image will have some variation due to the intrinsic shape of the source spectrum. As a result, the flattened object spectrum will have a shape influenced by the lamp. This effect can be removed in the step correcting for variable atmospheric transmission.

Raw object spectra will show large intensity variations due to the variable atmospheric transmission, especially near the edges of the atmospheric bands. These raw spectra can be divided by the spectrum of an atmospheric standard star to correct for this effect. Of course, the standard star should have an intrinsically featureless spectrum so that any feature in the raw spectrum is due to atmospheric absorption. In reality, all stars have some intrinsic spectral features at a high enough resolution (Lancon & Rocca-Volmerange 1992). The best one can do is to use stars which have relatively featureless spectra; what features do exist should lie in regions where the atmosphere has constant transmission. This is the case for A-type stars which have modest Bry absorption in the K-band and higher order Brackett line absorption in the H-band. The Bry absorption can be effectively removed by interpolating a straight line across the feature. An alternative method is to use spectra of late G-type stars at 2.16 μm ; these stars have very little Bry absorption. This method fails for the higher

order Brackett lines in the H-band because the atmosphere has quite variable transmission in the neighborhood of these transitions. Unfortunately, all other stars have a number of spectral features in the H-band. The best solution is to observe O-stars which have only a few HeII absorption lines in the H-band (Origlia et al. 1993). This difficulty was only fully appreciated after obtaining data, so only A-type and late-type stars were observed for atmospheric correction.

The standard stars are treated as objects from the point of view of data reduction, so their spectra will also be divided by the flat image. This means that the standard star spectra will be affected by the intrinsic shape of the flat lamp spectrum in the same way as the target spectra. Thus, when dividing the object spectra by the standard star spectra, effects due to the lamp will be cancelled.

The corrected spectrum will have a shape which is influenced by the intrinsic spectrum of the standard star. This can be corrected by multiplying the corrected spectrum by a black-body fit to the standard star. The "fit" is done by assuming that the spectral type of the standard star can be translated into a black-body temperature.

Wavelengths can be associated with pixel number across a spectrum by observing an emission line reference. The dispersion is non-linear, but theoretically soluble as shown in equation (17) and Figure 30a and b. Of course, other non-linear, and less analytically soluble, effects will change the resolution and wavelength-to-pixel map, i.e. distortion in the image plane due to the optics. In any case, spectra can be linearized by recording the OH emission lines from the sky or the lines from an arc lamp.

The most important part of this procedure is to obtain the emission-line spectrum without moving the telescope, slit, or grism between the emission-line

reference exposure and the object exposure. This requirement is necessary because moving the slit or grism will change the wavelength-to-pixel map; the source of this change is probably lost steps in the stepper motors which turn the filter and aperture wheels. We did not have an arc lamp system installed at the time of the runs, so the sky OH lines were used for wavelength calibration. Using the sky lines gives the extra benefit that separate frames for wavelength calibration are not needed - the OH lines are in the object frame. Of course, this means that the exposures have to be long enough to obtain reasonable S/N in the OH lines. Unfortunately, we relied upon perfect reproducibility of the wavelength-to-pixel fit after moving the slit, telescope, or grism, and subsequently used some very short exposures for the standard stars. The OH lines do not have enough S/N in these exposures, and fits for adjacent object frames are generally not directly applicable. We had to use these fits and try to offset the resultant standard star spectrum until atmospheric features disappeared from the corrected object spectra.

d. analysis methods

The spectra can be analyzed to get the spectral type of the star, the wind velocity for resolved lines, mass-loss rate, and the velocity shift of emission lines. The spectral type of the star can be identified in cases where spectra for optically classified stars can be used as comparison templates as discussed earlier, but several types of stars have very similar spectra, i.e. Ofpe/WN9 and WN9 stars. In some cases, like the one given above, this is not a major problem because stars with similar spectra are often in nearly the same evolutionary state. There are other instances, however, where two stars in greatly different stages of evolution have similar K-band spectra at $R \sim 500$. For instance, embedded YSO's have smooth, featureless spectra, just like O-stars (see

Hanson & Conti 1995 for spectra of YSO's and O-stars). The only way to spectroscopically distinguish these stars is to get very high S/N data so that small features, $W_\lambda \sim 2 \text{ \AA}$, can be seen.

Winds in WR stars were discussed in a previous section, and hot star winds, in general, are likely to be similar. The wind velocities can be determined by measuring the displacement of the blue absorption edge for a line with a P Cygni profile, e.g. the 2.058 \mu m HeI line is often seen with a P Cygni profile. An alternate method approximates v_∞ as $\Delta V_{\text{FWZI}}/2$, where FWZI is the full width at zero intensity of the emission line after subtracting the continuum level (Hamann et al. 1993). This method requires an unblended emission line; for instance, the Br γ line can be contaminated with the HeI $7 \rightarrow 4$ line and the HeII $14 \rightarrow 8$ line. In this case, all components have to be deblended; or a more appropriate line could be used. Helium contamination is only a problem in evolved stars, i.e. types less than WN7 in the WN sequence or any WC star. The emission at $2.112/2.113 \text{ \mu m}$ always contains the HeI doublet, so that it is never an appropriate emission line for measuring line widths. The 2.058 \mu m line is the most useful for calculating v_∞ by measuring the line width, although some other line must be used for the earliest types where helium is completely ionized.

As discussed earlier, the mass-loss rate can be approximated by getting the emission measure from radio observations and the velocity from blue shifted P Cygni absorption profiles. Another method assumes that the Br α or Br γ emission is optically thick and comes from a spherically symmetric, constant velocity, expanding wind (Simon et al. 1983). In this case, equation (19) holds, where V is in km/s, D is in kpc, the flux is in W/m^2 , and the constant is equal to $4.6(10^{-9})$ and $5.6(10^{-9})$ for Br α and Br γ respectively.

$$\dot{M} = 4.6(10^{-9}) V^{0.75} D^{1.5} \left(\frac{F(Br\alpha)}{3(10^{-15})} \right) M_{\odot}/yr. \quad (19)$$

The velocity shifts can be measured by fitting a gaussian to the emission line and comparing the line centroid to vacuum wavelengths for the lines. Vacuum wavelengths for some emission lines in the K-band are given in Table 11 (Davies 1991). The wavelength for the FeII line near 2.09 μm was taken from Hamann et al. (1994) after multiplying their value by the index of refraction for air, 1.00027.

Table 11: Vacuum Wavelengths for Emission Lines in the K-band

Species	Transition	Wavelength in μm
H2	1 \rightarrow 0 S(2)	2.0388
HeI	2p ¹ P ⁰ \rightarrow 2s ¹ S	2.0587
FeII	z ⁴ F ₃ \rightarrow c ⁴ F ₃	2.0894
H2	1 \rightarrow 0 S(1)	2.1218
Br γ	7 \rightarrow 4	2.1661
HeII	10 \rightarrow 7	2.1891
H2	1 \rightarrow 0 S(0)	2.2233

IV. Observations

The observations were taken during two runs of five nights each during June, 1994, and July, 1994, using the UCLA double-beam near-infrared camera (McLean et al. 1993, 1994). The seeing was excellent for the site with the FWHM < 2 pixels for most of the time.

A. instrument and setup, dates, filters, grisms, telco

The instrument was configured with K-band narrow-band filters in the short-wave filter wheel and 3 μm narrow-band filters in the long-wave filter wheel. The H and K prime filters were located in the short-wave filter wheel. The K grism was in the long-wave filter wheel, and the H grism was in the short-wave filter wheel. Observing logs, giving the dates, filters, and targets are given in the following tables.

In Table 12, filters are referred to by their central wavelengths, and SW and LW refer to the short-wave and long-wave channels. The "target" for the phase I survey was the whole survey region, although it was only completed on nights 2 and 3. Night 5 was used to observe missing areas from nights 1 and 4.

Table 12: Observing Log for Phase I

Date	SW1	SW2	LW1	LW2
June 17	2.058	2.085	3.092	3.150
June 18	2.058	2.085	3.092	3.150
June 19	2.166	2.085	3.092	3.150
June 20	H	K prime	3.092	3.150
June 21	2.058/2.166	H/K prime	3.092	3.150

Sources are labelled by their common names when possible in Table 13. Most of the "targets" do not have common names, although the objects with designations beginning with "H" follow Yusef-Zadeh & Morris (1987b) and Figer et al. (1994).

Other designations beginning with a number and having 4 or five numbers, XYZAB, are named according to: X = night number, Y = row in survey, Z = position in survey, AB (or just A) = star number in a list of stars for the YZ frame sorted in descending order by flux excess in the filter used on night X. For example, star 37345 had the 45th greatest excess in the image of row 7 position 3 (the central 7 pc) taken on night 3 (when the Bry filter was used). Objects beginning with a lower case letter "a" or "h" refer to targeted surveys of the A-D region and H region performed on night 5. These frames had longer exposures than the survey frames taken on the previous nights. In these cases, "11" is an internal tracking number, but the second two digits again refer to the objects' location in a list sorted by flux excess. Finally, Z211 and Q13521 are internal designations for two stars near the Quintuplet cluster. The labels "p" and "pguy" refer to the arced portion of the parachute and the central knot of the parachute respectively, i.e. the "parachute guy" (see position 65 in Figure 18).

Table 13: Observing Log for Phase II

Date	Targets	Calibration	WR
July 22	Z211, Q13521, H2B	AF, Q8, Q10	123 (WN8), 130 (WN8), 134 (WN6)
July 23	H1A, H5W, H5E, 37345, 37321, 37336, 37344, 37349, 37351	IRS15NE, IRS16	
July 24	36414, 36416, 36415, 36429, 36417, 36422, h1141, h1132, h1139, h1149, h1148		
July 25	H3, H6, H7, 365pguy, 365p, 3656, 3659, 36513, a1133, 36516, 37119		108 (WN9), 128 (WN4)
July 26	Z211, Q13521, 39211, 39228, 39217, 3926	IRS6, IRS16, Hubble 5	121 (WC9), 135 (WC8)

With help from Tim Liu and Frank Henriquez, automatic telescope position control was implemented so that the overhead between pointings was minimized to just the time necessary for the telescope to move. This was crucial for getting through the whole survey in the short amount of time that the Galactic Center was observable, and this facility is now a reliable part of our system.

Guiding was forfeited so that time was not lost searching for a guide star after moving the telescope. In most cases, this did not produce a noticeable drift during the short exposures; but an improved tracking rate should have been obtained at the beginning of the survey. This was not done on the first two nights where some drift can be seen in some of the images. On subsequent nights, the telescope was first slewed to the general area of the survey, and guiding was turned on for a short period of time so that the telescope tracker could calculate a more accurate tracking rate.

B. calibrations: standards, flats, bias, dark, sky, OH lines

Standard stars were observed throughout the nights during the phase I observations so airmass corrections could be made for photometry at the high airmass of the Galactic Center. Some of these stars were from Elias et al. (1982), but late-type stars from the Bright Star Catalog were also chosen because these stars will not have measurable $\text{Br}\gamma$ absorption. Some stars within the survey were also used as standards. This entails using published H and K magnitudes for these stars and converting to K prime using the relation given by Wainscoat & Cowie (1992).

Absolute calibration for the narrow-band surveys is not necessary because we are looking for flux excesses. In this case, the on-line frames must be multiplied by some number so that the same number of counts is found for each star which does not have emission-lines. An estimate of this factor can be found by iteratively multiplying

the on-line frames, subtracting the continuum frames, and seeing if most stars disappear in the differenced frame. Stars which have dramatically different intrinsic colors, or reddening, compared to the average for stars in the frame will not be subtracted perfectly. In this case, the broad-band photometry can be used to see if the apparent flux excess is due to the disparate apparent color.

Another method was used to make a relative calibration between on-line and continuum filters by observing narrow-band standard stars. These are stars which have very little reddening and intrinsically smooth spectra. These stars were observed throughout the night at various airmasses, and it is seen that the atmosphere absorbs much more light in some of the filters. For instance, light at 3.09 μm is absorbed in the atmosphere much more than light at 3.15 μm ; this is also evident in Table 7. In fact, the transmission ratio ($T_{3.15}/T_{3.09}$) will increase for larger airmass as larger column densities of absorbing material fall within the beam. Data for these relative calibrations for June 17 are shown in Figure 31. This figure shows the typical trend of a higher correction for higher airmass, but the slope and absolute values varied over the course of the run. For instance, the relative ratio of light in the cb to that in the eb filter was usually above 2, even at low airmass, for the other nights (c = continuum, e = emission-line, a = short-wave channel, b = long-wave channel). In fact, on June 20, the relative ratios appear to be flat from $z = 1$ to 1.3.

A "dark region" (see III.B.2.c.) was observed between every two survey rows to obtain a measure of the background sky contribution to the survey frames. The same integration time was used for survey and dark region frames so that the latter could also be used to measure the dark current. Separate bias frames were taken at the end of the night by inserting the "blank" filter into the beam.

For phase II, bias structure and dark current were measured by inserting the blank filter into the beam and using the same integration time that was used for the object frame. A flat frame was made by exposing the camera to the dome lamps provided at the observatory. The slit and grisms were inserted into the beam when taking these flat frames.

Relative Airmass Corrections

June 17

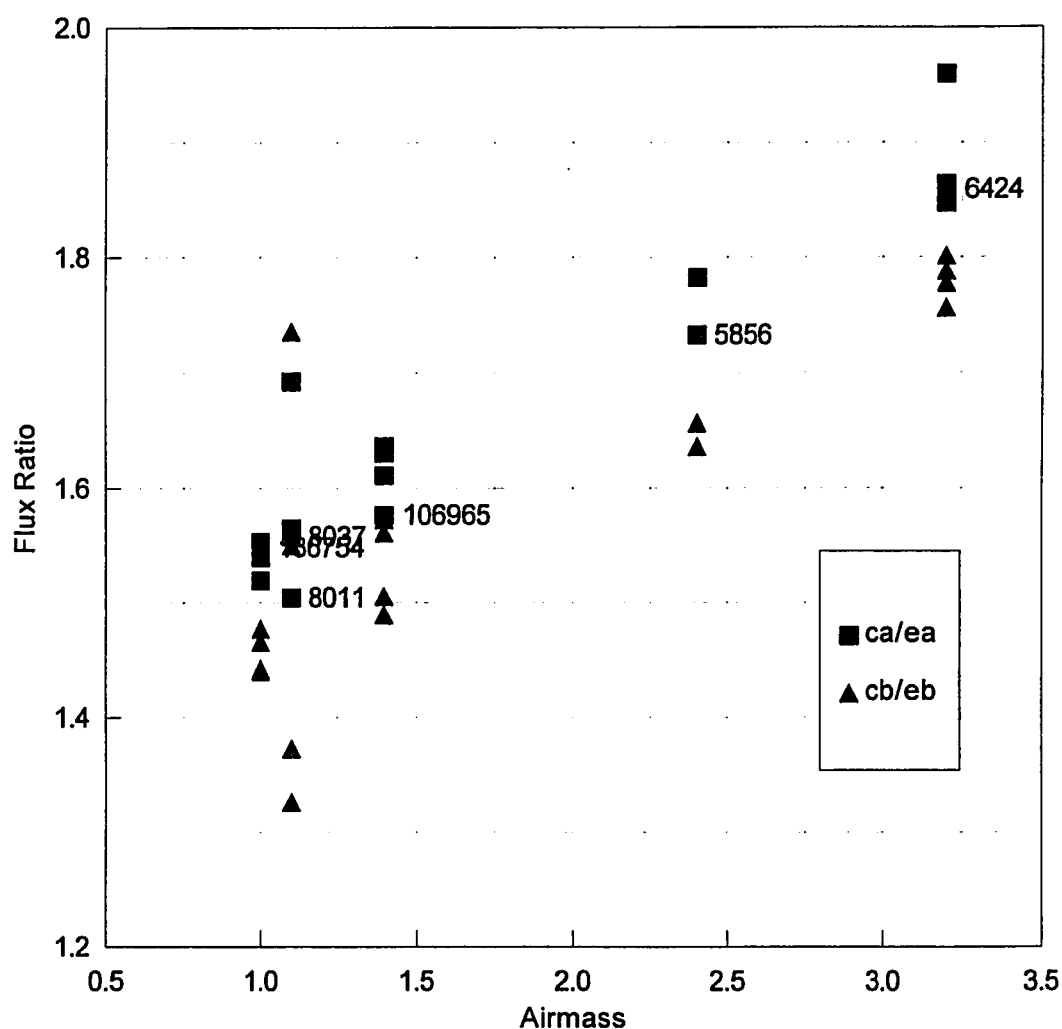


Figure 31. Relative airmass correction for June 17.

V. Data reduction

A. phase I

The data reduction for phase I can be broken up into two parts. The first part is the generic reduction which manipulates raw images into photometry for objects in the images. The second is the specific task of converting photometry into flux excesses so that target stars can be generated for phase II. The generic image reduction follows the usual procedure of removing unwanted array effects, i.e. bias structure, dark current, and variable QE, and subtracting background emission due to the sky and telescope.

"Flat" frames were generated by combining images using a median filter. Short-wave images of the survey contain too many stars, so they cannot be used to form the medianed image. Instead, frames of the dark spot were combined in a running median to form the flat frame. The long-wave images were relatively free of stars, so the survey frames were directly combined in a running median to form the flat frame. In both cases, bias frames were subtracted from the raw frames first; these bias frames had the same number of coadds as the survey frames with much less integration time. The sky emission and dark current were simultaneously subtracted from object frames by using the median frames. No scaling is necessary because the median image has an effective integration time equal to the integration time of all the frames used to form the median, and those frames have the same integration time as frames in the survey.

1. IRAF script TWOCHANGC

A custom IRAF script, TWOCHANGC, was written to reduce the data from FITS files all the way to text files containing object coordinates and photometry for each filter in a single night. The script allows for different processing for each filter. For instance, the user can request flat frames constructed out of running medians of

user chosen frames or already prepared flat frames whose names are specified in a list. The flattened images can be corrected for bad pixels by turning on bad pixel correction and specifying the relevant bad pixel maps. The task also allows the long-wave images to be registered to the short-wave image plane using the REGISTER task in IRAF; this task uses a general 3rd order polynomial fit in x, y, and xy, so that the long-wave and short-wave images have the same plate scale at each pixel. TWOCHANGC also allows all four frames per position to be aligned, using IMALIGN, so that each star will have the same coordinates in each of the four frames. Lastly, the script takes user defined thresholds and finds targets in frames corresponding to the user defined filter. For instance, the user might request that targets be found in the 3.092 μm filter by specifying "eb" (e = on-line, and b = long-wave channel) for DAOFIND. The parameter table for TWOCHANGC is shown below. A similar task, ONECHANGC, allows the same kinds of processing and output for only one channel; this was used during the short period of time between phase I and phase II when excesses between on-line and off-line filters within a single channel were calculated.

I R A F

Image Reduction and Analysis Facility

PACKAGE = user

TASK = twochangc

filter1 =	b Filter1 letter
filter2 =	c Filter2 letter
filter3 =	e Filter3 letter
filter4 =	c Filter4 letter
night =	19 Date of night
(inlist =	number) Three character file list root name
(inlist2=	skyflat) Sky image list root name
(inlist3=	biassub) Bias image list root name
(inlist4=	rfitsingc) Fits input list root name
(inlist5=	alignlots) Root name of file containing numbers for aligning and performing photometry
(inlist6=	flat) Flat image list root name if sequencing is not specified
(georoot=	xform) GEOMAP output root name

(prefix =	z) File prefix for aligned images
(readfit=	no) Read in fits files?
(compres=	yes) Are fits files compressed?
(uncompr=	no) Leave fits files uncompressed?
(biassub=	no) Subtract bias frames?
(flat =	no) Flat images?
(numhigh=	2) a-channel nhigh to reject from sky/flat
(numhigh=	2) b-channel nhigh to reject from sky/flat
(numlowa=	0) a-channel nlow to reject from sky/flat
(numlowb=	0) b-channel nlow to reject from sky/flat
(delbias=	no) Delete bias-subtracted files after flatting?
(filter1=	seq) Flat based on flat list or auto-sequence for filter1?
(filter2=	seq) Flat based on flat list or auto-sequence for filter2?
(filter3=	seq) Flat based on flat list or auto-sequence for filter3?
(filter4=	seq) Flat based on flat list or auto-sequence for filter4?
(fix =	no) Fix pixels?
(bpa =	/datab2/figer/iraf/imh/gemnmdbadpix11) Bad pixel file for NICMOS
(bpb =	/datab2/figer/iraf/imh/gemsbrcbadpix2) Bad pixel file for SBRC
(registe=	no) REGISTER frames between channels?
(delflat=	no) Delete flattened frames after registering?
(cut =	no) Trim images?
(cutsec =	[1:250,7:255]) Cut section after registering
(makelis=	no) Make coordinate lists?
(reffilt=	c) Reference filter for coordinate file and IMALIGN?
(refarra=	a) Reference array for coordinate file and IMALIGN?
(thold1 =	7000.) Threshold for daofind used to create coordinate
(suffix =	clist) Output file suffix for coordinate lists
(align =	no) Align frames within and between channels?
(trimb =	no) Trim images during imalign?
(mode2ze=	yes) Set mode to zero?
(phot =	no) Perform photometry on all 4 images?
(zmagn1 =	0.) Zero point magnitude for filter1
(zmagn2 =	0.) Zero point magnitude for filter2
(zmagn3 =	0.) Zero point magnitude for filter3
(zmagn4 =	0.) Zero point magnitude for filter4
(thold2 =	30.) Threshold for daofind used in photometry
(daoarra=	a) Array letter for daofind reference?
(daofilt=	c) Filter letter for daofind reference?
(fields =	xcenter,ycenter,msky,nsky,sum,area,mag) Fields for phot output
(delcoo =	yes) Delete .coo file when done?
(delmag =	yes) Delete .mag file when done?

2. the spreadsheet engine

A spreadsheet database engine was built to automatically read in the coordinates and photometry in four filters for all stars. The spreadsheet automatically calculates a scale factor so that the median flux excess for the 200 brightest stars, except the brightest 25 which might be saturated in one or more of the frames, was equal to zero. This empirical method accounts for variations in the atmospheric extinction ratio between the various filters as well as reddened continua for stars near the Galactic Center. The final output from the spreadsheet is a list of stars with the greatest excesses. These stars could then be examined individually for contamination due to ghosting or saturation.

3. choosing targets

Targets for phase II were chosen by using the three methods described in III.B.2.d. The photometric method was used as a starting point. There are 4 frames for each survey position on any given night, SW1, SW2, LW1, and LW2, where LW1 and LW2 correspond to the 3.092 μm and 3.150 μm filters on all nights, but SW1 and SW2 depend on the night in question (see Table 12). The coordinates for stars in each frame were assumed to be the same because the frames were registered before running DAOFIND. The coordinates and number of counts in each aperture were written to a file for every star.

There was a very short period of time between phase I and phase II, so that only the Br α and HeI surveys were searched for targets. Many more targets than could be observed in phase II were found, although most of these came from the Br γ survey. We decided to limit the targets to stars which are near interesting regions, i.e. previously known star-formation regions. For instance, Table 14 contains a list of output from the

spreadsheet engine for the Bry survey frame in row 6, position 4 (frame 364); this position contains the HII regions G-0.010+0.015 (H1) and G-0.015+0.027 (H2) (see I.D.2.).

Each star is listed in the order of greatest flux excess. Coordinates locate the centroid of the star in pixels. The sky count per pixel, total flux, area of the aperture, and the instrumental magnitude are listed for both filters. The "mag" includes the zero point, 17.5, for photometry in the continuum filter. The S/N is calculated from the continuum filter where the noise is the square root of the background in the aperture multiplied by $\sqrt{2}$. The excess, Δsum , is expressed as a percentage of excess flux in the on-line filter versus the flux in the continuum filter. Finally, a merit function, $\text{MF} = \Delta\text{sum} \times \text{S/N}$, separates faint stars with large excesses from bright stars. This is useful because photometry for the faint stars is more easily influenced by other stars in the aperture which have different colors than the target stars.

DAOFIND located a total of 1433 stars with net flux greater than 1σ ($\text{mag}_{2.085} \sim 17.5$) in frame 364. The output list was further constrained to stars with net flux $> 20\sigma$ in the Bry filter and 10σ in the continuum filter. The 20 stars with the greatest excesses are listed. The list reflects a newer calculation of the background which is slightly different from what was used between phase I and phase II. The old calculation subtracted a single median background calculated from the whole frame while the newer calculation subtracts only a local background. It was initially thought that the background was smooth enough so that it could be sampled all over the frame, thus obtaining a more accurate measure of the background. This might be true for some of the frames, but most frames have large variations in the background, so the newer calculation was adopted for the table. This effectively means that stars show up in a

slightly different order in excess ordered lists using the new versus the old calculation. For instance, a few of these stars were observed during phase II on July 24 (see Table 13), but 36414 now shows up as number 7 using the new calculation, i.e. 3647. This does not present a serious problem, except for nomenclature purposes, because the difference in flux excess between a star which is 7th on the list versus 14th is rather small, 50% versus 37%. In either case, this star would have been chosen for further investigation using the other techniques.

A scaling factor (see previous section) of 111.7% was applied to the on-line photometry. This roughly splits the excesses into half positive and half negative for all the stars which pass the constraints. A standard deviation of 9.5% was calculated for the excess. Figure 32 contains a bar chart giving the number of stars versus flux excess. The bins span 6% in excess. Notice that the median is around 0%, but the distribution has a noticeable tail toward positive excesses. The large standard deviation is probably due to variations in extinction, both because some stars are in the foreground and the extinction at the Galactic Center in this frame is patchy. This effect could be corrected by calculating a scaling factor for every single star assuming intrinsic colors for red giants and using the H and K photometry from night number 4 in phase I. This requires that data between nights are systematically combined, a task which is not yet completed.

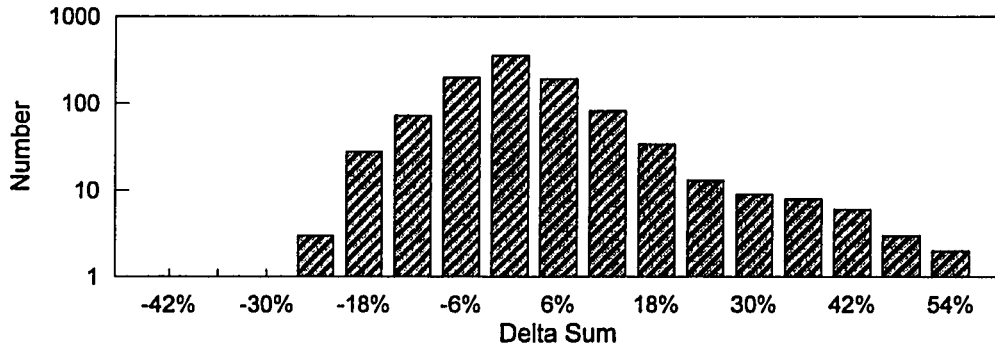
Table 14: Flux Excess for Frame 364

#	x	y	Br γ (2.166 μ m)				Continuum (2.085 μ m)				mag	S/N	Δ sum	MF
			sky	sum	area	Imag	sky	sum	area	Imag				
1	49.98	205.34	73.8	4742	28.6	-8.55	41.1	2699	28.6	-7.96	14.1	17	92.7%	16
2	99.76	235.91	18.3	9341	28.6	-9.86	-10.5	5514	28.6	-9.41	12.6	66	69.3%	46
3	11.67	219.99	57.7	4246	28.6	-8.54	66.8	3634	28.6	-8.09	13.9	20	68.4%	13
4	218.53	39.15	-23.2	1575	28.6	-8.38	-23.0	848	28.6	-7.94	14.1	17	66.2%	11
5	61.19	96.17	50.3	41574	28.6	-11.51	72.2	30964	28.6	-11.15	10.9	329	55.1%	181
6	75.75	50.98	57.2	4795	28.6	-8.75	98.7	5140	28.6	-8.42	13.6	26	52.1%	14
7	44.73	88.67	68.9	56776	28.5	-11.85	79.9	43079	28.5	-11.53	10.5	464	50.0%	232
8	122.24	53.09	96.2	306928	28.6	-13.71	102.1	233388	28.6	-13.41	8.6	2620	47.4%	1241
9	105.85	39.76	35.5	3858	28.6	-8.63	70.9	4203	28.6	-8.34	13.7	25	45.9%	11
10	86.07	226.06	-34.2	43924	28.4	-11.63	-70.2	32805	28.4	-11.35	10.7	396	44.1%	174
11	211.16	191.16	-64.3	53428	28.6	-11.86	-73.5	41622	28.6	-11.60	10.4	497	41.1%	204
12	73.91	84.99	99.7	221207	28.4	-13.35	103.0	179868	28.4	-13.12	8.9	2011	37.8%	761
13	117.23	85.71	-37.4	14613	28.5	-10.49	-46.7	11411	28.5	-10.26	11.8	145	37.4%	54
14	6.13	192.08	22.9	4883	28.4	-9.07	24.2	4147	28.4	-8.85	13.2	39	36.6%	14
15	107.84	242.79	-0.7	10585	28.6	-10.06	-31.3	7797	28.6	-9.85	12.2	99	36.3%	36

#	x	y	Br γ (2.166 μ m)				Continuum (2.085 μ m)				mag	S/N	Δ sum	MF
			sky	sum	area	Imag	sky	sum	area	Imag				
16	42.36	89.03	68.1	52717	28.6	-11.76	78.6	43876	28.6	-11.55	10.5	473	36.2%	171
17	96.60	123.84	-49.3	1266	28.6	-8.57	-45.7	893	28.6	-8.36	13.7	25	36.0%	9
18	67.88	172.75	7.3	39797	28.6	-11.49	-10.6	32528	28.6	-11.29	10.7	373	34.6%	129
19	114.00	230.79	1.5	5002	28.5	-9.24	15.9	4625	28.5	-9.05	13.0	47	32.7%	16
20	41.43	223.66	111.0	7635	28.4	-9.13	55.9	5389	28.4	-8.95	13.1	43	31.6%	14

Number Counts vs. Delta Sum

File = 364, Scale = 1.12



Number of Sources Above Thresholds = 1016 out of 1433 = 71%
Of 1016, 47% are negative, and 53% are positive

Figure 32. Number versus Δsum (Bry) for frame 364.

The next step after calculating the flux excesses is to examine each frame by eye for the most promising targets. Figure 33 shows a Bry and Bry minus continuum image. The on-line image has been scaled by 1.112 given by spreadsheet. H1 and H2 are seen in the upper left and upper middle parts of the frames respectively; notice the excess Bry emission associated with these objects. In the differenced image, there are many stars which have "negative" stars very near to them. This is the signature of a ghost pair where the ghost in one filter falls slightly away from the ghost in the other filter. Fortunately, most of the excess stars in this frame are not influenced by the ghost pairs.

Because there are many more potential targets than can be observed in phase II, the faintest targets were rejected for consideration, i.e. stars 3, 4, 6, 9, 14, and 17. In addition, some targets are located in regions of diffuse Bry emission, i.e. stars 1, 2, 15, 19, and 20; the excess in these apertures are, no doubt, due to contributions from the diffuse emission. Excluding these stars, there are about half a dozen stars which are prominent in the differenced image for frame 364. For instance, stars 5, 8, 10, 11, 12,

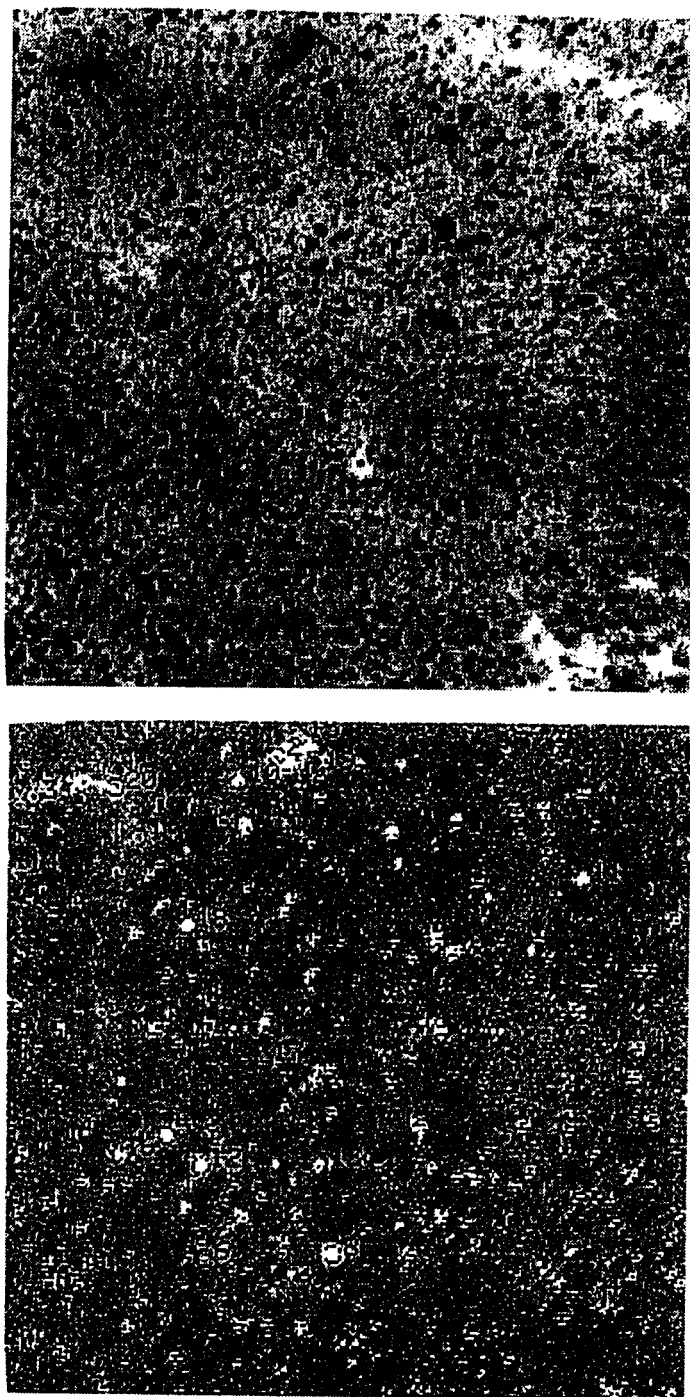


Figure 33. Continuum image (top) and Bry-continuum difference image (bottom) for location 64.

16, and 18 are all bright and have excesses greater than 35%. Occasionally, two nearby apertures will pick up the same star, i.e. 7 and 16.

Oddly enough, a known emission-line star associated with H2 does not show up in the list of the 20 stars with greatest excess. It does have $\Delta\text{sum} = 18\%$, placing it at number 45 in the list. This star is at the center of the diffuse Br γ emission from H2 and can be seen best in the unsubtracted image in Figure 33. The star was chosen as a candidate for phase II from a previous targeted survey by Figer et al. (1994). The first spectroscopic observations were done with CGS4 on the UKIRT 3.8 m telescope as part of service observations in the summer of 1993. The star was again observed spectroscopically during phase II, and Cotera (1995) also obtained a K-band spectrum. All of the spectra show a prominent, but narrow, Br γ line with $W_\lambda \sim 30\text{\AA}$ (CGS4) 60\AA (Gemini). By numerically integrating the spectra, we calculate $\Delta\text{sum} \sim 13\%$ (CGS4) and 20% (Gemini) where the latter value is in close agreement with the 18% excess measured in phase I.

The above procedures were repeated for each of the 40 survey locations taken on nights 1 & 2 (HeI survey) and night 3 (Br γ survey). All of the new targets showed an apparent excess in the Br γ survey while only two new stars, near the Quintuplet, showed excesses in the HeI survey. Of course, some of the previously known emission-line stars, i.e. the AF star in the central parsec, had excesses in the HeI images. A few of these stars were chosen as targets as a test of the system. The final target list is given in Table 13.

B. phase II

Spectroscopic data reduction is inherently much more difficult than the narrow-band data reduction because a spectrum contains data at many wavelengths, and some

of the important corrections to the data also vary with wavelength, i.e. sky background and quantum efficiency of the array. The spectra have to be calibrated to a wavelength scale, and even small misalignments between wavelength fits for the atmospheric standard star and the target star can result in large spurious peaks near sharp atmospheric features.

1. sky/bias/dark subtraction and flatting

Bias structure and dark current were recorded during the night while moving the telescope between observations. This minimizes the effects of changes in the detector temperature between the time of the observations and the time when the calibration frames were taken. Of course, these array effects can be subtracted by subtracting adjacent spectral images as long as there is no starlight in the adjacent frame at the same array location as the target star in the object frame. This method has the additional effect that sky contributions are subtracted fairly well, although a residual sky signal will still remain because sky emission is quite variable. Flat frames were obtained by illuminating the camera with continuum lamps provided by the observatory. These frames were taken with the same instrumental setup as the object frames, i.e. slit and grisms in the beam.

2. wavelength calibration

The Earth's atmosphere is usually a nuisance to astronomers because it absorbs almost all incoming light from stars at some wavelengths and it introduces time-variable wavefront aberrations for the light which is transmitted. However, the atmosphere does provide a natural wavelength calibration system for near-infrared spectroscopy. OH⁻ molecules in the atmosphere emit light at discrete wavelengths due to vibrational transitions within the molecule. This produces a pervasive emission-line

spectrum across the near-infrared spectrum which can be used to calibrate pixel number in the dispersion direction with wavelength (Ramsay et al. 1992). For this purpose, the exposure times have to be several minutes at an airmass of ~ 2.5 ; the OH^- line intensity scales roughly with the airmass (McCaughrean 1988).

The sky lines were identified and associated with vacuum wavelengths using the IDENTIFY task in IRAF. The vacuum wavelengths were obtained by assuming that the wavelength-to-pixel fit for the argon lamp was valid for the sky lines. The output database table from IDENTIFY was used as a starting point for the REIDENTIFY task which follows the emission lines up the slit adjusting the centroids as a function of y . The output from this task was then input into the FITCOORDS task to apply a general fit for pixel number (x,y) to wavelength using a high order polynomial ($n_x = 4$, $n_y = 3$). Figure 34a shows the deviation from a first order fit to wavelength versus pixel number for the K-band spectrum of an argon lamp where longer wavelengths have higher pixel numbers. This figure can be compared to the expected theoretical deviation shown in Figure 30b. Figure 34b shows the same data fit with the higher order polynomial. Now the residuals are quite small except for a few poorly fit lines. Fits to the OH^- lines are somewhat poorer with a standard deviation of $\sim 1 \text{ \AA}$ near the center of the band; this error corresponds to 15 km s^{-1} .

There are no OH^- emission lines in the K-band past $2.27 \text{ }\mu\text{m}$, but there are other sky emission lines of unknown origin between 2.31 and $2.42 \text{ }\mu\text{m}$. These lines were originally thought to be produced by the street lights in San Jose, but they are also apparent in sky spectra taken in Hawaii (Ramsay et al. 1992). Their origin is not of primary importance for the purposes of spectral calibration. Their central wavelengths were measured, again using the argon lamp fit, and included in the sky emission line

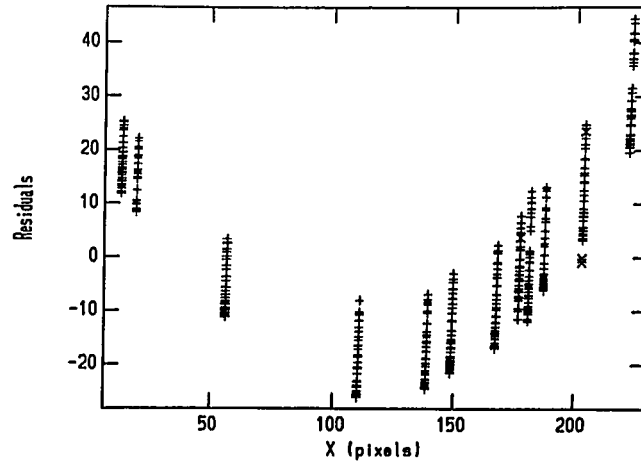


Figure 34a. Deviation from a first order fit. Residuals are in Å.

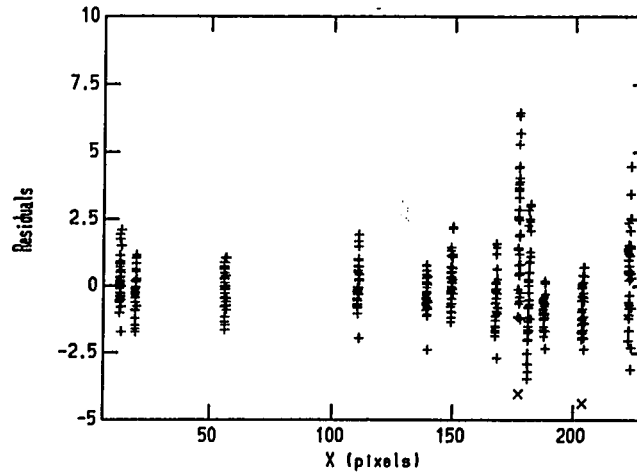


Figure 34b. Deviation from a higher order fit. Residuals are in Å.

database for the fits.

Figure 35 shows the sky emission spectrum on top of the thermal background from the sky and the telescope where the intensity scale is in counts and the exposure time was 300 seconds; the spectrum is a sum of 10 rows, so the intensity scale can be divided by 30 to give counts $s^{-1} \text{ pixel}^{-1}$. The central wavelengths from sky emission lines are shown above each line. Notice the emission lines longward of $2.28 \mu\text{m}$ which

have uncertain origin. Some of these lines are blends, but they can still be used as calibrators as long as the relative strength of individual components within the blend remain constant. The general fit to the spectrum in Figure 35 is shown in Figure 36. Table 15 gives the central wavelengths for the emission lines and the difference between our measurements and the measurements in the databases found in IRAF and Ramsay et al. (1992). The average difference between our wavelengths and the other wavelengths are 1.9 Å (IRAF) and 8.9 Å (Ramsay et al. 1992).

This procedure of fitting the wavelength to pixel number had to be repeated for every object spectral frame because the fit changes by as much as 2 pixels between objects. Poorly fit points were marked so that they would not be used in the final fit. These final fits were applied to the spectral image by using the TRANSFORM task in IRAF.

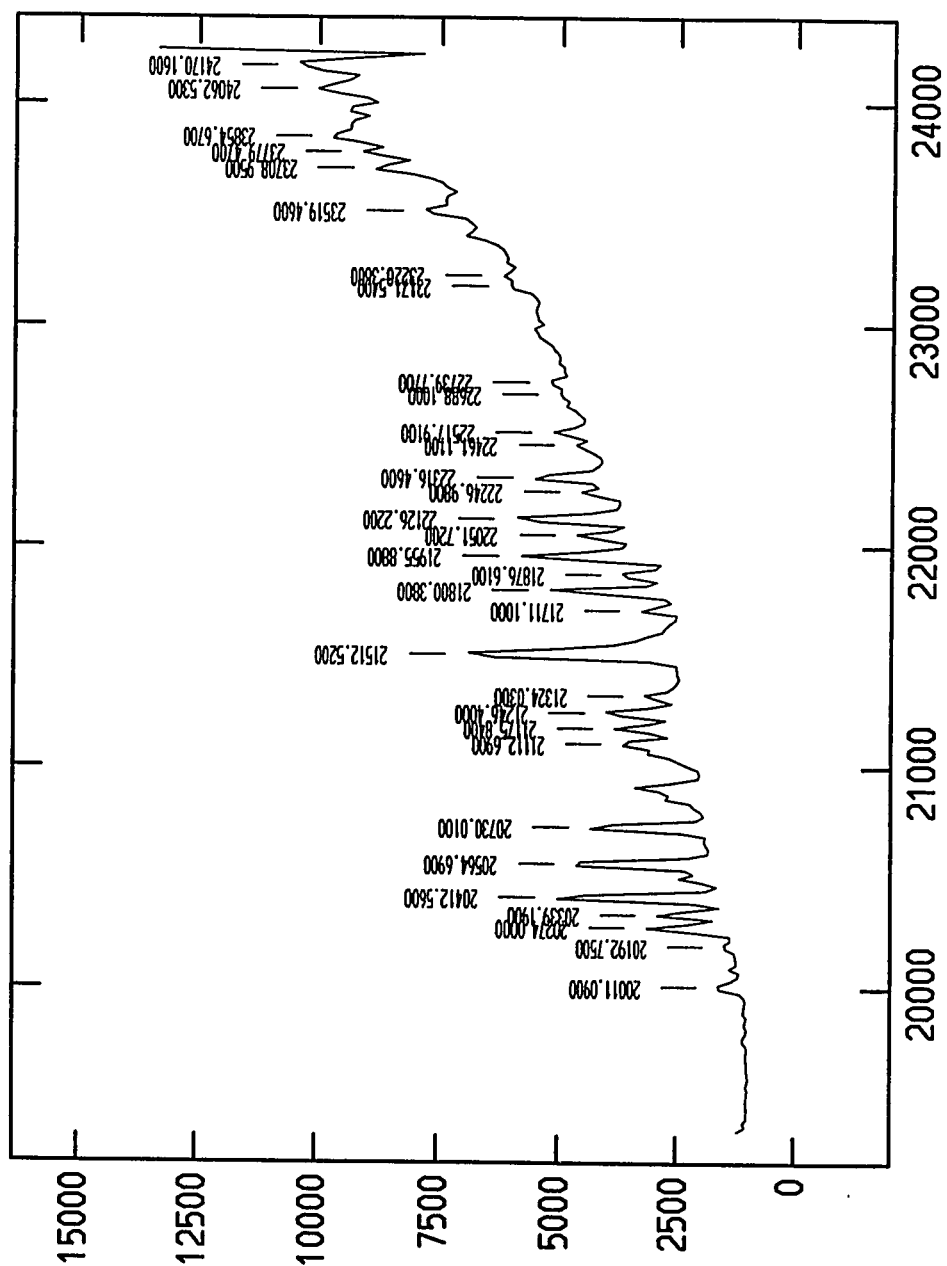


Figure 35. Sky spectrum. Intensity scale is in counts for a 300 second exposure per pixel for 10 summed rows.

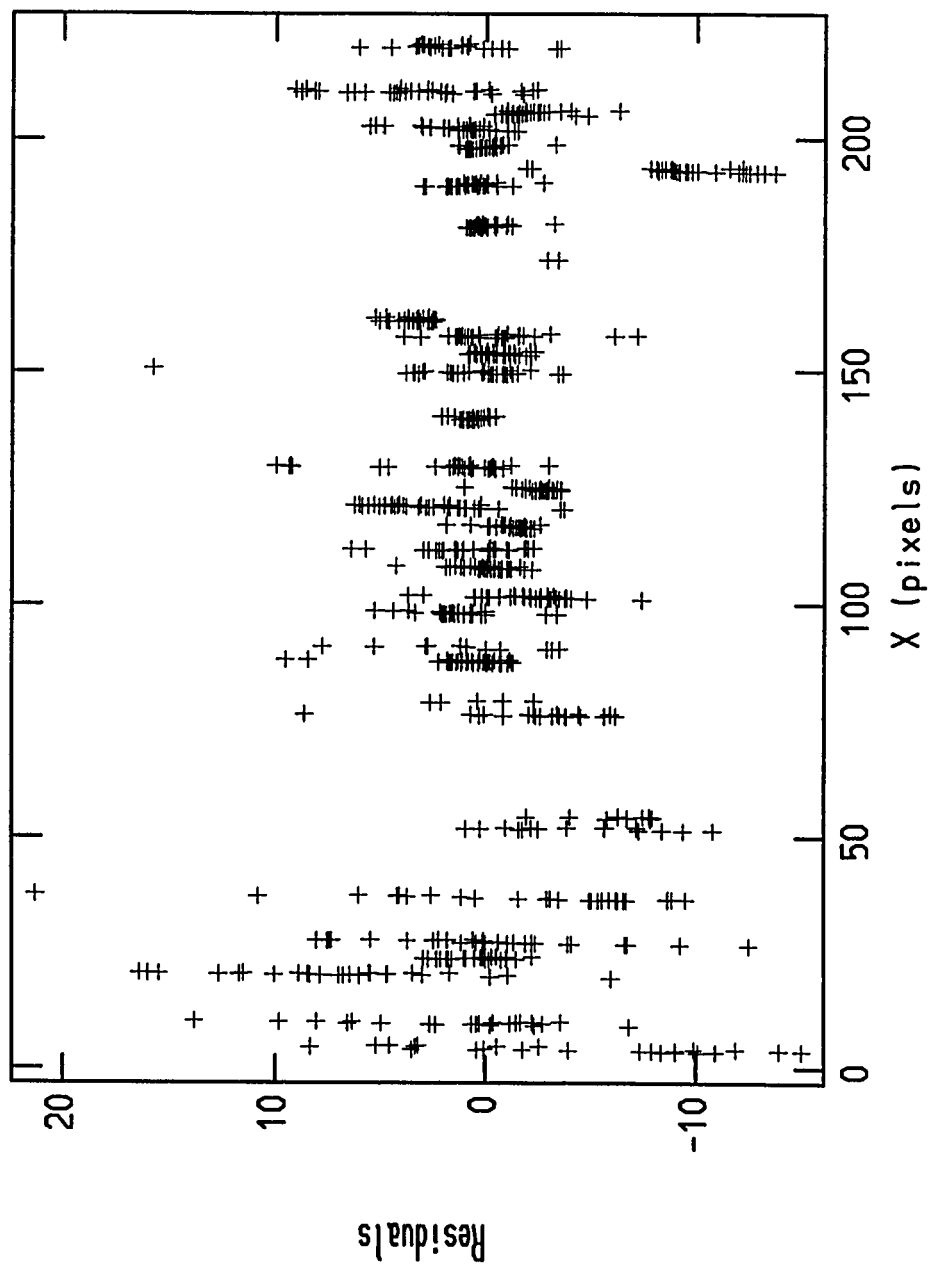


Figure 36. Wavelength to pixel number fit for sky lines.

Table 15: Central Wavelengths for Sky Emission Lines

Gemini	IRAF	Ramsay	Δ_{IRAF}	Δ_{Ramsay}
	19518.1			
	19561.1			
	19593.2			
	19642.5	19635		
	19699	19685		
	19702.9			
	19736.2			
	19751.5	19756		
	19771.8			
	19839.7	19845		
20011.09	20008.2	20003	2.89	8.09
	20033.2			
20192.75	20193.3	20218	-0.55	-25.25
20274.00	20275.9	20270	-1.9	4
20339.19	20339.5	20315	-0.31	24.19
20412.56	20412.7	20400	-0.14	12.56
20493.42	20499.3	20470	-5.88	23.42
20564.69	20563.6	20556	1.09	8.69
	20672.9			
20730.01	20729	20722	1.01	8.01
20856.96	20860.3	20854	-3.34	2.96
20932.99	20909.6	20897	23.39	35.99
21064.83	21068		-3.17	
	21096.6			
	21105.7			
21112.69	21115.9	21110	-3.21	2.69

Gemini	IRAF	Ramsay	Δ_{IRAF}	Δ_{Ramsay}
	21156.1			
21175.84	21176.6	21183	-0.76	-7.16
	21232.5	21250		
21246.40	21249.7		-3.3	
	21279.1			
	21318			
21324.03	21326	21333	-1.97	-8.97
	21505	21518		
	21507.3			
21512.52	21512.1		0.42	
21559.74	21537.6		22.14	
	21580.7			
21711.10	21711.1	21704	0	7.1
21800.38	21802.2	21792	-1.82	8.38
21876.61	21873.5	21870	3.11	6.61
21955.88	21955.6	21938	0.28	17.88
22051.72		22042		9.72
22126.22	22125.5	22108	0.72	18.22
22246.98	22247.9	22225	-0.92	21.98
22316.46	22312.7	22309	3.76	7.46
22461.11	22460.3		0.81	
22517.91	22518		-0.09	
22688.10				
22739.77	22742	22742	-2.23	-2.23
23171.54				
23220.36				
23519.46				

Gemini	IRAF	Ramsay	Δ_{IRAF}	Δ_{Ramsay}
23708.95				
23779.47				
23854.67				
24062.53				
24170.16				

3. aperture extraction

Once the images were transformed, individual apertures were extracted using APALL in IRAF. This task is actually made up of many individual tasks which allow the user to interactively select apertures centered on objects in the frame. Background apertures can also be defined so that an average signal at each pixel can be subtracted from the object spectrum. In general, the apertures were defined to contain only light from each object and background apertures were defined to subtract sky and diffuse emission. For instance, light from the objects in the central parsec is contaminated by the diffuse Br γ emission of the mini-spiral, so the background apertures there were selected so that this extra emission was subtracted.

In general, the spectra are tilted by a few pixels from edge-to-edge across the array due to a small tilt of the grism with respect to the array. This is compensated by tracing the spectrum versus wavelength within the APALL task. The resultant apertures are then tilted according to this trace.

4. correction for telluric absorption and filter profile

The extracted spectra show noticeable absorption due to the Earth's atmosphere and the K filter profile. This can be corrected by dividing the spectra by the spectrum of an atmospheric standard star. Most stars have some intrinsic absorption features in

the H and K bands, but A-type stars only have Br-series absorption. A raw spectrum for the A2V star BS6378 is shown in Figure 37. The Br γ absorption feature has been replaced by an interpolated line at 2.166 μm . Notice the very deep absorption near 2.01 and 2.06 μm due to atmospheric CO $_2$. The strong cutoff shortward of 2 μm is due to the K filter.

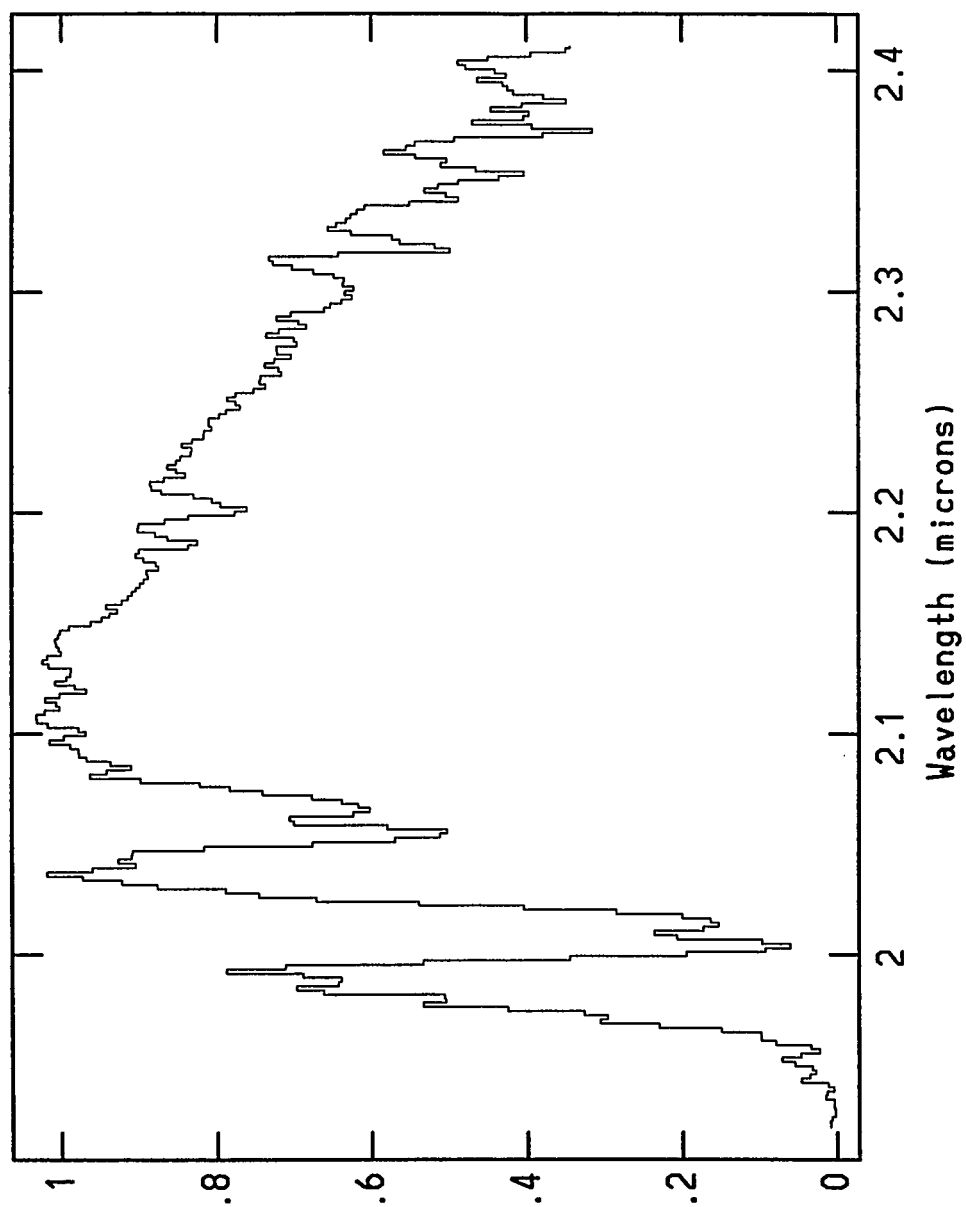


Figure 37. Raw spectrum for BS6378.

5. flux calibration

After correcting for atmospheric absorption, the spectra will have a shape which is influenced by the standard star which was used. This shape can be taken out of the final spectra by multiplying by a black-body fit to the standard star's spectrum. MK1DSPEC in IRAF was used to generate a synthetic spectrum having intensity versus wavelength according to the black-body function. Temperatures were taken from Theodossiou & Danezis (1991) according to the spectral subtypes listed in the Bright Star Catalog.

6. dereddening

The DEREDDEN task was used to correct the spectra for interstellar extinction. This task uses the extinction law from Cardelli et al. (1989), and the input parameter, R in equation (8b), was set to 3.09. Individual extinction values at V were also input. An extinction of 30 magnitudes at V was assumed for all stars at the Galactic Center except stars within the Quintuplet frame where 19 magnitudes was assumed. This value is justified in Chapter VIII.

7. equivalent widths and line ratios

Equivalent widths, see equation (12), were measured using the "k" option in the SPLIT facility in IRAF. The continuum is estimated by linear interpolation between two continuum points on either side of the emission line. A gaussian is fit to the emission line and the equivalent width is just the wavelength-weighted sum under the gaussian profile normalized to the continuum. The absolute flux in emission lines was calculated by multiplying the equivalent width by the value of the flux in the continuum where the latter was estimated by the photometry extracted from phase I.

VI. Data

This chapter contains final reduced data for the survey target stars. Broadband images of the whole survey are shown. The photometry is given for the stars in the phase II target list. Finally, the normalized, flux-calibrated, and dereddened spectra are shown.

A. Survey image

Figure 38 is a color image of the survey with H coded as blue and K' coded as red. The variability in extinction can be seen in this picture, and its effects on photometry are discussed in section VII.A.

B. Photometry

Photometry was obtained by using a 4.2'' diameter aperture and a 7'' wide annulus with inner radius 5.6'' from the center of the aperture to sample the background. Photometric zero points were estimated using three methods. The first method used published photometry for IRS9 and IRS11 in the central cluster (Becklin et al. 1978). Both stars gave zero points which were within 0.17 magnitudes of each other for H and K'. The final zero points using this method are 20.68 for K' and 21.01 for H at an airmass of about 2.6. These values were tested by comparing measured photometry for several stars within the inner few minutes of the Galactic Center to published values from Haller (1992) (see Figure 39). Haller's K band photometry was converted into K' photometry by using the conversion relation from Wainscoat & Cowie (1992). There seems to be a systematic difference of about -0.10 and -0.18 magnitudes in K' and H respectively between the two sets of photometry.

The second method involved observing photometric standard stars from the list given by Elias et al. (1982). This method gave zero points of 20.37 and 20.80 for K'

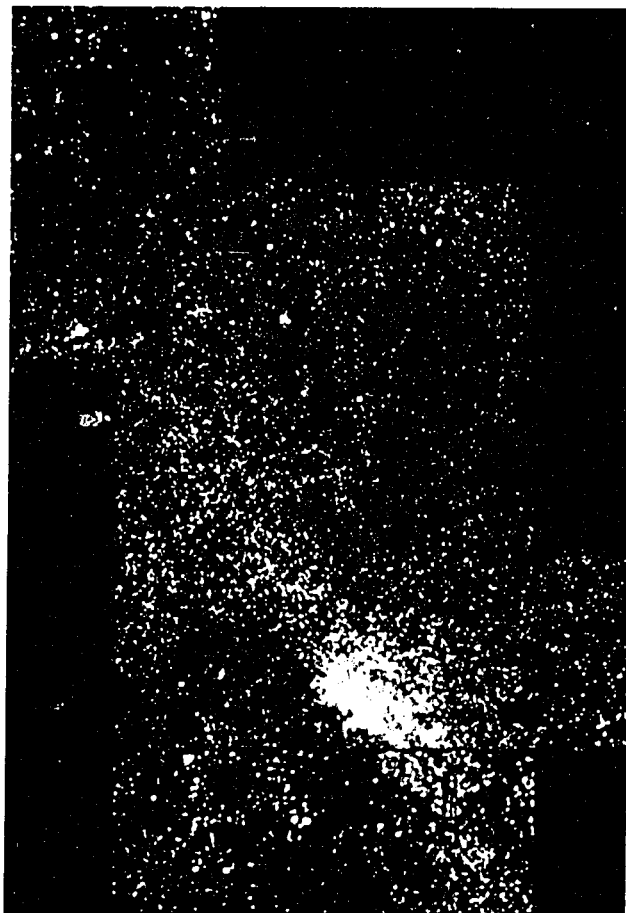


Figure 38. Color picture of survey where H has been coded as blue and K as red.

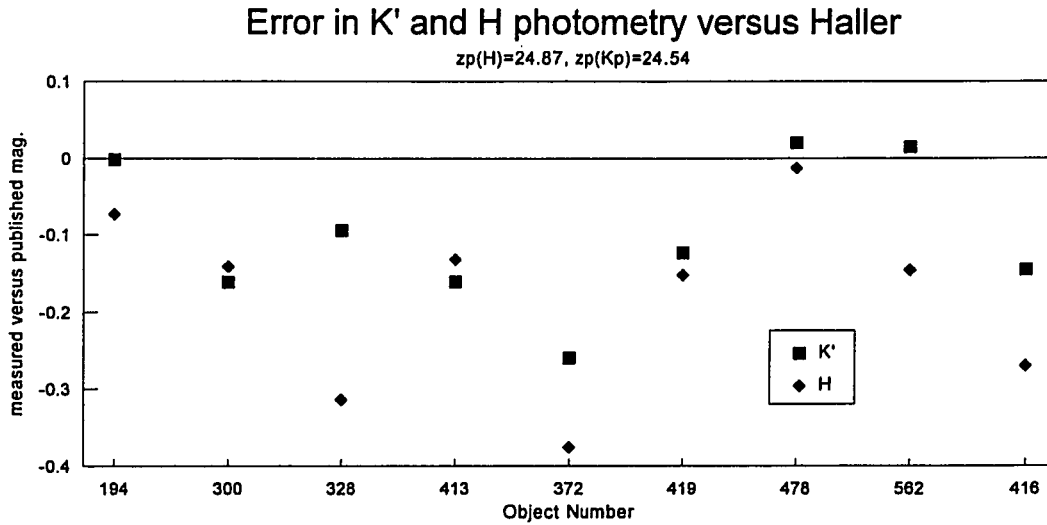


Figure 39. Difference between photometry from this study to published photometry from Haller (1992).

and H respectively at an airmass of one for the beginning of the night. Additional standard stars were observed at the end of the night, but the zero points from these observations were lower by 0.15 magnitudes. Evidently, the sky became more opaque later in the night. The atmospheric extinction coefficient could not be measured accurately because standard stars at high airmass were not observed. In any case, zero points for stars in the survey, where the airmass is ~ 2.6 , should be lower than those for the standard stars, where the airmass is ~ 1 . Thus, the values measured using the second method are inconsistent with the zero points measured using the first method.

The last method uses photometry from data taken with IRCAM at UKIRT. Images were taken of the HII regions about 10' north of the Galactic Center (Figer et al. 1994). H and K photometry was measured for 40 stars in a frame a few arcminutes north of H1. This was compared to measured photometry for the same stars in the survey. After converting K to K', the calculated zero points were 20.62 (0.08) and

20.72 (0.06) for K' and H where the standard deviation divided by the square root of the number of data points is in parenthesis.

The three methods produce quite disparate results. The zero points probably drifted by no more than 10% during the survey period because instrumental magnitudes for stars in the dark spot varied by less than this amount; therefore a more accurate zero point could be determined in the future by reobserving the dark spot on a night where the extinction coefficient is well determined. This will be done during an upcoming observing run.

Table 16 gives the final photometry for the targets observed in phase II, where the zero point from the first method were used. The coordinates, in pixel units, refer to object position in the K' images. The errors are ± 0.2 magnitudes and are dominated by uncertainties in the zero points for the brighter stars and by confusion in the fainter stars.

Table 16: Aperture Photometry for Targets

	X	Y	K'	H	K	H-K
AF	122.99	71.98	10.64	12.02	10.30	1.73
H2	97.10	222.90	9.89	11.53	9.48	2.05
37345	62.19	125.86	8.82	10.78	8.33	2.45
37321	53.27	103.78	9.41	11.47	8.90	2.58
37336	58.99	204.88	8.89	11.31	8.29	3.03
37351	222.96	109.85	10.07	12.15	9.55	2.60
H1A	17.61	209.42	10.56	12.60	10.05	2.55
H5W	144.98	234.45	11.58	13.08	11.21	1.88
H5WN	146.69	229.12	12.65	15.20	12.01	3.19
H5EA	112.17	144.23	11.40	13.99	10.75	3.24

	X	Y	K'	H	K	H-K
H5EB	110.21	204.83	11.51	13.57	11.00	2.57
H5EC	112.92	227.01	12.30	14.19	11.83	2.36
H5ED	105.93	238.81	9.57	11.56	9.07	2.49
36414	76.86	213.84	10.90	13.18	10.33	2.85
36443	132.94	195.88	10.22	12.83	9.57	3.26
36416	35.59	76.05	10.67	13.79	9.89	3.90
36415	51.98	83.91	11.03	14.01	10.29	3.73
36429	64.26	72.77	9.17	10.99	8.72	2.28
36417	112.48	40.93	8.86	10.79	8.38	2.41
36422	201.95	178.93	10.66	12.93	10.09	2.84
H1141	242.12	241.82	10.13	12.97	9.42	3.54
H1132	151.31	202.48	8.61	10.59	8.12	2.47
H1139	148.74	216.96	11.41	14.46	10.65	3.82
H1149	142.11	225.48	9.88	12.25	9.29	2.96
H6	183.73	24.88	13.71	16.19	13.09	3.10
H3A	67.02	34.13	12.11	13.35	11.80	1.55
H3B	65.89	86.93	12.43	14.24	11.98	2.26
H3C	64.12	99.89	11.68	13.59	11.20	2.40
H3D	65.75	142.87	11.66	13.07	11.31	1.76
3656	137.74	165.21	11.38	14.20	10.68	3.53
3659	184.54	204.27	9.84	11.81	9.35	2.46
36513	158.79	98.81	10.31	12.35	9.80	2.55
A1133A	166.98	73.13	11.12	12.41	10.80	1.62
A1133B	165.95	156.77	11.76	12.10	11.67	0.42
A1133C	167.00	220.17	10.92	13.73	10.22	3.51
36516	59.06	242.95	9.77	12.05	9.21	2.84
37119	47.05	216.91	11.39	14.15	10.70	3.46

	X	Y	K'	H	K	H-K
39211	141.74	47.95	10.31	13.39	9.54	3.85
39217	188.83	217.00	12.71	16.61	11.74	4.87
3926	215.14	58.81	10.29	13.06	9.60	3.46
39238	217.07	181.15	12.27	14.99	11.59	3.40
39228	84.82	155.02	11.32	14.22	10.59	3.63
X1	143.36	9.74	10.22	11.62	9.87	1.76
X2	143.46	30.87	10.34	12.17	9.88	2.30
X3	143.92	38.67	11.79	13.40	11.39	2.00
X4	143.01	44.05	11.52	13.22	11.09	2.13
X5	141.03	53.87	11.04	12.37	10.70	1.67
X6	143.95	72.04	13.14	14.21	12.88	1.34
X7	144.85	85.82	12.12	13.65	11.74	1.92
X8	145.53	100.77	9.74	11.68	9.26	2.42
X9	144.96	107.77	11.06	12.76	10.63	2.13
X10	144.87	121.10	9.65	10.86	9.35	1.51
X11	142.00	126.55	11.25	12.80	10.87	1.93
X12	145.40	148.90	10.67	12.35	10.25	2.10
X13	142.90	169.78	10.61	12.35	10.18	2.18
X14	140.80	62.75	11.16	12.49	10.83	1.66
X15	141.03	136.67	12.14	13.47	11.81	1.66
X16	141.92	184.94	11.45	12.32	11.23	1.09
Z211	172.50	126.70	10.85	12.28	10.49	1.79
37113	168.09	76.82	9.40	11.72	8.83	2.89

An alternate method for measuring fluxes was attempted by fitting a point spread function (PSF) to the target stars. This could be important for the fainter stars because the images typically contain a thousand stars, barely less than the confusion

limit of $256^2/\pi r^2 = 2300$ for $r = 3$ pixels. Because of this confusion, aperture photometry will be in error due to several stars being all or partially within a single aperture; although the errors for bright stars should be much less than for faint stars. The flux from a star can be estimated by fitting a PSF to the inner core of light. Of course, there must be at least a few stars in each frame which are well separated from neighboring stars so that a point spread function can be generated.

This technique accounts for instrumental and atmospheric effects, but a single PSF for a given night will fail to account for variations in seeing and guiding between individual frames. Instead a PSF must be generated for every single frame which amounts to $4 \text{ filters/night} \times 4 \text{ nights} \times 40 \text{ positions/filter} = 640$ frames. Assuming that the process of defining a PSF takes about 0.5 hours of interactive time, this method will require 320 hours of work. Due to the intensive nature of this approach, PSF fitting was reserved only for selected target stars. Otherwise, aperture photometry was used.

Table 17 gives photometry using the PSF method for 16 stars listed in Table 16. The differences with respect to the aperture photometry are listed in the last four columns. As expected, the well-separated stars can be accurately photometered with an aperture or a PSF fit. In some cases, for instance X13, the aperture photometry is badly contaminated by nearby stars. Also, the apparent color of a star can change substantially when a neighboring star has dramatically different color, for example X4.

Table 17: PSF Photometry for Selected Targets

	K'	H	K	H-K	$\Delta K'$	ΔH	ΔK	$\Delta(H-K)$
X1	10.20	11.77	9.81	1.96	-0.02	0.15	-0.06	0.21
X2	10.33	12.38	9.82	2.56	-0.01	0.21	-0.06	0.27
X3	11.67	13.45	11.23	2.22	-0.12	0.05	-0.17	0.22
X4	11.64	13.94	11.06	2.88	0.12	0.73	-0.03	0.76
X5	11.06	12.46	10.70	1.76	0.02	0.09	0.00	0.09
X6	12.98	14.15	12.69	1.46	-0.16	-0.07	-0.18	0.12
X7	12.21	14.17	11.73	2.44	0.09	0.51	-0.01	0.52
X8	9.66	11.67	9.16	2.51	-0.08	-0.01	-0.10	0.09
X9	11.23	12.98	10.80	2.18	0.18	0.22	0.17	0.05
X10	9.70	10.89	9.40	1.49	0.04	0.03	0.05	-0.02
X11	11.36	12.98	10.95	2.03	0.10	0.18	0.08	0.10
X12	10.83	12.56	10.39	2.17	0.16	0.22	0.14	0.08
X13	11.14	12.90	10.70	2.20	0.53	0.55	0.53	0.02
X14	10.92	12.63	10.49	2.15	-0.24	0.15	-0.34	0.49
X15	12.12	13.51	11.78	1.74	-0.02	0.05	-0.03	0.08
X16	11.61	12.60	11.37	1.23	0.17	0.28	0.14	0.14

C. Flux excess for template stars

The following figures show flux excesses in the narrow-band filters for the template stars. Stars with 6-digit designations, 4 digit designations, and 3 digit designations are in the HD catalog, BSC, and WR catalog respectively. The bars are labelled with spectral types for all but the HD stars which are A-types from Elias et al. (1982).

As expected, the standard stars have very little excess, and the measurements are probably dominated by photometric errors. The WC stars earlier than WC9 appear

to have flux deficits in the Br γ and HeI filter, but this is actually a flux excess in the "continuum" filter centered at 2.085 μm . This is expected because the CIV emission near 2.078 μm (see Figure 20) is generally stronger than emission near 2.058 μm or 2.166 μm for earlier subtypes. The WC9 star, WR121, has an excess of $\sim 25\%$ in the 3.09 μm , while earlier subtypes in the WC sequence have excesses up to 150%. This behavior is probably due to increasing CIV emission for earlier subtypes. A similar trend is seen for the 10 \rightarrow 9 and 13 \rightarrow 11 CIV lines near 2.42 μm in Figure 20.

Notice that WN8 stars show a considerable variation in their flux excesses. As seen later, this variation is also apparent in their spectra. The HeI excess is $\sim 10\text{-}20\%$ in WR123, $\sim 40\%$ in WR124, $\sim -5\%$ in WR156, and is uncertain in WR130 due to poor photometry. The Br γ excesses range between $\sim 20\text{-}35\%$, for WR123 and WR130, to $\sim 60\text{-}70\%$ for WR124 and WR156. These characteristics are also evident in the spectra shown later (see Figure 52). The excesses near 3.09 μm cover a large range of $\sim 10\text{-}70\%$ for the WN subtypes. The excesses for the WN9 star, WR108, are less than 20% for all complexes. The earliest subtypes, WN6 (WR134 and WR136) and WN4 (WR128), tend to have very small excesses, if any, near 2.058 μm , $\sim 20\text{-}50\%$ excess near 2.166 μm , and $\sim 70\text{-}150\%$ near 3.09 μm .

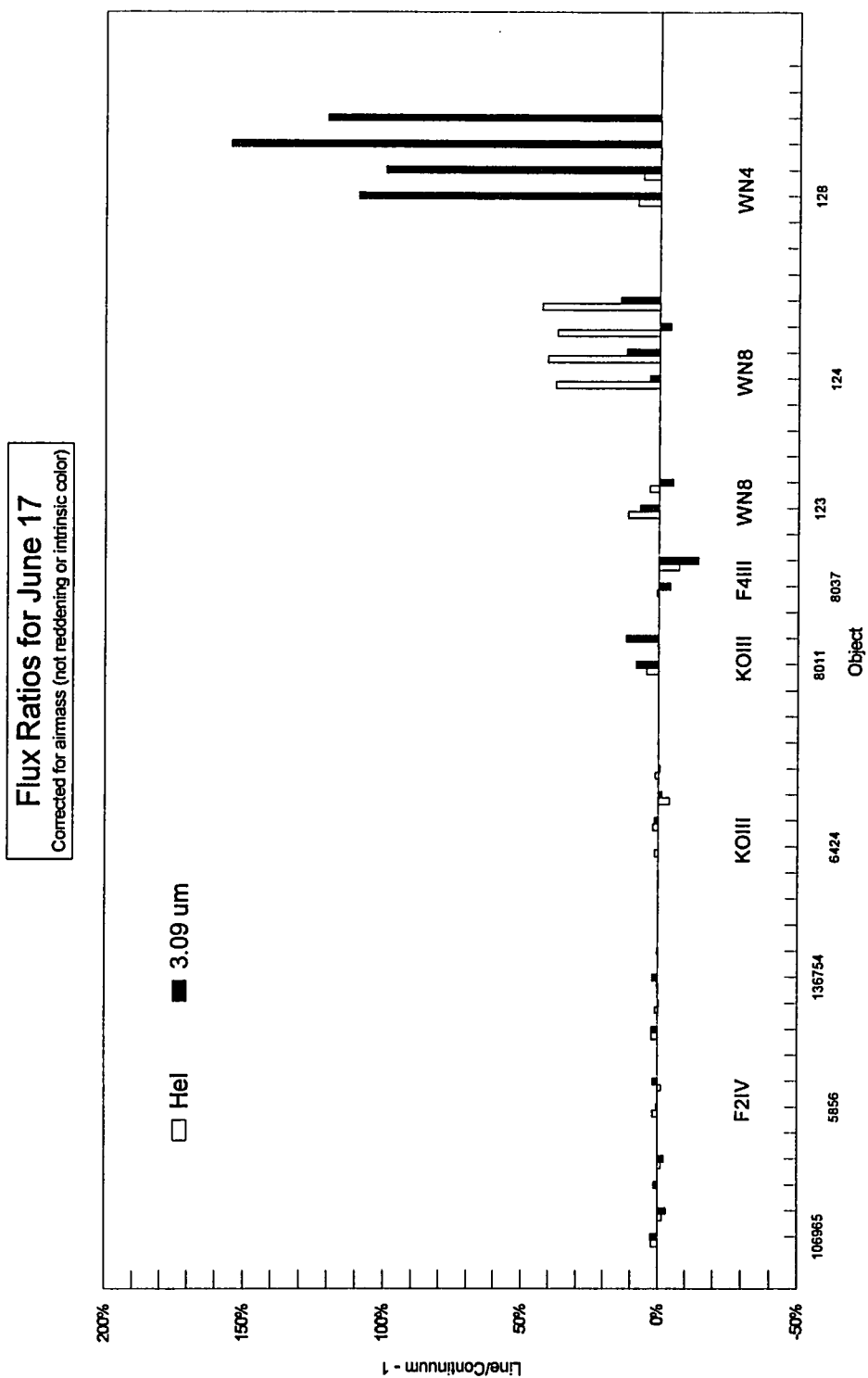


Figure 40. Flux excesses for template stars observed on June 17, 1994.

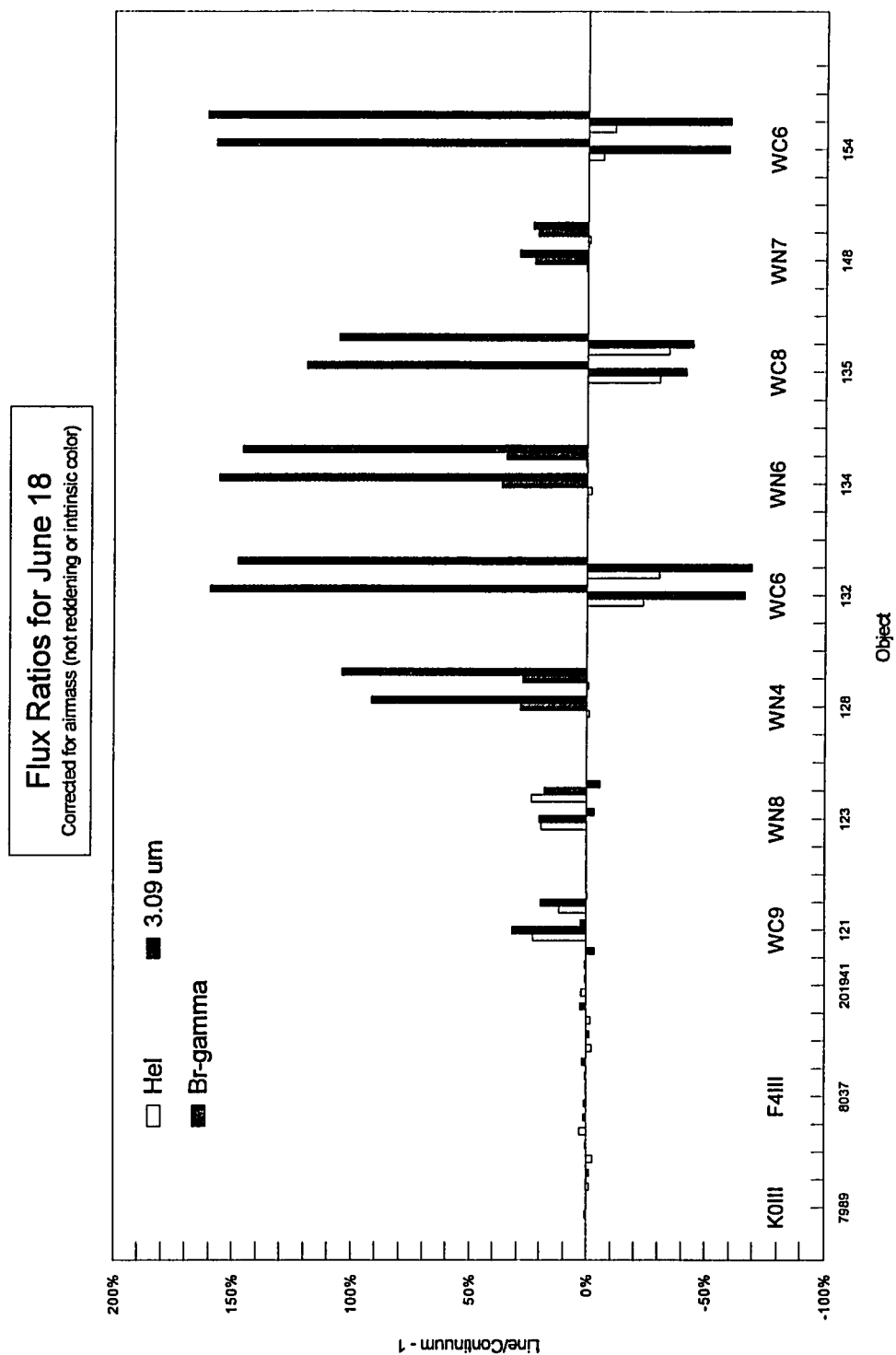


Figure 41. Flux excesses for template stars observed on June 18, 1994.

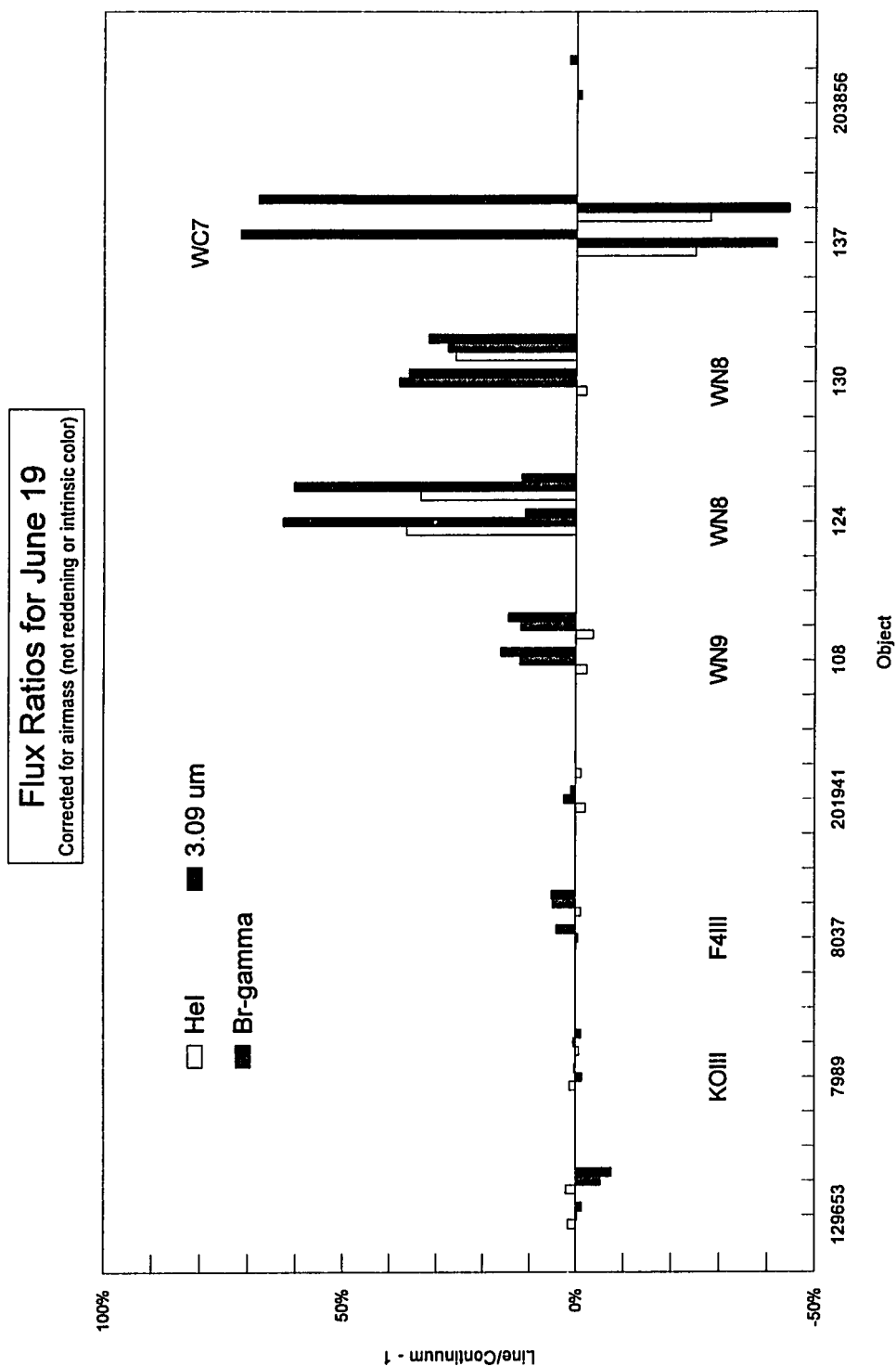


Figure 42. Flux excesses for template stars observed on June 19, 1994.

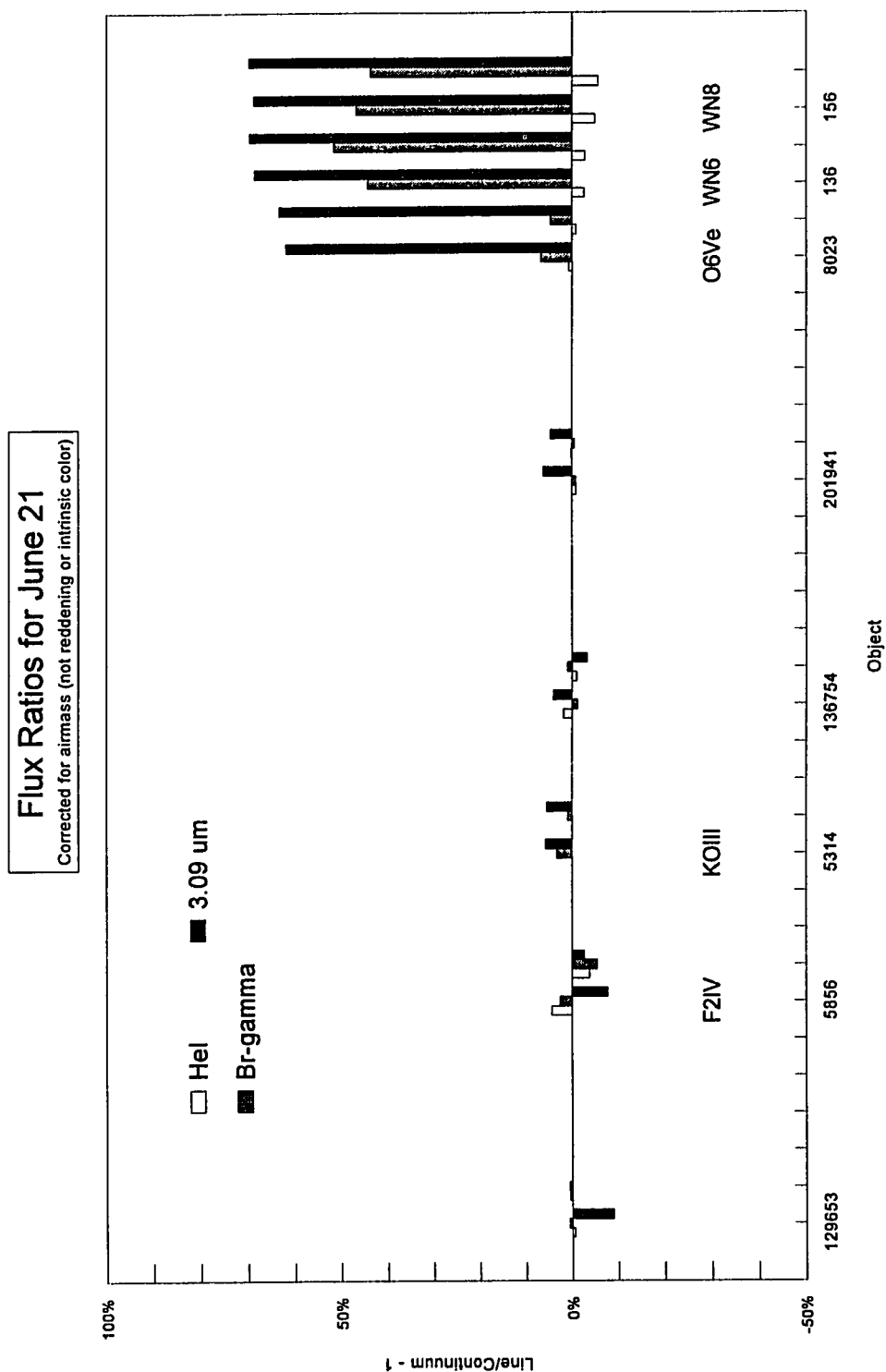


Figure 43. Flux excesses for template stars observed on June 21, 1994.

D. Spectra

The following pages contain final dereddened and flux-calibrated spectra for all of the targets in phase II as well as some serendipitous stars which happened to fall within the slit. All of the spectra have been normalized to a flux of 1 where major tick marks increment by units of 1, and minor tick marks are at half-integral values. The wavelength range is 2.0 to 2.4 μm where major tick marks are at every 0.1 μm and minor tick marks are at every 0.05 μm . The designations were taken from the literature when possible, although some objects have only been observed in this work. In some cases, finding charts have been included.

The spectra tend to fall into two categories, emission-line spectra and deep absorption spectra. The former indicate a hot star generating emission lines in an expanding wind or an HII region near a hot star. The deep absorption spectra are due to very late-type stars with deep water absorption associated with the 1.9 μm and 2.7 μm bands (Woolf et al. 1964). A spectrum of one water absorption star (see Figure 44), 37345, is shown along with a spectrum of the M7III star SW Vir, the latest star in the Kleinmann & Hall atlas (1986). Star 37345 was chosen from the Bry survey, and it was later found to be the infrared counterpart to a newly discovered water maser (Levine et al. 1995). Later, and thus cooler, stars tend to have even deeper water absorption in their atmospheres (cf. Lancon & Rocca-Volmerange 1992).

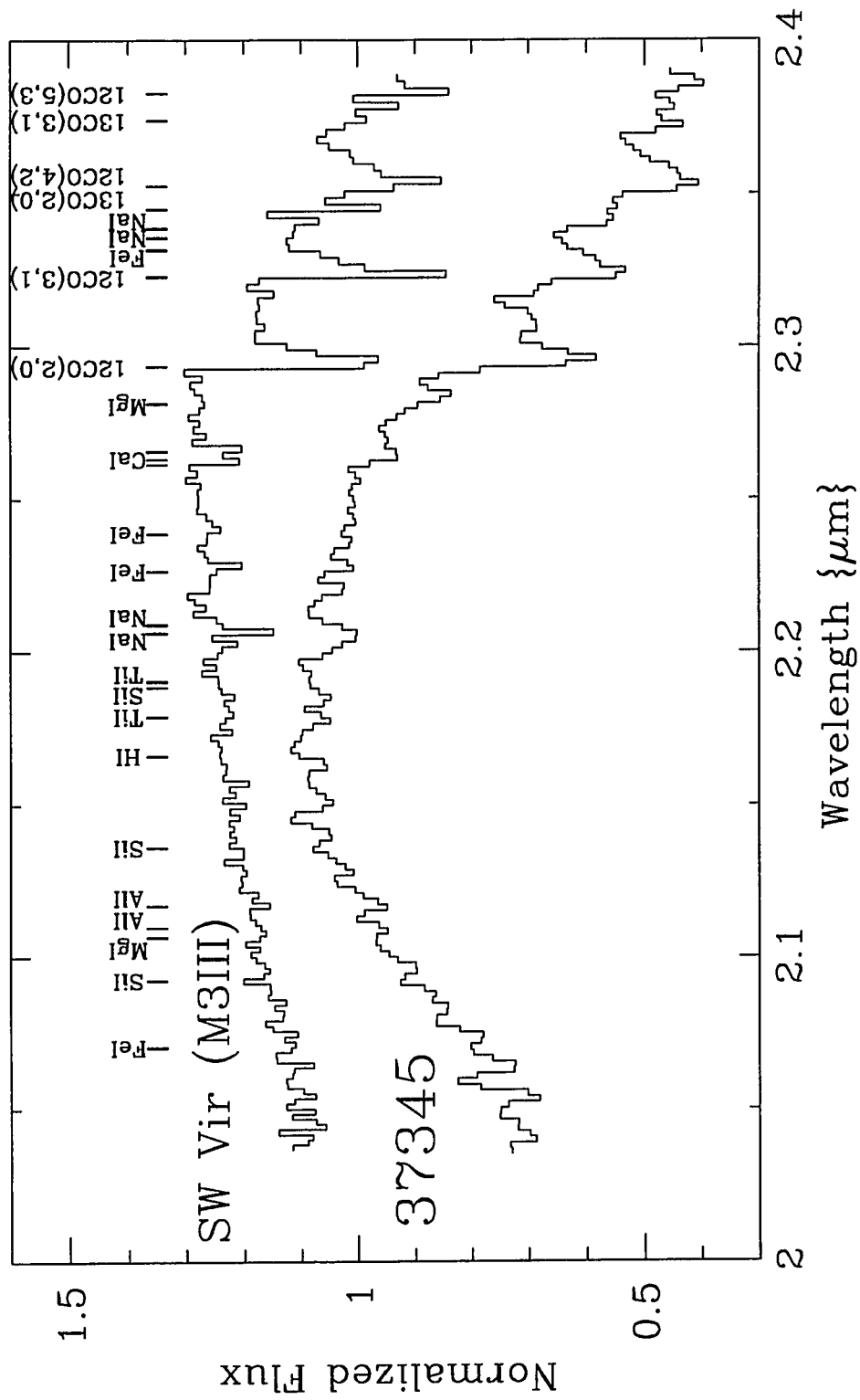


Figure 44. Spectra for water maser counterpart, object 37345, and SW Vir.

The next 5 figures contain spectra for stars in the Quintuplet. Figure 7 is useful for identifying the locations of stars whose spectra are shown in Figure 45a and Figure 45b. Figure 45c locates stars with spectra shown in Figure 45d, Figure 45e, and Figure 45f.

Figure 45a shows spectra for the 2 newly discovered emission-line stars, Star 1 (WN9) and Star 2 (WC9), not to be confused with q1 and q2 from Moneti et al. (1994). These stars are discussed further in section VIII. Spectra for two WC template stars are also shown. Notice that WR135 has a much higher $F_{2.078}/F_{2.058}$ ratio as compared to WR121 or Star 2. This sensitivity to sub-type allows a positive classification for Star 2 as a WC9 star. Star 3 is an LBV candidate, and it is discussed in section VIII. as well. The suspected YSO, Q1, has a relatively flat spectrum which can be fit by a 1000 K black-body; it was used as an intermediate atmospheric standard for Star 1.

Figure 45b shows spectra for the two previously known emission-line stars, as well as several other stars, in the Quintuplet. The numbered designations follow Moneti et al. (1994) as in Figure 7 while the lettered designations follow Nagata et al. (1990). QG is also known as 11a&b, and QD is also known as 13a&b. Spectra in the upper four panels were very difficult to extract because of crowding, but background apertures were chosen on either side of each star. QD is another probable emission-line star discovered in this study; but the helium emission line at 2.058 μm is quite weak and in a difficult wavelength region because of the varying atmospheric absorption. For instance, notice that Q5 and Q3 seem to have a small peak near this wavelength, but they also have CO absorption features. The spectrum for QD is unlike any of the template spectra where the latter always have Br γ emission if HeI emission is present.

The spectrum is flat, confirming that this star is not cool, and Nagata et al. (1990) and Moneti et al. (1994) give a K magnitude for this star which is roughly equal to the K photometry for Q8 and Q10. Assuming the same extinction for these sources, QD is also a likely hot supergiant with $L \sim 10^{5-6} L_{\odot}$. The spectrum for QG has lower S/N, but this source lies within an arcsec of HeII 3.09 μm emission seen in our narrow-band images. This star is fainter than the others, so higher S/N data will be obtained with longer exposures during future observations. Q5 appears to be a typical red giant. Q3 has a spectrum which can be fit with a 1000 K black-body making it quite similar to the spectrum for Q1.

Figure 45d shows spectra for some sources which were serendipitously positioned in the slit while observing the star 2, the new WC9 star. Spectra for these stars are shown in Figure 45c. X1, 2, and 4 are late-type stars where X2 shows considerable water absorption. The single-pixel feature near 2.166 μm in the spectrum of X4 is probably spurious.

X5 and 6 might have relatively flat spectra, but the S/N is very low compared to the other spectra. Their colors are relatively blue with respect to many of the other sources in the field, being similar to or bluer than the colors for the hot stars, Q8 and Q10. Higher quality data for these stars will be taken in the near future, to better determine if these stars do not have CO absorption and to see if the apparent emission features in their spectra are real. The apparent emission line near 2.190 μm is very close to the expected location for the HeII 2.189 μm feature; the implied velocity shift would be $\sim 165 \text{ km s}^{-1}$. The line near 2.166 μm in the spectrum for X6 has a measured velocity shift of 109 km s^{-1} with respect to the vacuum wavelength of Br γ , remarkably

close to velocity shifts measured for other emission-line objects in this cluster (see Table 19).

X7 is probably a late-type star as a hint of the CO absorption bandheads can be seen, and its color is quite red, $H-K=2.44$. The apparent dip at $2.166 \mu\text{m}$ might be interesting; however a more certain classification awaits higher S/N data.

Figure 45e contains more stars which serendipitously fell along the slit. The decline in flux toward longer wavelengths for X8 and X9 might be due improper background subtraction, and these stars would have to be positioned in the slit more accurately in future observations; nevertheless, their spectra show a hint of CO absorption and their red colors are consistent with late-type stars. X10 is a likely emission-line star with a prominent helium line at $2.058 \mu\text{m}$. Its $H-K$ color is relatively blue like the case for X6. It has a K magnitude of 9.4 from Table 17. This gives $L \sim 10^{5.7} L_{\odot}$ assuming appropriate parameters for the Quintuplet, $DM = -14.65$, and $A_K = 2.1$, and a conservative estimate of $BC_K = -2$ for a hot star. The spectra and $H-K$ colors for X11, 12, and 13 are consistent with late-type stars.

Figure 45f shows spectra for the last three sources listed in Table 17. X14 appears to have a relatively flat spectrum with a dip at $2.16637 \mu\text{m}$ implying a velocity shift of 35 km s^{-1} if the feature is identified with $\text{Br}\gamma$ absorption; this shift is on the order of the error. The $H-K$ color is about the same as the newly discovered WC9 star which is assumed to have intrinsically red colors (see Chapter VIII.) The implied luminosity is $\sim 10^5 L_{\odot}$ assuming $BC_K = -2$. This luminosity is roughly equivalent to the luminosity of an O8V star, but such a star would have $BC_K \sim 3.5$ (Panagia 1973). X15 has a relatively flat spectrum, but better atmospheric correction is needed near $2.06 \mu\text{m}$. This relatively faint star should really be reobserved by accurately placing the

object directly within in slit. X16 probably has CO absorption, and the steep dereddened slope confirms that this spectrum was probably dereddened more than necessary; the very blue colors, with respect to other Quintuplet members, confirms this.

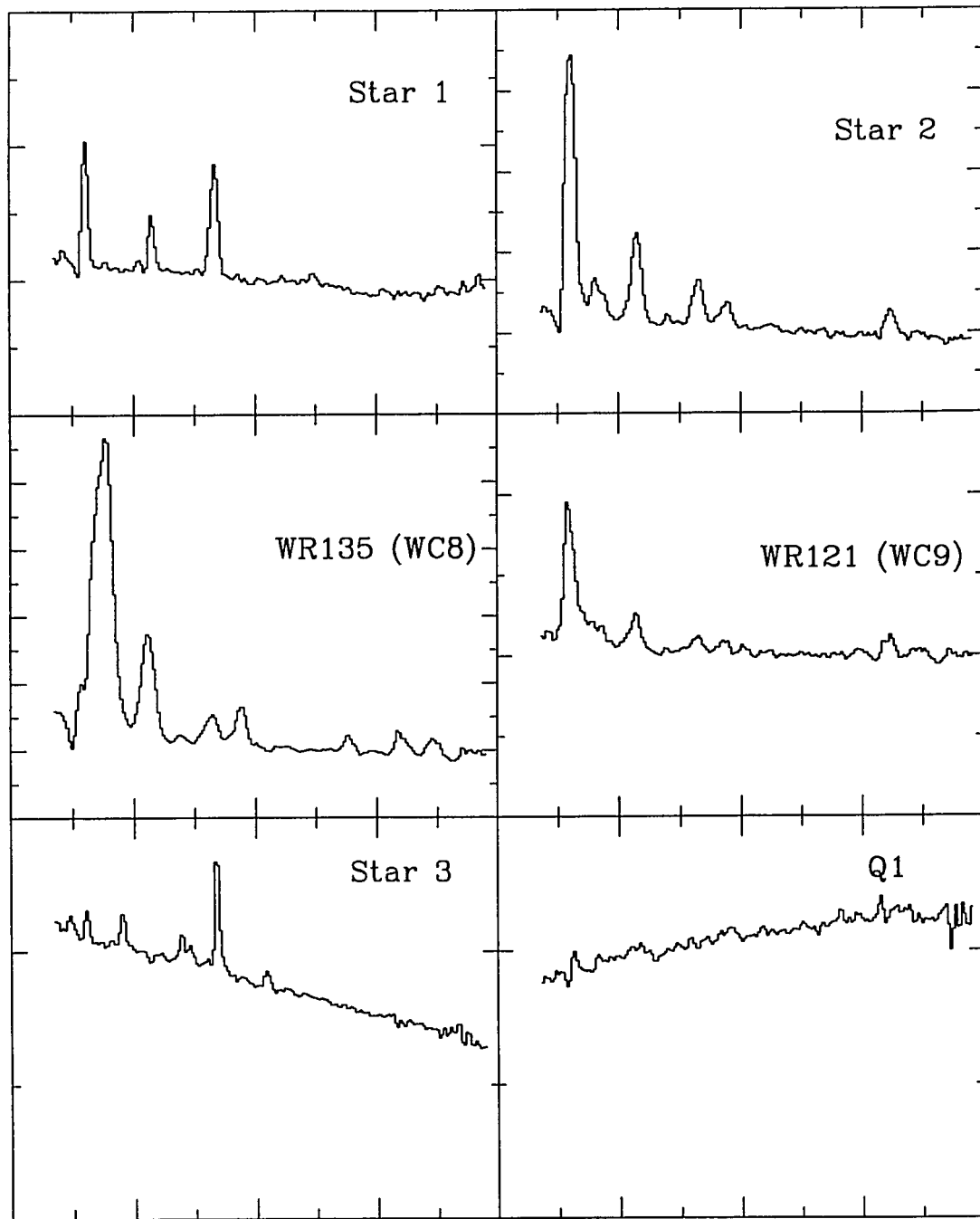


Figure 45a. Spectra for new Quintuplet emission-line stars, WC template stars, and Q1.

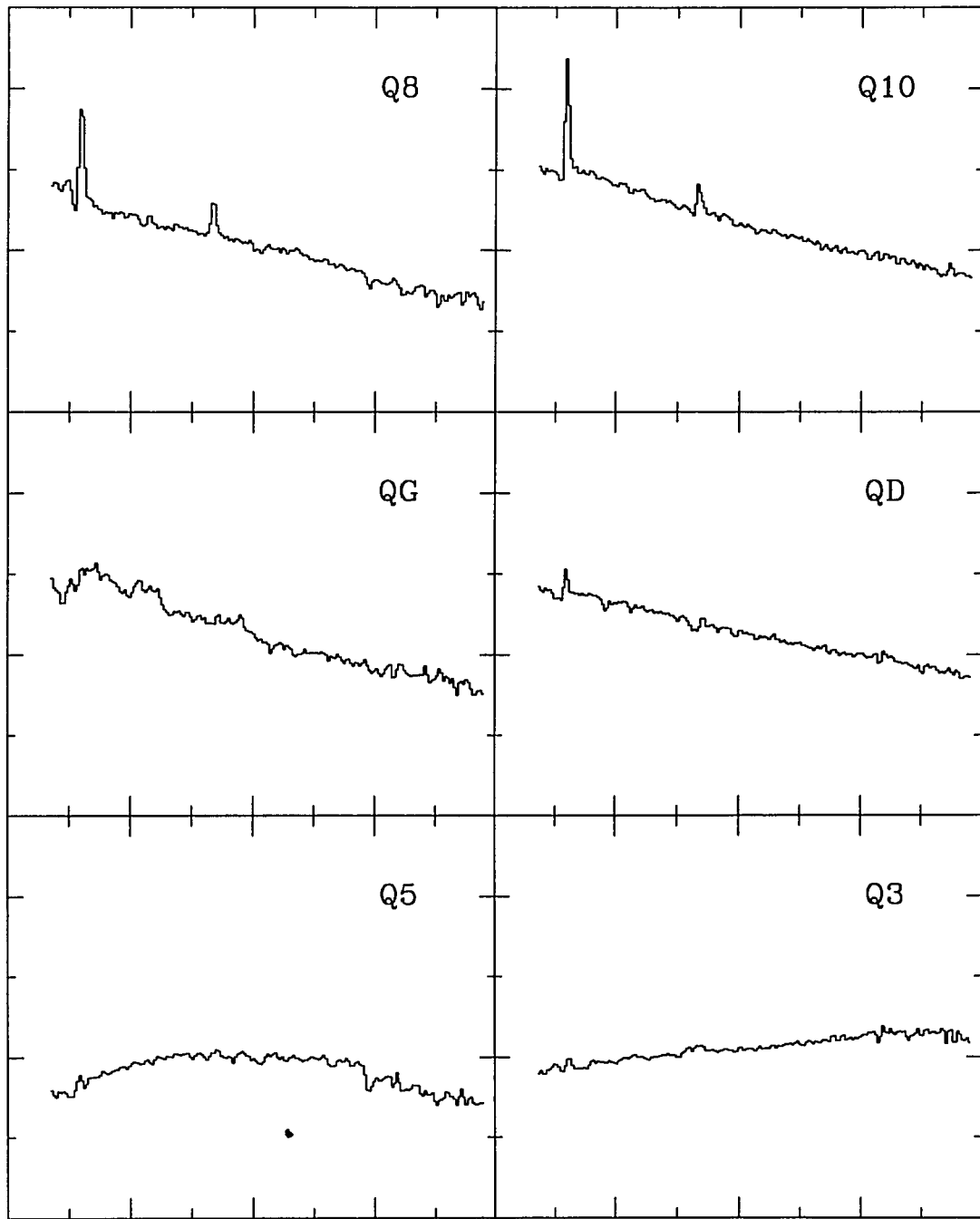


Figure 45b. Spectra for previously known Quintuplet stars: Q8, Q10, QG, QD, Q5, Q3.

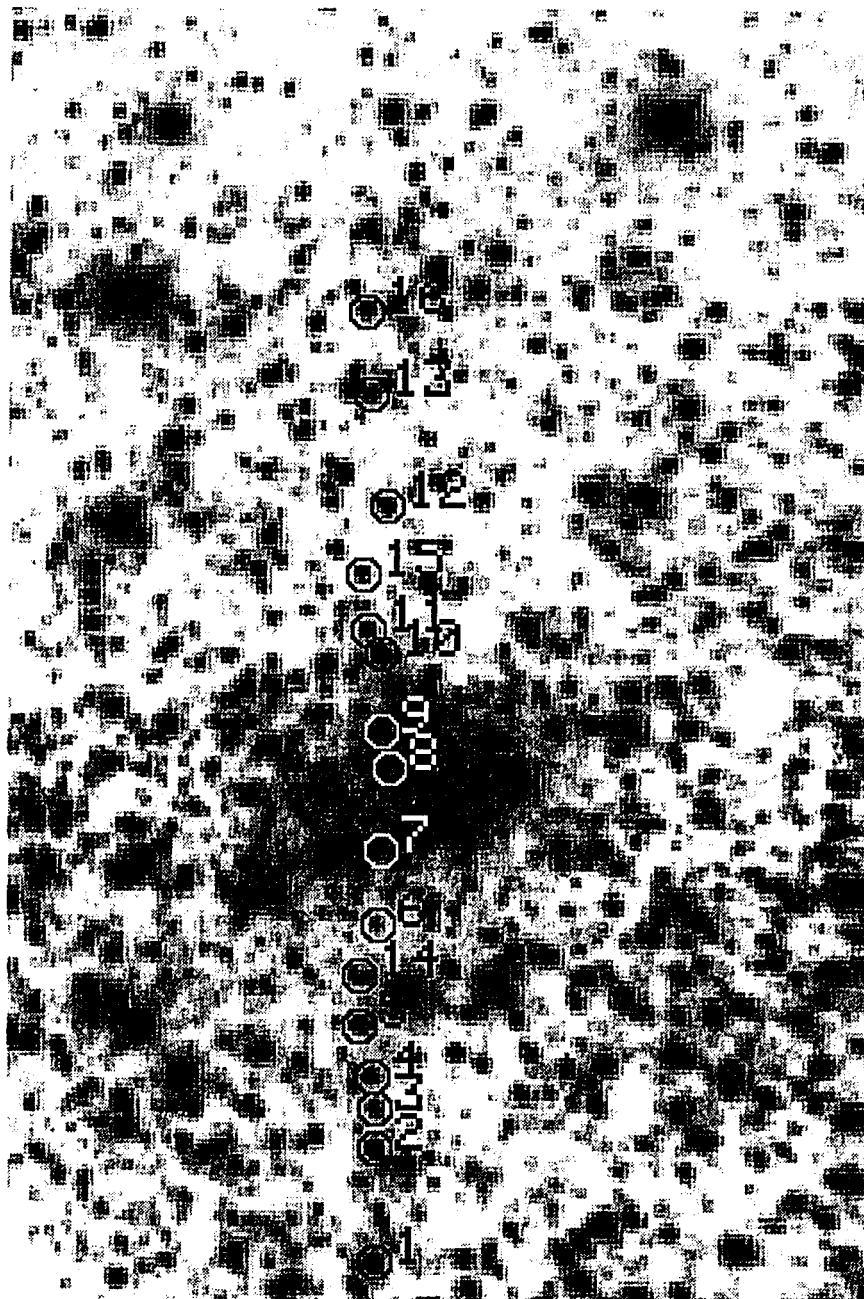


Figure 45c. Identifying K' image for stars in the Quintuplet.

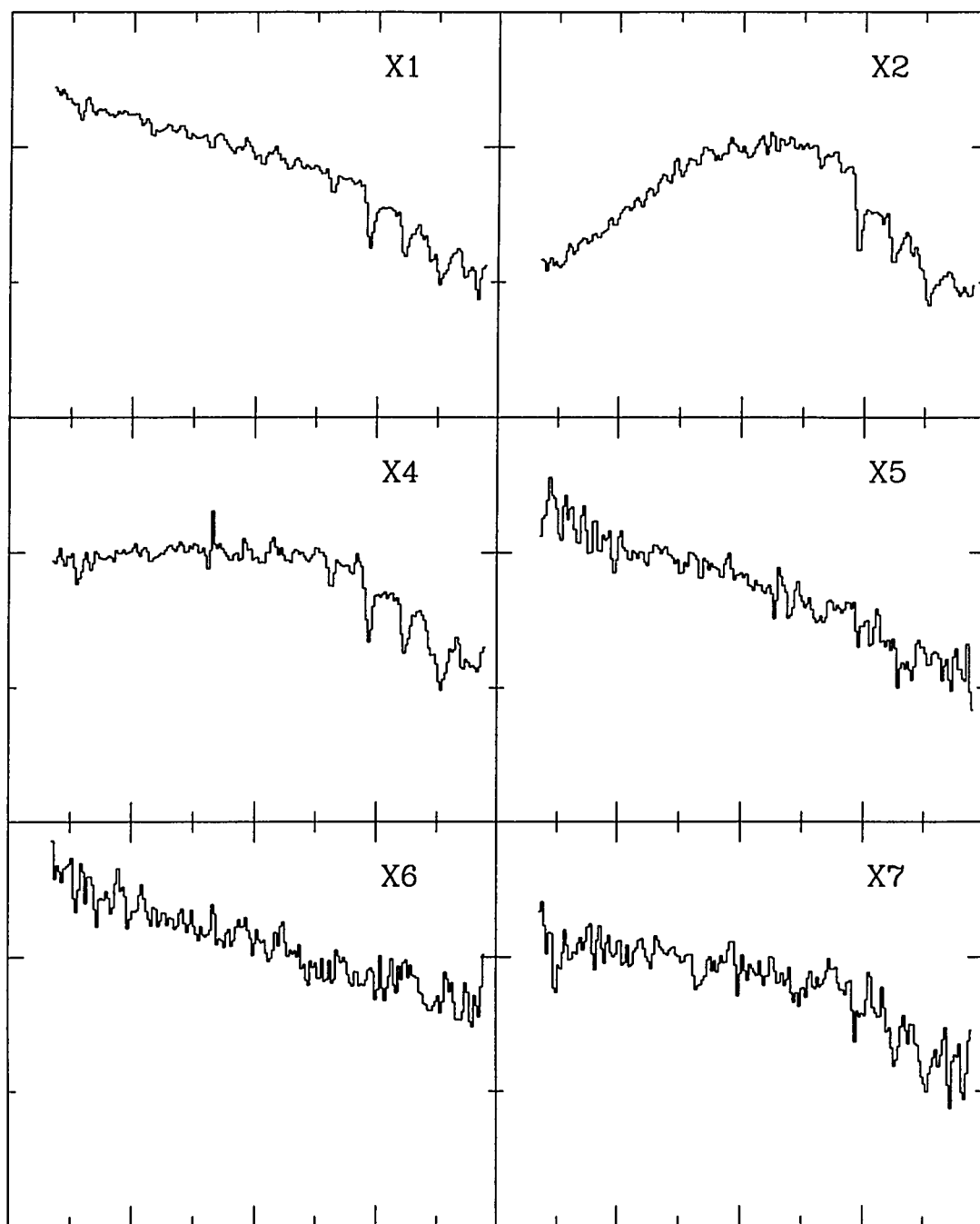


Figure 45d. Spectra for serendipitous Quintuplet stars: X1, X2, X4, X5, X6, X7.

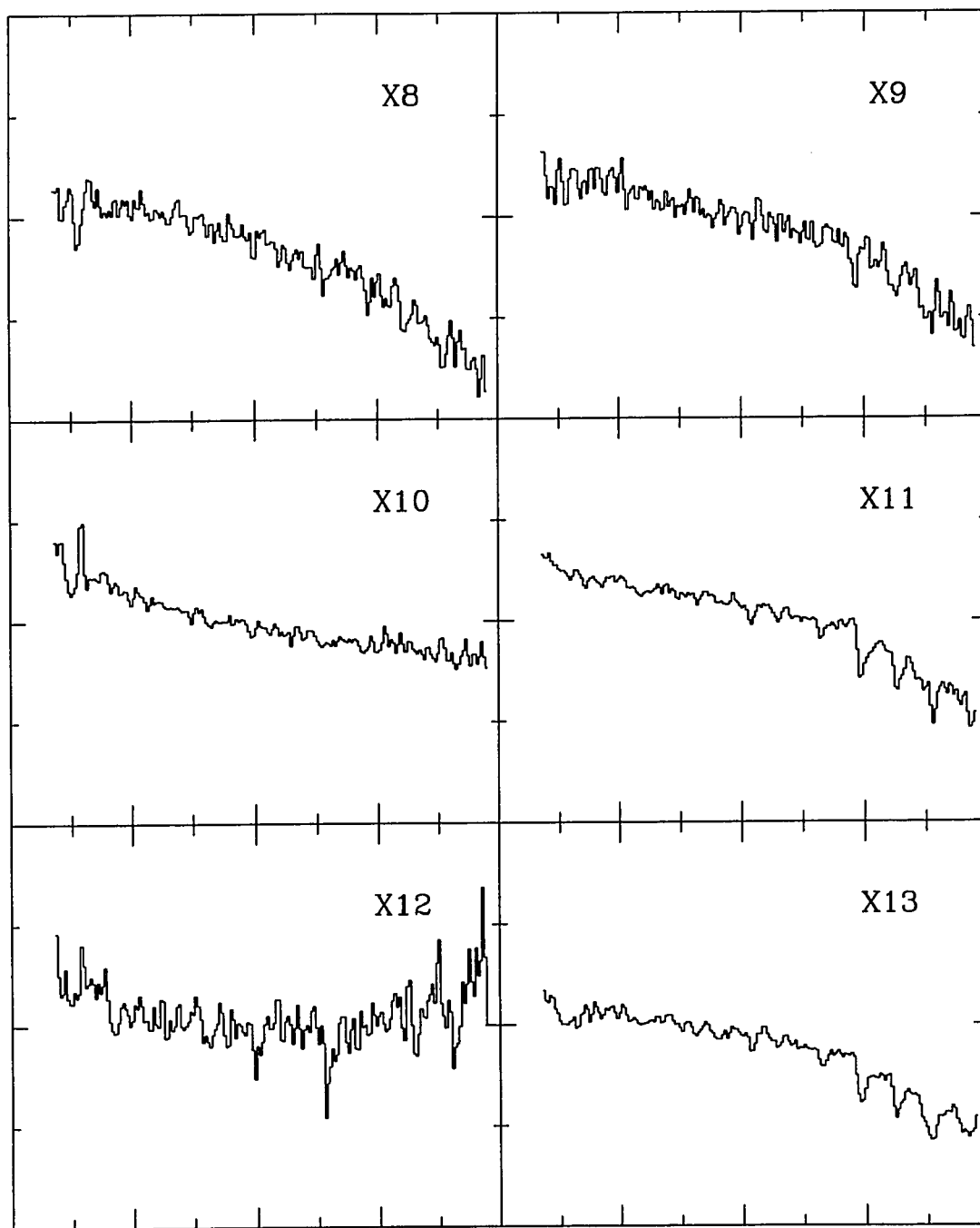


Figure 45e. Spectra for serendipitous Quintuplet stars: X8, X9, X10, X11, X12, X13.

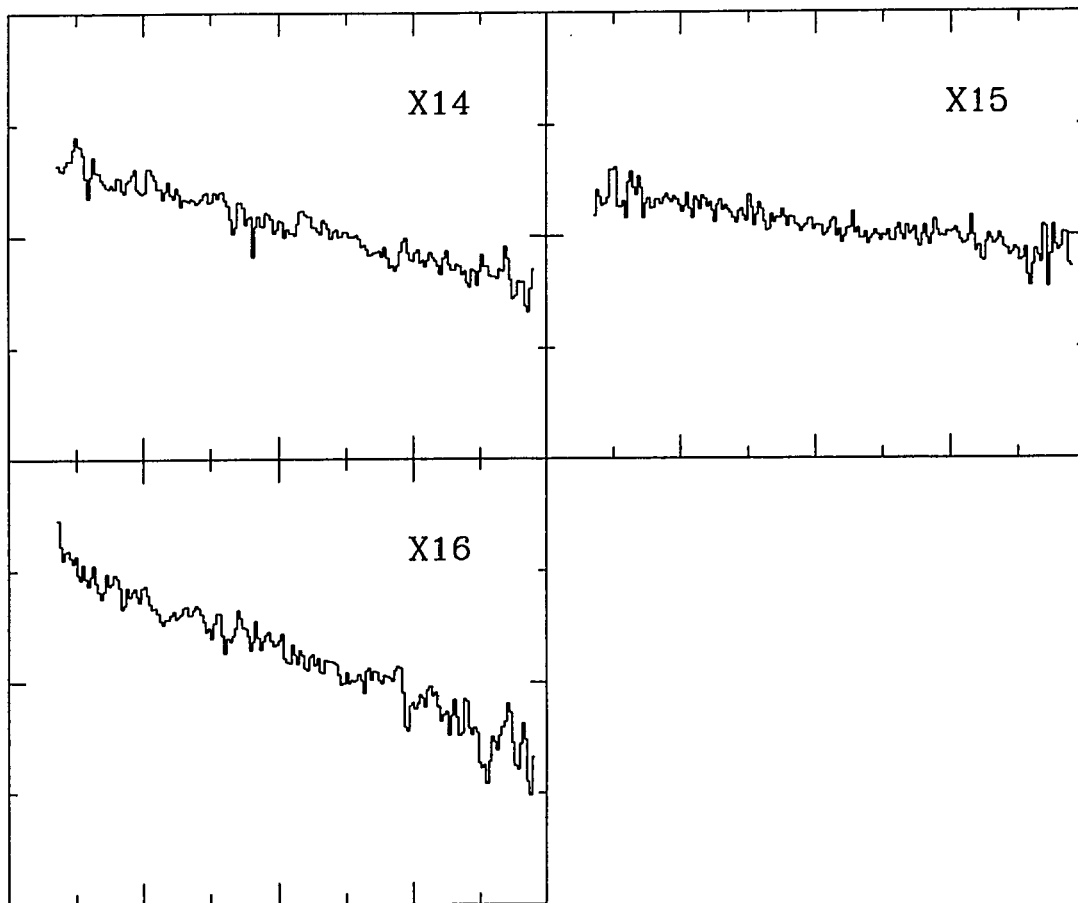


Figure 45f. Spectra for serendipitous Quintuplet stars: X14, X15, X16.

Figure 46a contains spectra for four stars near the HII region at G0.012+0.039 (H3 according to Yusef-Zadeh & Morris 1987b). Only H3D is within the Br γ emission in this region while the other stars are further to the south and happened to fall within the slit. H3N is an extracted spectrum of the nebular regions are evidenced by the Br γ emission line; although some contribution from a late-type star is evident in the CO absorption band heads and the generally declining slope.

Figure 46b shows spectra for stars near G-0.010+0.015 (H1), G-0.015+0.027 (H2), and G0.041+0.020 (H5W). H1C is a new star which is $\sim 1''$ south of H1A (Figer et al. 1994). The proximity to H1A makes the aperture extraction very difficult, but the spectrum does have a continuum slope consistent with a star. The spectrum appears to be relatively featureless at this resolution and S/N; a firm spectral classification will await higher resolution and S/N. H1A has deep CO absorption and $K \sim 10.6$ giving $L \sim 10^{3.6} L_{\odot}$ assuming $BC_K \sim 2.8$ for a late-type star (Elias et al. 1985); this places the star amongst the red giants.

H1N was extracted from the nebular regions surrounding H1; it shows a typical emission-line spectrum with lines of Br γ and, perhaps, HeI.

H2B appears to be a hot star with narrow emission lines. The luminosity is $\sim 10^{6.1} L_{\odot}$ assuming $A_K = 3.0$, $K = 9.1$, and $BC_K = -2.0$ (Figer et al. 1994). This luminosity is too large compared to the inferred ionizing rate from the HII region, $N_{\text{Lyc}} = 10^{48.6}$ photons s^{-1} , according to the values from Panagia (1973). The bolometric correction is probably not much less than the adopted value because the continuum slope is declining for longer wavelengths even though the spectrum was dereddened assuming $A_K = 3.0$, somewhat less than the derived value of 3.3. In any case, this star is likely to be an O or B supergiant which has not yet entered the Wolf-Rayet phase.

H5WN is a pure emission-line spectrum where the continuum is probably due to heated dust. In fact, the image from Figer et al. (1994) shows considerable flux in the K-band which cannot be attributed to the Br γ line emission. H5WA is the star just north of H5W, and it shows a relatively flat continuum spectrum. A certain spectral classification will await higher S/N data.

Figure 46c shows spectra for two stars which happened to fall within the slit, H5EA and H5EB, while obtaining spectra for H5EC and H5ED. H5EC is probably a composite of nebular emission and heated dust while H5ED is a spectrum of the star $\sim 6''$ to the north of H5EC. H6 is a pure emission-line spectrum of the nebular region G0.046+0.022.

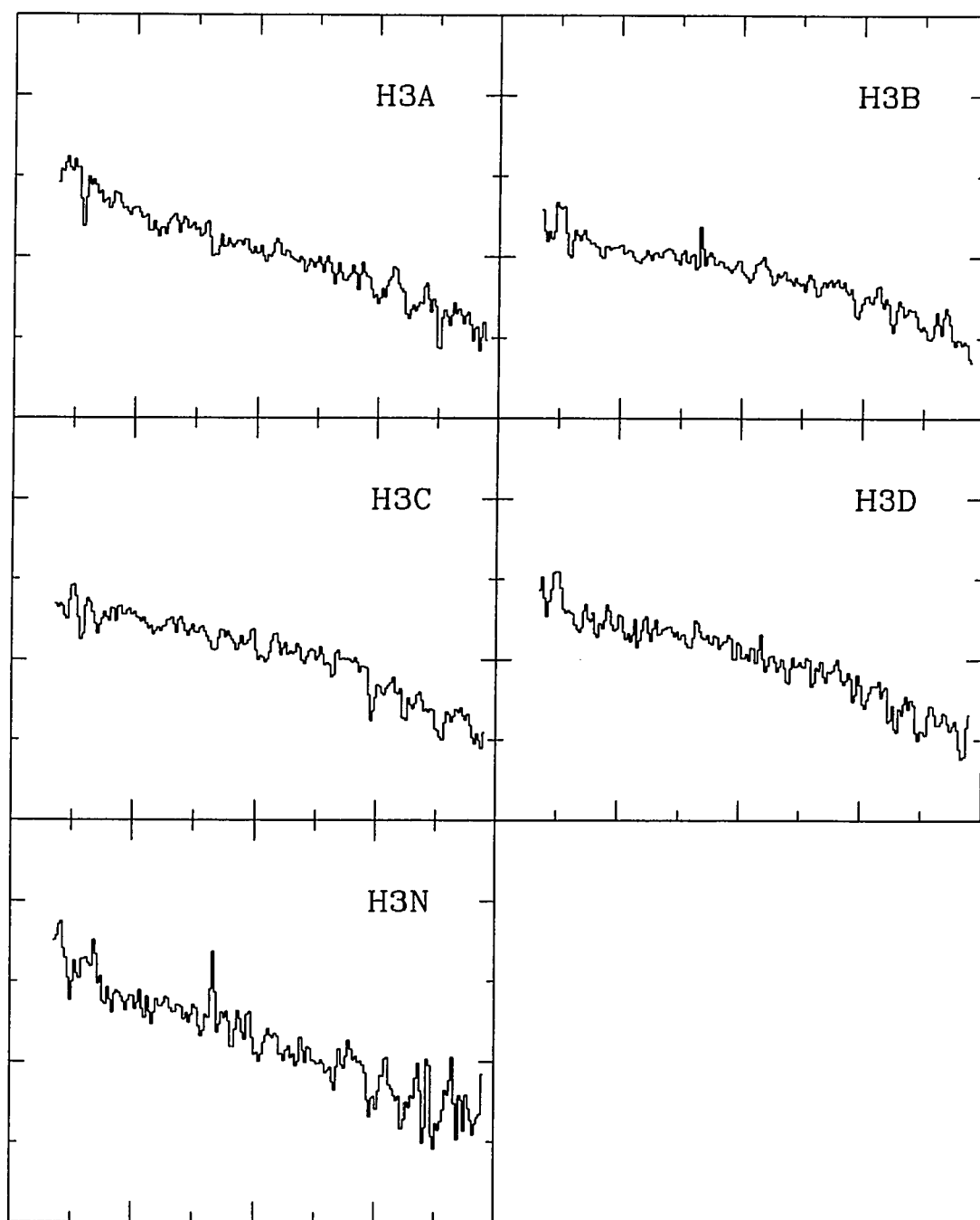


Figure 46a. Spectra for stars near H3: H3A, H3B, H3C, H3D, H3N.

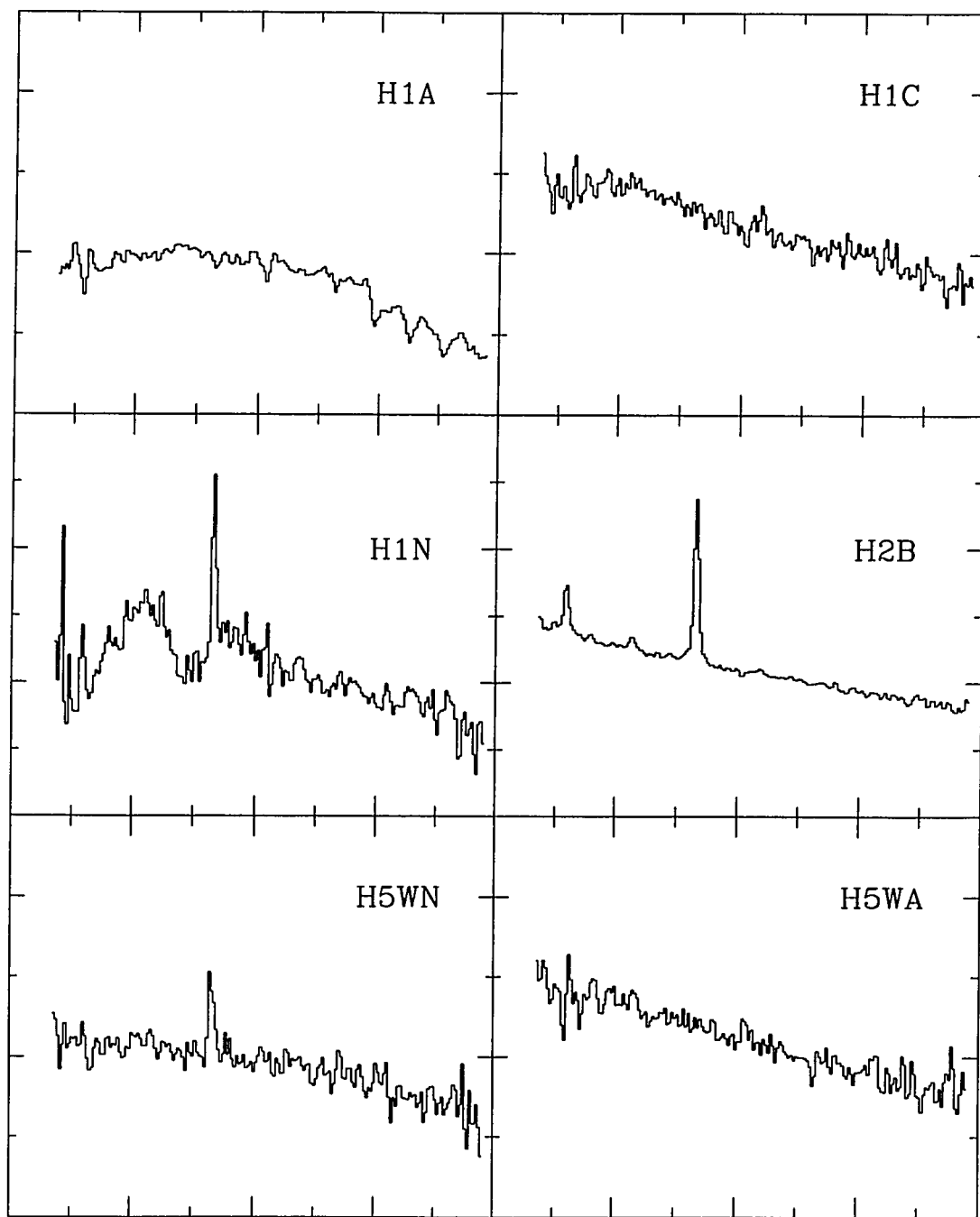


Figure 46b. Spectra for stars near H1, H2, H5W: H1A, H1C, H1N, H2B, H5WN, H5WA.

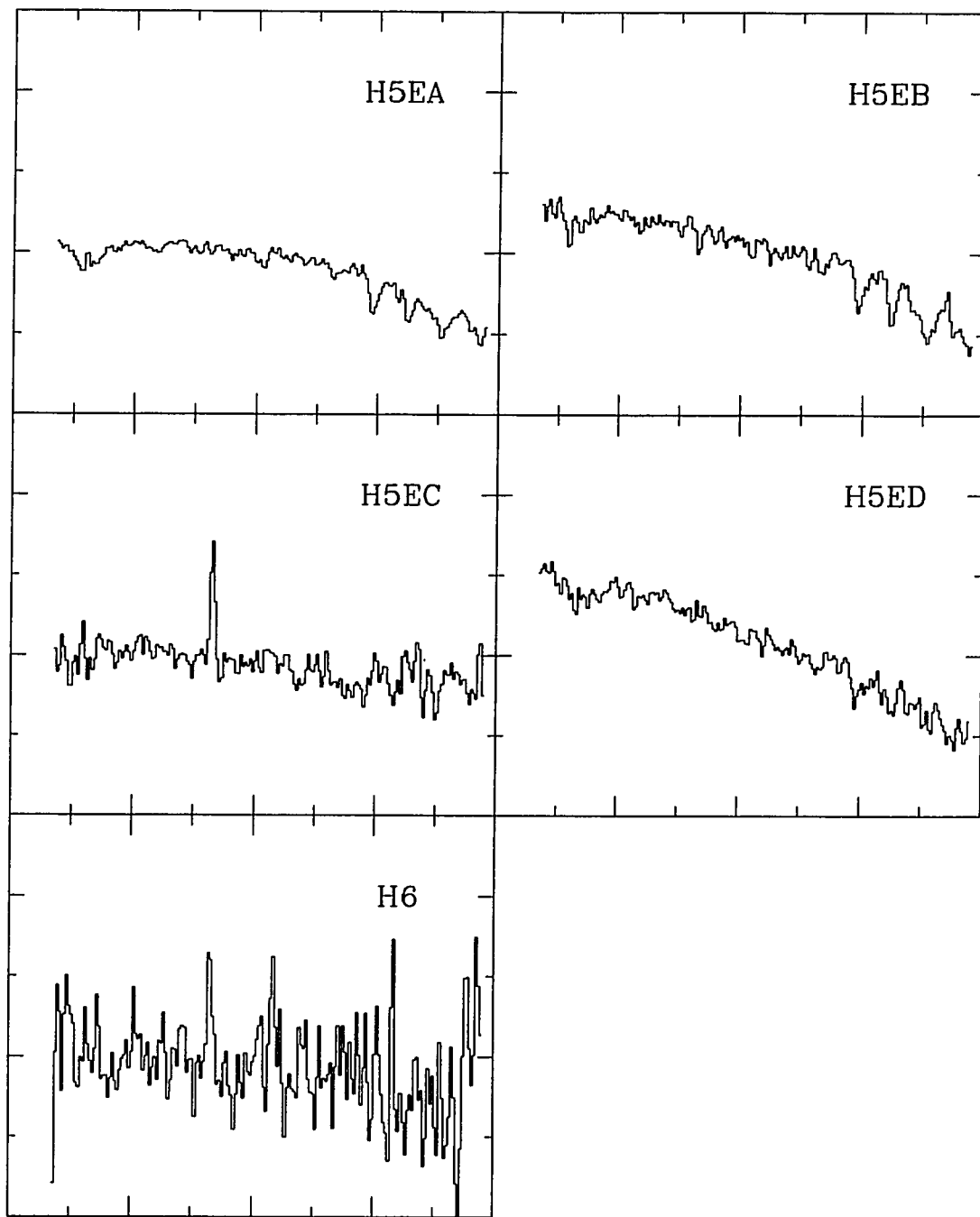


Figure 46c. Spectra for stars near H5 and H6: H5EA, H5EB, H5EC, H5ED, H6.

Figure 47a and Figure 47b show spectra for suspected Br γ stars near H1 and H2 originally imaged in frame 364 and h11. All of these stars have very red colors in H-K, and their spectra exhibit the classical hump in the K-band indicative of water absorption. These stars are probably very late-type giants, i.e. M8III or later.

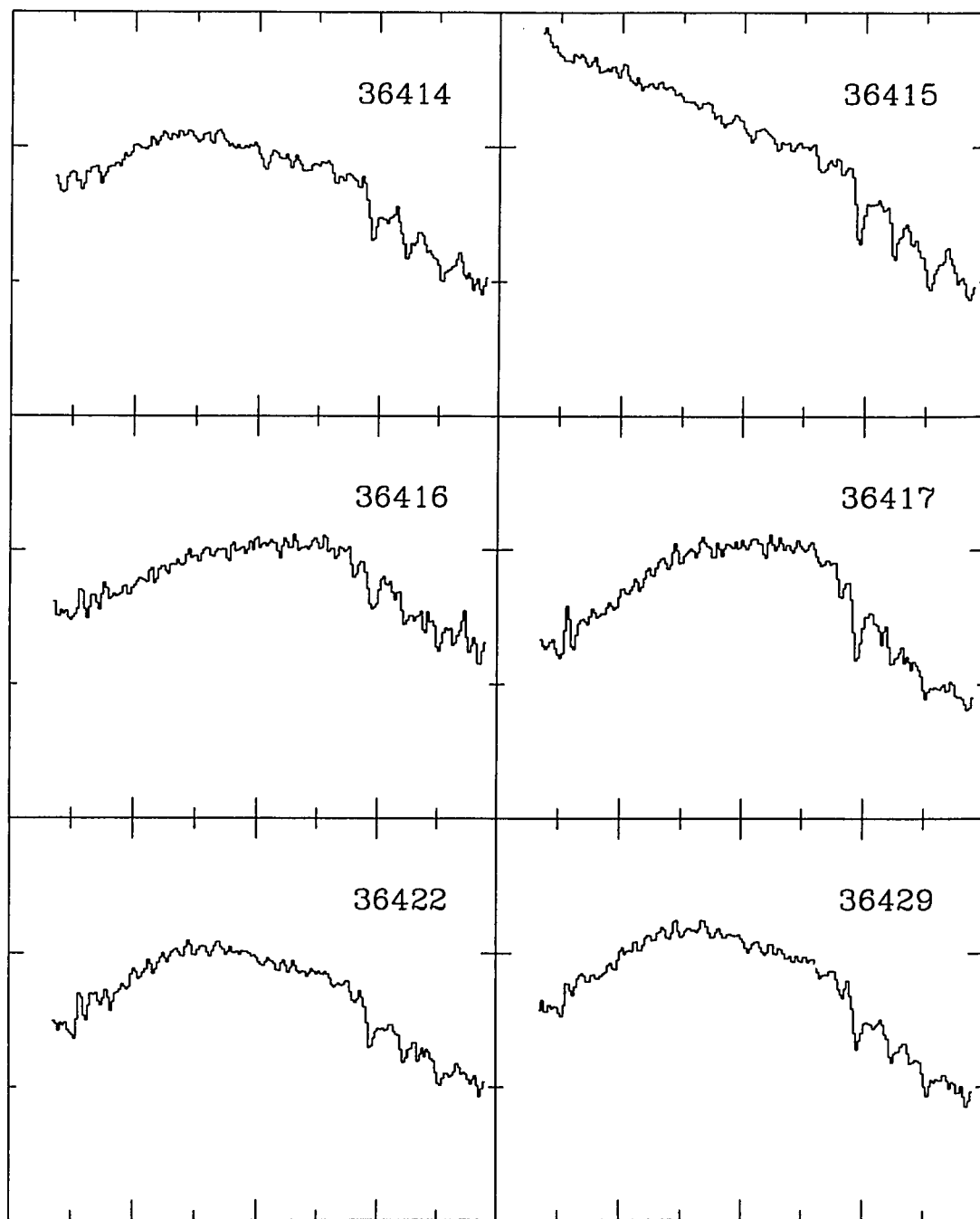


Figure 47a. Spectra for stars in frame 364: 36614, 36415, 36416, 36417, 36422, 36429.

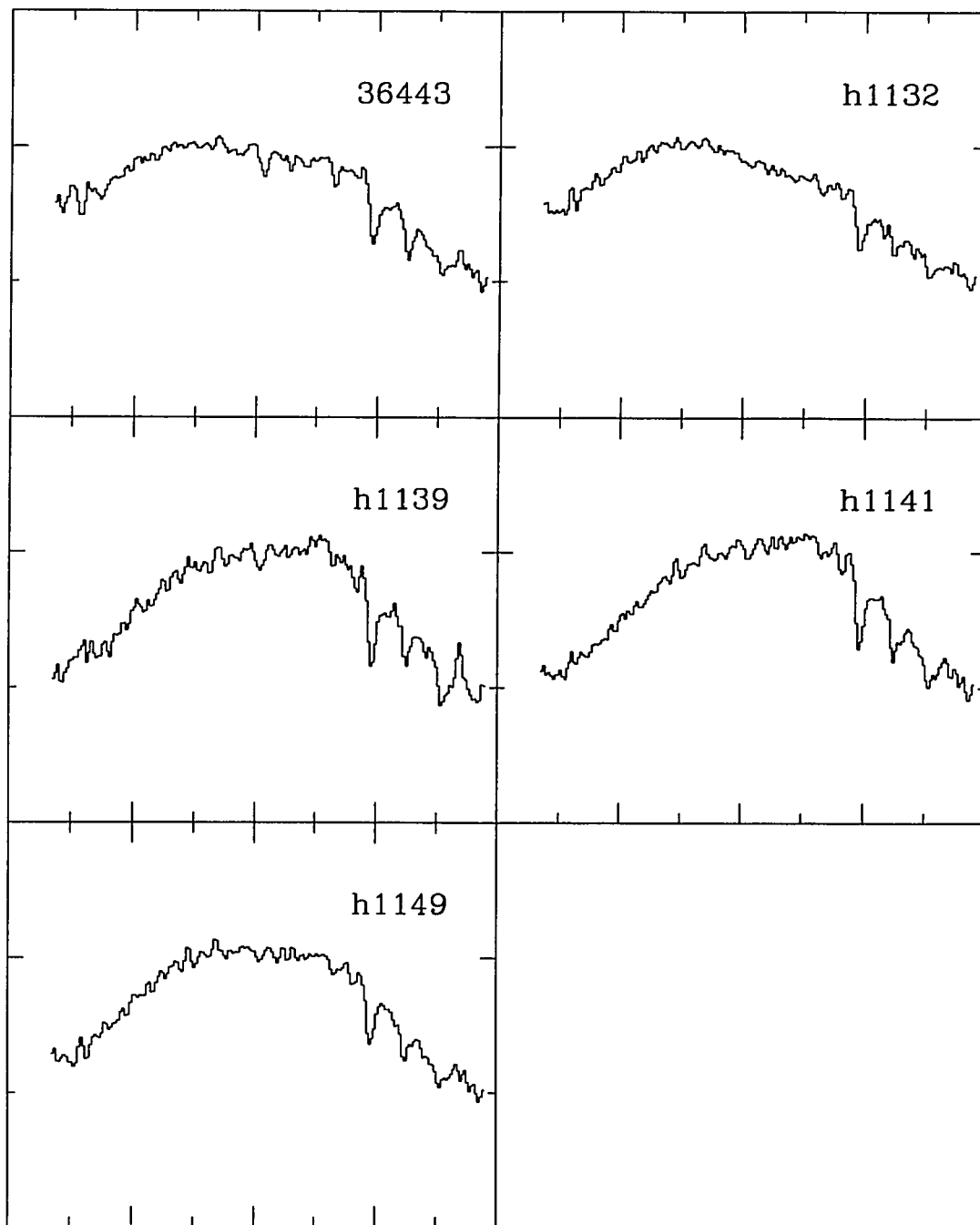


Figure 47b. Spectra for stars in frame 364 and h11: 36443, h1132, h1139, h1141, h1149.

Figure 48a shows emission-line spectra for the nebular regions to the west of Sgr A and spectra of some target stars. The nebular regions show pure emission-line spectra with Br γ and HeI emission. The stellar spectra are dominated by water absorption and indicate that the stars are very late-type giants.

Figure 48b shows spectra for stars in the immediate frame east, A11, and southwest, 371, of the Galactic Center. These stars are probably red giants with slightly different amounts of water absorption. All have very red colors in H-K consistent with their locations in heavily extinction regions of the survey; except for A1133B which is a foreground star having $H-K = 0.42$.

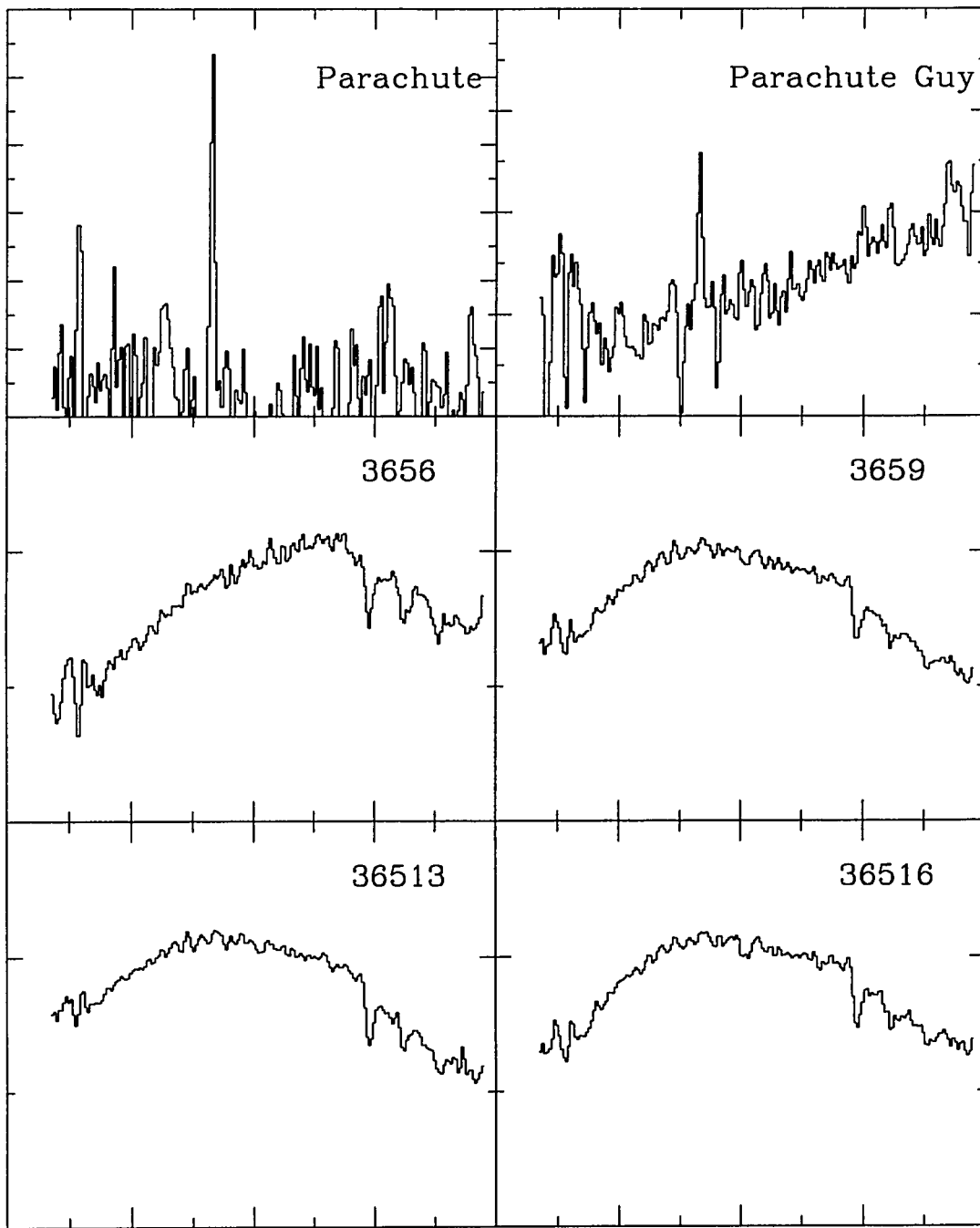


Figure 48a. Spectra for stars near the "Parachute": nebular region, 3656, 3659, 36513, 36516.

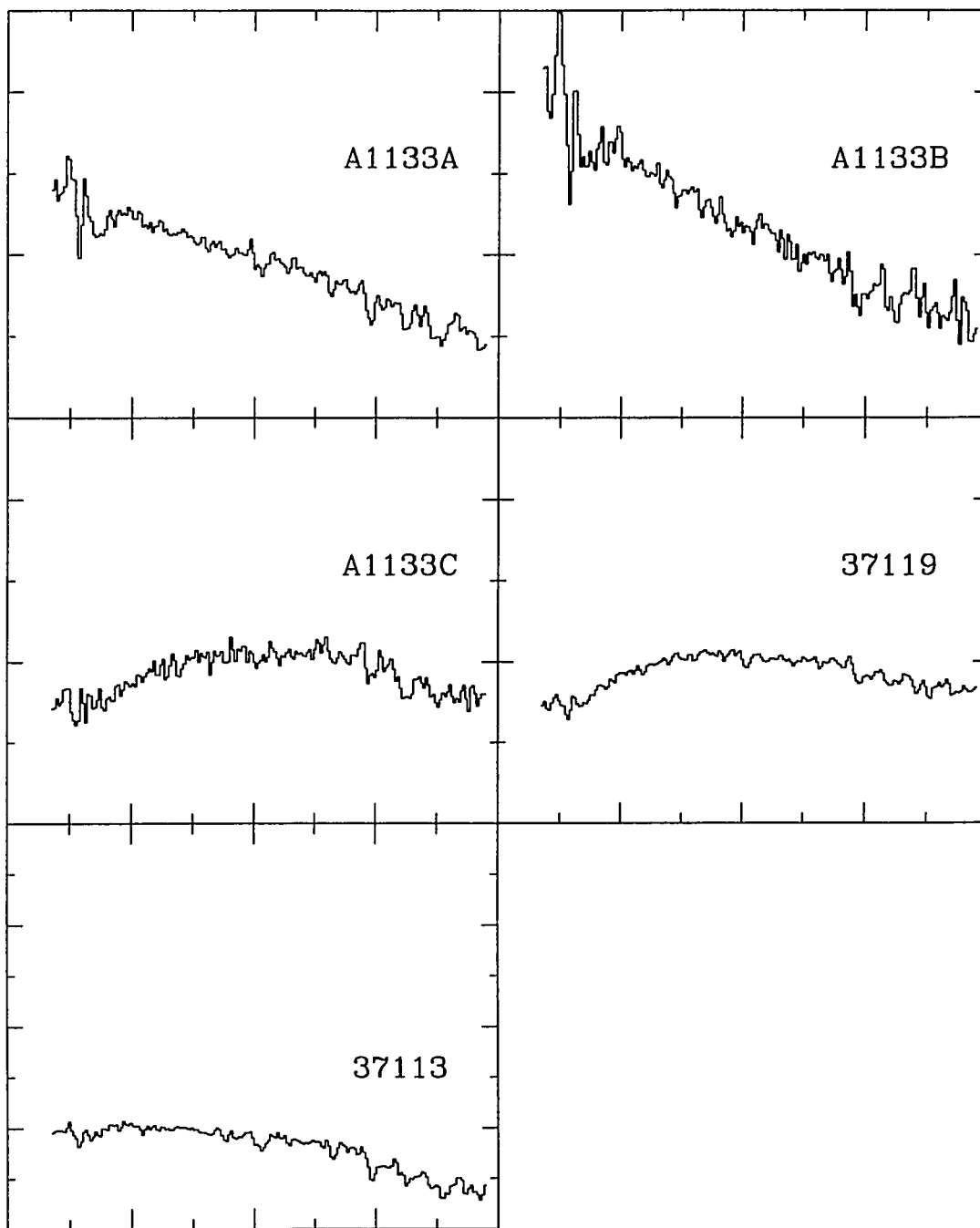


Figure 48b. Spectra for stars in frames A11 and 371: A1133A, A1133B, A1133C, 37119, 37113.

Figure 49a shows spectra for some very bright water-absorption stars within 4 pc of the Galactic Center; their locations with respect to the Galactic Center are shown in Figure 49b. The spectrum for 37345 was also shown in comparison to a late-type red giant in Figure 44. These stars are all quite red having implied luminosities in the range 10^4 to $10^5 L_{\odot}$ assuming $DM = 14.65$, $A_K = 3$, and $BC_K = 2.8$ (Levine et al. 1995). The extinction is probably a lower limit as these stars have very red colors in H-K. It is difficult to estimate the color excess for such stars because their intrinsic colors are quite uncertain.

Haller (1992) has observed three of these stars (37345 = 520, 37321 = 527, 37336 = 534) where his designations are given in parenthesis. He notes that these stars are all long period variables with amplitudes at least as large as 0.5 to 1.2 magnitudes at K. In fact, our photometry for 37336 is about 1 magnitude brighter than Haller's value. The same is true for 37321, but its photometry is likely to be contaminated by a nearby star causing our aperture photometry to differ with his PSF fitting photometry.

These stars were probably born in a burst of star-formation 10^7 to 10^8 years ago along with many other bright red stars seen in Figure 49b and observed by Haller (1992); although the long-period variables observed by Haller are probably much older.

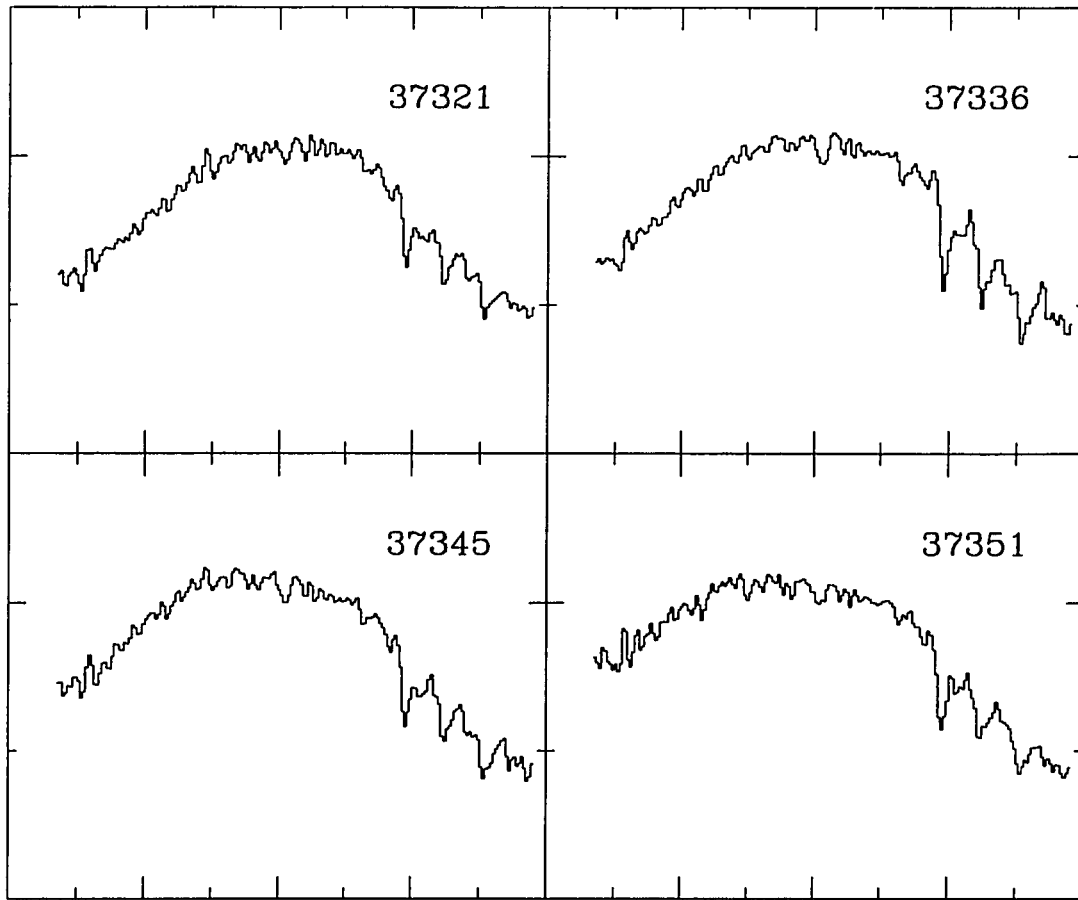


Figure 49a. Spectra for water-absorption stars within 4 pc of the GC: 37321, 37336, 37345, 37351.

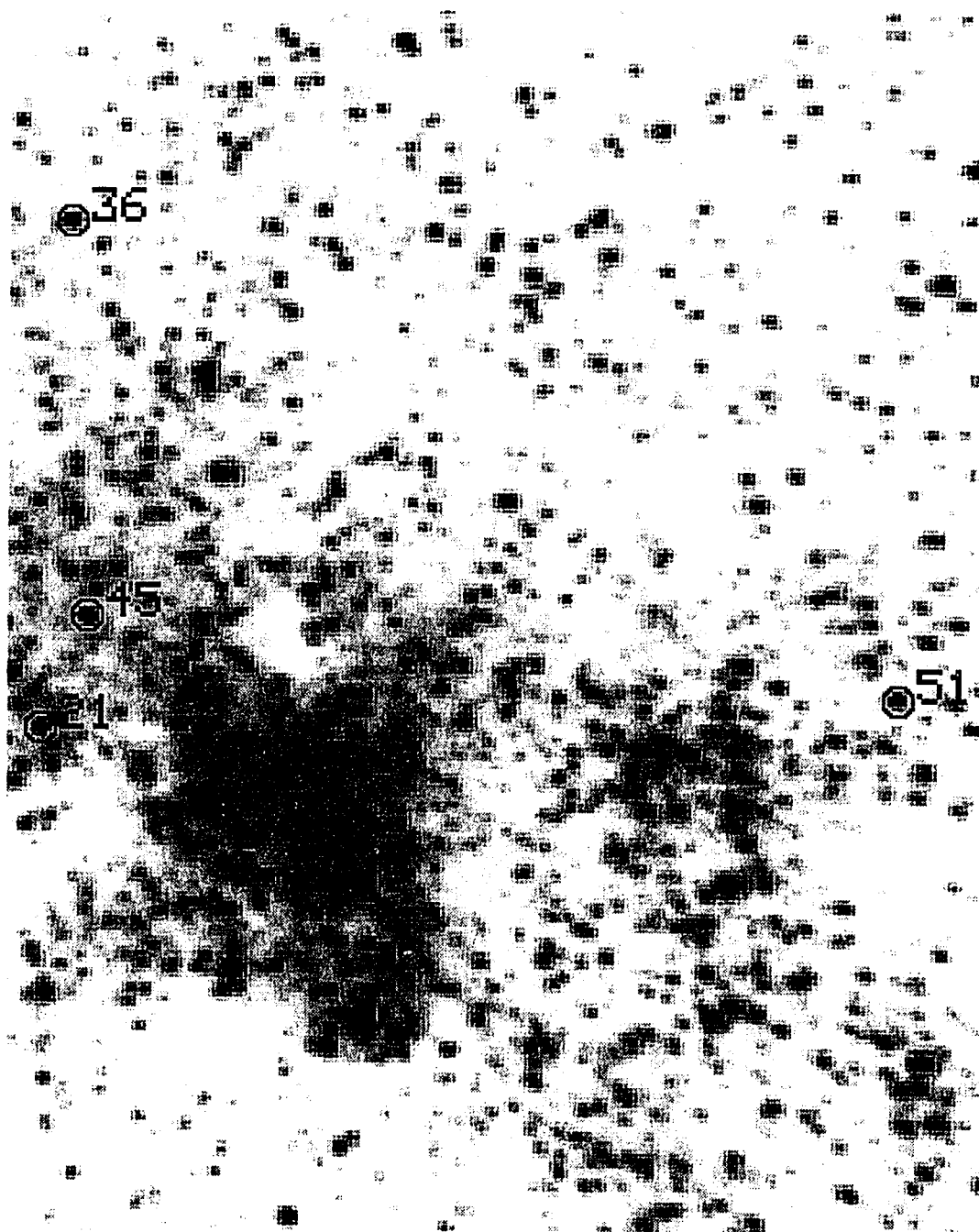


Figure 49b. Identifying K' image for water-absorption stars near the Galactic Center.

Figure 50 shows spectra for stars in the frame containing G-0.14-0.09. These stars are typical water-absorption giants or supergiants. Their colors in H-K are very red. Assuming that $A_K = 1.8E_{H-K}$, we can calculate $A_K \sim 8$ for the reddest star in this figure, 39217; this gives a luminosity of $\sim 10^5 L_\odot$ assuming $BC_K = 2.8$. The dereddened spectrum would be straight and declining toward longer wavelengths if $A_K \sim 8$ was used.

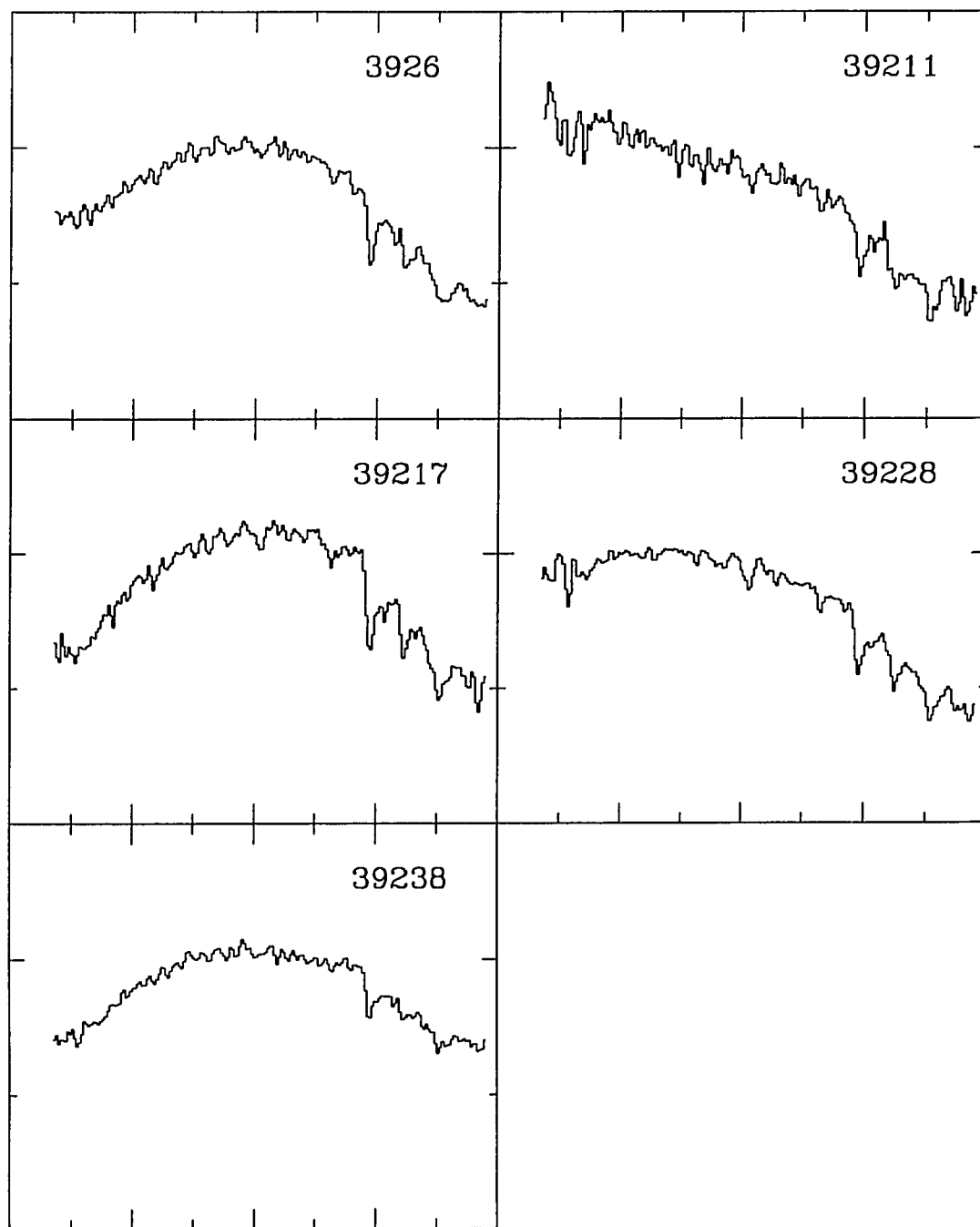


Figure 50. Spectra for water-absorption stars near G-0.14-0.09: 3926, 39211, 39217, 39228, and 39238.

The next four figures contain spectra for stars in the central cluster of the Galaxy. Only three stars were specifically targeted for phase II observations; these stars were chosen because their spectra have been published by many authors. Their spectra then serve as a check for our spectroscopy. Of course, in the crowded inner parsec region, many stars will fall within the slit, most hopelessly confused with their neighbors. Some of the stars were separated well enough so that their spectra could also be extracted.

Some of the stars were observed twice. For instance, while targeting IRS15NE, we were able to obtain spectra for IRS14NE/SW, IRS16C/SW, IRS8, a maser star north of the Galactic Center (IM), and 5 previously unnamed stars which we call IA, IB, IC, ID, and IE. Separately, while targeting IRS7, we were able to obtain spectra for IRS14NE, IRS15NE, IRS16NW, IRS20, IRS33, and 4 previously unnamed stars which we call IF, IG, IH, IJ. The unnamed stars can be located in Figure 51e.

Figure 51a contains spectra for 3 previously known emission-line stars, AF, IRS15NE, and IRS16C/SW. The spectra for AF and IRS16C/SW are consistent with published spectra (cf. Blum et al. 1995a and references therein). Curiously, the spectrum for IRS15NE does not have very strong emission in HeI or Br γ as shown in Geballe et al. (1994); in addition, it has CO absorption. AFN was extracted from the western extreme of the Sgr A "mini-spiral" inbetween IRS6E and IRS6W. The continuum can be fit by a 1200 K black-body. IRS14NE/SW appears to be a rather unremarkable late-type star showing some CO absorption; the apparent Br γ absorption line is probably due to poor background subtraction. IRS8 has a relatively flat spectrum which can also be fit by a 1200 K black-body. There might be some line emission at Br γ and HeI, but it was very difficult to extract a good background for this

star as it sits amidst diffuse Br γ emission. It is not clear whether the Br γ emission is due to this star or due to the intense UV field from the central cluster of hot stars. The dust temperature argues for a local heating source. This source is quite similar to the very red featureless Quintuplet sources with featureless spectra. Perhaps IRS8 is also an enshrouded protostar.

Figure 51b shows spectra for some of the previously unnamed stars. Most of these stars are late-type as can be seen by the deep CO absorption band-heads. The apparent HeI emission line in ID is probably due to improper atmospheric correction; although this star should be targeted for further observation. IM is one of the OH/IR stars discussed by Winnberg et al. (1985). It shows the characteristic water-absorption seen in the maser counterpart star, 37345.

Figure 51c shows spectra for two new emission-line stars, IRS20 and IRS33, as well as IRS14NE and IRS7. The two new stars differ from many of the other Galactic Center emission-line stars because Br γ is so much stronger than the HeI line. This might be due to improper background subtraction because these stars are situated within the diffuse Br γ emitting gas. There appear to be several other spectral features in the spectra for both stars, but the S/N is too low. For instance, the feature near 2.2166 μ m in IRS33 could be due to [FeIII] as has been previously seen in the ionized gas (Allen et al. 1990; Lutz et al. 1994). This suggests that all the emission features might be due to background contamination, but the lack of CO absorption indicates that, at least, IRS33 is not a late-type star. Additionally, Eckart et al. (1995) show a HeI line-minus-continuum image in which IRS33 appears prominently.

Figure 51d contains spectra for the remainder of the previously unnamed stars. These all appear to be late-type stars. We failed to detect emission lines in IRS15NE and IRS16NW where the peak near $2.35\text{ }\mu\text{m}$ in the latter is spurious.

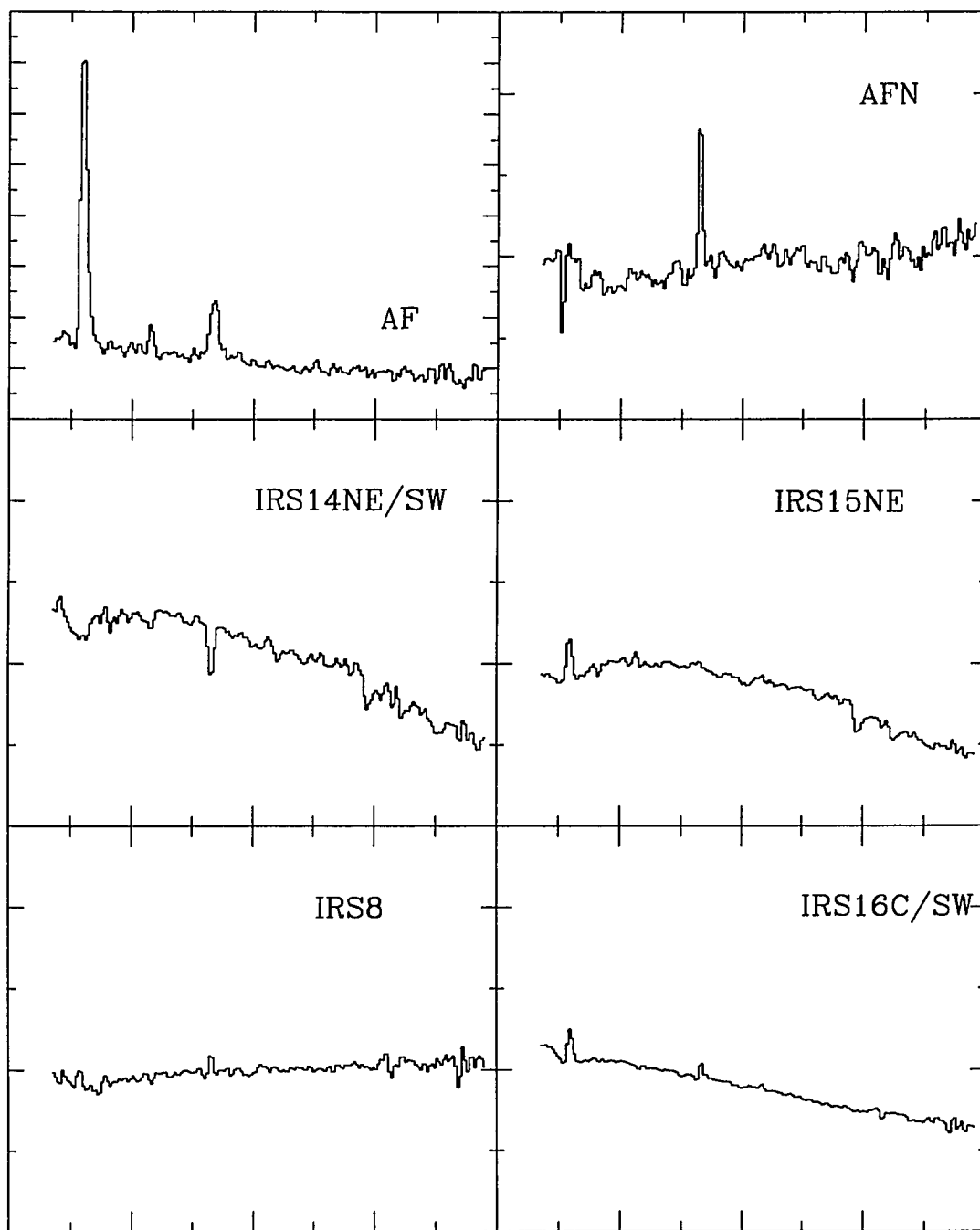


Figure 51a. Spectra for Galactic Center objects: AF, AFN, IRS14NE/SW, IRS15NE, IRS8, IRS16C/SW.

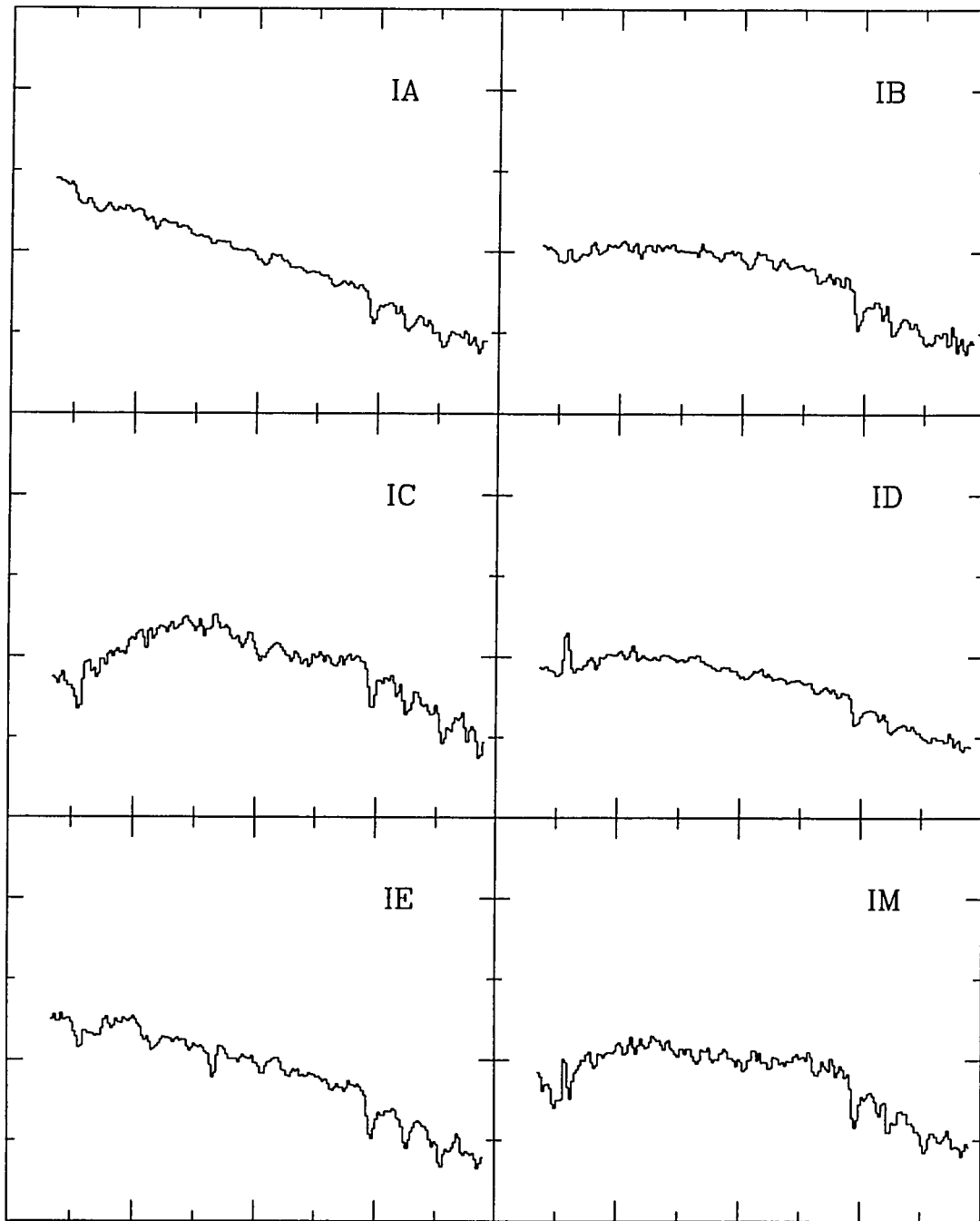


Figure 51b. Spectra for Galactic Center stars: IA, IB, IC, ID, IE, IM.

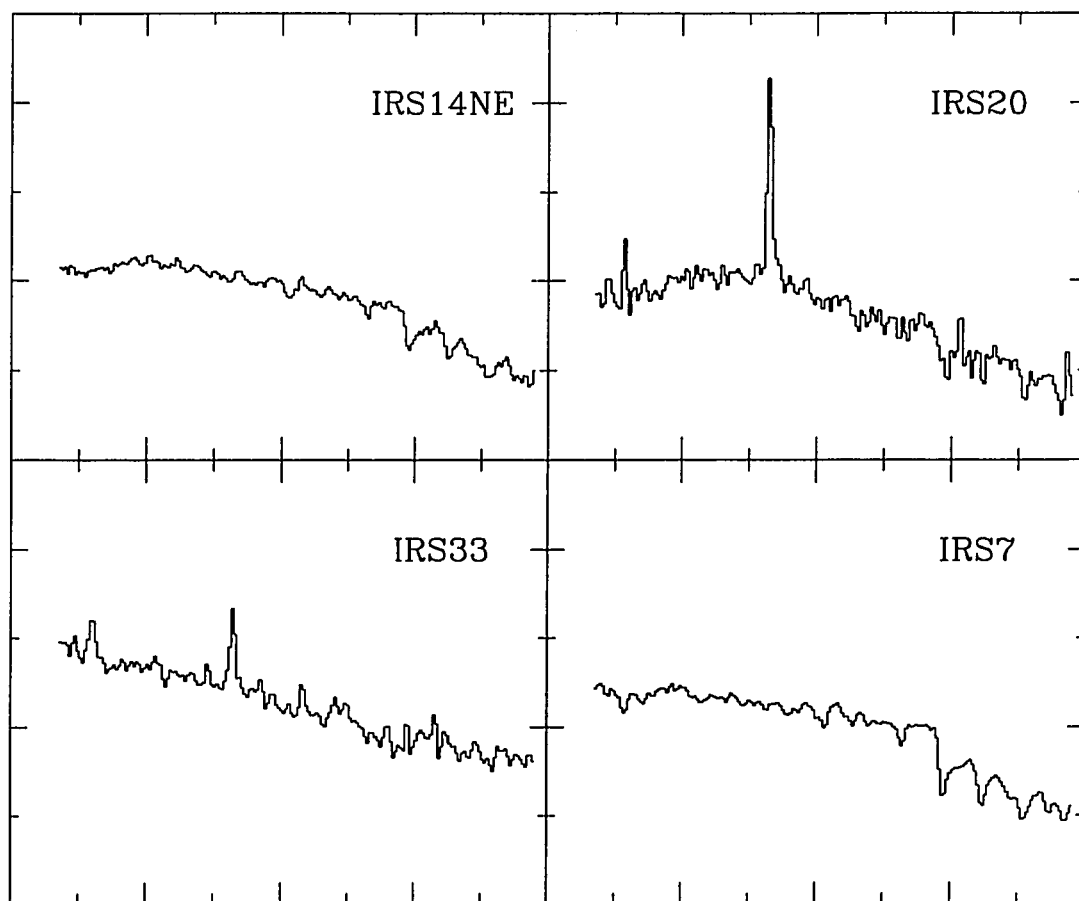


Figure 51c. Spectra for Galactic Center stars: IRS14NE, IRS20, IRS33, IRS7.

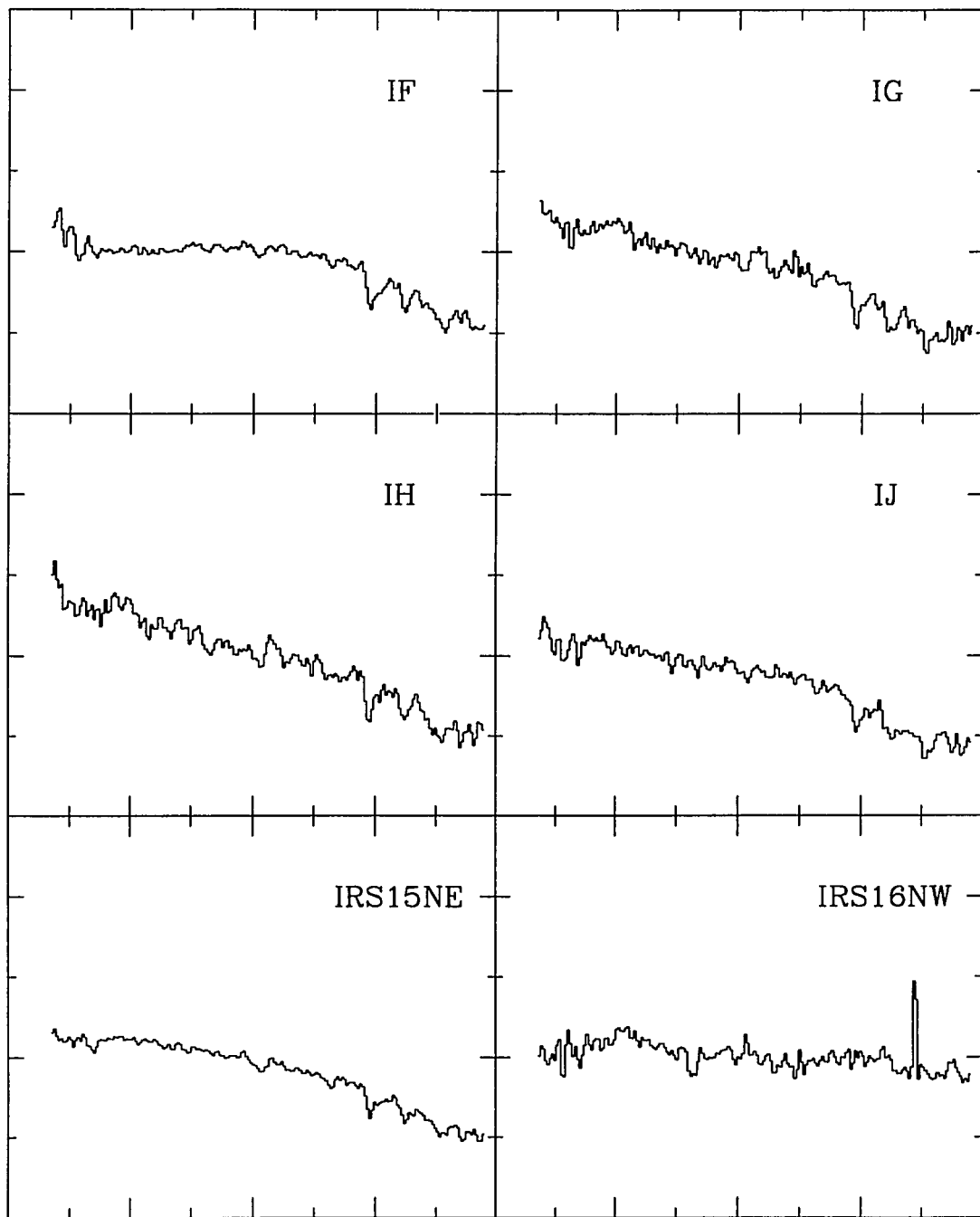


Figure 51d. Spectra for Galactic Center stars: IF, IG, IH, IJ, IRS15NE, IRS16NW.



Figure 51e. Identifying K' image for stars near the inner parsec.

Figure 52 contains spectra for 6 Galactic Wolf-Rayet stars (van der Hucht et al. 1988). Spectra for WR135 (WC8) and WR121 (WC9) star were shown in Figure 45a.

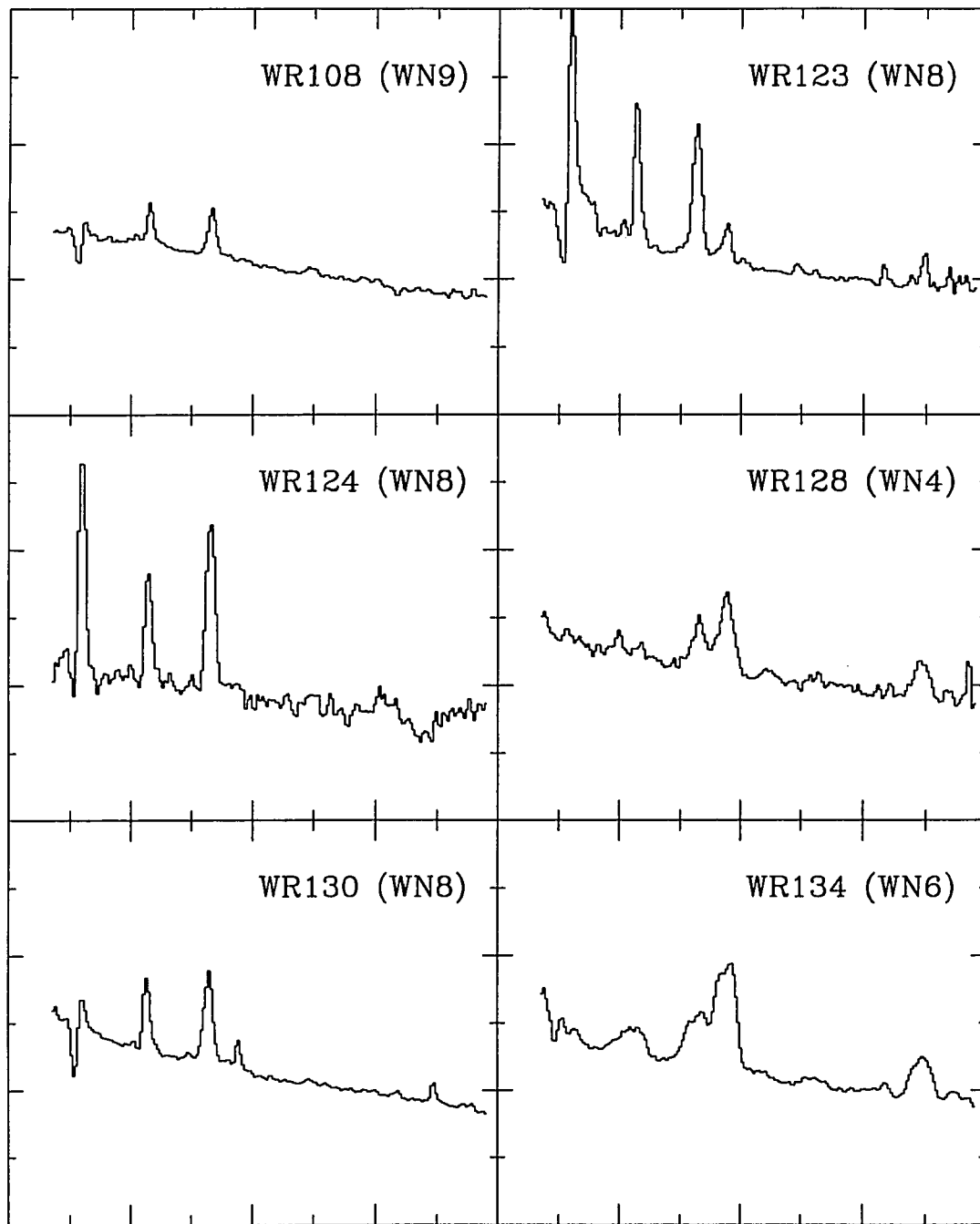


Figure 52. Spectra for Wolf-Rayet template stars: 108, 123, 124, 128, 130, 134.

VII. Analysis

The observations were very efficient, and the resulting data set can be probed to determine whether the emission-line objects are truly near the Galactic Center. In this chapter, I analyze the data to obtain an estimation of the large-scale extinction. This can be used to argue that the molecular clouds, and therefore the associated emission-line stars, are at the Galactic Center. Individual apparent colors for the emission-line stars are already consistent with a location at the Galactic Center, so the large-scale extinction will be used as confirming evidence.

All the emission-line stars exhibit an emission line near $2.166\ \mu\text{m}$ due primarily to Br γ . One exception is star 2, the new WC9 star. WC9 stars lack hydrogen, so the emission line near $2.166\ \mu\text{m}$ is thought to be from HeI and HeII. For the other emission-line stars, however, I have measured the shift in velocity of the Br γ line with respect to the expected vacuum wavelength. The same was also done for nebular regions when possible. In all cases, these velocities suggest a physical connection between the emission-line objects and nearby HII regions within the errors of the measurement. In fact, the Quintuplet stars are shown to have the same velocity as G0.15–0.05 (the "Pistol"), and this velocity is consistent with the whole group of objects participating in the space motion of stars near the Galactic Center.

A. Extinction from stellar data

The extinction in the survey area is quite patchy, as can be seen in Figure 1 where the stellar surface number density varies by at least an order of magnitude between the most heavily extincted region and the Galactic Center. The extinction can be estimated by modelling the number of sources per area given some assumptions about the extinction law, the number of stars along the line of sight to the Galactic

Center, and the number density law for stars near the Galactic Center. An alternate method only relies on assumptions about intrinsic stellar colors and the extinction law, and this method requires observations at 2 or more wavelengths.

Intrinsic stellar colors span a relatively small range in the near-infrared (Koorneef 1983), and the average star in the survey will have colors appropriate to K and M giants, i.e. both $(H-K)_0$ and $(K-m_{3.15})_0 \sim 0.20$. The extinction at K is expressed in equation (20) as a function of color excess where the constants have been calculated

$$\begin{aligned} A_K &= C_{HK} E(H-K) = 1.8 E(H-K), \text{ or} \\ &= C_{km_{3.15}} E(K-m_{3.15}) = 2.4 E(K-m_{3.15}). \end{aligned} \quad (20)$$

using equations (7) and (9) which give $A_H/A_K = 1.55$, $A_{3.15}/A_K = 0.58$. The values are somewhat different than those given in Table 4 ($A_H/A_K = 1.49$ and $A_{3.15}/A_K = 0.71$), although they are very nearly equal to the values given by Becklin et al. (1978) where extinction at 3.15 μm is found by interpolation. The difference between values in Table 4 and those calculated from equation (9) are due to the fact that the latter values are from a fit to a smooth curve. The reason these values were used instead of those in Table 4 will be explained below.

The assumption that a star has "normal" intrinsic color can be checked by using a third wavelength and plotting color versus color for the star, e.g. $(H-K)$ versus $(K-m_{3.15})$. Stars of normal color will be displaced along the reddening vector which has a slope of $C_{HK}/C_{K m_{3.15}} = 1.3$ for the values in equation (20). Using values in Table 4, $C_{HK} = 2.0$ and $C_{K m_{3.15}} = 3.4$ giving a slope of 1.7. Most stars fall along the reddening vector when it is drawn with a slope of 1.3 instead of 1.7 and this is why the former was used in the color-color plots. The higher slope would indicate that almost all stars

at the Galactic Center have intrinsic colors very different from red giants, a possibility which is highly unlikely.

K versus H-K diagrams are shown in Figure 53 where each panel corresponds to one frame in the survey according to the schematic in Figure 18. Panel numbers follow the usual "row+column" numbering scheme also used in Figure 18. The vertical axes are for K while the horizontal axes are for H-K where the axis labels are shown for panel 75. The total range of each panel is 17 to 7 in K and 0 to 4 in H-K where the region below $K \sim 12$ is badly undersampled due to confusion. Rows 8 and 9 are not included because they were observed on night number 5 when the seeing was much worse with $d_{\text{FWHM}} \sim 2.6''$ as opposed to $\sim 1.5''$ on night 4 when rows 1 through 7 were observed.

Table 18 gives a summary of the raw data used in the figure. The columns refer to: frame number, number of stars with $H < 14$ and $K < 13$, average H-K, median H-K, standard deviation, and implied A_K using equation (20).

The color-magnitude diagrams are populated mostly by red giants, and the giant branch can clearly be seen (see Figure 24). The most well defined giant branch can be seen in frame 41 where the extinction appears to be very smooth in Figure 38. This contrasts with the case where there is noticeable extra extinction contributed by a cloud at the Galactic Center. For instance, $M_{0.25+0.01}$ and $M_{-0.13-0.08}$ are clearly causing a spread in H-K in the upper left frames and the lower left frames respectively. This spread argues for many of the stars being within the cloud as long as the mean H-K is consistent with a location at the Galactic Center; although the shift in the mean H-K in frame 12 cannot be easily explained by this model. The panels between the Thermal Arched Filaments and the Galactic Center also show a large range in H-K, and this is

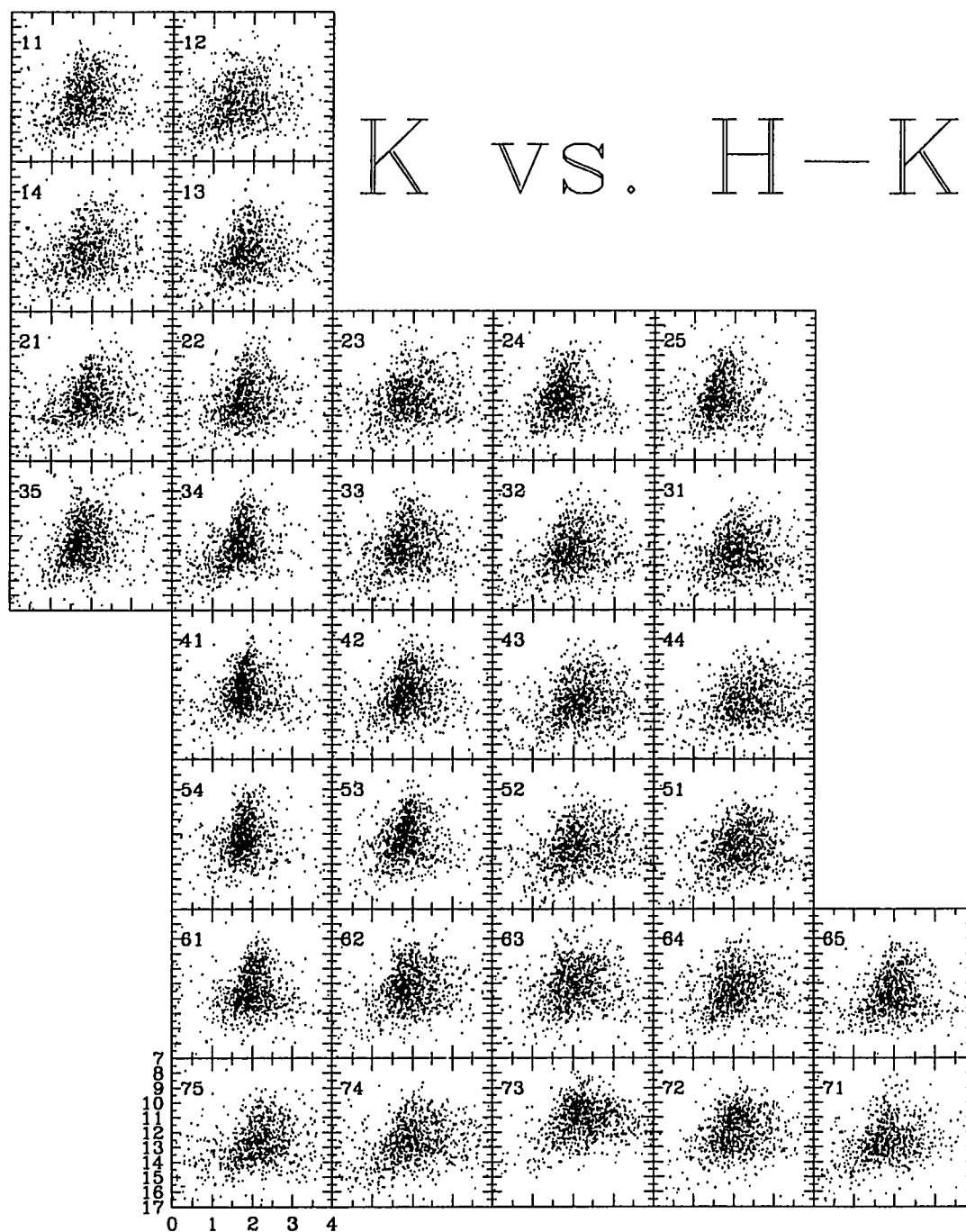


Figure 53. K ($K = 17$ to 7) versus H-K diagrams ($H-K = 0$ to 4).

probably due dust associated with the to the -30 km s^{-1} cloud (see section I.D.2.). The panels corresponding to frames 65 and 71 indicate large variations in extinction, and these frames also contain tendrils of extinction which can be seen in the color picture. The panel for frame 73 contains data for the central cluster, but the photometry is probably of much lower quality than for the other panels.

Table 18: Statistics for data used in Figure 53

frame	#	H-K		Std	A_K
		Avg	Med		
11	269	1.78	1.81	0.46	2.9
12	246	1.53	1.52	0.57	2.4
13	204	1.80	1.79	0.46	2.9
14	211	1.80	1.83	0.58	2.9
21	227	1.89	1.92	0.56	3.1
22	268	1.77	1.82	0.54	2.9
23	259	1.82	1.83	0.58	2.9
24	309	1.68	1.69	0.38	2.7
25	316	1.59	1.63	0.45	2.6
31	146	1.86	1.95	0.63	3.2
32	187	1.87	1.91	0.58	3.1
33	291	1.74	1.80	0.51	2.9
34	339	1.68	1.71	0.38	2.7
35	414	1.79	1.76	0.42	2.8
41	430	1.75	1.76	0.40	2.8
42	328	1.83	1.84	0.48	3.0
43	153	2.00	2.04	0.59	3.3
44	116	2.17	2.24	0.58	3.7

frame	#	H-K		Std	A_K
		Avg	Med		
51	225	2.00	2.10	0.60	3.4
52	194	1.97	2.01	0.57	3.3
53	447	1.81	1.84	0.39	3.0
54	456	1.75	1.77	0.41	2.8
61	348	1.94	1.98	0.46	3.2
62	424	1.86	1.84	0.47	3.0
63	415	1.96	1.96	0.54	3.2
64	326	1.91	1.96	0.54	3.2
65	278	1.93	1.96	0.46	3.2
71	271	1.72	1.74	0.53	2.8
72	483	2.02	2.02	0.45	3.3
73	664	2.20	2.18	0.48	3.6
74	257	1.91	1.94	0.60	3.1
75	200	2.04	2.15	0.64	3.5
Avg		1.86	1.88	0.51	3.03
Std		0.15	0.16	0.08	0.28

Color-color diagrams are shown in Figure 54. Again, panel numbers follow the "row+column" numbering method used in Figure 18. The panel for frame 75 is labelled with H-K values along the vertical axis and $K-m_{3.15}$ values along the horizontal axis.

The sample has been limited to stars with $H < 14$, $K < 13$, and $m_{3.15} < 10$. This was done because errant photometry for faint stars will contaminate a color-color diagram in unpredictable ways, as opposed to the case of the color-magnitude diagrams. The reddening vector is drawn from 0.2,0.2 and has a slope of 1.3, as explained above. Some panels have data points to the upper left of the reddening vector, but this is likely

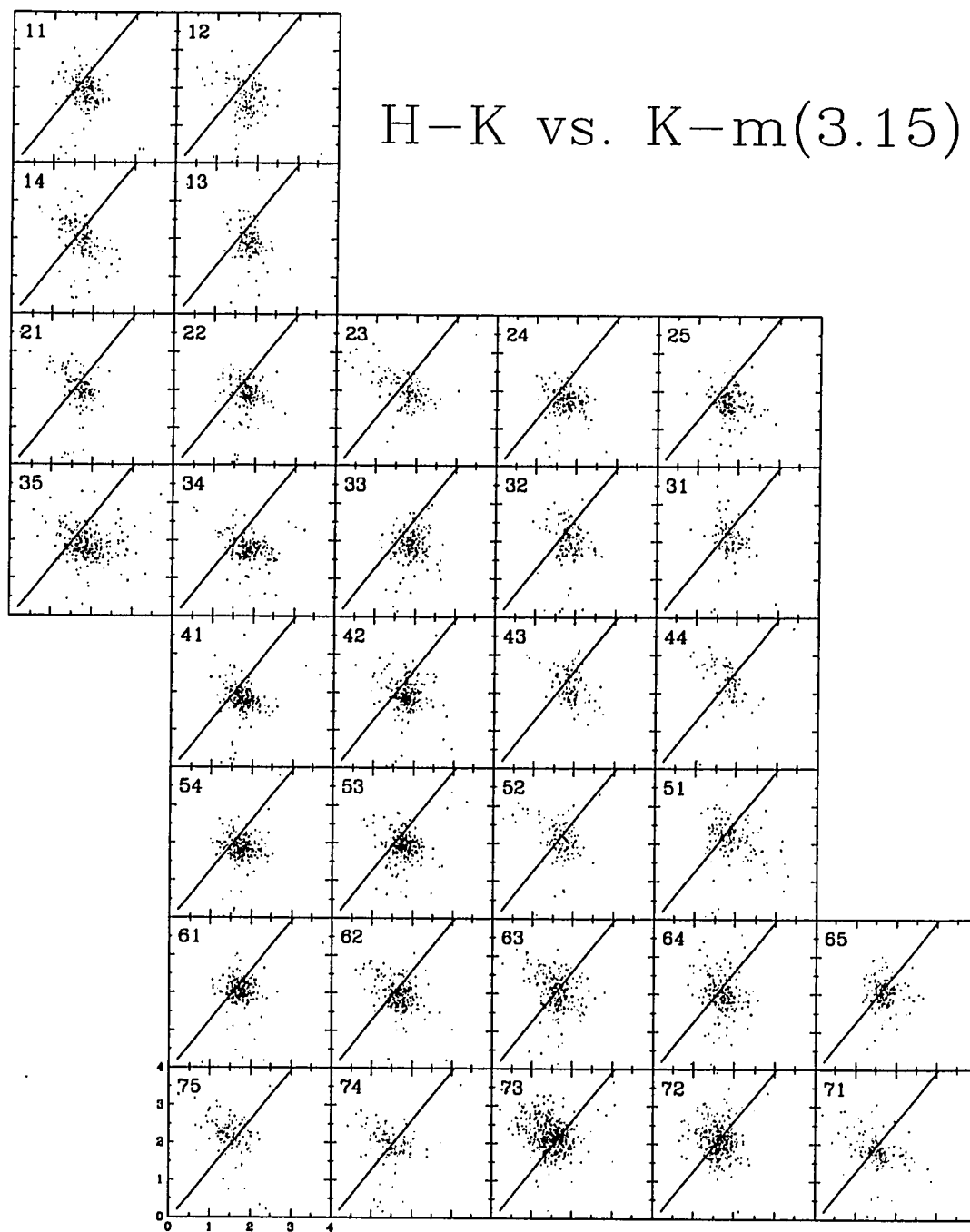


Figure 54. $H-K$ versus $K-m_{3.15}$ diagrams.

to be due to bad background subtraction in the $3.15\ \mu\text{m}$ frames where a noticeable ring of light can be seen in the frames; panels 12, 23, 52, and 63 are notable in this regard. The concentrated core of data points seems to be a bit below and to the right of the reddening vectors in most panels, and this is likely to be due to errors in the zero points or the extinction law. Relative shifts from panel to panel are probably significant. The red objects in panel 35 and, perhaps, 51 are reminiscent of the embedded young stellar objects thought to be in M17 (Hanson & Conti 1995). In fact, frame 35 contains the Quintuplet cluster which is known to have 5 very red stars, and these stars can be seen to the right of the reddening vector (see also Moneti et al. 1994). The number of stars in each panel is related to the amount of extinction to the stars in the panel. Relative differences from panel-to-panel are significant because the same photometric threshold were used for each panel. To some extent, the number of data points will also be related to the true spatial number density of stars at the Galactic Center; however, the effects of extinction probably dominate.

The average A_K varies between 2.4 and 3.7 over the truncated survey region shown in the figures. The most accurate extinction value for any single star can probably best be estimated by calculating $E(H-K)$ for the individual star instead of using the values in Table 18. In fact, Figure 1 shows variations in extinction over spatial scales much smaller than one survey frame. However, the average extinction in each panel can be used to locate molecular features along the line of sight because the frame size is about the same size as the molecular clouds covered in the survey.

B. Extinction from Br γ emission

The discovery of Wolf-Rayet stars in the Quintuplet cluster is very interesting, but the survey covers several other suspected sites of star-formation as discussed in

section I.D.2. In that section, it was noted that most of the star-formation sites have associated ionized gas. In fact, the presence of thermal radio emission is usually taken as an indicator of star-formation because the gas is assumed to be ionized by nearby hot stars.

In most cases, the HII region which produces the thermal radio emission can also be seen in the Bry images. The expected Bry flux is given in equation (21) (Wynn-Williams et al. 1978); the first coefficient is for $T_e = 10000K$ and the second coefficient is for $T_e = 5000K$.

$$S_{Bry}(W/m^2) = (8.8 - 15)(10^{-15}) S_{6cm}(Jy). \quad (21)$$

The Bry flux from the HII regions in the survey can be estimated from the narrow-band survey. The Bry zero-point has been estimated to be ~ 17.3 by assuming that K-band photometry for 37345, the maser counterpart, will give the same result as photometry using the Bry filter. An error of ± 0.3 magnitudes is assessed due to the assumed error in the zero-point for the K-band photometry and the error introduced by assuming that the K-band magnitude gives an accurate flux at $2.16 \mu m$. The flux for a zero magnitude star at $2.16 \mu m$ can be interpolated from Koornneef (1983) and is found to be $4.7(10^{-10}) W/m^2/\mu m$. The Bry filter has an effective width of $0.023 \mu m$ giving a flux of $1.3(10^{-18}) W/m^2$ for a source which produces one count per second. The total integration time was 64 seconds, so that a source which gives one count will have a flux of $2.0(10^{-20}) W/m^2$. The intrinsic noise in the data is background limited where the background flux rate is approximately 55 and 58 counts/second in the Bry and continuum filters respectively, and the gain is $19 e^-/count$. The noise is then calculated

to be 19 counts per pixel, or $4.0(10^{-19})$ W/m² per pixel. The total noise in an aperture will be the noise per pixel times the square root of the number of pixels in the aperture.

G-0.14-0.09 is the only major thermal radio feature which is not seen in the Br γ images. Perhaps not coincidentally, no emission-line stars were found in the region. This could mean that the photoionizing source is: 1) a main-sequence O-star, 2) a later star with too little mass to evolve into a Wolf-Rayet star, or 3) deeply embedded within the associated molecular cloud, M-0.13-0.08. In all three cases, the source could ionize nearby gas without being seen as an emission-line object in our survey. Possibility 3 could be explored by comparing the expected Br γ flux to the flux limit of the Br γ survey.

The 6 cm flux for this HII region is 87 ± 7 mJy according to Ho et al. (1985). A flux of $(7.7 \rightarrow 13)(10^{-16})$ W/m² in Br γ is then expected using equation (21). The source can be covered by an aperture with $r = 5'' = 7$ pixels giving a total area of 160 pixels². The total noise in this aperture is estimated to be 246 counts or $5.0(10^{-18})$ W/m². Assuming $A_K \sim 3$, the expected flux is $4.4(10^{-17})$ W/m² giving an expected S/N of about $18 \rightarrow 30$. The morphology of this region (see Figure 3) shows two intensity peaks at 2 cm. The flux for one of these peaks is about 11.1 mJy per $2.4'' \times 1.2''$ beam or about 6 pixels. The expected S/N is then $\sim 11 \rightarrow 19$ assuming $A_K \sim 3$. A lower-limit for A_K to G-0.14-0.09 can be estimated by using the fact that it was not detected. Assuming that it was not detected above 3 sigma above the noise, the implied extinction is 4.3 or 4.8 assuming $T_e = 5000K$ or $10000K$ respectively. After considering errors in the zero-point, this indicates that the extinction to the HII region is at least 1 magnitude greater than the assumed extinction in Figure 25.

We are still in the preliminary stages of using the Br γ flux for extinction measures, so results for the other regions are not yet available. A preliminary measurement of the extinction to the A–D HII regions using the Br γ flux gives $A_K \sim 2$ for sources A, B, and C, while D appears to be more heavily extinguished. The extinction indicates that the first three sources are on the near side of M–0.02–0.07, while D is embedded. This is in agreement with the extinction derived from mid-infrared fine structure lines for these sources (Serabyn & Gusten 1987); however, these authors find $A_{12.8} \sim 1$ for A–C, or $A_K \sim 3.1$ using the extinction law from Rieke et al. (1989). This value is much more consistent with what would be expected for stars at the Galactic Center, so our estimates appear to be a bit too low. We will investigate this further in the future.

C. Velocity

Wavelength shifts with respect to the vacuum rest wavelength (see Table 11) were measured for Br γ emission in the emission-line stars and nebular regions using the IRAF facility SPLIT (see section V.B.7.). In some cases, additional emission lines could be used, but the S/N was normally much higher for the Br γ line. In addition, the HeI can easily be influenced by slight mis-correction of atmospheric absorption, so this line was not used to calculate velocities. The velocity shifts, ΔV , and line widths, ΔV_{FWHM} , are given in Table 19 where both are in units of km s^{-1} . The one sigma errors are estimated to be 28 km s^{-1} based on the dispersion of the fits to the sky OH lines near $2.166 \text{ }\mu\text{m}$. Line-widths are not quoted for $\Delta V_{\text{FWHM}} < 540 \text{ km s}^{-1}$, the line-widths measured for the planetary nebula Hubble 5. The nomenclature follows the spectra shown in section VI.C. In the following discussion, line shifts and widths for the HeI

line at $2.0581 \mu\text{m}$ will be referenced with a subscript whereas unsubscripted values are for the Br γ line.

The object list has been broken up into groups according to location in the survey. The first four objects are located in the central parsec. AFN coincides with the westernmost extension of the minispiral between IRS6E and IRS6W. Others have measured very narrow line-widths for this clump of gas, i.e. $\Delta V_{\text{FWHM}} = 144 \text{ km s}^{-1}$, and a velocity shift of -146 km s^{-1} (Herbst et al. 1993). Krabbe et al. (1991) measured a velocity shift of -150 km s^{-1} and line-width of 500 km s^{-1} in the HeI $2.058 \mu\text{m}$ line. Both the blueshifts and line-widths are consistent with our measurements. The AF star has $\Delta V_{\text{HeI}} = 300 \text{ km s}^{-1}$ and $\Delta V_{\text{FWHM,HeI}} = 920 \text{ km s}^{-1}$ according to Krabbe et al. (1991), $\Delta V_{\text{HeI}} = 200 \text{ km s}^{-1}$ and $\Delta V_{\text{FWHM,HeI}} = 750 \text{ km s}^{-1}$ according to Allen et al. (1990), $\Delta V = -71 \text{ km s}^{-1}$ and $\Delta V_{\text{FWHM}} = 429 \text{ km s}^{-1}$ according to Herbst et al. (1993), and $\Delta V_{\text{FWHM,HeI}} = 800 \text{ km s}^{-1}$ and $\Delta V_{\text{FWHM}} = 1000 \text{ km s}^{-1}$ according to Blum et al. (1995a). The values from Herbst et al. (1993) appear to be anomalous with respect to the other values and ours. We were able to obtain a high S/N measurement of the HeI line for this star, and we get $\Delta V_{\text{HeI}} = 256 \text{ km s}^{-1}$ and $\Delta V_{\text{FWHM,HeI}} = 810 \text{ km s}^{-1}$. The $2.166 \mu\text{m}$ line might have an apparent relative blueshift with respect to the HeI line because Br γ could be contaminated by HeI for this star. There are no other published values for IRS20 and IRS33. In fact, IRS33 was only recently shown to be an emission-line star in the HeI images from Eckart et al. (1995). Our measured velocities are consistent with the velocity of the diffuse emission, but our linewidths are greater than those measured by Herbst et al. (1993).

The Quintuplet stars and Pistol nebular region show roughly the same ΔV when accounting for the fact that Star 1, which we have elsewhere classified as a WN9 star,

will have HeI and Br γ emission near 2.166 μm . In fact, the sense of the contamination is consistent with this idea because the emission-line corresponding to the hydrogenic transition of HeI will be blueshifted with respect to the analogous hydrogen line. The line-width of the 2.166 μm line is somewhat larger than that for the 2.0581 μm line, $\Delta V_{\text{FWHM,HeI}}$, again consistent with a blend near Br γ . Otherwise, the median ΔV for the Pistol, 127 km s^{-1} , seems to be representative for the system considering the errors. Individual measurements for the Pistol were taken from single frames in order to see if the velocities were reproducible. In fact, the first four values for the Pistol were taken from the first night of the run and the second set from the last night of the run. Both sets are consistent within the errors.

The HII regions just north of the Galactic Center have nearly zero velocity shifts with a small bias toward negative velocities. Only two of the measurements, H2B and H5EC, correspond to stars where stellar winds could broaden the emission-line. H5WN and H6 are nebular HII regions, so their line-widths are dubious. In fact, the spectrum for H5WN was constructed from a single frame, and the two individual spectra used for H6 give very different velocity widths. In any case, where the values should be trusted there is good agreement with recombination-line velocities for the associated HII regions where Zhao et al. (1993) find velocity shifts in the range of -28 to -58 km s^{-1} and very narrow line-widths $\sim 45 \text{ km s}^{-1}$.

Table 19: Br γ line shifts and widths

Object	ΔV	ΔV_{FWHM}
AFN	-129	
AF	153	1204

Object	ΔV	ΔV_{FWHM}
IRS20	-182	609
IRS33	-221	650
Q8	139	581
Q10	135	637
Star 1	34	996
Star 3	157	
Pistol a	102	581
Pistol b	179	
Pistol c	103	
Pistol d	127	
Pistol e	128	
Pistol f	138	
Pistol g	116	595
Pistol h	139	664
Median	127	
Std	23	
H1N	-26	
H2B	-3	678
H3	3	
H5EC	-39	581
H5WN ^l	-31	775
H6 ^l	-109	567
Para. Guy	-17	

Object	ΔV	ΔV_{FWHM}
Para.	-64	

¹See text for problems with these objects.

The "Parachute Guy" and "Parachute" can be seen in the 20 cm contour map from Pedlar et al. (1989) located at 17h42m10s and 17h42m05s in RA respectively, and both have the same DEC, $-28^{\circ}57'30''$. The presence of Br γ emission confirms the assertion that these regions are thermal. The velocities in the table represent the only published measurements for these regions.

VIII. Discovery of Emission-line Stars in the Quintuplet

Based on a paper by Donald F. Figer, Ian S. McLean, and Mark Morris 1995,
accepted for publication in *Astrophysical Journal Letters*

A. Abstract

As part of a 1800 pc² survey of the Galactic Center region in the lines of HeI (2.058 μ m), Br γ (2.166 μ m), and the HeII/CIV complex (3.09 μ m), we have found two new Wolf-Rayet stars, a WN9 and a WC9, near the Galactic Center. K-band spectra of both stars show broad helium emission lines, and the WC9 shows broad carbon emission lines. A third emission-line star in the region has a spectrum and luminosity similar to an LBV. The stars are within 2 pc, in projection, of the Quintuplet cluster (AFGL2004) and are probably members of this cluster on the basis of their proximity and expected ages.

All three stars are evolved descendants of massive main sequence stars having $M_{\text{initial}} \geq 50 M_{\odot}$ (WC9), $\geq 20 M_{\odot}$ (WN9), and $\geq 40 M_{\odot}$ (LBV candidate). The LBV candidate has a luminosity of $L \sim 10^{6.3} L_{\odot}$, comparable to that of η Carinae ($L = 10^{6.5} L_{\odot}$), one of the most luminous stars in the local group of galaxies.

A total of 5 emission-line stars are now known to reside in the "Quintuplet," and they collectively produce $N_{\text{Lyc}} \sim 10^{49}$ photons/s. The new LBV candidate generates enough ionizing photons to account for the "Pistol" HII region (G0.15-0.05), while the nearby "Sickle" (G0.18-0.04) may be ionized by a population of O-stars accompanying the 5 emission-line stars.

B. Introduction

The large interstellar extinction to the Galactic Center, $A_V \sim 27$, obscures the types and spatial distribution of stars near the center, a problem circumvented by

employing infrared cameras operating at wavelengths where the extinction is about one tenth the value at optical wavelengths. We performed a survey to assess the ubiquity of young, hot, and luminous stars near the Galactic Center by observing an area $\sim 24'$ NS \times $12'$ EW ($= 60 \times 30$ pc) in narrow-band filters centered on the emission lines of: HeI ($2.058 \mu\text{m}$), CIV ($2.078 \mu\text{m}$), Br γ ($2.166 \mu\text{m}$), and CIV/HeII ($3.092 \mu\text{m}$). Preliminary data reduction has revealed two new helium emission-line stars in the Quintuplet region (AFGL2004) (Nagata et al. 1990; Okuda et al. 1990; Glass et al. 1990). We classify these stars as WC9 and WN9. A third star, which Moneti et al. (1994) refer to as the "serendipitous" source, shows narrow emission-lines similar to lines seen in the spectra of LBV's; our data suggest that it is one of the most luminous stars in the Galaxy, $\text{Log}(L/L_{\odot}) = 10^{6.3}$.

C. Observations

We obtained narrow-band images on 5 nights in June, 1994, and spectra on 5 nights in July, 1994. The UCLA double-beam near-infrared camera (McLean et al. 1993, 1994) was used on the University of California Observatories' (UCO) 3-m Shane telescope for both runs, giving a plate scale of $0.70''$ per pixel for the short-wavelength channel and $0.68''$ per pixel for the long-wavelength channel. For the $2 \mu\text{m}$ narrow-band images, the frames were dark-subtracted, and then sky-subtracted and flat-fielded by using medianed images of a heavily-extincted "dark spot" near the Galactic Center at RA $17^{\text{h}}41^{\text{m}}37^{\text{s}}$, DEC $-28^{\circ}53'00''$ (1950). These steps were accomplished for the $3 \mu\text{m}$ images by using mode-scaled running medians of adjacent survey frames. Spectra were obtained using grisms and a fixed slit of dimensions $1.4''$ (2 pixels) by $120''$. The final spectra were extracted following the procedures in Massey et al. (1992) and are discussed in Chapter V of this work. The FWHM for unresolved lines was $\sim 38 \text{ \AA}$ (525

km s⁻¹) in the K band. A stars were observed at a similar time and air mass to the targets in order to correct for atmospheric absorption. Brackett series absorption was removed from these spectra by interpolation. Wavelength calibration was done using OH sky lines (Ramsay et al. 1992).

Star 1 was observed for 18 minutes on July 22 and July 26. The "Quintuplet" star, q1 (nomenclature from Moneti et al. 1994), was used as an intermediate atmospheric standard; both stars were in the slit at the same time. Star 2 was observed for 12 minutes on July 26, and the A2V star BS6378 ($T = 9120$ K; Johnson 1966) was used as the atmospheric standard. Star 3 was observed for 6 minutes on July 26, and the atmospheric standard was BS6378. WR121 (WC9) was observed for 1 minute on July 26, and the A2V star BS7598 was used as the atmospheric standard.

The dereddened and flux-calibrated spectra (see Figure 55, Figure 56, and Figure 57) were scaled so that the flux density matched the photometry measured in June. Note that the intensity scale of the spectrum for WR121 has been divided by 10 to allow a better comparison with the spectrum of star 2. Table 20 contains photometry, using a 4.2" diameter aperture, and presents line-widths for the HeI line at 2.058 μ m. As a check, we find $\Delta V_{\text{FWHM}} \sim 810$ km s⁻¹ for the AF star; this compares well with values found previously (800 km s⁻¹, Blum et al. 1995a; 920 km s⁻¹, Krabbe et al. 1991; 750 km s⁻¹, Allen et al. 1990). The designations for the two previously known emission-line stars, q8 and q10, follow Moneti et al. (1994); the classifications for these stars are uncertain.

Table 20: Parameters for the Quintuplet Emission-line Stars

Name	RA			DEC			Type	K	H-K	M_K	$\log(L/L_\odot)$	ΔV
	h	m	s	°	'	"						
star 1	17	43	3.6	-28	48	9.7	WN9	10.5	1.9	-6.3	5.2	740
star 2	17	43	5.1	-28	49	11.6	WC9	11.4	2.1	-5.4	4.9	1270
WR121	18	41	35.0	-03	51	4.0	WC9	6.0	1.3	-5.8	5.0	1020
star 3	17	43	4.8	-28	48	56.9	LBV	7.1	1.8	-9.7	6.3	710
q8	17	43	5.5	-28	48	31.3	?	8.8	1.8	-8.0	5.9	660
q10	17	43	4.7	-28	48	30.5	?	8.5	1.8	-8.3	6.0	<550

¹Coordinates are for Equinox 1950

²See text for errors

³ ΔV are measured FWHM for the 2.058 μm HeI line

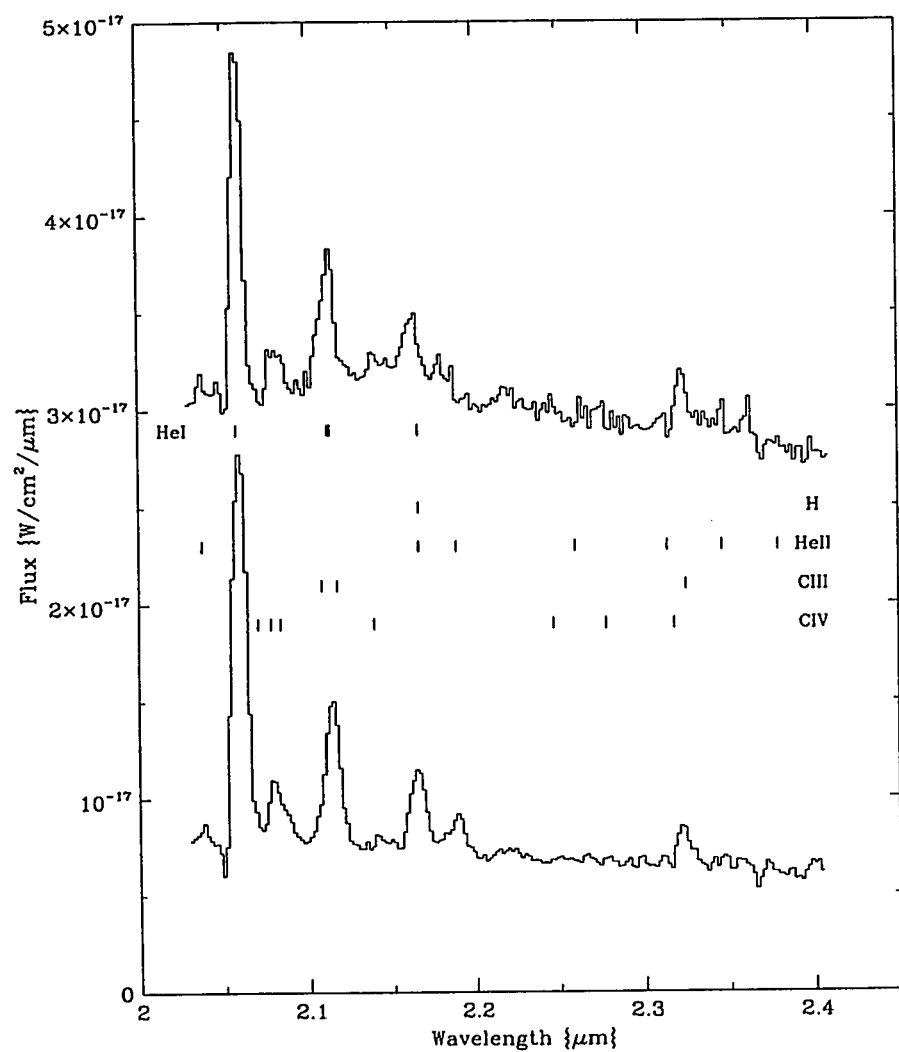


Figure 55. K-band spectrum (R-530) of star 2 (bottom) and the new WC9 star WR121 (top). The intensity scale of the spectrum for WR121 has been divided by 10. All spectra have been dereddened and flux-calibrated.

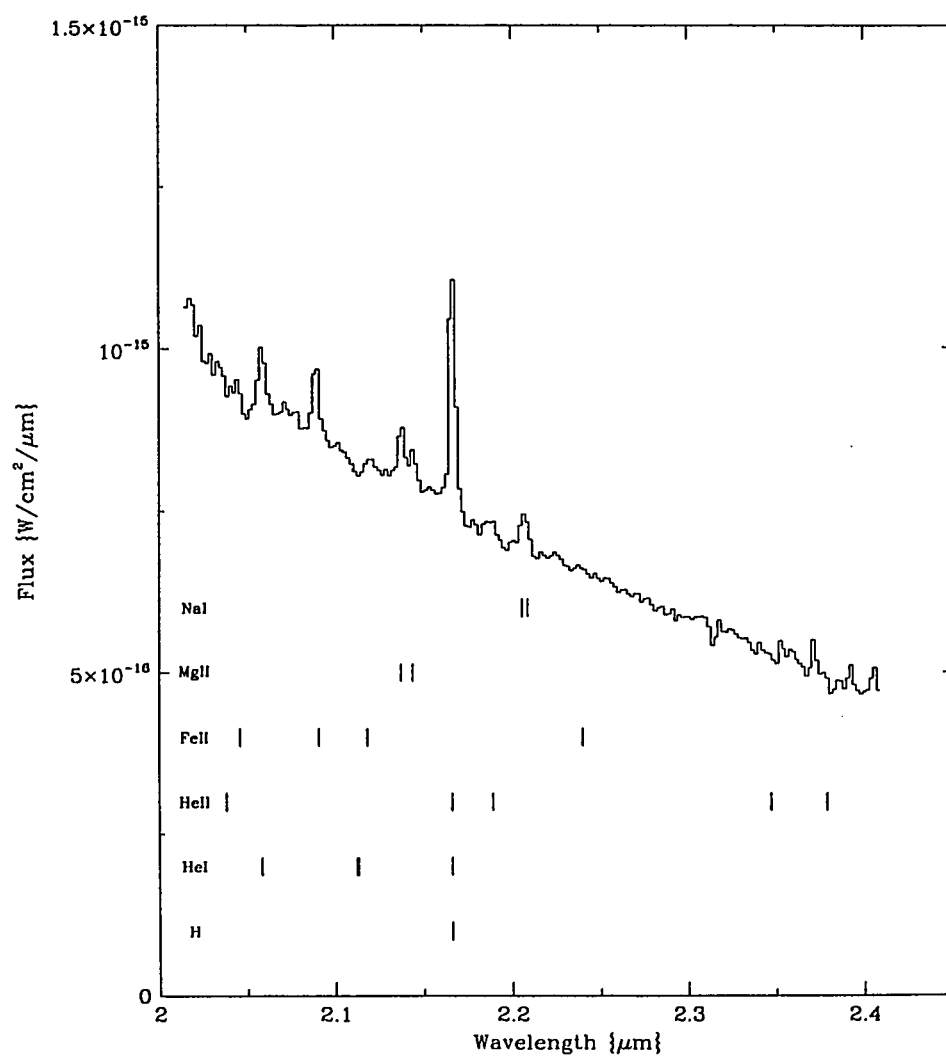


Figure 56. K-band spectrum of the new LBV candidate, star 3.

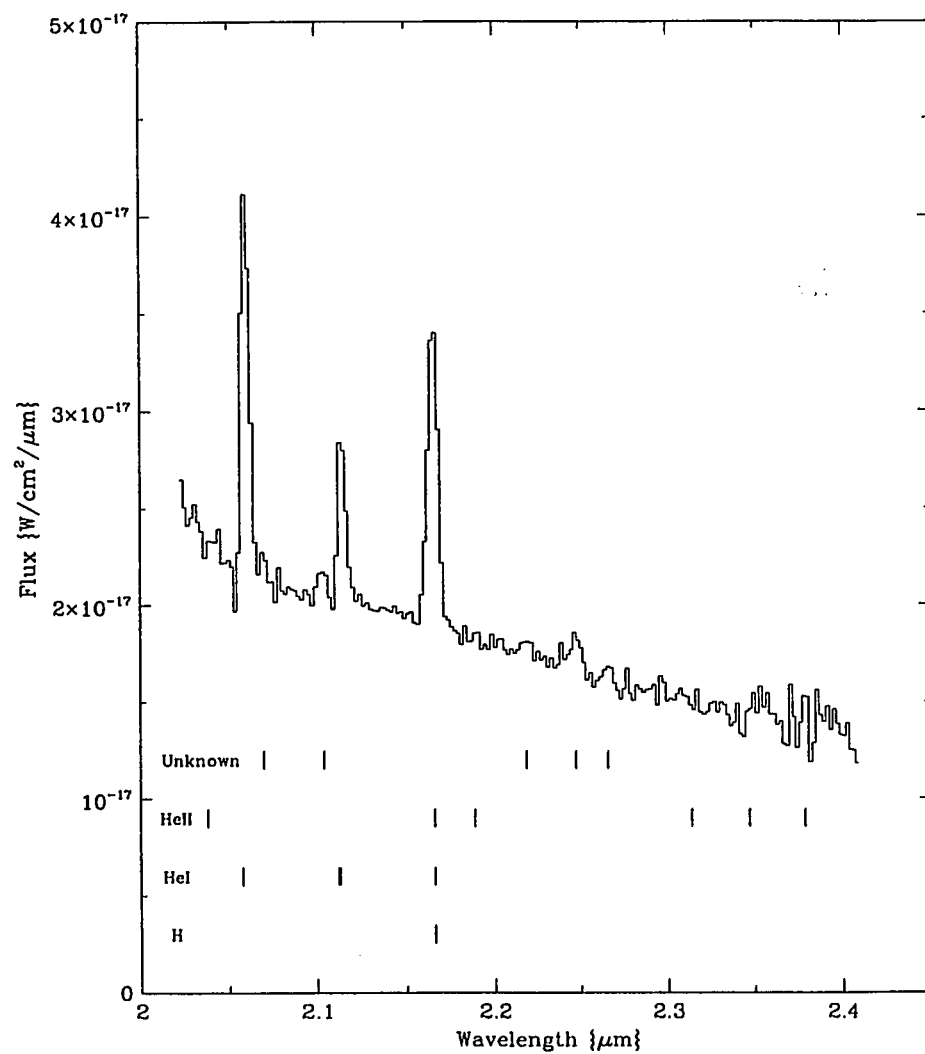


Figure 57. K-band spectrum of the new WN9 star, star 1.

Using photometry from Williams et al. (1987) and the extinction law from Rieke et al. (1989), we calculate $A_K = 0.68$ and $M_K = -5.8$ for WR121. We calculate $\log(L/L_\odot) = 5.0$ assuming $M_V = -4.8$ (van der Hucht et al. 1988) and $BC_V = -3.0$ (Smith et al. 1994) for all WC9 stars. This implies a $BC_K = -2.0$ for WR121, a value consistent with other WC9 stars, given the assumed luminosity. WC9 stars are typically surrounded by dust and have $(H-K)_0 = 0.9 \pm 0.4$ where the error is the standard deviation for the sample in Williams et al. (1987). Using $(H-K)_0 = 0.9$ and $BC_K = -2.0$ for star 2, we calculate $A_K = 2.1$ ($-0.7, +0.8$), $M_K = -5.4$ ($-0.7+0.8$), and $\log(L/L_\odot) = 4.9 \pm 0.3$. The extinction was verified by dereddening the spectrum of star 2 until it had the same slope as the dereddened spectrum of WR121. We adopt this extinction (equivalent to $A_V = 19 -6, +7$) for the remaining sources; it is in the range given by Okuda et al. (1990) ($A_V = 16-25$), while Glass et al. (1990) give $A_V = 22$.

Stars within the LBV class have a wide range of BC_K : 0 to -3.5 according to Blum (1995a), so we use the arithmetic mean of their sample, $BC_K = -1.4$, for star 3. Even assuming the most extreme cases for BC_K and A_K , we calculate $\log(L/L_\odot) = -5.5$ to -7.5 , comfortably in the range of luminosities for known LBVs (Humphreys 1989). We assume $BC_K = -2.0$ for the remaining sources, and the errors are the same as those given above for star 2.

D. Discussion

The spectra of star 2 and WR121 are remarkably similar, and the presence of carbon is assured by the CIV line at $2.078 \mu\text{m}$ and the CIV/CIII complex at $2.318/2.325 \mu\text{m}$ (Eenens et al. 1991). The emission line near $2.11 \mu\text{m}$ has a FWHM of 1440 km s^{-1} , more than would be expected from just the HeI complex at

2.112/2.113 μm , and CIII emission is a likely contributor to this blend. The displacements of the absorption components of the 2.058 μm line from line center are within the range of velocities observed for other WC9 stars (Eenens and Williams 1994). Maeder (1991b) gives $M_{\text{initial}} \geq 50 M_{\odot}$, $Z \geq 0.02$, and $\tau_{\text{age}} < 2.5 \times 10^6$ yrs for WC9 stars. Blum et al. (1995b) give an ionizing flux of $\geq 5 \times 10^{48}$ photons/s for the new WC9 star they discovered in the central parsec of the Galaxy; we adopt this value as a lower limit.

The spectrum of star 3 is similar to the spectra of LBV's, notably HD316285 (McGregor et al. 1988b), S Dor (Blum et al. 1995a), and η Car (Hamann et al. 1994). LBV's are generally believed to be evolved from main-sequence stars with $M_{\text{initial}} > 40 M_{\odot}$ (Maeder and Conti 1994). An absorption feature at $\sim 2.112 \mu\text{m}$ can be seen in star 3 and is believed to be due to the 2.112/2.113 HeI complex; this feature also appears in absorption in B0I stars (Hanson & Conti 1994) and in emission in η Car, HD316285, and S Dor. The other identified lines of NaI, MgII, FeII, HeII, HeI, and H, are variously seen in the spectra of these and other LBV's (Hamann et al. 1994; McGregor et al. 1988a,b; Blum et al. 1995a). The H band spectrum (not shown) shows additional iron lines at 1.644 μm , 1.688 μm , and 1.745 μm . Cotera et al. (1994) classify star 3 as a B[e] and offer a spectrum of He3-1191 for comparison, but He3-1191 has been reclassified as a PPN with $L < 10^3 L_{\odot}$ (Le Bertre et al. 1989), while we calculate $L \sim 10^{6.3} L_{\odot}$ for star 3. The LBV classification might provide a *raison d'être* for the "Pistol" radio feature (Yusef-Zadeh & Morris 1987a), G0.15–0.05, which might have been created by photoionized ejecta from past eruptive stages of the star (Lamers 1989; Davidson 1989). The Pistol requires $\sim 3.9 \times 10^{48}$ ionizing photons/s (Yusef-Zadeh et al. 1989), and we calculate $\sim 3.4 \times 10^{48} \text{ s}^{-1}$ (Panagia 1973) produced

by the LBV candidate, assuming that its flux is similar to that of a B0I star with $T_{\text{eff}} \sim 30,000$ K (Humphreys 1989).

Star 1 is similar to other GC He-emission line stars (Krabbe et al. 1991) in that they all show emission lines of HeI at $2.058 \mu\text{m}$ and Br γ ; however, important distinctions remain. The spectrum is marked by HeI emission lines, but $F_{2.058}/F_{\text{Br}\gamma} \sim 0.9$ is much less than the typical values for the helium stars in the central cluster [e.g., IRS16C has $F_{2.058}/F_{\text{Br}\gamma} \sim 2.08$ and the AF star has $F_{2.058}/F_{\text{Br}\gamma} \sim 2.88$ (Blum et al. 1995a)]. On the other hand, $F_{2.112}/F_{\text{Br}\gamma} \sim 0.4$ for the new star, whereas the GC stars all have less than this value, except for IRS13 and AHHNW (Blum et al. 1995a). Likewise, the other Quintuplet He emission-line stars, q8 and q10, barely have any detectable flux in the $2.112/2.113 \mu\text{m}$ complex, as measured in our own data (or see Geballe et al. 1994). ΔV_{FWHM} for the new star is somewhat greater than in q8 and q10; however it is in the range measured for Galactic Center stars (Krabbe et al., 1991). Star 1 is likely to be an evolved massive star like the Ofpe/WN9 stars or WN9 stars (Blum et al. 1995a). We tentatively identify star 1 as a WN9 type, although the classification is ambiguous. Maeder (1991b) gives a minimum initial mass of $20 M_{\odot}$ for WN-type stars having high metallicity, $Z > 0.04$. The relatively cool temperature for this star implies a low ionizing flux; for example, Najarro et al. (1994) calculate a rate of $< 10^{48} \text{ s}^{-1}$ for the AF star at the Galactic Center.

The "Sickle" HII region, G0.18-0.04, (Yusef-Zadeh et al. 1984) requires $\sim 3 \times 10^{50}$ ionizing photons/s (Harris et al. 1994). The net contribution from the 5 known emission-line stars is on the order of 1049 photons/s. While this rate is insufficient to ionize the Sickle, the total rate from the Quintuplet cluster may be much greater due to contributions from a probable population of accompanying O and B stars.

Acknowledgments

We acknowledge useful discussions with Peter Conti. We also thank Murray D. Silverstone for assisting with the observations.

IX. Conclusions

A. Emission-line stars near the Galactic Center

Our survey successfully revealed 6 new emission-line stars near the Galactic Center. Two of these stars have been classified as WN9 and WC9 types, where the latter is the first unambiguously identified Wolf-Rayet star in the survey region. These two stars are part of the Quintuplet cluster, where we have also discovered two other emission-line stars which have a somewhat ambiguous spectral classification. These other two stars, X10 and QD, have a relatively weak HeI emission line with little or no Br γ emission. The final two stars, IRS20 and IRS33, are members of the central cluster where there are over a dozen previously known emission-line stars. These stars have relatively narrow emission lines, with Br γ stronger than HeI, so they are probably supergiants in an intermediate evolutionary stage between the main sequence and the WR stage.

In addition to finding and classifying these newly discovered stars, we have successfully classified a previously known emission-line star near the Quintuplet as an LBV candidate. LBVs are extremely rare in the Galaxy and represent a delicate stage of evolution where a star is barely able to hold its outer layers against radiation pressure. This star is one of the most luminous stars in the local group of galaxies.

Another star, H2B, discovered in our study a year earlier, was found to have an emission-line spectrum typical of OB supergiants. The luminosity is inferred to be $\sim 10^{6.1} L_{\odot}$, too large compared to the inferred ionizing rate from radio continuum data. The resolution to this problem might be a more positive BC $_{\kappa}$ or improved stellar models. This star is surrounded by warm dust, consistent with it being recently formed.

In addition to these spectral classifications, we have measured velocities for some of these stars and associated ionized gas. The velocities are consistent with those measured from radio recombination line data, and we offer two new velocities for gas in the parachute, where radio recombination-line velocities have not been measured. The velocities for some of the Quintuplet emission-line stars and the Pistol HII region are the same within the uncertainties; this is consistent with a physical connection between the Quintuplet and the Pistol. The velocity for H2B is consistent with the velocity for the surrounding HII region.

Our new extinction measurements agree with the generally accepted value of $A_K \sim 3$, but we find large variations from frame to frame and even for stars within a single frame. These large variations should serve as an important caveat for those using the "canonical" extinction to the Galactic Center in calculating absolute magnitudes or in dereddening spectra.

No emission-line stars were found outside of the previously known star-formation sites. The lack of new emission-line stars over much of the survey region indicates that star-formation is localized to sites with thermal radio emission. In one case, G-0.14-0.09, no emission-line stars are seen near the HII region; but this might be explained by the extraordinarily large extinction to this ionized gas. The lack of emission-line stars near H1, H3, H5, and H6, suggests that the ionizing sources are probably O-stars still on the main-sequence.

The new information suggests a more consistent picture of the star-forming regions near the Galactic Center. In all cases, emission-line stars within 50 pc of the Galactic Center are associated with star-forming regions and thermal radio emission. Most of the emission-line stars are not deeply embedded, and it is expected that they

contribute significantly to the ionizing flux which produces the HII regions. This is consistent with the suggestion that some of the HII regions are near the surfaces of molecular clouds.

The emission-line stars within the inner parsec seem somewhat less peculiar now that other stars with similar near-infrared spectra have been found over the survey region. The new and previously known emission-line stars have changed our perspective on the central cluster quite dramatically. It is now striking that the central cluster is so similar to, rather than different from, nearby clusters. In fact, starburst and stellar evolution models can probably be used to predict the supergiant population in the central cluster, as well as in nearby clusters (Krabbe et al. 1995). Evidently, molecular clouds near the Galactic Center can routinely produce these massive emission-line stars, despite the extraordinary internal velocities within the clouds and the strong magnetic fields in the region.

B. Remaining questions and future prospects

There is much more information to be extracted from data taken for this project. The target list for phase II was generated by examining the Br γ and HeI surveys. The HeII/CIII/CIV (3.09 μ m) survey still needs to be inspected for emission-line stars. This survey can detect WR stars earlier than WN8, while the Br γ and HeI surveys are better suited to detecting the later WR subtypes. In fact, a preliminary search of frame 35, the frame containing the Quintuplet, reveals two more likely WR stars having 50% and 150% flux excesses at 3.09 μ m. The first star also has an excess in the inverse survey where the image taken with the 2.058 μ m filter is subtracted from the image taken with the 2.085 μ m filter. The flux excesses at 3.09 μ m and 2.085 μ m are best matched by the excesses measured for the template WC7 star, WR137. The second star has a small

excess at Br γ and no excess at 2.085 μ m. These properties are best matched by the template WN4 star, WR128.

Spectra for these stars, as well as for other stars targeted from the remaining surveys, will be obtained in the Summer of 1995. The instrument setup will be identical to that used for phase II of last year. In addition, more spectra of template WR stars will be obtained to make a more complete K-band spectral atlas of WR stars.

Two new narrow-band surveys will be obtained this summer using a second continuum filter at 2.25 μ m for the Br γ survey and a CO bandhead filter at 2.29 μ m. The images at 2.25 μ m and 2.085 μ m can be averaged together to obtain a better measure of the continuum at 2.166 μ m; this will serve to exclude the water-absorption stars from being interpreted as having Br γ emission. The CO survey will reveal the late-type giant population, and is expected to provide evidence that the background emission from stars in the Quintuplet and Arches-cluster comes from stars which have not yet evolved off the main sequence.

The discovery of stars with featureless K-band spectra and relatively blue colors is intriguing. These stars might be embedded young stellar objects or early-type main-sequence stars. These two types of stars can be distinguished by the weak Br γ , HeI, and HeII absorption features in the latter. The equivalent widths for these lines are as small as $W_\lambda \sim 2 \text{ \AA}$, which is about the same as that measured for the weak absorption feature at 2.11 μ m in the LBV candidate. Such a weak feature could be detected at the 4σ level if the integration times give $S/N \sim 80$ in the continuum. For an O-star at the Galactic Center, i.e. $K \sim 13$, this requires an exposure time of ~ 45 minutes.

If a complete assay of the O-stars and WR stars in each cluster can be made, the total ionizing flux from the hot stars can be calculated and compared to what is

required to ionize nearby HII regions. In addition, such an assay will give the key number ratios, WC/WN and WR/O, for determining the histories of individual star-formation regions. The new model predictions from Parker (1995) and Meynet (1995) can be compared to the observed number ratios to better constrain the time since the burst, the metallicity, and the IMF. Alternatively, if the measured number ratios are far outside what are expected, then they can be used to constrain massive star evolutionary models.

This thesis, and the aforementioned future work, is an excellent preparation for a similar project using NIRSPEC, a recently funded near-infrared echelle spectrometer to be built by the UCLA Infrared Imaging Detector Laboratory for use on the Keck II telescope. This instrument will provide resolving powers $\sim 25,000$ between 1 to 5 μm , with selectable slit widths between 0.2" and 1.0" and slit lengths up to 30". The task of detecting absorption features with $W_\lambda \sim 2 \text{ \AA}$, i.e., in O-star spectra, at the Galactic Center becomes very easy, requiring integration times less than 1 minute. This instrument and telescope will be uniquely powerful for observing stars in regions of high source confusion, like the Galactic Center; it is nearly impossible to determine WC/WN and WR/O ratios within the central cluster with present instrumentation because of confusion. It is for this reason that these numbers will be pursued only in star-formation regions within our survey region, but outside of the central parsec. Only when NIRSPEC becomes operational can this project be extended into the inner parsec of the Galactic Center.

REFERENCES

- Abbott, D. C., & Conti, P. S. 1987, *Ann. Rev. Astron. & Astroph.*, 25, 113
- Allen, D. A., Hyland, A. R., & Hillier, D. J. 1990, *MNRAS*, 244, 706
- Allen, D. A., & Swings, J. P. 1972, *A&A*, 20, 333
- Anantharamaiah, K. R., Pedlar, A., Ekers, R. D., & Goss, W. M. 1991, *MNRAS*, 249, 262
- Armandroff, T., & Massey, P. 1985, *ApJ*, 291, 685
- Armstrong, J. T., Ho, P. T. P., & Barrett, A. H. 1985, *ApJ*, 288, 159
- Armstrong, J. T., & Barrett, A. H. 1985, *ApJS*, 57, 535
- Bally, J., Stark, A. A., Wilson, W., & Henkel, C. 1988, *ApJ*, 324, 233
- Becklin, E. E., Matthews, K., Neugebauer, G., & Willner, P. 1978, *ApJ*, 220, 831
- Becklin, E. E., & Neugebauer, G. 1978, *PASP*, 90, 657
- Becklin, E. E., Gatley, I., & Werner, M. W. 1982, *ApJ*, 258, 135
- Blum, R. D., DePoy, D. L., & Sellgren, K. 1995a, *ApJ*, in press
- Blum, R. D., Sellgren, K., & DePoy, D. L. 1995b, *ApJL*, 440, L17
- Cardelli, J. A., Clayton, G. C., & Mathis, J. S. 1989, *ApJ*, 345, 245
- Casement, L. S., McLean, I. S., & Rischer, R. E. 1993, in *Infrared Detectors and Instrumentation*, ed. A. Fowler (Bellingham:SPIE), 569
- Chiosi, C., Bertelli, G., & Bressan, A. 1992, *Ann. Rev. Astron. & Astroph.*, 30, 235
- Chiosi, C., & Maeder, A. 1986, *Ann. Rev. Astron. & Astroph.*, 24, 329
- Clayton, D. D. 1983, *Principles of Stellar Evolution and Nucleosynthesis* (Chicago: University of Chicago Press), 48
- Conti, P. S., Garmany, C. D., de Loore, C., & Vandebaren, D. 1983, *ApJ*, 274, 302
- Conti, P. S. 1988, O-stars and WR stars, *NASA SP-497*, eds. P. S. Conti, & A. Underhill, 168
- Conti, P. S., & Vacca, W. D. 1990, *AJ*, 100, 431

- Conti, P. S. 1991, in *Massive Stars in Starbursts*, eds. C. Leitherer, N. R. Walborn, T. M. Heckman, & C. A. Norman (Cambridge: Cambridge University Press), 21
- Conti, P. S., Hanson, M. M., Morris, P. W., Willis, A. J., & Fossey, S. J. 1995, *ApJ*, submitted
- Cotera, A. S., Erickson, E. F., Simpson, J. P., Colgan, S. W. J., & Reike, M. 1992, *BAAS*, 24, 765
- Cotera, A. S., Erickson, E. F., Allen, D. A., Colgan, S. W. J., Simpson, J. P., & Burton, M. G. 1994, in *Proc. of the Airborne Astronomy Symp. on the Galactic Ecosystem: From Gas to Stars to Dust*, eds. M. R. Haas, J. A. Davidson, & E. F. Erickson (San Francisco: ASP), 511
- Cotera, A. S. 1995, PhD Thesis, Stanford University
- Cox, P., Krugel, E., & Mezger, P. G. 1986, *A&A*, 155, 380
- Cox, P., & Mezger, P. G. 1989, *ARA&A*, 1, 49
- Crowther, P. A., Hillier, D. J., & Smith, L. J. 1995, *A&A*, 293, 172
- Davidson, K. 1989, in *Physics of Luminous Blue Variables*, eds. K. Davidson, A. F. J. Moffat, & H. J. G. L. M. Lamers (IAU Conf. Proc. 113), 101
- Davidson, J. A., Morris, M., Harvey, P. M., Lester, D. F., Smith, B., & Werner, M. W. 1994, in *The Nuclei of Normal Galaxies: Lessons from the Galactic Center*, eds. R. Genzel, & A. I. Harris (Dordrecht: Kluwer), 231
- Davidson, J. A., Werner, M. W., Wu, X., Lester, D. F., Harvey, P. M., Joy, M., & Morris, M. 1992, *ApJ*, 387, 189
- Davies, J. K. (ed.) 1991, *UKIRT Observer's Manual*, 2.7.5
- Dent, W. A., Werner, M. W., Gatley, I., Becklin, E. E., Hildebrand, R. H., Keene, J., & Whitcomb, S. E. 1982, *AIP Conf. Proc.*, 83, *The Galactic Center*, ed. R. Riegler, & R. Blandford (New York: AIP), 33
- Divan, L., & Burnichon-Prevot, M.-L. 1988, *O-stars and WR stars*, NASA SP-497, eds. P. S. Conti, & A. Underhill, 1
- Downes, D., Goss, W. M., Schwarz, U. J., & Wouterloot, J. G. A. 1978, *A&AS*, 35, 1
- Eckart, A., Genzel, R., Hofmann, R., Sams, B. J., & Tacconi-Garman, L. E. 1995, *ApJ*, submitted
- Eenens, P. R., Williams, P. M., & Wade, R. 1991, *MNRAS*, 252, 300

- Eenens, P. R., & Williams, P. M. 1994, MNRAS, 269, 1082
- Ekers, R. D., van Gorkom, J. H., Schwarz, U. J., & Goss, W. M. 1983, A&A, 122, 143
- Elias, J. H., Frogel, J. A., Matthews, K., Geugebauer, G. 1982, AJ, 87, 1029
- Elias, J. H., Frogel, J. A., & Humphreys, R. M. 1985, ApJS, 57, 91
- Feynman, R. P., Leighton, R. B., & Sands, M. 1963, The Feynman Lectures on Physics (Addison-Wesley Publishing Co.: Reading), 30-4
- Figer, D. F., Becklin, E. E., McLean, I. S., & Morris, M. 1994, in Infrared Astronomy with Arrays, ed. I. S. McLean (Dordrecht: Kluwer), 545
- Figer, D. F., McLean, I. S., & Morris, M. 1995, ApJL, accepted
- Gatley, I., Becklin, E. E., Werner, M. W., & Harper, D. A. 1978, ApJ, 220, 822
- Gatley, I. 1989, in IAU Symp. 136, The Center of the Galaxy, ed. M. Morris (Dordrecht: Kluwer), 645
- Geballe, T. R., Genzel, R., Krabbe, A., Krenz, T., & Lutz, D. 1994, in Infrared Astronomy with Arrays, ed. I. S. McLean (Dordrecht: Kluwer), 73
- Genzel, R., Stacey, G. J., Harris, A. I., Townes, C. H., Geis, N., Graf, U. U., Poglitsch, A., & Stutzki, J. 1990, ApJ, 356, 160
- Glass, I. S., Moneti, A., & Moorwood, A. F. M. 1990, MNRAS, 242, 55P
- Goss, W. M., Schwarz, U. J., van Gorkom, J. H., & Ekers, R. D. 1985, MNRAS, 215, 69P
- Gusten, R., & Downes, D. 1980, A&A, 87, 6
- Gusten, R., & Downes, D. 1981, A&A, 99, 27
- Gusten, R., & Downes, D. 1983, A&A, 117, 343
- Gusten, R., & Henkel, C. 1983, A&A, 125, 136
- Gusten, R. 1989, in IAU Symp. 136, The Center of the Galaxy, ed. M. Morris (Dordrecht: Kluwer), 89
- Haller, J. W. 1992, PhD Thesis, The University of Arizona
- Hamann, W.-R., Koesterke, L., & Wessolowski, U. 1993, A&A, 274, 397

- Hamann, W.-R., Leuenhagen, U., Koesterke, L., & Wessolowski, U. 1992, *A&A*, 255, 200
- Hamann, F., DePoy, D. L., Johansson, S., & Elias, J. 1994, *ApJ*, 422, 626
- Hanson, M. M., & Conti, P. S. 1994, *ApJL*, 423, L139
- Hanson, M. M., & Conti, P. S. 1995, *ApJL*, submitted
- Harris, A. I., Krenz, T., Genzel, R., Krabbe, A., Lutz, D., Poglitsch, A., Townes, C. H., & Geballe, T. R. 1994, in *The Nuclei of Normal Galaxies: Lessons from the Galactic Center*, eds. R. Genzel, & A. I. Harris (Dordrecht: Kluwer), 223
- Heiles, C. 1994, *ApJ*, 436, 720
- Herbst, T. M., Beckwith, S. V. W., Forrest, W. J., & Pipher, J. L. 1993, *ApJ*, 105, 956
- Hillier, J. D. 1983, in *IAU Symp. 99, Wolf-Rayet stars: observations, physics, and evolution*, eds. C. W. H. de Loore, & A. J. Willis (Dordrecht: Kluwer), 225
- Ho, P. T., Jackson, J. M., Barrett, A. H., & Armstrong, J. T. 1985, *ApJ*, 288, 575
- Humphreys, R. M. 1989, in *Physics of Luminous Blue Variables*, eds. K. Davidson, A. F. J. Moffat, & H. J. G. L. M. Lamers (IAU Conf. Proc. 113), 3
- Humphreys, R. M. 1993, in *Massive Stars: Their Lives in the Interstellar Medium*, eds J. P. Casinelli, & E. B. Churchwell (ASP Conf. Proc. 35), 179
- Jackson, J. M., Geis, N., Genzel, R., Harris, A. I., Madden, S., Poglitsch, A., Stacey, G. J., & Townes, C. H. 1993, *ApJ*, 402, 173
- Johnson, H. L. 1966, *Ann. Rev. Astron. & Astroph.*, 4, 193
- Jones, T. J., & Hyland, A. R. 1986, *AJ*, 92, 805
- Killeen, N. E. B., Lo, K. Y., & Crutcher, R. 1992, *ApJ*, 385, 585
- Kiriakidis, M., Fricke, K. J., & Glatzel, W. 1993, *MNRAS*, 264, 50
- Kleinmann, S. G., & Hall, D. N. B. 1986, *ApJS*, 62, 501
- Kobayashi, Y., Okuda, H., Sato, S., Jugaku, J., & Dyck, H. M. 1983, *PASJ*, 35, 101
- Koesterke, L., Hamann, W.-R., & Wessolowski, U. 1992, *A&A*, 261, 535
- Koornneef, J. 1983, *A&A*, 128, 84
- Krabbe, A., Genzel, R., Drapatz, S., & Rotaciuc, V. 1991, *ApJL*, 382, L19

- Krabbe, A., Genzel, R., Eckart, A., Najarro, F., Lutz, D., Cameron, M., Kroker, H., Tacconi-Garman, L. E., Thatte, N., Weitzel, L., Drapatz, S., Geballe, T., Sternberg, A., & Kudritzki, R. 1995, *ApJ*, in press
- Lamers, H. J. G. L. M. 1989, in *Physics of Luminous Blue Variables*, eds. K. Davidson, A. F. J. Moffat, & H. J. G. L. M. Lamers (IAU Conf. Proc. 113), 135
- Lancon, A., & Rocca-Volmerange, B. 1992, *A&AS*, 96, 593
- Landini, M., Natta, A., Salinari, P., Oliva, E., & Moorwood, A. F. M. 1984, *A&A*, 134, 284
- Langer, N. 1989, *A&A*, 220, 135
- Langer, N., Hamann, W.-R., Lennon, M., Najarro, F., Pauldrach, A. W. A., & Puls, J. 1994, *A&A*, 290, 819
- Le Bertre, T., Epchtein, N., Gouiffes, C., Heydari-Malayeri, M., & Perrier, C. 1989, *MNRAS*, 225, 417
- Lebofsky, M. M., & Rieke, G. H. 1987, in *AIP Conf. Proc. 155, The Galactic Center*, ed. D. C. Backer (NY: AIP), 71
- Lee, H. M., & Nelson, L. A. 1988, *ApJ*, 334, 688
- Leep, E. M., Perry, D. N., Conti, P. S. 1983, *ApJ*, 268, 228
- Levine, D. A., Figer, D. F., Morris, M., & McLean, I. S. 1995, *ApJL*, accepted
- Linke, R. A., Stark, A. A., & Frerking, M. A. 1981, *ApJ*, 243, 147
- Lis, D. C., Menten, K. M., Serabyn, E., & Zylka, R. 1994, *ApJL*, 423, L39
- Liszt, H. S., van der Hulst, J. M., Burton, W. B., & Ondrechen, M. P. 1983, *A&A*, 126, 341
- Lucy, L. B., & Abbott, D. C. 1993, *ApJ*, 405, 738
- Lundstrom, I., & Stenholm, B. 1984, *A&AS*, 58, 163
- Lutz, D., Krabbe, A., Genzel, R., Blietz, M., Drapatz, S. & van der Werf, P. P. 1994, in *The Nuclei of Normal Galaxies: Lessons from the Galactic Center*, eds. R. Genzel, & A. I. Harris (Dordrecht: Kluwer), 373
- Maeder, A. 1989, in *Physics of Luminous Blue Variables*, eds. K. Davidson, A. F. J. Moffat, & H. J. G. L. M. Lamers (IAU Conf. Proc. 113), 15
- Maeder, A. 1991a, *A&A*, 242, 93

- Maeder, A. 1991b, QJRAS, 32, 217
- Maeder, A., & Conti, P. S. 1994, Ann. Rev. Astron. & Astroph., 32, 227
- Maeder, A., & Meynet, G. 1987, A&A, 182, 243
- Maeder, A., & Meynet, G. 1989, A&A, 210, 155
- Maeder, A., & Meynet, G. 1994, A&A, 287, 803
- Maillard, J. P., & Chauville, J. 1976, Journal of Molecular Spectroscopy, 63, 120
- Massey, P., Valdes, F., & Barnes, J. 1992, in IRAF Users Guide (Tucson: NOAO)
- McCaughrean, M. J. 1988, PhD Thesis, University of Edinburgh
- McGregor, P. J., Hillier, D. J., & Hyland, A. R. 1988a, ApJ, 334, 639
- McGregor, P. J., Hyland, A. R., & Hillier, D. J. 1988b, ApJ, 324, 1071
- McGregor, P. J. 1989, in Physics of Luminous Blue Variables, eds. K. Davidson, A. F. J. Moffat, & H. J. G. L. M. Lamers (IAU Conf. Proc. 113), 165
- McLean, I. S., et al. 1993, in Infrared Detectors and Instrumentation, ed. A. Fowler (Bellingham:SPIE), 513
- McLean, I. S., et al. 1994, in Instrumentation in Astronomy VIII, ed. D. Crawford (Bellingham:SPIE), 457
- McLean, I. S. 1995, in IAU Symp. 167, New Developments in Array Technology & Applications, ed A. G. Davis Philip, K. A. Janes & A. R. Upgren (Dordrecht: Kluwer), 1069
- Meynet, G. 1995, A&A, in press
- Meynet, G., Maeder, A., Schaller, G., Schaerer, D., & Charbonnel, C. 1994, A&AS, 103, 97
- Mezger, P. G., Zylka, R., Salter, C. J., Wink, J. E., Chini, R., Kreysa, E., & Tuffs, R. 1989, A&A, 209, 337
- Moneti, A., Glass, I. S., & Moorwood, A. F. M. 1994, MNRAS, 268, 194
- Morris, M. 1993, ApJ, 408, 496
- Morris, M. 1994, in The Nuclei of Normal Galaxies: Lessons from the Galactic Center, eds. R. Genzel, & A. I. Harris (Dordrecht: Kluwer), 185

- Morris, M., Davidson, J. A., & Werner, M. W. 1995, in Proc. of the Airborne Astronomy Symp. on the Galactic Ecosystem: From Gas to Stars to Dust, eds. M. R. Haas, J. A. Davidson, & E. F. Erickson (San Francisco: ASP), 477
- Nagata, T., Woodward, C. E., Shure, M., Pipher, J. L., & Okuda, H. 1990, ApJ, 351, 83
- Nagata, T., Hyland, A. R., Straw, S. M., Sato, S., & Kawara, K. 1993, ApJ, 406, 501
- Nagata, T., Woodward, C. E., Shure, M., & Kobayashi, N. 1995, AJ, 109, 1676
- Najarro, F., Hillier, D. J., Kudritzki, R. P., Krabbe, A., Genzel, R., Lutz, D., Drapatz, S., & Geballe, T. R. 1994, A&A, 285, 573
- Odenwald, S. F., & Fazio, G. G. 1984, ApJ, 283, 601
- Okuda, H., Shibai, H., Nakagawa, T., Matsuhara, H., Kobayashi, Y., Kaifu, N., Nagata, T., Gatley, I., & Geballe, T. R. 1990, ApJ, 351, 89
- Oliva, E., & Origlia, L. 1992, A&A, 254, 466
- Origlia, L., Moorwood, A. F. M., & Oliva, E. 1993, A&A, 280, 536
- Palmer, C., & Loewen, E. (eds.), 1994, Diffraction Grating Handbook (Milton Roy Company: Rochester), 56
- Panagia, N. 1973, AJ, 78, 929
- Panagia, N., & Felli, M. 1975, A&A, 39, 1
- Parker, J. W., Heap, S. R., & Malumuth, E. M. 1995, ApJ, in press
- Pauls, T., Downes, D., Mezger, P. G., & Churchwell, E. 1976, A&A, 46, 407
- Pedlar, A., Anantharamaiah, K. R., Ekers, R. D., Goss, W. M., van Gorkom, J. H., Schwarz, U. J., & Zhao, J.-H. 1989, ApJ, 342, 769
- Poglitsch, A., Stacey, G. J., Geis, N., Haggerty, M., Jackson, J., Rumitz, M., Genzel, R., & Townes, C. H. 1991, ApJL, 374, L33
- Ramsay, S. K., Mountain, C. M., & Geballe, T. R. 1992, MNRAS, 259, 751
- Rieke, G. H., Rieke, M. J., & Paul, A. E. 1989, ApJ, 336, 752
- Salpeter, E. E. 1955, ApJ, 121, 161
- Schmutz, W., Hamann, W.-R., & Wessolowski, U. 1989, A&A, 210, 236

- Schroeder, D. J., & Hilliard, R. L. 1980, *Applied Optics*, 19, 2833
- Sellgren, K., Hall, D. N. B., Kleinmann, S. G., & Scoville, N. Z. 1987, *ApJ*, 317, 881
- Serabyn, E. & Gusten, R. 1987, *A&A*, 184, 133
- Serabyn, E., & Gusten, R. 1991, *A&A*, 242, 376
- Serabyn, E., & Morris, M. 1994, *ApJL*, 424, L91
- Serabyn, E., Lacy, J. H., & Achtermann, J. M. 1992, *ApJ*, 395, 166
- Shu, F. H., Adams, F. C., & Lizano, S. 1987, *Ann. Rev. Astron. & Astroph.*, 25, 23
- Silverstone, M. D. 1994, C-Project (UCLA: Los Angeles)
- Simon, M., Felli, M., Cassar, L., Fischer, J., & Massi 1983, *ApJ*, 266, 623
- Smith, L. F. 1968, *MNRAS*, 140, 409
- Smith, L. F., & Hummer, D. G. 1988, *MNRAS*, 230, 511
- Smith, L. F., Shara, M. M., & Moffat, A. F. J. 1990, *ApJ*, 358, 229
- Smith, L. F., Meynet, G., & Mermilliod, J. C. 1994, *A&A*, 287, 835
- Sofue, Y. 1985, *PASJ*, 37, 697
- Spitzer, L. 1978, *Physical Process in the Interstellar Medium*, (New York: John Wiley & Sons), 160
- Stark, A. A., Bally, J., Wilson, R. W., & Pound, M. W. 1989, in *IAU Symp. 136, The Center of the Galaxy*, ed. M. Morris (Dordrecht: Kluwer), 129
- Taylor, G., Morris, M., & Schulman, E. 1993, *AJ*, 106, 1978
- Theodossiou, E., & Danezis, E. 1991, *Astrophys. & Space Sci.*, 183, 91
- Tsuboi
- Uchida, K. & Gusten, R. 1995, *A&A*, in press
- van de Hulst, H. C. 1946, *Recherches Astr. Obs. d'Utrecht*, 11, part 1
- van der Hucht, K. A., Conti, P. S., Lundstrom, I., and Stenholm, B. 1981, *Space Sci. Rev.*, 28, 227

- van der Hucht, K. A., Hidayat, B., Admiranto, A. G., Supelli, K. R., & Doom, C. 1988, *A&A*, 199, 217
- Wainscoat, R. J., & Cowie, L. L. 1992, *AJ*, 103, 332
- Walborn, N. R. 1971, *ApJS*, 23, 257
- Wannier, P. G. 1989, in *IAU Symp. 136, The Center of the Galaxy*, ed. M. Morris (Dordrecht: Kluwer), 107
- Williams, P. M. 1983, in *IAU Symp. 99, Wolf-Rayet stars: observations, physics, and evolution*, eds. C. W. H. de Loore, & A. J. Willis (Dordrecht: Kluwer), 73
- Williams, P. M., & Eenens, P. R. J. 1989, *MNRAS*, 240, 445
- Williams, P. M., van der Hucht, K. A., & The, P. S. 1987, *A&A*, 182, 91
- Winnberg, A., Baud, B., Matthews, H. E., Habing, H. J., & Olton, F. M. 1985, *ApJL*, 291, L45
- Wolf, C. J. E., & Rayet, G. 1867, *Comptes Rendus*, 65, 292
- Woolf, N. J., Schwarzschild, M., & Rose, W. K. 1964, *ApJ*, 140, 833
- Wright, A. E., & Barlow, M. J. 1975, *MNRAS*, 170, 41
- Wynn-Williams, C. G., Becklin, E. E., Matthews, D., & Neugebauer, G. 1978, *MNRAS*, 183, 237
- Yusef-Zadeh, F. 1986, PhD Thesis, Columbia University
- Yusef-Zadeh, F., Morris, M., & Chance, D. 1984, *Nature*, 310, 557
- Yusef-Zadeh, F. & Morris, M. 1987a, *AJ*, 94, 1178
- Yusef-Zadeh, F. & Morris, M. 1987b, *ApJ*, 320, 545
- Yusef-Zadeh, F., Morris, M., & van Gorkom, J. H. 1989, in *IAU Symp. 136, The Center of the Galaxy*, ed. M. Morris (Dordrecht: Kluwer), 275
- Zhao, J.-H., Desai, K., Goss, W. M., & Yusef-Zadeh, F. 1993, *ApJ*, 418, 235
- Zylka, R., Mezger, P. G., & Wink, J. E. 1990, *A&A*, 234, 133